

Sensitivity and Noise Analysis of 4 km Laser Interferometric Gravitational Wave Antennae

by

Rana Adhikari

Submitted to the Department of Physics

in partial fulfillment of the requirements for the degree of

Doctor of Philosophy

at the

MASSACHUSETTS INSTITUTE OF TECHNOLOGY

July 2004

© Rana Adhikari, MMIV. All rights reserved.

The author hereby grants to MIT permission to reproduce and
distribute publicly paper and electronic copies of this thesis document
in whole or in part.

Author
Department of Physics
July 7, 2004

Certified by
Rainer Weiss
Professor
Thesis Supervisor

Certified by
Peter Fritschel
Principal Research Scientist
Thesis Co-Supervisor

Accepted by
Thomas J. Greytak
Associate Department Head for Education

Sensitivity and Noise Analysis of 4 km Laser Interferometric Gravitational Wave Antennae

by

Rana Adhikari

Submitted to the Department of Physics
on July 7, 2004, in partial fulfillment of the
requirements for the degree of
Doctor of Philosophy

Abstract

Around the world, efforts are underway to commission several kilometer-scale laser interferometers to detect gravitational radiation. In the United States, there are two collocated interferometers in Hanford, Washington and one interferometer in Livingston, Louisiana. Together, these three interferometers form the Laser Interferometric Gravitational-wave Observatory (LIGO).

The core of the work described in this thesis is the modeling and reduction of the noise in the interferometers which limits their ultimate sensitivity.

A vital component of the noise reduction is the modeling, design, and implementation of ~ 100 feedback control systems. The most critical of these systems are described and motivated.

Although improvements are continuously being made to the stability and noise character of these detectors, several months of data have been collected. Various efforts are underway to search through these data for gravitational wave signals. Included here, is a description of a search made through the data for signals from the ringdown of the quasi-normal modes of Kerr black holes.

In addition, several possible future improvements to the detectors are outlined.

Thesis Supervisor: Rainer Weiss
Title: Professor

Thesis Co-Supervisor: Peter Fritschel
Title: Principal Research Scientist

Acknowledgments

I have had the uncommon luck of working with many people in the project. Its probably true that I've learned something from each and so a complete list of people I would thank would make this thesis so thick that even fewer people would read it. Instead I will just thank the people who have given me the most work to do.

To Mike, thanks for teaching me how to drag wipe optics and how to calibrate a scope probe. Thanks for yelling at me if I (or any other grad student) made a mess in the machine shop. Thanks for all the free food and for taking that lemon off of my hands.

To Peter, thanks for putting up with all of those bad measurements, ideas, and electronics. And for that timely invitation to help out with that 15 meter cavity.

To Rai, thanks for hiring me. This is the longest I've ever held a job. Thank you for letting me practice with one of your interferometers for a few years. And most of all for being an example of the integrity and the passion with which science should be done.

-
- Rana February 17, 2007

Contents

Introduction	19
1 Gravitational Radiation	21
1.1 Gravitational Radiation in General Relativity	22
1.1.1 Measurable Effect on Free Masses	23
1.1.2 Radiation Amplitudes	24
1.2 Astrophysical Sources	25
1.2.1 Monochromatic Signals	25
1.2.2 Stochastic Background	27
1.2.3 Bursts	27
1.2.4 Binary Inspiral	28
1.2.5 Ringdowns	30
2 Gravitational Wave Antennae	33
2.1 Resonant Mass Detectors (Bars)	34
2.2 Laser Interferometers	34
2.2.1 The Michelson Interferometer	35
2.2.2 Fabry-Perot Resonators	37
2.2.3 Power Recycling	37
3 Signal Extraction	41
3.1 Signal Readout Scheme	42
3.2 Elements of the Sensing Matrix	44

3.3	Dark Port Signal Generation	48
4	The Noises	51
4.1	Displacement Noises	52
4.1.1	Seismic Noise	52
4.1.2	Thermal Noise	54
4.1.3	Radiation Pressure	59
4.1.4	Actuator Electronics Noise	60
4.1.5	Angle to Length	63
4.2	Sensing Noises	65
4.2.1	Laser Amplitude Noise	65
4.2.2	Laser Frequency Noise	66
4.2.3	Oscillator Amplitude Noise	68
4.2.4	Oscillator Phase Noise	70
4.2.5	Beam Clipping on the Optical Tables	71
4.2.6	Auxilliary Length Controls	72
4.2.7	Shot Noise	74
4.2.8	Readout Electronics	76
4.3	Some Notes about the Noise	77
4.3.1	The Status of the Noise	77
4.3.2	A Brief History of the Noise	78
4.3.3	Evolution of Phase Sensitivity	80
5	The Control Systems	87
5.1	The Length Control Loops	89
5.1.1	Allowed Residual Deviations	90
5.1.2	Noise Pollution	94
5.1.3	The real loops	95
5.1.4	The Common Mode Servo	98
5.2	Angular Controls	105
5.3	Local Damping	107

5.4	Seismic Servos	109
5.4.1	Microseismic Feed-Forward	111
5.4.2	Piezo-electric Pre-Isolator	113
6	Calibration	115
6.1	Interferometer Response Model	116
6.2	Actuator Calibration	118
6.2.1	Absolute Calibration	118
6.2.2	Frequency Response	119
6.3	Calibration tracking	119
6.4	Directions for the future	119
7	Data Analysis for Black Hole Ringdowns	121
7.1	Overview of the Method	122
7.1.1	Matched Filtering	123
7.1.2	Data Conditioning	126
7.1.3	Template Bank Generation	128
7.2	Coincidence Analysis	129
7.2.1	Time	129
7.2.2	Frequency	129
7.2.3	Q	129
7.2.4	Amplitude	130
7.3	Simulations	130
7.3.1	Software Injections	130
7.3.2	Hardware Injections	134
7.4	Results	135
7.4.1	Distribution of triggers	135
7.4.2	Coincident Events	136
7.5	Examination of the Remaining Coincidences	138
7.5.1	Study of the Remaining Events	139
7.6	Future Improvements	142

7.7 Conclusions	143
8 The Future	145
8.1 Possible Future Improvements	146
8.1.1 Seismic Isolation	146
8.1.2 Output Mode Cleaner	146
8.1.3 Thermal Compensation	147
8.1.4 Oscillator Phase Noise	148
8.1.5 Laser Frequency Noise	149
8.1.6 Wavefront Sensing	150
8.1.7 Increased Laser Power	150
8.1.8 Low Noise DAC	151
8.1.9 Sweet Spot on the Suspension	152
8.1.10 Low internal mode noise	152
8.1.11 DC Readout	153
8.2 Estimating the future performance	154
Conclusion	157
Appendices	158
A Tables of Parameters	159
B Definitions and Conventions	163
C Mode Cleaner	167
C.1 Noise	170
C.1.1 Radiation Pressure	170
C.1.2 VCO Phase Noise	172
C.1.3 Servo Electronics	172
C.1.4 Acoustics/Clipping/Scattering	173
D Lock Acquisition	175

E Cavity Formulas	179
F Characterization of the Optical Parameters	181
F.1 Cavity Length Measurements	181
F.1.1 Arm Cavity Lengths	181
F.1.2 Schnupp Asymmetry	182
F.1.3 Recycling Cavity Length	183
F.1.4 Mode Cleaner Length	183
F.2 Transmissivity, Reflectivity, and Loss	183
F.2.1 Common arm loss via recycling gain	184
F.2.2 Differential arm loss via PRC to AS.Q & CMRR	184
F.2.3 T_{ITM}	185
F.2.4 T_{ETM}	185
F.2.5 $R_{BS} - T_{BS}$	185
F.3 Contrast	186
F.4 Metrology	186
G Interferometer Sub-Systems	187
G.1 Core Optics	187
G.2 Suspensions	187
G.2.1 Local Sensing and Actuation	188
G.3 Seismic Isolation	189
G.4 Pre-Stabilized Laser	189
G.4.1 Laser	189
G.4.2 Frequency Stabilization Servo (FSS)	190
G.4.3 Pre-Mode Cleaner (PMC)	192
G.4.4 Intensity Stabilization Servo (ISS)	192
G.5 Input Optics	193
H The Photodetectors	195
H.1 AS_I Servo	197

List of Figures

1-1	Effect of gravitational waves on Test particles	24
1-2	Known Pulsars	26
2-1	Michelson Diagram	35
2-2	PRM Diagram	38
3-1	Length Definitions	42
3-2	LLO Optical Plant	45
4-1	Seismic Spectra	53
4-2	BSC Stack Transfer Function	54
4-3	Violin Modes	58
4-4	Actuation Electronics	60
4-5	Coil Driver	61
4-6	Dewhitening Filter	62
4-7	DAC Noise	63
4-8	Frequency Noise Couplings	69
4-9	POB Noises	73
4-10	Sensing Electronics	77
4-11	S3 Noise	81
4-12	LLO Noise History	82
4-13	S1 Noise Curves	83
4-14	S2 Noise Curves	84
4-15	S3 Noise Curves	85

4-16 Phase Noise	86
5-1 LSC Block Diagram	90
5-2 Length Disturbances	94
5-3 Length Loops	95
5-4 Residual Fringe Offsets	96
5-5 Laser Frequency Noise	99
5-6 CM Servo Block Diagram	100
5-7 CM Actuators	101
5-8 CM Loops	102
5-9 CM Noise	103
5-10 Residual Frequency Noise	104
5-11 ASC Block Diagram	107
5-12 OSEM wiring	108
5-13 SUS Screen	109
5-14 Pendulum Damping	110
5-15 Tidal Prediction	112
5-16 PEPI Performance	114
6-1 L ₋ Servo Model	117
7-1 Ringdown Pipeline	123
7-2 Template Spacing (f,Q)	125
7-3 Template Spacing (M,a)	126
7-4 Parameter Estimation	131
7-5 L1 Detection Efficiency	132
7-6 H1 Detection Efficiency	133
7-7 Injection Amplitudes	134
7-8 Histograms of the Bands	135
7-9 Number of triggers v. Frequency	136
7-10 Histogram of Coincidences	137

7-11 Time Lags	138
8-1 S5 Noise	155
C-1 Mode Cleaner Noise Budget	171
G-1 Suspension Diagram	188
G-2 BSC Stack	190
H-1 Simplified Photodetector Schematic	196
I-1 Peanut (plus)	200
I-2 Peanut (cross)	201
I-3 Peanut (un-polarized)	202

List of Tables

7.1	Coincident Events in S2	139
A.1	Fundamental Constants	159
A.2	Large Optic's Parameters	160
A.3	Variable Definitions	161
A.4	Acronym Definitions	162
C.1	Small Optic's Parameters	169
C.2	Mode Cleaner Parameters	169
H.1	Nominal PD Parameters	198

Introduction

A handful of kilometer scale, laser interferometers have begun operation in the last few years with the goal of detecting gravitational waves. They are all steadily approaching their designed sensitivities, alternating data taking runs with further detector improvements. This worldwide network of observatories includes the German-British GEO600 ¹ [1], the Japanese TAMA ²[2], and a set of 3 interferometers in the United States called LIGO ³ [3, 4]. Also expected to come on-line in the near future is the Italian-French VIRGO ⁴ [5]. All of these observatories employ (or will employ) enhanced Michelson interferometers illuminated by highly stabilized, medium power lasers operating at 1064 nm. All of the interferometers' optics are suspended by seismic isolation systems and are housed in high to ultra-high vacuum beamtubes.

This thesis only describes the LIGO detectors, concentrating on the Louisiana 4 km interferometer.

Chapter 1 describes briefly the generation of gravitational waves, speculations on possible sources, and their detectability based on a theoretical noise estimate of the interferometers.

Chapter 2 motivates the design of the power recycled, Fabry-Perot Michelson interferometer configuration used in LIGO.

Chapter 3 describes the scheme used to readout the signals containing information about the interferometer lengths and also the gravitational wave signal.

Chapter 4 lists all of the significant noise sources, their coupling mechanisms, and

¹ <http://www.geo600.uni-hannover.de>

² <http://tamago.mtk.nao.ac.jp>

³ <http://ligo.caltech.edu>

⁴ <http://www.virgo.infn.it>

makes estimates for their contribution to the total noise budget. This chapter and the following one are the core of the thesis.

Chapter 5 discusses the control systems, mainly focusing on the length controls: the motivation for controls, the troubles with their noise, and some transfer functions of control loops.

Chapter 7 describes a search made through the data for damped sinusoid signals.

Chapter 8 gives examples of work that can be done on these first generation of interferometers to dramatically increase the event rate.

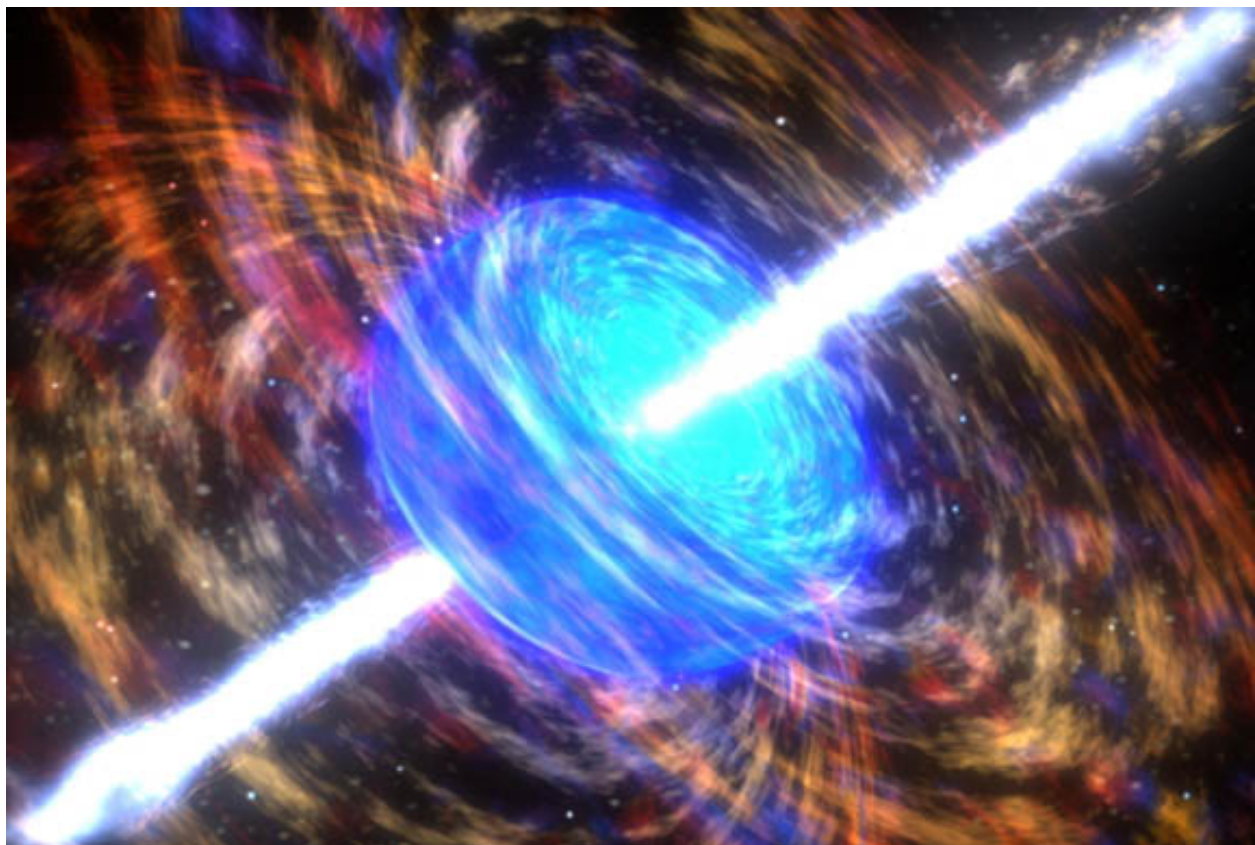
The Appendices provides some further details on topics which are briefly mentioned in the main text.

This work, and the LIGO Laboratory, is supported by the National Science Foundation⁵, grant PHY-0107417.

⁵<http://www.nsf.gov/>

Chapter 1

Gravitational Radiation



This chapter describes gravitational waves and their possible sources.

Section 1.1 describes the concept of gravitational waves and the space-time strain which we expect to measure in the far-field of a radiator.

Section 1.2 discusses 4 different classes of signals and is a review of current source strength and rate estimates.

1.1 Gravitational Radiation in General Relativity

The theory of General Relativity [6] describes gravity as a consequence of the curvature of space and time (or space-time). One of the predictions of the theory is gravitational radiation from fluctuating mass-energy distributions [7]. Although these ripples can, in principle, severely distort the space and time very near the radiator, far from the source one can express the effect of these waves as small perturbations to the otherwise flat space-time background. In this weak field limit the space-time metric can be approximated as

$$g_{\mu\nu} \simeq \eta_{\mu\nu} + h_{\mu\nu}, \quad \text{where} \quad |h_{\mu\nu}| \ll 1 \quad (1.1)$$

and where $\eta_{\mu\nu}$ is the Minkowski metric representing flat space and $h_{\mu\nu}$ is the perturbation to flat space due to the gravity wave.

By an adept coordinate transform [7] the gravitational wave may be written as:

$$h_{\mu\nu}(z, t) = \begin{pmatrix} 0 & 0 & 0 & 0 \\ 0 & -h_+ & h_\times & 0 \\ 0 & h_\times & h_+ & 0 \\ 0 & 0 & 0 & 0 \end{pmatrix} \cos \omega \left(\frac{z}{c} - t \right) \quad (1.2)$$

where ω is the gravitational wave frequency and the two independent polarizations are h_+ and h_\times .

1.1.1 Measurable Effect on Free Masses

From an observers point of view, we can ask about what the measurable effects are of gravitational waves. To answer this we set up two free masses, one located at the origin and one located a distance, $x = L$, from the origin. We can measure the separation between these two masses by sending a plane wave of light from the origin to bounce off of the far mass and measure the phase of the return wave. The accrued round trip phase is:

$$\Phi_{rt}(t_{rt}) = \int_0^{t_{rt}} 2\pi f dt \quad (1.3)$$

where t_{rt} is the time it takes for the light to make one round trip and f is the frequency of the light. In the absence of radiation, we can do the integral by changing it into an integral over length. To do this we use the flat space metric, $\eta_{\mu\nu}$, to relate space and time for light ($t_{rt} = 2L/c$ and $dt = dx/c$).

In the presence of a gravitational wave, we instead use Equation 1.1 to calculate the space-time interval so now the round trip phase is

$$\Phi_{rt}(t_{rt}) = 2 \frac{2\pi f}{c} \int_0^L \sqrt{|g_{xx}|} dx \simeq 2(1 - h_+/2) \frac{2\pi L}{\lambda} \quad (1.4)$$

in the case of a "plus" oriented wave with a period much longer than the round trip light travel time. Repeating this integral, but doing the integration now along the y-axis, we get that $\Phi_{rt} \simeq 2(1 + h_+/2)(2\pi L/\lambda)$. The difference in the phase shift between the two arms gives $\Delta\Phi \simeq 2h_+(2\pi L/\lambda)$.

Interpreting the phase shifts as length measurements indicates that the apparent length of each arm is stretched and compressed as the gravity wave passes. A diagram of this is shown in Figure 1-1. The length shift is proportional to the original distance between the masses,

$$\frac{\Delta L}{L} = \frac{1}{2}h_+ \quad (1.5)$$

which is why a gravitational wave is usually said to cause a strain in space.

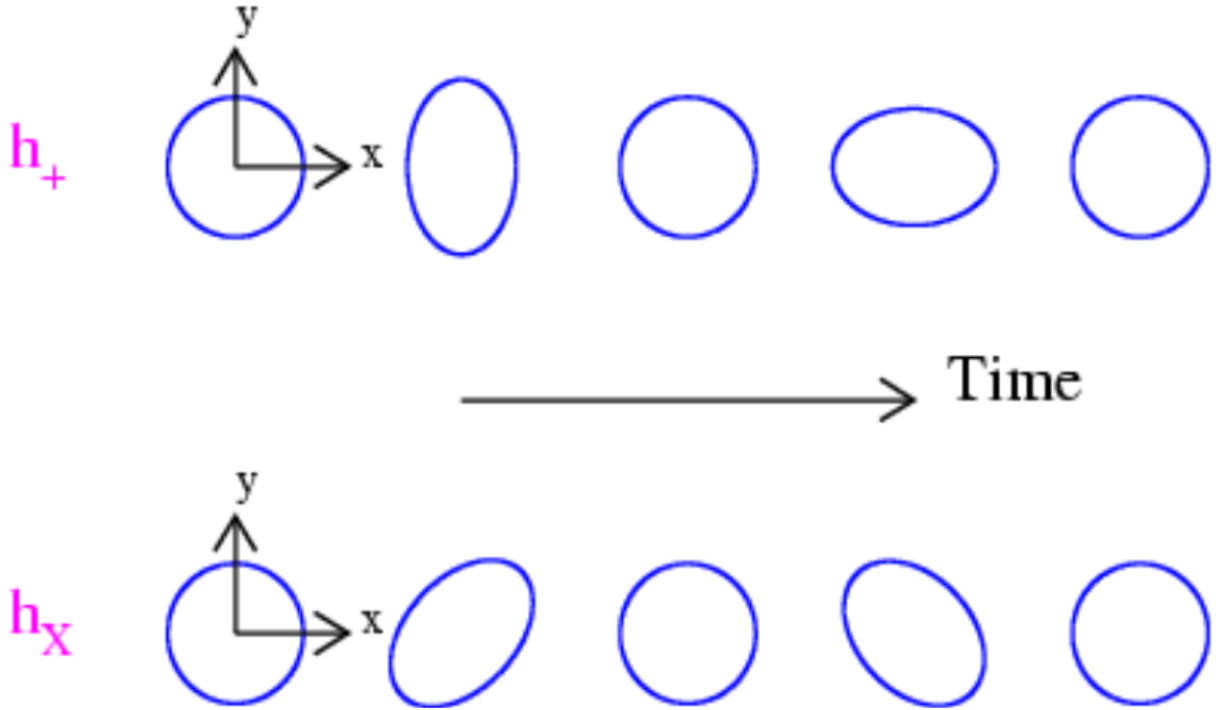


Figure 1-1: Shown are the effects of + and \times waves propagating in the z direction on a circle of test particles in the x - y plane.

1.1.2 Radiation Amplitudes

Conservation of mass-energy, linear momentum, and angular momentum rule out monopole, dipole, and "magnetic" dipole radiation, respectively. With no conservation law to rule it out, the leading term in gravitational radiation is the oscillating quadrupole mass-energy distribution. In addition, for the wave to carry away energy from the source, the amplitude of the wave must decay as $\sim 1/r$.

A rough estimate for the strain amplitude is[8]:

$$\begin{aligned}
 h &\sim \frac{G \ddot{Q}}{c^4 r} \\
 &\sim \frac{G E_{kin}^{ns}}{c^4 r} \\
 &\sim 10^{-19} \left(\frac{E_{kin}^{ns}}{M_\odot c^2} \right) \left(\frac{1 \text{ Mpc}}{r} \right)
 \end{aligned} \tag{1.6}$$

using the estimate that the non-spherical kinetic energy, E_{kin}^{ns} , contributing to gravitational radiation is roughly equal to the second time derivative of the quadrupole moment, \ddot{Q} . This is a very optimistic estimate assuming a huge amount of energy is converted into gravitational waves in a neighboring galaxy. However, it indicates an upper limit to expected signal strengths.

The radiated energy (luminosity) is related to the strain by [9]:

$$\begin{aligned}\frac{dE_{GW}}{dt} &= \frac{c^3 r^2}{4G} (h_+^2 + h_x^2) \\ &\simeq 10^{34} \left(\frac{r}{1 \text{ Mpc}} \right)^2 \left(\frac{|h|}{10^{-23}} \right)^2 \text{ Watts}\end{aligned}\tag{1.7}$$

This estimate gives a very small measurable strain, even though the radiated energy is quite large; space-time is a very 'stiff' wave medium.

1.2 Astrophysical Sources

The following sections briefly describe some types of gravitational wave sources and their predicted strengths, frequencies, and detection rates. A more extensive survey can be found in Refs. [8, 10]

Later in the thesis (Chapter 7), a search for ringdowns of black hole quasi-normal modes is described. To accompany that work, the end of this chapter describes the generation of ringdown signals.

1.2.1 Monochromatic Signals

One class of signal being searched for emits radiation at a single frequency, producing a long continuous wave in the source's reference frame. The most commonly described monochromatic source is the radiation from a non-axisymmetric pulsar. The time-dependent quadrupole moment necessary to generate gravitational waves may come from a wobbling rotation (spin axis not aligned with a principle axis) or a small deviation of the pulsar shape from perfect axial symmetry (a bump). In the latter case the gravitational wave strain can be written as [8]

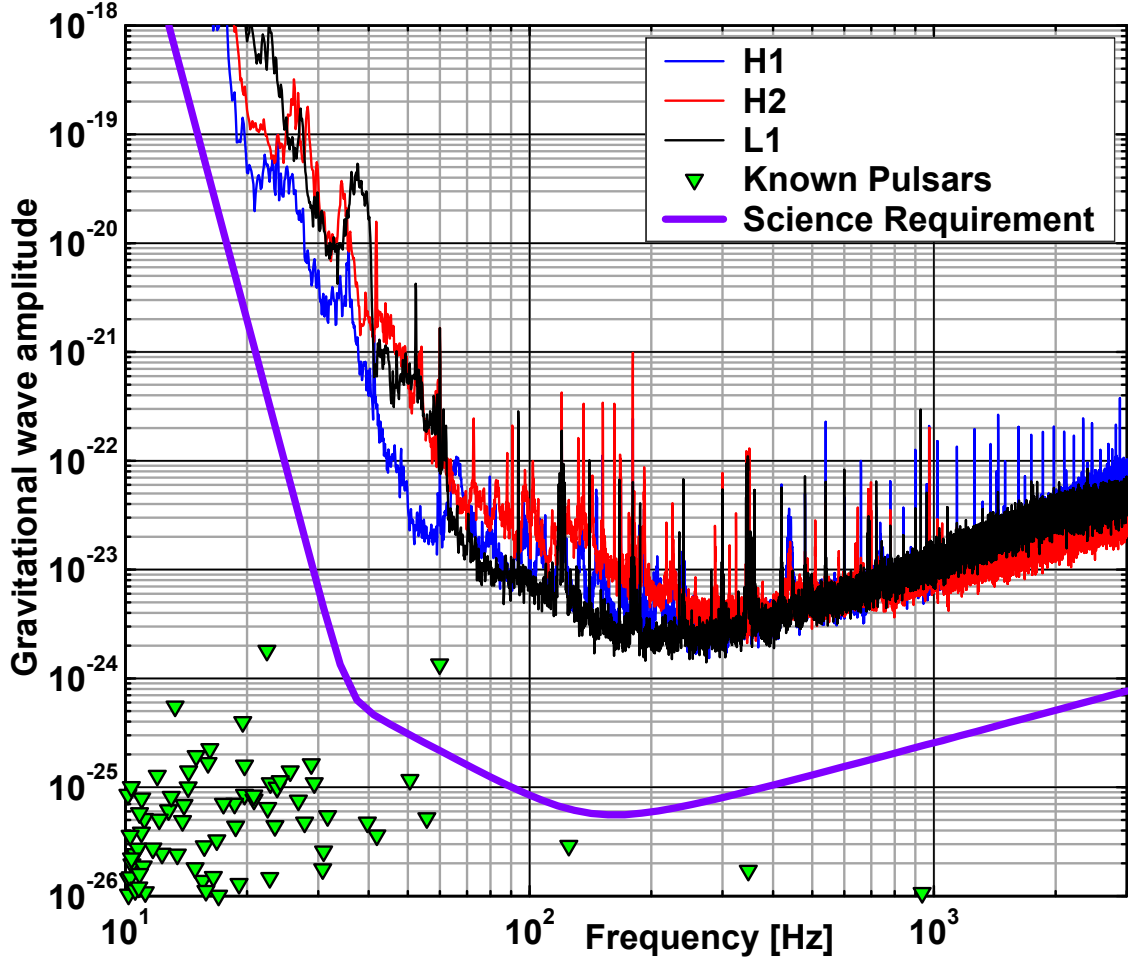


Figure 1-2: Upper limits on the amplitudes of many known pulsars compared to the upper limit set by each interferometer separately during the second LIGO science run (S2). The pulsar amplitude limits are made by assuming that all of the rotational energy loss of the pulsar goes into gravitational radiation. The 'SRD' curve is the LIGO Science Requirement for a 4 km interferometer after 1 year of integration.

$$h \sim 2 \times 10^{-26} \left(\frac{f_{rot}}{1 \text{ kHz}} \right)^2 \left(\frac{10 \text{ kpc}}{r} \right) \left(\frac{\epsilon}{10^{-6}} \right) \quad (1.8)$$

where f_{rot} is the frequency of rotation, r is the distance between the source and the detector, and $\epsilon \equiv (I_{xx} - I_{yy})/I_{zz}$, is the equatorial ellipticity.

It has been suggested [11] and somewhat supported by observation [12] that low-mass X-ray binaries (LMXBs) reach an equilibrium where the spin-up torque due to accretion is balanced by the spin-down from gravitational wave emission.

Upper Limits and Measurements

Searches have been made for gravitational wave signals from pulsars; see for example [13, 14, 15] and references therein.

Figure 1-2 shows upper limits on the amplitudes of many known pulsars compared to the upper limit set by each interferometer separately during the S2 run. The amplitude of the dots are calculated by assuming that all of the rotational energy loss of the pulsar, determined by measuring the spin-down rate, goes into gravitational radiation.

1.2.2 Stochastic Background

Quite different in character from monochromatic sources is the stochastic background of gravitational radiation [16]. A stochastic background can have both cosmological and astrophysical sources such as amplification by inflation of zero-point metric fluctuations, phase transitions in the early universe, cosmic strings, and a large number of unresolved foreground sources such as binaries and supernovae [17].

Schemes for detecting a stochastic background generally involve cross-correlating the output of two or more detectors [18, 19, 17, 16].

The past and present analyses of a stochastic background have made some assumptions about the statistical character of the signal: it is isotropic, unpolarized, stationary, and Gaussian. These assumptions are discussed by Allen [20];

See [16] for a review of current upper limits and prospects for the future.

1.2.3 Bursts

A very large class of events are the unmodeled transients, or bursts. These are searched for quite differently than most of the other types of signals in this chapter. Most approaches involve looking for excess power in many narrow bands.

Some examples of the anticipated types of burst events being searched for are asymmetrical core collapse in supernovae, coalescence and merger of intermediate mass black holes, and most interestingly, the unknown.

Previous Searches

A review of burst searches made with resonant bar detectors is described elsewhere [21, 22]. Here I list past searches for gravitational wave bursts using laser interferometers and the strain amplitudes they were sensitive to:

- R. Forward Malibu, CA 1977 $h > 10^{-14}$ for 150 hours.
- D. Dewey MIT 1.5m 1985 $h > 10^{-13}$
- Glasgow / Max Planck 1989 $h > 5 \times 10^{-16}$
- LIGO/GEO S1 (Aug. 2002, 17 days) $h > 10^{-18}$
- LIGO/GEO S2 (Feb. 2003, 2 months) $h > 10^{-19}$

1.2.4 Binary Inspiral

An extensively studied source of gravitational wave is the decaying orbit of two compact objects, usually referred to as a binary inspiral. In the LIGO band, these objects can be neutron stars and/or black holes (NS/NS, BH/NS, BH/BH).

The waveforms, from the NS/NS inspiral, are believed to be sufficiently well modeled that one can search for these signals using a matched filter technique [23]. The BH/BH waveforms are much more difficult to calculate [24] and there is not as much confidence in these waveforms. Nevertheless, a matched filter search for these signals is currently being pursued as well.

As the orbit of the two bodies progresses in time, the orbital period and separation decrease due to energy loss through gravitational radiation. As the orbital separation decreases, the amplitude and frequency of the signal increase until the binary separation falls below the Innermost Stable Circular Orbit (ISCO) and the two stars plunge together and merge.

Reconstructing the merger of two neutron stars or two black holes is a very computationally intensive exercise and there are numerous, highly active efforts to calculate

these dynamics and the associated gravitational radiation waveforms using fast supercomputers [25].

Rate Estimates

The recent discovery of PSR J0737-3039 [26], a highly relativistic binary pulsar, increased the predicted rate of galactic NS/NS inspirals detectable by LIGO from one every few decades to one every few years [27]. Previous estimates of merger rates were dominated by the parameters of the famous PSR B1913+16 [28, 29]. This new binary (actually the first detected double pulsar system) has a 3X shorter coalescence time and a 7X smaller luminosity. These factors have radically changed the population and merger rate estimates for NS/NS binaries in the galaxy.

Although, at the time of this writing, there have been 7 double neutron star systems discovered [30], the detection rate estimates for LIGO are still precariously dependent on the tightest, darkest binary.

Upper Limits and Measurements

A few searches have been made so far for the signatures from NS/NS inspiral events [31, 32, 33]. No detections have been claimed yet. The stated upper limits for NS/NS inspirals in the galaxy are:

- Caltech 40m 4400 / year
- TAMA DT6 5000 / year (within 6 kpc)
- LIGO S1 170 / year
- LIGO S2 50 / year

The Caltech 40m upper limit comes from a short run made in November of 1994 using the 40 m prototype in Pasadena, CA in a non-recycled, non-optically recombined state. The TAMA DT6 (6th Data Taking run) data is from a recombined but not power recycled 300 m interferometer. Both the LIGO S1 & S2 data were taken with power-recycled interferometers operating in coincidence.

1.2.5 Ringdowns

There are three distinct phases in the coalescence of two compact objects. In the first stage, the two objects orbit each other. The orbit slowly decays due to energy loss into gravitational radiation. At the end of the inspiral phase, the two objects plunge together. For black holes, this is the complicated merger phase which is being studied numerically with fast supercomputers [34].

At some point after the merger, the black hole settles down to the point where it can be represented as a Kerr[35] black hole undergoing quasi-normal mode (QNM) oscillations [36]. This phase is called the ringdown phase. The ringdown phase does not necessarily require a binary inspiral; any perturbed Kerr black hole will ringdown through the emission of gravitational waves. In this sense, the ringdown signal is one of the purest waveforms predicted by General Relativity.

The most general stationary black hole metric is the Kerr-Newman metric[37], which has only three free parameters: mass (M), spin (J), and charge (Q). Two important special cases of this metric are the Schwarzschild metric (charge = 0, spin = 0):

$$ds^2 = - \left(1 - \frac{2GM}{c^2r}\right) c^2 dt^2 + \left(1 - \frac{2GM}{c^2r}\right)^{-1} dr^2 + r^2 d\theta^2 + r^2 \sin \theta^2 d\phi^2 \quad (1.9)$$

and the Kerr metric (charge = 0):

$$ds^2 = - \left(1 - \frac{2Mr}{\Sigma}\right) c^2 dt^2 - \frac{4aMr \sin \theta^2}{\Sigma} dt d\phi + \frac{\Sigma}{\Delta} dr^2 + \Sigma d\theta^2 + \left(r^2 + a^2 + \frac{2Mra^2 \sin \theta^2}{\Sigma}\right) d\phi^2 \quad (1.10)$$

where

$$a \equiv \frac{J}{Mc}, \quad \Delta \equiv r^2 - \frac{2GMr}{c^2} + a^2, \quad \Sigma \equiv r^2 + a^2 \cos \theta^2 \quad (1.11)$$

The theory of black hole perturbations and the associated radiation has a long history [38]. In 1957, Regge and Wheeler studied a perturbed Schwarzschild black hole

and found that it was stable to small perturbations [39]. In the 70s, work by Chandrasekhar, Detweiler, Zerilli, and others analyzed perturbations of Kerr black holes and the resulting gravitational waves. This work showed that gravitational radiation from the quadrupole mode has the form of an exponentially damped sinusoid [40]. Approximate analytical expressions for the central frequency (f) and the quality factor (Q) are given in fits made by Echeverria [41] to the numerical results of Leaver [42]:

$$f \simeq 32 \text{ kHz} \left(\frac{M_\odot}{M} \right) [1 - 0.63(1 - \hat{a})^{3/10}] \quad (1.12)$$

$$Q \simeq 2(1 - \hat{a})^{-9/20} \quad (1.13)$$

The ringdown waveform is [43]:

$$h_{ave}(t) = A e^{-\pi f t / Q} \cos(2\pi f t) \quad (1.14)$$

where

$$A \simeq \frac{6 \times 10^{-21}}{\sqrt{Q(1 - 0.63(1 - \hat{a})^{3/10})}} \left(\frac{\text{Mpc}}{r} \right) \left(\frac{M}{M_\odot} \right) \left(\frac{\epsilon}{0.01} \right)^{1/2} \quad (1.15)$$

is the amplitude, suitably averaged over spin-axis orientations and source sky positions, M is the mass of the black hole, ϵ is the fraction of the black hole's rest mass which gets converted into gravitational radiation, and $\hat{a} = (c/G)(J/M^2)$ is the dimensionless spin parameter which goes from 0 (Schwarzschild) to 1 (extreme-Kerr). It should be noted that this dimensionless \hat{a} is *not* the same as the a used in Equations 1.10 and 1.11.

For a $10 M_\odot$ Schwarzschild black hole, if we take as a dynamical time the perimeter of the event horizon divided by the speed of light, we can also calculate a characteristic frequency, $f_S = (2\pi R_S/c)^{-1} = c^3/(4\pi GM) \simeq 1.6 \text{ kHz}$, which is quite close to the estimate of 1.2 kHz from Equation 1.12. The low Q of 2 (from Equation 1.13) tells us that almost all of the energy is released in just a couple cycles.

Getting some physical intuition for the radiation from a Kerr black hole is some-

what more difficult. An interpretation from Detweiler [44] is that in a spinning black hole, the metric perturbation from the pulsation gets a frequency boost from the dragging of the inertial frame through which it passes. As the hole approaches the extreme-Kerr limit ($\hat{a} \approx 1$), the frequency of the wave as observed at infinity gets shifted up to $\sim 2.7 \times$ the frequency of an equivalent mass Schwarzschild black hole.

Rate Estimates

Given these formulae, we can estimate what black hole mass range is of interest for LIGO. The lowest detectable black hole QNM frequency will be ~ 50 Hz; this corresponds to a $640 M_\odot$ maximally spinning BH or a $240 M_\odot$ BH with no spin. At the upper edge of the band, ~ 5 kHz, we could detect a $6.4 M_\odot$ BH with maximum spin or a $2.5 M_\odot$ BH with no spin. This latter mass may result from the inspiral of the $1.4/1.4 M_\odot$ NS/NS binaries.

Flanagan and Hughes [36] estimate ringdown wave amplitudes and SNR's in first-generation and advanced detectors. They optimistically estimate an upper bound on the radiation efficiency of $\epsilon = 0.03$.

They estimate that the ringdown from a $\sim 100\text{-}700 M_\odot$ BH, with a Q of ~ 12 , would be seen with an $\text{SNR} > 10$ at distances out to 100 Mpc with a first generation LIGO interferometers. For these intermediate mass sources, the inspiral waveform would have too low of a frequency to be detectable.

Previous Searches

There have been two searches done to date for black hole ringdowns in the Milky Way: one done by Creighton [43] using a single template on the data from the Caltech 40 m interferometer [32]; more recently, the TAMA group [45] has conducted a search for ringdowns using data from their 300 m interferometer during their Data Taking 6 run.

Chapter 2

Gravitational Wave Antennae



A gravitational wave detector must be a transducer for turning space-time strain into a recordable signal (current, voltage, etc.). Since the coupling of gravitational radiation to matter is very weak, much effort has been devoted to constructing very efficient transducers. This chapter briefly motivates the optical configuration used in LIGO and then describes the gravitational wave signal readout path.

2.1 Resonant Mass Detectors (Bars)

Four decades after they had been predicted by theory, Joseph Weber reported on a method for detecting gravitational waves using a large aluminum bar[46]. The idea was that a passing gravitational wave would induce a strain on the bar, exciting the bar's resonant modes. For reasons detailed elsewhere[47, 48], the community was never able to verify Weber's subsequent claims of detection[49] although various theories[50, 51] were developed to explain the enormous apparent flux of gravitational wave energy.

Following Weber's pioneering work, various international efforts to increase the sensitivity of resonant mass detectors began. Today's best bars are seismically isolated and cryogenically cooled to reduce the natural vibration of the bar, and the use of SQUIDs to readout the signals has dramatically increased the sensitivity[52].

There are also highly ambitious proposals[53] for more sophisticated geometries (spheres, dodecahedrons, etc.) designed to improve the bandwidth and directional sensitivity of the resonant mass detectors.

2.2 Laser Interferometers

The idea of measuring the geodesic deviation with pulses of light was first published by Pirani in 1956 [54]. The first prototype interferometer for gravitational wave detection was built in the early 70s in Malibu [55]. Almost all of the limiting noise sources which we contend with today were laid out by R. Weiss in a study done at MIT [56].

Many different interferometer configurations are sensitive to gravitational waves (see [57] and references therein). This section will describe briefly each of the sub components of the power-recycled, Fabry-Perot Michelson interferometer configuration used in LIGO.

All of the kilometer-scale interferometers in the world are planned to be variants of the power-recycled Michelson scheme. Alternative interferometer configurations, such as Sagnac interferometers [58, 59] and resonant recycling [60], have also been explored.

2.2.1 The Michelson Interferometer

The core of the LIGO interferometer is a Simple Michelson (SM) interferometer. The SM consists of a light source (a laser in our case) illuminating a 50/50 beamsplitter. The transmitted and reflected beams from the beamsplitter travel perpendicular paths, are reflected from two end mirrors, and then recombine at the beamsplitter.

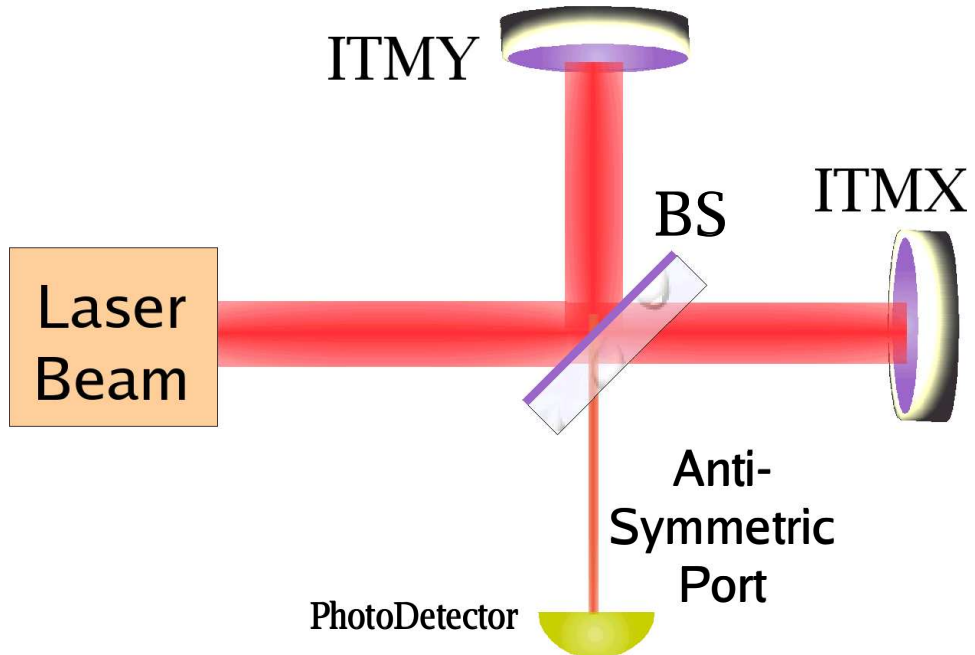


Figure 2-1: A basic Michelson type interferometer. The field from the laser comes in from the symmetric side of the beamsplitter. The light from the two arms interferes destructively at the AS port.

The resulting electric field at the Anti-Symmetric (AS) port is a function of the effective optical path difference for the beams in the two arms.

$$E_{AS} = E_{in}(r_{ex}t_{bs}r_{bs}e^{i2\phi_x} - r_{ey}t_{bs}r_{bs}e^{i2\phi_y}) \quad (2.1)$$

where ϕ_x & ϕ_y are the phases accumulated by the light in a single trip down each arm (i.e. $\phi_{rt} = 2\phi_x$) and t_{bs} & r_{bs} are the field transmission and reflection, respectively, of the beamsplitter.

For an optical interferometer, the electromagnetic radiation is at frequencies greater than 10^5 GHz. This is too high a frequency to detect with present day technologies. Instead, detectors are used which are sensitive to the envelope of the field. For visible and near infrared wavelengths, one such detector is the photodiode, which emits a current. This photo-electron current is proportional to the average photon flux, or power, on the detector.

If we ask what the power at the AS port is for the case in which the end mirrors have identical reflectivities ($r_{ex} = r_{ey} = r_e$), we get from Equation 2.1 that:

$P_{AS} = E^*E = 4|E_{in}|^2(r_e t_{bs} r_{bs})^2 \sin(\phi_-)^2$ where $\phi_- = \phi_y - \phi_x$. The phase sensitivity is $\frac{dP}{d\phi_-}$. In the simple case where $r_e = 1$ and $r_{bs} \times t_{bs} = 1/2$, we get

$$\frac{dP}{d\phi_-} = 2P_{bs} \sin(\phi_-) \cos(\phi_-) \quad (2.2)$$

where $P_{bs} \equiv |E_{in}|^2$. The measured power fluctuations due to shot noise (more in Section 4.2.7) are:

$$\delta P_{shot} = \sqrt{\frac{2hc}{\lambda} P_{bs} \sin^2(\phi_-)} \quad (2.3)$$

and so the equivalent *phase noise* is just the ratio:

$$\begin{aligned} \frac{\delta\phi_-}{\sqrt{\text{Hz}}} &= \sqrt{\frac{1}{2} \frac{hc}{\lambda} \frac{1}{P_{bs}} \frac{1}{\cos^2(\phi_-)}} \\ &\simeq 3 \times 10^{-11} \left(\frac{100\text{W}}{P_{bs}} \right)^{1/2} \frac{\text{radians}}{\sqrt{\text{Hz}}} \end{aligned} \quad (2.4)$$

where the estimate is for the LIGO laser wavelength of 1064 nm and the phase offset in the Michelson is small.

2.2.2 Fabry-Perot Resonators

Looking at Equation 1.5, a clear way to increase the strain sensitivity is to make very long arms in a Michelson interferometer. For terrestrial interferometers, the arm length is limited by technical annoyances such as cost and the availability of a large, quiet piece of land. A technique which is almost as good as having long arms is to bounce the beam multiple times in each arm.

This type of delay line [61], was proposed [56] as a way of increasing the signal gain of the interferometers. Experiments with this topology [62] uncovered technical problems due to scattered light which make this idea impractical, although it has been pointed out that operating the interferometer with white light is a possibility.

An alternative to this method is to overlap the multiple reflections on the same spot on the mirror [60]. By making the input mirror of the arm into a partial transmitter and adjusting the separation between the mirrors carefully, the input mirror and end mirror can be made into a Fabry-Perot resonator [63]. The disadvantage with this technique compared to the delay lines is that the cavity must be operated near resonance to achieve the high power buildup and resultant phase shift gain which the delay line has at any operating point. This resonant operation is achieved through the use of feedback control of the cavity length.

2.2.3 Power Recycling

In the Michelson shown in Figure 2-1, the light returning from the two arms interferes constructively in the direction heading back to the laser. Effectively then, the Michelson interferometer looks like a highly reflecting mirror, when it is adjusted for maximum darkness at the anti-symmetric port. This reflected light would be dumped somewhere and not contribute to the signal gain of the interferometer.

By placing a partially transmitting mirror between the laser and the beamsplitter,

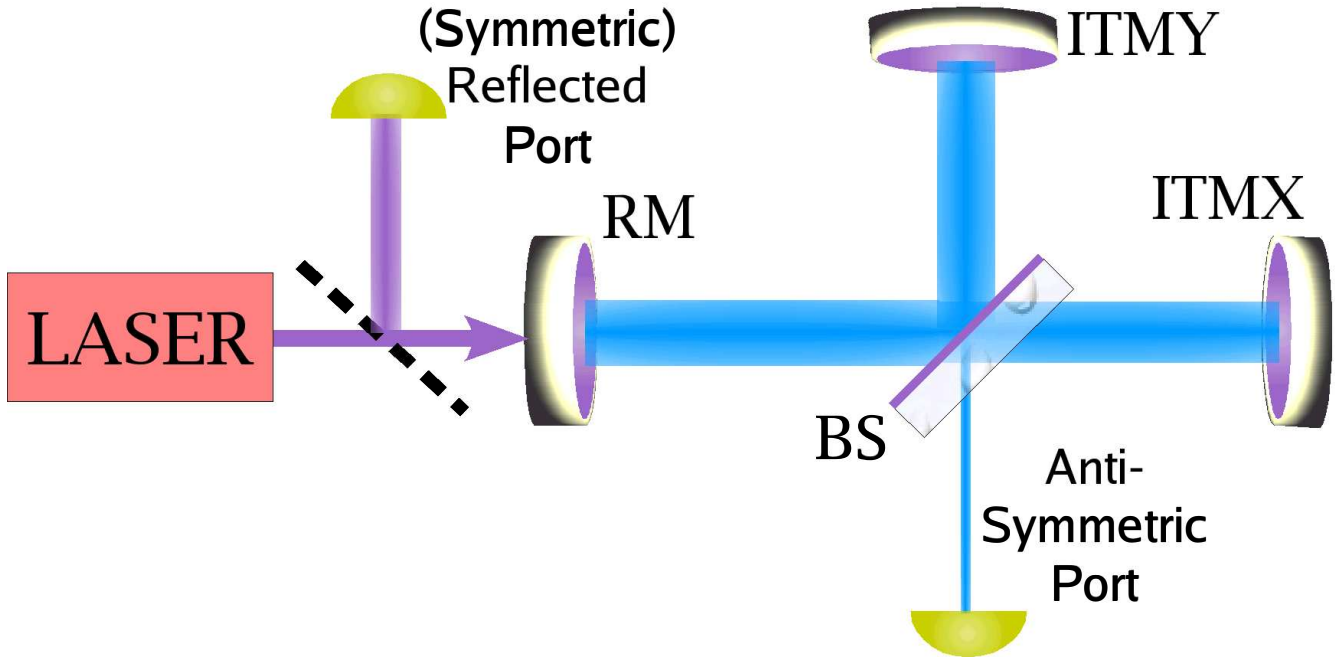


Figure 2-2: A partially transmitting mirror on the symmetric side of a Michelson makes power-recycled Michelson.

as shown in Figure 2-2, one can send this light back into the interferometer. The Michelson part of the interferometer acts on the incoming light like a high reflectance mirror and can potentially form a high finesse, Fabry-Perot cavity with this new mirror. This technique is called power recycling [64, 65, 60] and the added mirror is the power recycling mirror (RM).

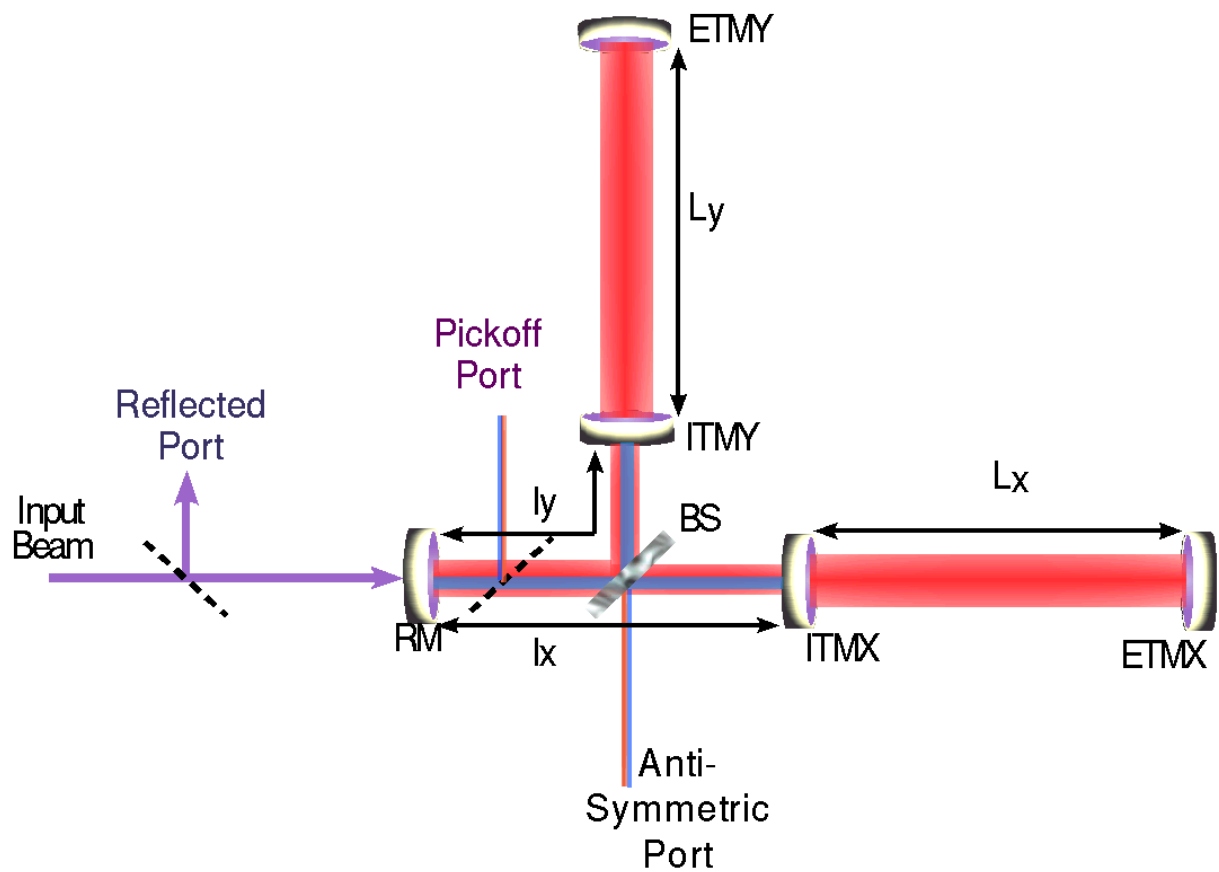
The following are some further qualitative comments about power recycling which are more quantitatively described in the following chapters:

- The RM transmission is chosen to equal as closely as possible, all of the other losses experienced by the carrier field in the interferometer (see Appendix F for details on losses). The matching is done so that all of the carrier light is coupled into the interferometer. The power gain achieved through power recycling is $\sim 40\text{-}50$ in LIGO.
- The increased power available in the Michelson increases the shot noise limited *phase* sensitivity of the Michelson by putting more light on the Beamsplitter (see Equation 2.4).

- The resonance linewidth of the big coupled cavity, formed by the power recycling mirror and the arm cavities, is much narrower than the linewidth of the arm cavity alone. The coupled cavity pole, f_{cc} , is equal to f_c/\mathcal{F}_{RC} , the arm cavity pole frequency divided by the Finesse of the recycling cavity. The beauty of this narrowing is that the *carrier* field which is in the interferometer has been passively filtered by a ~ 1 Hz low pass filter on top of all of the active stabilization. In this way, we would be able to achieve another factor of 100 suppression of the technical laser noise.
- Power recycling does not reduce the bandwidth of the gravitational wave readout at the anti-symmetric port, since differential signals produced in the arms *are not recycled*.

Chapter 3

Signal Extraction



In order to achieve the strain sensitivity goal, multiple resonant cavities are used to store the light in the interferometer. To keep the cavities on resonance an active feedback system is employed. This chapter will describe how the cavity lengths are sensed and controlled.

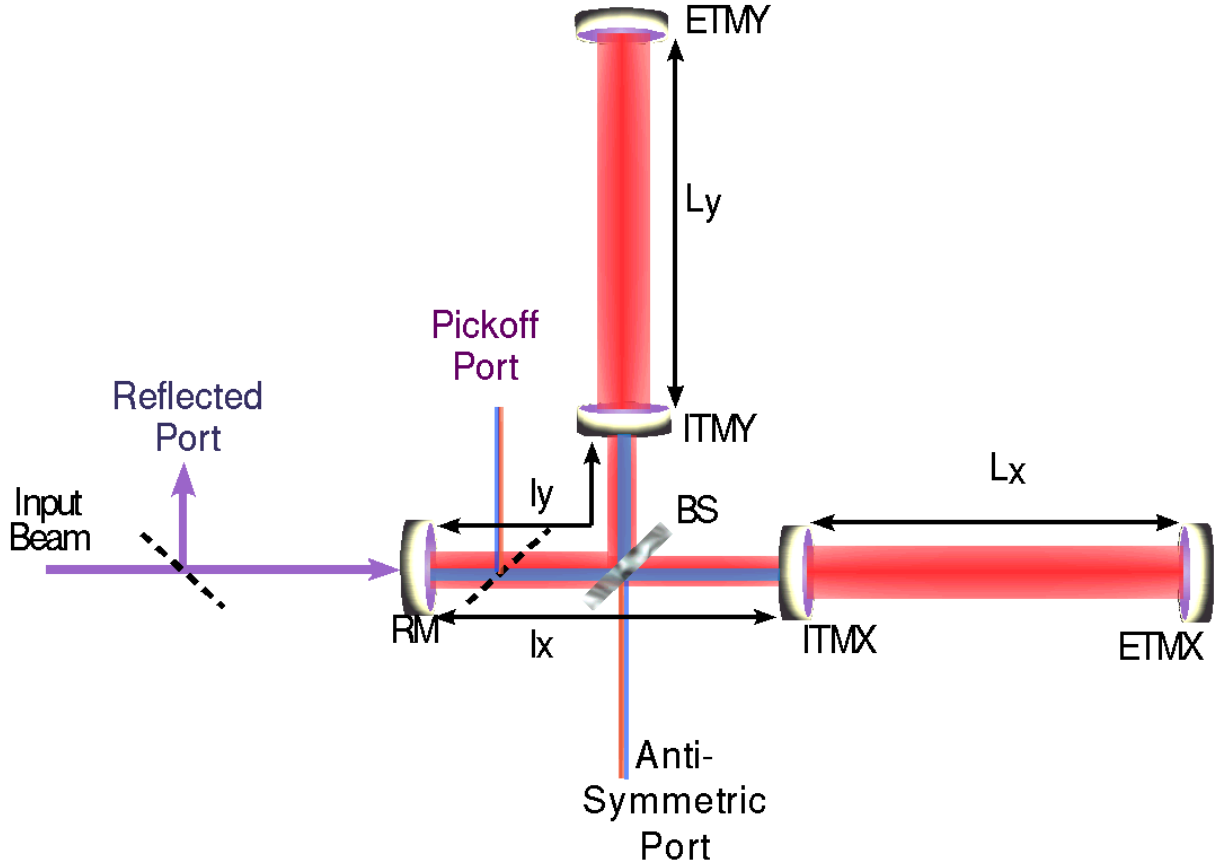


Figure 3-1: Designations of length degrees-of-freedom and signal readout ports. Further details in Appendix B

3.1 Signal Readout Scheme

The steady state signal readout problem is this: to find the functions that relate the change of a length with optical signals at the readout ports. This solutions is a sensing matrix of the form

$$\vec{V} = \overleftrightarrow{S} \otimes \vec{X} \quad (3.1)$$

where \vec{V} is the vector of voltage readouts, \vec{X} is the vector of mirror motions, and \overleftrightarrow{S} is the sensing matrix. Each element of \overleftrightarrow{S} can be frequency dependent.

Previous works [66, 67] have calculated this matrix. This section and the rest of the thesis will use the more modern notation of [67]. **Appendix B includes the definitions of variables used in the following formulas.**

The physical detector used in the sensing scheme is a photodiode. Since this detector is only sensitive to power and not the electric field directly, the trick in the readout is to produce power fluctuations on the readout ports.

To make the measurements at a frequency at which the technical laser noise is small, the beam incident on the interferometer is phase modulated at an angular (radio) frequency, $\omega_m \approx 2\pi \times 25$ MHz. The resulting electric field is:

$$\begin{aligned} E_{in} &= E_0 e^{i\Gamma \cos(\omega_m t)} \\ &\simeq E_0 \left\{ J_0(\Gamma) + iJ_1(\Gamma)e^{+i\omega_m t} + iJ_1(\Gamma)e^{-i\omega_m t} - J_2(\Gamma)e^{+i2\omega_m t} - J_2(\Gamma)e^{-i2\omega_m t} \right\} \end{aligned} \quad (3.2)$$

where Γ is the modulation depth in radians, ω_m is the modulation angular frequency, J_n is the n^{th} order Bessel function of the first kind, and E_0 is the unmodulated field of the laser. In the LIGO interferometers, $\Gamma \approx 0.4$.

The first order Radio Frequency (RF) sidebands and carrier field can be treated as three fields, each at different frequencies. Each field will have different reflection and transmission coefficients at each point within the complex coupled cavity system of the interferometer. The signal readout scheme used in LIGO takes advantage of this dispersion. The scheme is a variant of a (now standard) RF reflection locking technique [68, 69]. To implement this, the RF photodetector signal at each port is demodulated at the modulation frequency used to drive the Pockels cell. The In-phase (cosine) and Quadrature-phase (sine) components are then separately recorded and/or used in the feedback control (see Chapter 5).

The naming convention for the interferometer lengths is described in Appendix B. For the output signals the convention is: (Port)_Quadrature. So for example the

POB_Q signal is the quadrature phase of the demodulated signal from the recycling cavity Pick-Off of the Beamsplitter. The REFL signals refer to the signals taken from the light reflected back to the symmetric port from the interferometer and the AS signals are from the Anti-Symmetric port.

As is the convention in [66] and [67], all of these signal formulae are only valid for frequencies below the arm cavity free spectral range (~ 37.5 kHz for a 4 km cavity). The expressions were derived using the 'audio sideband' approach: a mirror moving at a frequency, f_a , impresses phase modulation sidebands on the reflected field at $\pm f_a$ relative to the incident field. So an incident field with three frequency components will be reflected with nine frequencies.

Effects from higher order spatial modes are not included here.

3.2 Elements of the Sensing Matrix

The control system (Chapter 5) adjusts the arm lengths to produce a dark fringe for the carrier. Since the Michelson arm lengths are not equal, dark for the carrier field does not necessarily mean dark for the sidebands. This arm length asymmetry ($l_- \approx 17$ cm) has been designed to transmit a few percent of the sideband power from the recycling cavity to the AS port.

Signals at the AS port come from the carrier field beating against the static sideband field. Differential changes in the arm cavity lengths (L_-) or in the Michelson length (l_-) cause a first order differential phase shift in the carrier fields returning to the beamsplitter from each arm.

$$[L_- \rightsquigarrow AS_Q] = -\aleph g_{crt_{sb}} r'_c \frac{1}{1 + if/f_c} k \delta L_- \quad (3.3)$$

The notation of the L.H.S. of Equation 3.3, and all of the following equations representing elements of the sensing matrix, denotes a transfer function from one degree of freedom to one readout signal.

Changes occurring faster than the storage time of the arm cavities do not experience the full buildup of the cavity and are attenuated compared to low frequencies.

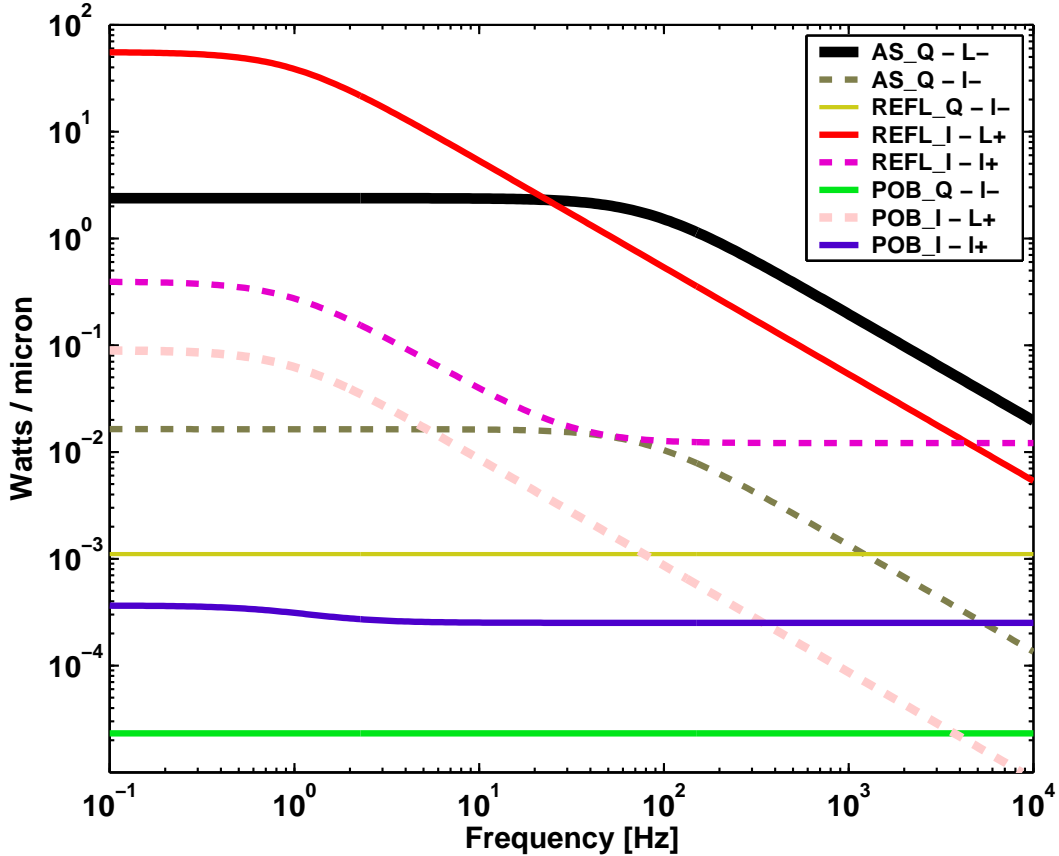


Figure 3-2: Plotted are the signal strengths for the L1 interferometer in Watts at the modulation frequency per micron of optic motion. The solid lines are the diagonal plant elements used for the interferometers main length loops. The dashed lines are off-diagonal elements. A pickoff fraction of 80 ppm has been used to calculate the POB signals. All curves are for the ~ 1.6 W of input power in L1 during the S2 run.

Gravitational wave strain signals are read out through this same mechanism and so are similarly attenuated at high frequencies.

$$[l_- \rightsquigarrow AS_Q] = \aleph g_{cr} t_{sb} r_c \frac{1}{1 + if/f_c} k \delta l_- \quad (3.4)$$

Changes in the Michelson length also show up in this signal but down by a factor of r'_c/r_c (which is ~ 140 for the LIGO interferometers). This factor is the 'phase gain' or build-up factor of the arm cavities. Fluctuations above the arm cavity pole are not resonant in the arm cavities. Since the arms are over-coupled cavities, the sign of the reflected field changes depending on whether the incident field is resonant or not. So

the high frequencies get a sign flip and fall out of resonance in the recycling cavity.

The field reflected from the interferometer contains signals contributed by both the sidebands and the carrier since both are resonant in parts of the interferometer.

$$[L_+ \rightsquigarrow REFL_I] = 2\aleph g_{cr}^2 r_{sb} r_c' \frac{1}{1 + if/f_{cc}} k \delta L_+ \quad (3.5)$$

Common mode changes of the arm lengths affect only the carrier field since the sidebands are not resonant in the arms. This signal has 2 factors of g_{cr} in it; one, since the carrier field in the arms is amplified by the recycling cavity and another, because the common arm signal is resonant in the recycling cavity. At the reflected port, these carrier audio sidebands beat against the static RF sidebands.

$$[l_+ \rightsquigarrow REFL_I] = 2\aleph \left[g_{sb}^2 r_{cr} r_M + g_{cr}^2 r_{sb} r_c \frac{1}{1 + if/f_{cc}} \right] k \delta l_+ \quad (3.6)$$

The REFL_I signal produced by a change of the power recycling cavity average length (l_+) is more complicated. Since both the sidebands and carrier are resonant in the recycling cavity, both are modulated by the l_+ length change. The carrier component is filtered above ~ 1 Hz by the coupled cavity resonance and so the main contribution above 100 Hz is from the RF sidebands' audio sidebands beating with the static carrier.

$$[l_- \rightsquigarrow REFL_Q] = -\aleph g_{sb} t_{sb} r_{cr} k \delta l_- \quad (3.7)$$

The quadrature phase signals at the REFL and PO ports are produced in a different way. Changes in the Michelson length change produce differential changes in the sideband fields reflected from the Michelson back towards the RM. At the reflected port, the difference between the amplitudes of the upper and lower sidebands produce a signal 90 degrees out of phase with the REFL_I signal. In a symmetric arm length Michelson interferometer, there would be no Q-phase signal, since the reflectivity for the sidebands would be a quadratic function of l_- .

$$[L_+ \rightsquigarrow POB_I] = -2\aleph \frac{g_{cr}^2 g_{sb}}{t_{RM}} r_M r'_c \frac{1}{1 + if/f_{cc}} k \delta L_+ \quad (3.8)$$

The signal from the pick off inside the recycling cavity is very similar to the one in reflection. The main difference being that it does not depend delicately on the coupling of the sideband to the recycling cavity, but instead is produced by beating the carrier audio sidebands against the resonant sideband field.

$$[l_+ \rightsquigarrow POB_I] = 2\aleph \frac{g_{cr} g_{sb}}{t_{RM}} r_M r_c \left[g_{cr} \frac{1}{1 + if/f_{cc}} - g_{sb} \right] k \delta l_+ \quad (3.9)$$

Very similar to the $[l_+ \rightsquigarrow REFL_I]$ element. The main difference is that the local oscillator field is the carrier field inside the recycling cavity instead of the carrier reflected from the interferometer.

$$[l_- \rightsquigarrow POB_Q] = -\aleph \frac{g_{cr} g_{sb}^2}{t_{RM}} t_M k \delta l_- \quad (3.10)$$

This element also appears to be similar to the REFL port element but there are two important differences. First, the signal is independent of the sign of the carrier coupling since it uses the internal recycling cavity field. Second, the dominant carrier field in reflection can be the non-modematched component. This will produce a spurious signal through beating with non-modematched sideband field.

Since each readout signal is sensitive to multiple degrees of freedom there is some choice to be made in selecting a particular configuration. It is fairly clear from these equations and Figure 3-2 that only AS_Q may be used for reading out the differential arm length. This leaves some other combination of the Q-phase signals to read out l_- . In the absence of beam distortions, we would be free to choose whichever combination of the two gives the best SNR. In the case of the l_- readout, we use the POB_Q signal to avoid the junk signal from the mode-mismatch of the carrier and sidebands.

The case for the common mode signals is a little less clear, since in both REFL_I and POB_I the L_+ signal is totally dominating the weak l_+ signal. In a perfectly stable, noiseless interferometer one could take this 2×2 signal matrix and invert it

properly to obtain linearly independent readouts of both degrees of freedom.

In the real world, this is problematic for two reasons: first, the small fraction of light from the internal recycling cavity pickoff is so small (~ 100 ppm) that the signal-to-noise ratio is much poorer than the reflected port where all of the light is available and second, even if the noise were not an issue, this matrix inversion would require subtracting two large signals to produce a very small signal (the l_+ signal) and would be overly sensitive to variations in the optical gain at the REFL and POB ports. To avoid these issues, the REFL_I signal is fed back to the laser frequency with a high gain, high bandwidth loop (see Section 5.1.4), effectively driving the REFL_I signal to zero. Solving for the newly flattened plant by setting REFL_I = 0, gives a new solution for POB_I which is only sensitive to l_+ :

$$[l_+ \rightsquigarrow POB_I] = -2\Re \frac{g_{sb}^2 r_M}{t_{RM} r_{sb}} [g_{cr} r_{sb} r_c + g_{sb} r_{cr} r_M] k \delta l_+ \quad (3.11)$$

3.3 Dark Port Signal Generation

Equation 3.3 only deals with the Q phase signal which we use for the gravitational wave signal readout and the differential arm length control. It was assumed that the only carrier field at this port comes from the differential arm length offset. However, a carrier field may also exist in the other phase. In principle, this should not produce a signal unless there is a corresponding sideband field in the “wrong” phase. Including fields in both phases we get:

$$\begin{aligned} \frac{E_{AS}}{E_0} = & J_0(\Gamma) g_{cr} \left[\frac{\delta r_c}{2} + i r'_c k \Delta L_- \right] \\ & \times J_1(\Gamma) t_M \left[\frac{\delta g_{sb}}{2} \cos \omega_m t + i 2 g_{sb} \sin \omega_m t \right] \end{aligned} \quad (3.12)$$

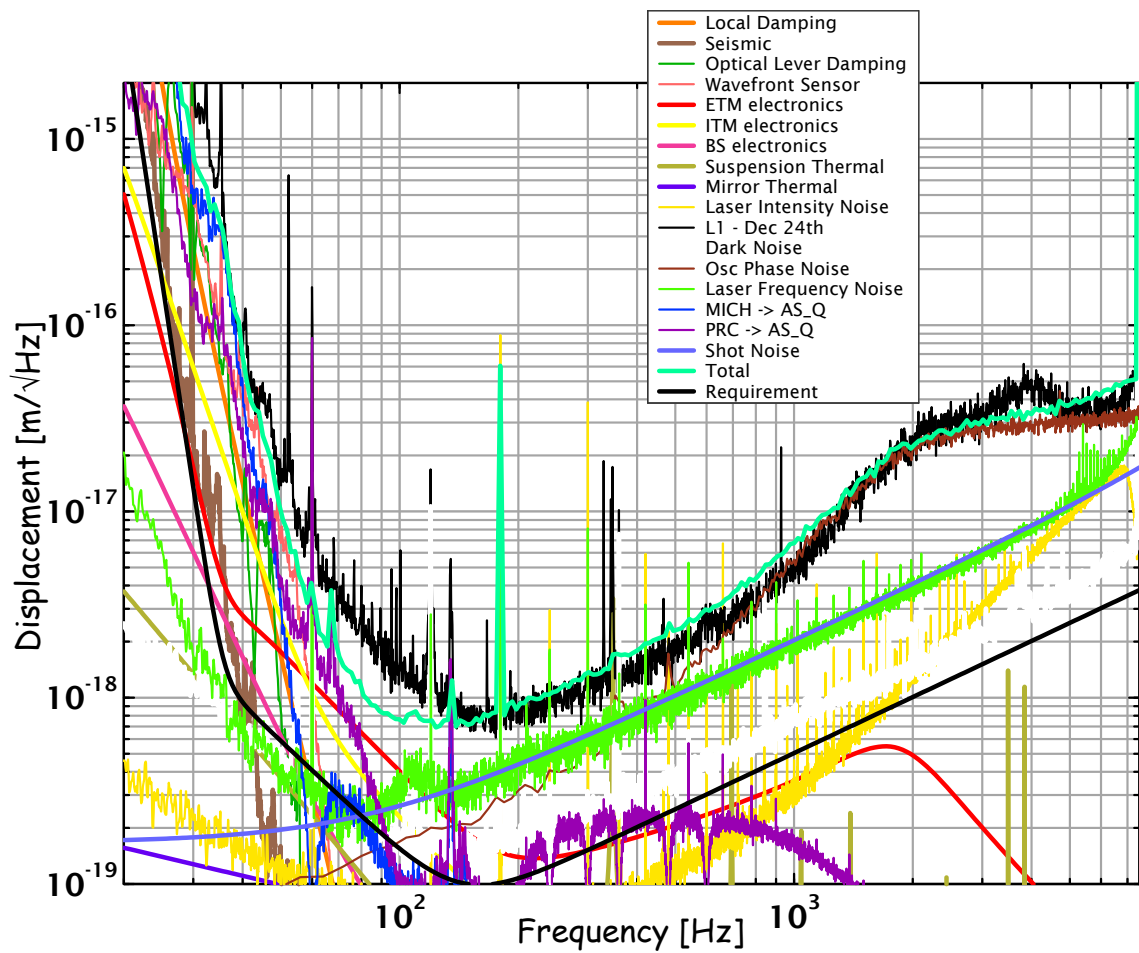
where we have included two asymmetries: δr_c is the difference in the arm cavities’ resonant reflectivities for the carrier and δg_{sb} is the difference in the recycling gain between the upper and lower first order RF sidebands.

The AS_Q signal is produced by the beat between the imaginary part of the carrier field and the imaginary part of the sideband field. The AS_I signal is produced by the real components and only exists in the presence of the two asymmetries.

$$S_{\text{AS,I}} = \frac{1}{8} \aleph g_{cr} t_M \delta r_c \delta g_{sb} \quad (3.13)$$

Chapter 4

The Noises



There are many noise sources in the LIGO interferometers. In this chapter, those noises which contaminate the gravitational wave readout channel and are of a comparable amplitude to the strain noise goal are described.

The noises are categorized as either a displacement noise, one which directly moves the suspended mirrors, or as a sensing noise, one which appears in the readout signal but is not caused by a gravitational wave.

4.1 Displacement Noises

The displacement noises in this section are only those that cause a differential change in the arm cavity lengths. We are also mainly concerned with noise in the 40-7000 Hz band where the interferometer is designed to be sensitive to gravity waves.

4.1.1 Seismic Noise

The test mass mirrors are on the earth and so vibrations of the earth's surface could directly show up as a strain noise. A rough estimate for the displacement spectral density of the ground noise above 0.1 Hz at a quiet site is $x(f) = \frac{10^{-8}}{f^2} \frac{\text{m}}{\sqrt{\text{Hz}}}$. At 100 Hz, this would still be 7 orders of magnitude above the LIGO displacement noise goal. A combination of passive and active isolation techniques are used to reduce the seismic coupling.

Noise Characteristics

- Excepting dramatic events such as earthquakes and subway cars, the largest ground motions seen everywhere are from the ≈ 6 second period ‘microseism’ [70]. The primary microseism is generated by ocean waves having a $\approx 12\text{-}15$ second period. The secondary microseism, which is much larger, is produced by standing waves on land from a large number of sources.
- The power in the 0.5-10 Hz band is largely due to man made noise. The operation of the Livingston interferometer has been seriously impaired by this noise.

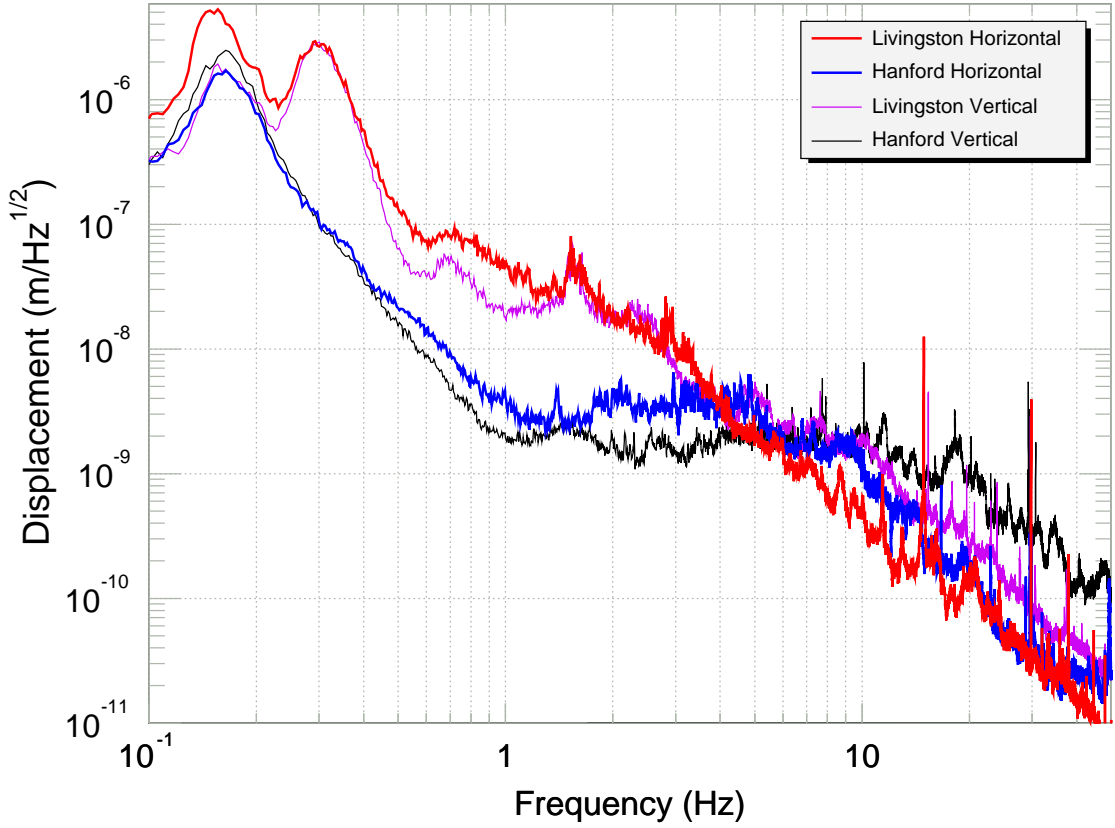


Figure 4-1: Amplitude spectral density of the daytime displacement noise of the ground at both LIGO sites.

The noise is so large that the interferometer only operates reliably from the end of the workday (6-8 PM on weekdays) until the beginning of the workday (5-6 AM).

- Above 10 Hz, most of the noise is self inflicted. The acoustic and vibrational environment at the observatories has been compromised by the HVAC systems. Efforts are underway to remediate this by balancing fans, installing acoustic isolation and damping material, and isolating the noisiest components with springs.

Seismic Isolation

To attenuate this noise, the core interferometer optics are each suspended as pendula (see Section [?]) by a single loop of steel wire. The pendulum length is set to put the

resonant frequency to $f_p \simeq 0.75$ Hz. This reduces the coupling between ground noise and optic motion by $\sim (\frac{f_p}{f})^2$ above f_p . To get the rest of the required attenuation,

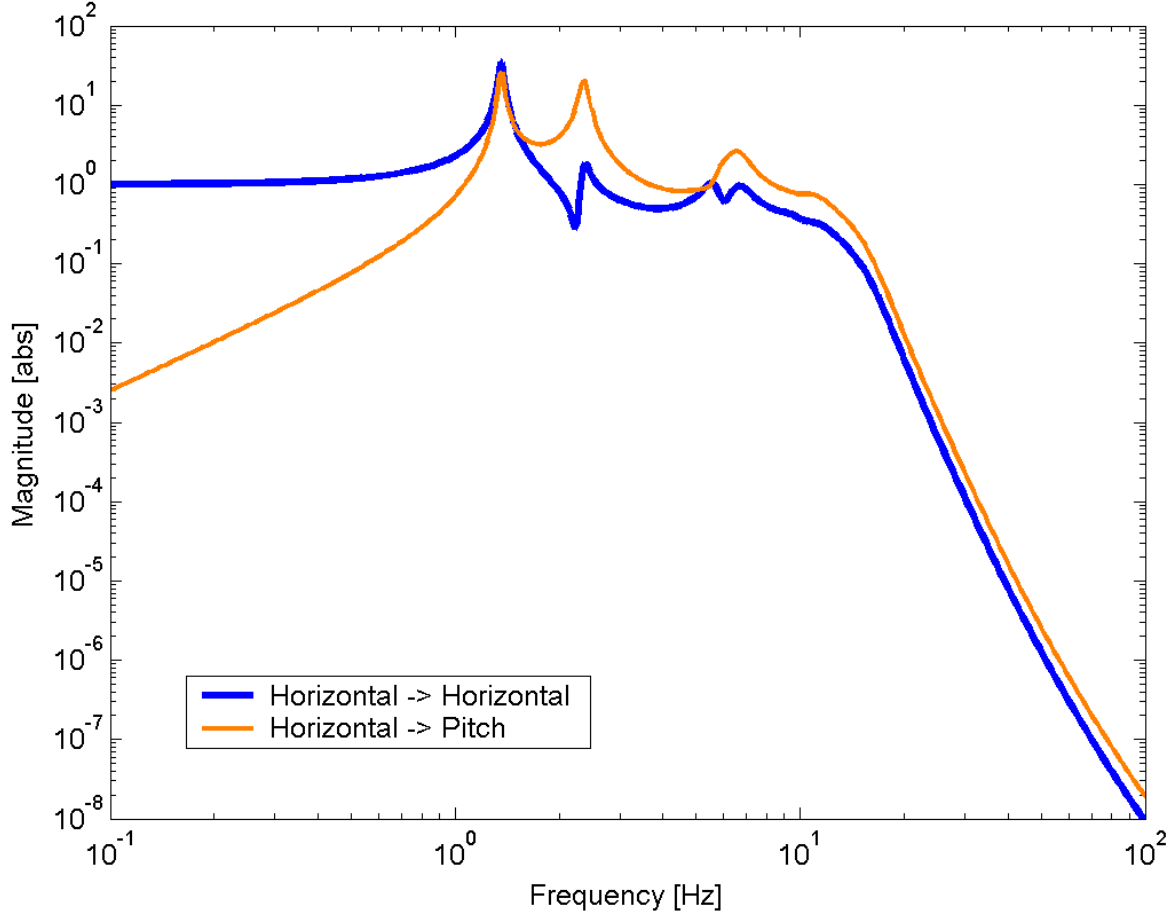


Figure 4-2: Modeled Isolation Stack Transfer Functions.

the pendulum structure is placed upon a stack of four alternating mass-spring layers (see Figure G-2). Each of these layers gives another attenuation factor proportional to f^{-2} , giving ≈ 100 dB of attenuation at 40 Hz and > 140 dB at 100 Hz[71].

4.1.2 Thermal Noise

At frequencies where seismic motion has been sufficiently filtered, the interferometer's strain sensitivity will be limited by thermal noise.

The suspended mirror is in a radiative thermal equilibrium with the vacuum chambers which are at room temperature. The thermal motions of the individual particles

of the glass, the mirror coating, and the mirror's suspension system can cause fluctuations in the measured cavity length.

The reason that the thermal energy of the whole mirror / suspension system comes into play is that there is a coupling between all of the internal modes of the system and the motion of the mirror's surface. This coupling ensures that there is a continuous flow of energy between the degree of freedom we are trying to measure and all of the other internal degrees of freedom.

The energy flow works both ways; the energy in one of the mirrors modes will slowly dissipate as it couples into all the other modes. A general theme in the thermal noise reduction game is reducing, as much as possible, all sources of dissipation which damp motions *in the degree of freedom we are measuring*.

The relation between the amount of fluctuation of the mirror surface and the dissipation in the system is described by the Fluctuation-Dissipation theorem[72]:

$$S_x(f) = \frac{k_B T}{\pi^2 f^2} \text{Re}[Y(f)] \quad (4.1)$$

where $S_x(f)$ is the power spectral density of fluctuations in a degree of freedom x , k_B is Boltzmann's constant, T is the temperature of the system, f is the frequency of the motion and $Y(f)$ is the complex mechanical admittance (inverse of the impedance) of the system. One expression for admittance which is particularly useful is[73]:

$$Y(f) = \frac{v(f)}{F_{therm}} = i \frac{2\pi f x(f)}{F_{therm}} \quad (4.2)$$

where F_{therm} is the thermal driving force, x is the readout variable, and v is the time-derivative of the readout variable.

In the case of a Fabry-Perot cavity, we are principally interested in one degree of freedom: the one that makes a signal in our strain readout channel. It takes a very special type of test mass motion to make it to this signal port. Thermal fluctuations excite all of the internal degrees of freedom of the mirror (pitch, yaw, roll, pringle), but most of these mirror surface motions only scatter light out of the cavity's fundamental mode into higher order modes which do not resonate in the cavity. The strain noise

that we measure comes from piston motions of the mirror along the cavity axis (there are some small couplings between the degrees of freedom so in principle we have to also ensure that the noise in the non-critical degrees of freedom is not too large).

In the LIGO interferometers, we can separate the thermal noise sources into two convenient categories: the fused silica mirrors which form the arm cavities and the steel suspension wire which supports the optics.

Test Mass Thermal Noise

The original estimates of test mass thermal noise made in the 20th century were based on a normal mode decomposition of the optic's internal modes [74]. However, this method requires one to measure the Q of every mechanical resonance up to ~ 100 kHz in order to estimate the thermal noise accurately. A more direct approach described by González and Saulson[75], applied to mirrors by Levin[76], is to calculate the admittance for our readout variable, assuming a homogeneous loss in the bulk.

In addition to loss in the glass substrate of the mirror, loss in the dielectric coatings on the face of the optic[77] has been identified as a significant source of thermal noise. Approximately 30 alternating, $1/4$ wavelength, layers of Ta_2O_5 and SiO_2 are used to make the coatings. Although the amount of coating material is small compared to the size of the mirror, its mechanical losses are ~ 1000 times greater than the fused silica substrate.

The power spectral density of displacement noise for a single mass is [77]:

$$S_x(f) \simeq \frac{2 k_B T}{\pi^{3/2} w Y_S f} \left[\phi_S + \frac{2 d_c}{\sqrt{\pi} w} \phi_C \right] \quad (4.3)$$

The nominal values for these parameters are listed in Table A.2. Using the best guess estimates at the time of this writing, the thermal noise from the substrate is approximately the same as that from the coatings. The total substrate thermal noise contribution from all four mirrors is:

$$\delta L_-(f) \simeq 5 \times 10^{-20} \left(\frac{100 \text{ Hz}}{f} \right)^{1/2} \left(\frac{\phi_S}{1 \times 10^{-7}} \right)^{1/2} \frac{\text{m}}{\sqrt{\text{Hz}}} \quad (4.4)$$

The coating thermal noise contribution is:

$$\delta L_-(f) \simeq 2.5 \times 10^{-20} \left(\frac{100 \text{ Hz}}{f} \right)^{1/2} \left(\frac{\phi_C}{2 \times 10^{-4}} \right)^{1/2} \frac{\text{m}}{\sqrt{\text{Hz}}} \quad (4.5)$$

taking into account that the ETM coatings have almost twice as many layers as the ITM. There are some indications [78] that the intrinsic loss in fused silica can be as low as 10^{-8} . If this turns out to be the case for the LIGO optics then the total mirror thermal noise contribution to the interferometer strain noise would be reduced by a factor of ≈ 2 .

Suspension Thermal Noise

The core optics in the interferometer are each suspended by a single loop of steel music wire, ≈ 0.3 mm in diameter. The thermal noise for the LIGO suspensions has been previously analyzed [79] using a full 6 degree of freedom model of a mirror supported by an anelastic steel beam. The often used model for the loss is that of a frequency independent internal friction. The following section compares the model predictions with the data from the interferometers.

As in the above case of test mass thermal noise, there are 2 pieces of information needed to estimate the noise contribution: The transfer function between force and test mass motion (the admittance) is one. The other is the source term: in our case random thermal forces distributed over the suspension structure.

The admittance is known and can easily be calculated numerically. The thermal force distribution, however, depends on the loss distribution in the system.

One of the dirt effects in suspension thermal noise is excess loss introduced at the suspension point [80]. This can come from rubbing due to improper clamping of the suspension wire [81]. This excess source of loss is difficult to determine ahead of time and can best be established by in-situ measurements. This was done by measuring the quality factors of the 'violin' modes of the suspension wire in two ways:

First (the easiest way, after the fact) the power spectrum of the strain channel was examined. Vibrations of the mass from the thermal fluctuations in the wire dominate

the signal in the 340-360 Hz band. Due to slight asymmetries in the suspensions (such as wire thickness, length and cross-sectional ellipticity), each side of the wire loop has a slightly different frequency.

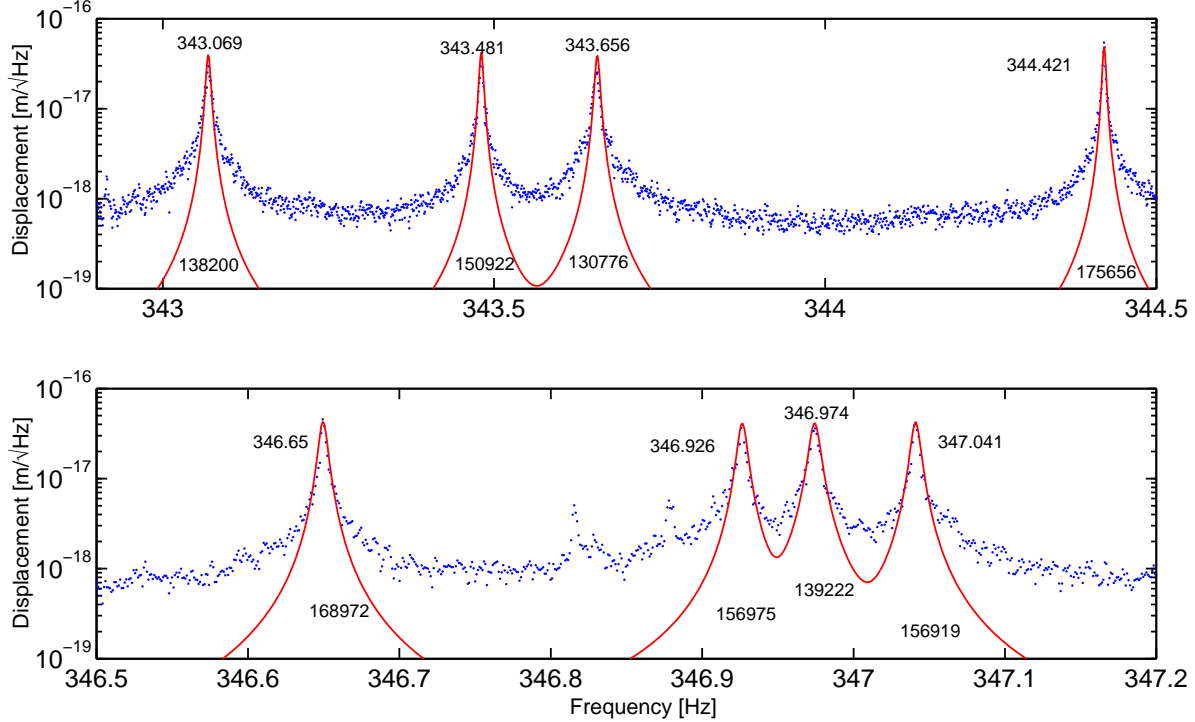


Figure 4-3: Displacement noise from the suspensions' violin modes. Plotted also is the fit to the data and the fitted frequencies and Q's.

A non-linear least squares fit to a Lorentzian curve was performed on each peak. The frequency and Q from each fit is shown in Figure 4-3. Using the model from [79], we can place an upper limit on the average loss angle for the violin modes of $\phi \lesssim 0.001$. From the fit we can see that there is excess power in the wings of each peak; there is more than one expects from a simple Lorenzian model for the peak. One possible source of this excess noise is drift in the interferometer's optical gain on several minute time scales. The next iteration of this measurement will have to use a gain corrected displacement readout.

Another weakness of this method is that it relies on several hours of data in which the interferometer is assumed to be static. In reality, a 1 degree C change in the temperature of the wire would result in a 10X larger drift (≈ 30 mHz) than what we

are trying to measure.

To avoid the drift issues one would like to make a quick measurement. One way is to measure the decay time for violin mode excitations which only takes $\tau = Q/(\pi f_{vio}) \simeq 100$ seconds. This has the drawback of interrupting science data taking but in principle has a much better chance of success and should be pursued in the future to better estimate the suspension thermal noise.

4.1.3 Radiation Pressure

Technical radiation pressure noise comes from power fluctuations of the input beam coupling to differential displacement noise through slight asymmetries in the arms. Characterization of the LIGO optics (see [82] and Appendix F) allows us to estimate these couplings. Three sources of asymmetry are:

- Imbalance in the masses of the mirrors. ($\sim 0.3\%$)
- Imbalance in the arm cavity buildups. ($\sim 2\%$)
- The beamsplitter splitting ratio is not exactly 50/50. ($\sim 0.5\%$)

For this noise to pose a problem, the power fluctuations on the input beam must be rather high. Since the double cavity resonance attenuates all carrier power fluctuations above 1 Hz, we find that in our signal band the contribution is a few orders of magnitude below the sensitivity goal.

Quantum Radiation Pressure

Quantum radiation pressure, however, is not attenuated in this way. Quantum mechanical radiation pressure noise in the interferometer comes from the zero point fluctuations of the vacuum field which enters through the dark port of the Michelson [83]. A field which enters through the dark port affects the two arms differentially. These fluctuations give rise to a fluctuating force. The resulting displacement is:

$$x(f) = 2 \times \frac{2 \delta P}{mc(2\pi f)^2} = \frac{1}{2\pi^2 m c f^2} \sqrt{\frac{2hcP}{\lambda}} \quad (4.6)$$

The differential displacement for a nominal set of parameters is:

$$\Delta L_-(f) \approx 10^{-22} \left(\frac{10.5\text{kg}}{m} \right) \left(\frac{100\text{Hz}}{f} \right)^2 \left(\frac{P_{in}}{1\text{W}} \right)^{1/2} \frac{\text{m}}{\sqrt{\text{Hz}}} \quad (4.7)$$

which is far below any reasonable estimate for the interferometer noise floor.

4.1.4 Actuator Electronics Noise

Usually when interferometer noise is described, things like seismic, thermal, and shot noise are considered. As of this writing, the noise source which has gotten the most work has been electronics noise in the test mass actuator.

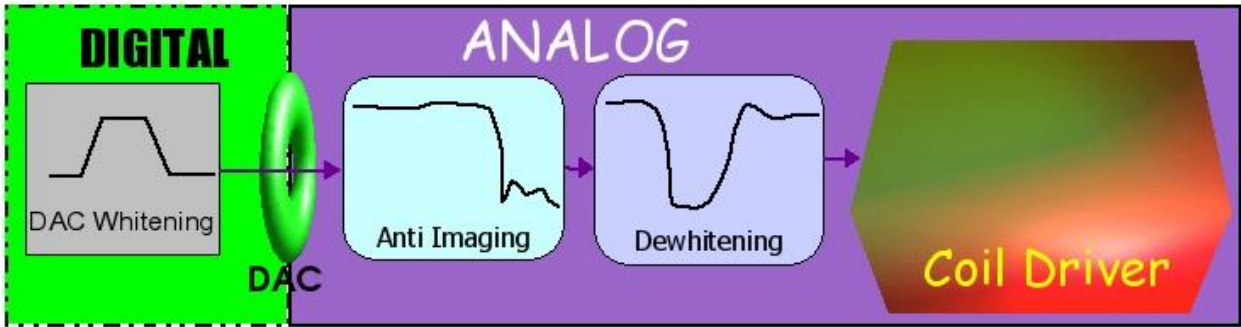


Figure 4-4: The chain of digital and analog filters beginning with the pre-DAC whitening and ending with the box driving the current into the actuator coils

The electronics which drive the test masses span the largest dynamic range of any piece of electronics in the system. At the low frequencies it must correct for the large ground fluctuations caused by storms and humans, whereas at ~ 100 Hz it must be quiet enough to not mask the gravitational wave signals.

Coil Driver

The final electronics unit which drives the coils for the suspended optic (described in Section G.2.1) is called the coil driver. There are 2 competing requirements on the coil drivers. They must have a low enough spectral density of current fluctuations that this electronics noise fall below other more fundamental noises (seismic, thermal).

They must also be able to provide enough force to acquire lock and maintain the cavity resonance in the presence of large seismic disturbances.

The following figure shows how the low noise (RUN mode) and large range (ACQUIRE mode) are accommodated.

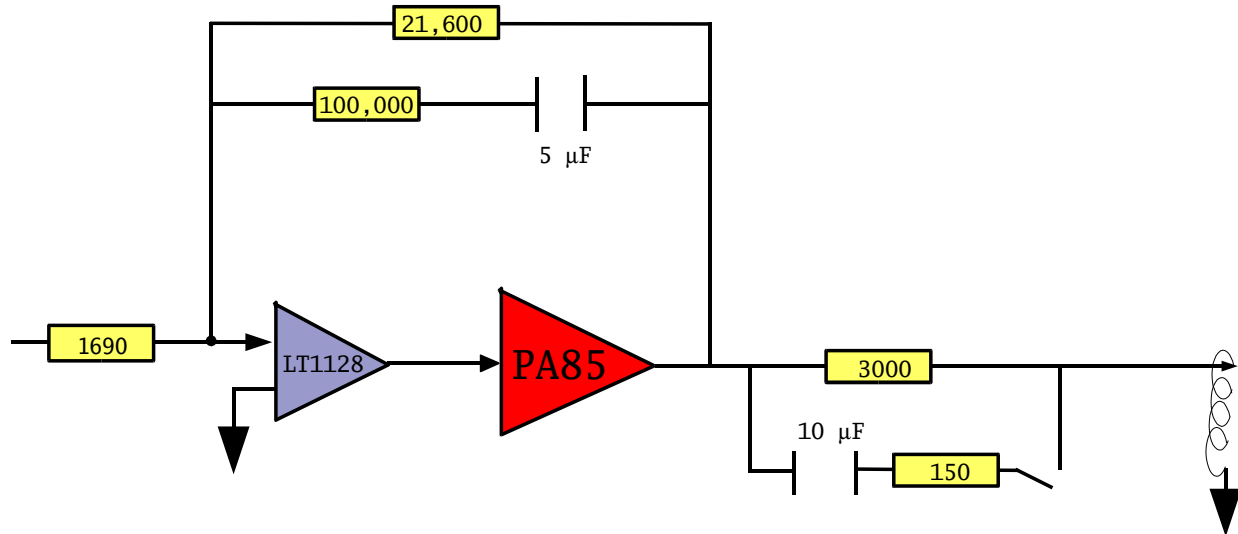


Figure 4-5: Simplified block diagram of the coil driver circuit for one face coil on one of the large optics. Closing the relay transitions from RUN to ACQUIRE mode. The yellow rectangles are resistors and the two spaced lines are capacitors.

A high voltage power amplifier (± 150 V, PA85) supplies current to the actuator coil through a series resistor. In order to have a large dynamic range for lock acquisition, a remotely controlled relay can engage a low impedance bypass around the large series resistor. This gives a factor of ~ 20 more force.

Since the servo system must hold the cavity within its narrow linewidth during the switch a digital filter is employed to compensate the different analog transfer functions. After acquiring lock the relay is switched open and the digital compensation filter is turned off, leaving the overall transfer function unchanged.

DAC Noise

Since the servo which controls the differential arm length is digital, the drive signal to the coil driver must pass through a digital-to-analog converter (DAC).

The LIGO DACs are 16-bit and have a 16384 Hz sampling rate. The dynamic range ($V_{pp}/V_{noise}(f)$) is $\approx 10^6$ in a 1 Hz bandwidth.

By contrast, the coil current spectrum must be able to supply 10 mA_{pk} at very low frequencies to accommodate the microseism and have a noise of less than 10 pA/ $\sqrt{\text{Hz}}$ from 40-150 Hz. This gives a $\sim 1000X$ mismatch in the dynamic range between the DAC and the optic's coil currents.

To satisfy both high and low frequency needs, an analog filter is inserted between the DAC and the coil driver (the 'dewhitening' filter of Figure 4-7). The filter has a unity gain at low frequencies but then an attenuation of 4000 from 40-150 Hz. The magnitude response of the filter is shown in Figure 4-6. Since the current noise to displacement noise transfer function goes down like $1/f^2$, the requirement on the coil current noise is much relaxed above the target displacement noise minimum at 150 Hz. To keep the servo transfer function constant a digital inverse of the analog filter

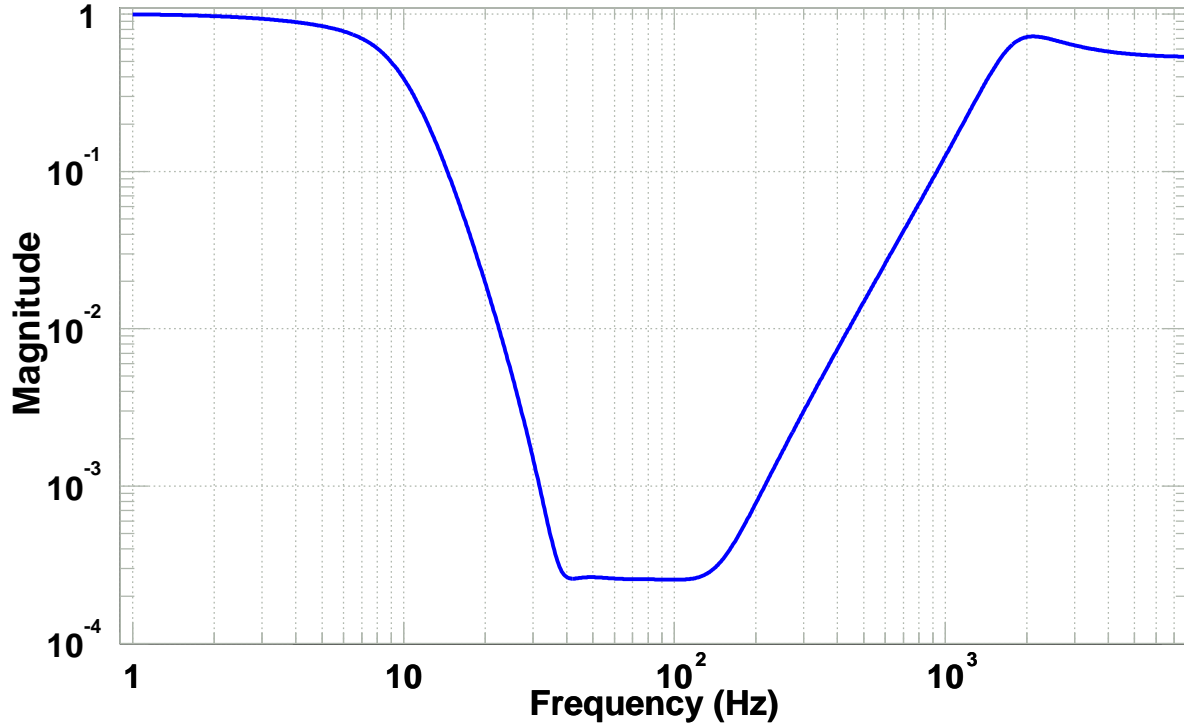


Figure 4-6: Magnitude transfer function of the post-DAC dewhitening filter

is used to condition the signal before the DAC. There is a potential for saturation in the DAC, due to the amplification in this inverse filter. To reduce the dynamic range

of the signal sent to the DAC, the dewhitening filter is designed to only attenuate in the 40-150 Hz band where the noise requirements are most critical.

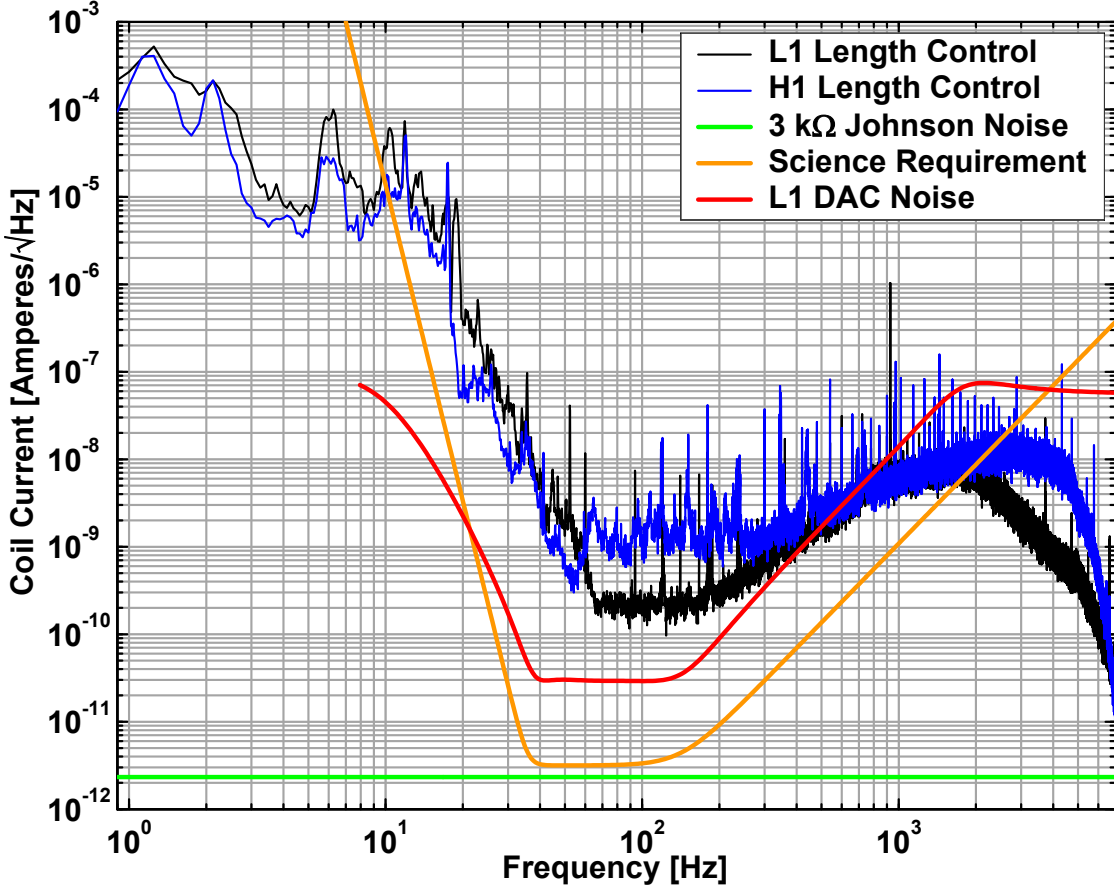


Figure 4-7: A comparison of coil current noise from the electronics with the signal levels during S2. Also shown are the Johnson noise from a $3\text{ k}\Omega$ resistor in series with the coil and the level of current noise required to meet the LIGO Science Requirement.

4.1.5 Angle to Length

This section describes the mechanism for angular fluctuations of the optic to affect the optical cavity length. The sources of angular fluctuations below 15 Hz are chiefly seismic. Above 15 Hz most of the angular noise comes from the angular control servos (see Section 5.2).

The primary mechanism which couples angular noise into apparent length fluctuations is the lever arm effect. If the beam is displaced from the mirror's axes

of rotation, a tilt will shift the phase of the entire beam mimicking a length shift: $\delta x = d \tan \theta$, where x is the translation of the optic along the cavity axis, d is the de-centering of the beam, and θ is the optic's rotation angle.

A second effect is cross-coupling of angular torque into piston motions of the optic through imbalances in the magnets' dipole moments and the actuation electronics. The gravitational wave frequency band is far enough above the pendulum eigenfrequencies that we may treat the optic like a free mass. The torque applied by the control system is $\mathfrak{T} = 4F_c R / \sqrt{2}$, where \mathfrak{T} is the torque, F_c is the force per coil and R is the radius of the optic. The displacement inducing force is $F_x = \alpha 4F_c$, where α is the imbalance in the coils. The angle to length coupling may then be written as:

$$\begin{aligned}\delta x &= \delta\theta \left[\frac{F_x/m}{\mathfrak{T}/J} + d \right] \\ &= \delta\theta \left[\frac{\sqrt{2}}{4} \alpha \left(R + \frac{H^2}{3R} \right) + d \right]\end{aligned}\tag{4.8}$$

using the moment of inertia $J = \frac{1}{4}MR^2 + \frac{1}{12}MH^2$ for a cylinder (see Figure G-1).

In order to minimize the total noise, we adjust the coil gains individually to minimize the overall angle \rightsquigarrow length coupling for both pitch and yaw rotations without regard to the actual mechanism. This method minimizes the noise at just one position on the mass, but can be done for whatever position the beam is at. The alignment control system prevents long term beam drift and so once optimized the noise should remain minimized.

The procedure to balance is to inject a sine wave into the pitch / yaw feedback path and then adjust the digital coil gains while reading back the response in the strain channel at the same frequency. We were able to automate this procedure and got an angle \rightsquigarrow length coupling of 2×10^{-4} meters/radian; equivalent to a beam decentering of 0.2 mm or $\sim 0.3\%$ of a beam diameter. This level of balancing requires adjusting the coil gains at the 0.5% level.

The obvious drawback to this method is that it does not actually center the beam on the optic. Decentering can increase the sensitivity to thermal noise in the suspensions angular eigenmodes (more on centering in Section 8.1.9).

This method was not in place for the S2 run and so there the coupling was significantly worse, ≈ 0.1 meters/radian.

4.2 Sensing Noises

Sensing noise includes noise which comes in on the laser, noise generated in the interferometer (scattering), noise in the readout electronics, and shot noise from the quantum statistics of the photons at the AS port.

4.2.1 Laser Amplitude Noise

Laser amplitude noise has three coupling mechanisms:

- Power fluctuations in the arms can produce differential lengths changes in the arm cavities if there is an imbalance in the stored power or the masses of the mirrors. As discussed above in Section 4.1.3, this effect is negligible.
- Power fluctuations in the mode cleaner can produce laser frequency noise through radiation pressure induced displacements of the low mass (~ 0.25 kg) MC mirrors. This is described in more detail in Appendix C.
- Power fluctuations at the anti-symmetric port modulate the gain of the strain readout channel. Low frequency arm length fluctuations are upconverted into the gravitational wave band through this amplitude modulation.

An input beam with low frequency amplitude modulation can be written as:

$$E_{in} = E_0 \left(1 + \frac{\Delta A}{A} \right) \cos \omega t \quad (4.9)$$

where A is the amplitude of the unmodulated laser light. The noise signal in AS_Q will be the multiple of two time series: $\delta G(t)\delta L_-(t)$. $G(t)$ is the optical gain at the AS port and $\delta L_-(t)$ is the L_- servo's error point.

The coupling to the anti-symmetric port signal can be written as [67]:

$$S_{\text{AS_Q}} = \aleph g_{cr} t_{sb} r'_c \left\{ k \Delta L_- * \left[\frac{\Delta A}{A} \left(1 + \frac{1}{(1 + if/f_{cc})(1 + if/f_c)} \right) \right] \right\} \quad (4.10)$$

where $*$ is the convolution of Fourier transforms of the two time series. Above the double cavity pole, f_{cc} , the carrier fluctuations are filtered out and so the optical gain modulation comes from the amplitude noise on the RF sidebands which travel unfiltered to the AS port.

Since laser amplitude noise is usually characterized by measurements of the power, it is convenient to note that $2\Delta A/A = \Delta P/P$. Another commonly used expression for the power fluctuations is the Relative Intensity Noise (RIN) which is equal to $\delta P_{rms}(f)/P$.

Combining Equations 4.10 and 3.3 we get the apparent differential arm signal due to laser power fluctuations:

$$\delta L_-(f) = 5 \times 10^{-21} \left[\left(\frac{\text{RIN}(f)}{1 \times 10^{-7}} \right) * \left(\frac{\Delta L_-(f)}{1 \times 10^{-13}\text{m}} \right) \right] \left(1 + \frac{f}{f_c} \right) \frac{\text{m}}{\sqrt{\text{Hz}}} \quad (4.11)$$

Measurements of the intensity noise coupling have revealed that this bilinear coupling term is dominated by a (currently) unexplained linear coupling which is the equivalent of having a static $\Delta L_- \simeq 3 \times 10^{-13}\text{m}$.

4.2.2 Laser Frequency Noise

Fluctuations in the frequency of the laser can couple into the interferometer's differential strain readout through imperfections in the optics. The frequency noise of the laser is intrinsically limited by spontaneous emission from the upper state into the laser mode. The spectral density of the frequency fluctuations is given by

$$\nu(f) = \frac{1}{2\pi \tau_{st}} \sqrt{\frac{h\nu}{P_{laser}}} \quad (4.12)$$

which is a form of the Schawlow-Townes limit[84, 85]. Substituting parameters for the LIGO master oscillator give $\nu(f) \approx 30 \text{ mHz}/\sqrt{\text{Hz}}$. In reality, the frequency noise is dominated by technical noise (thermal, acoustic, electronics) below 100 kHz.

To achieve the necessary frequency stability the laser frequency fluctuations are suppressed by several stages of active stabilization. This frequency stabilization scheme is detailed in Section 5.1.4. The following paragraphs mainly detail how the unsuppressed frequency noise can couple into the strain readout.

Although there are multiple mechanisms for frequency noise to show up at the AS port, they have a common theme: an imbalance between the two arms of the interferometer spoils the otherwise perfect subtraction of laser noise.

To calculate the signal due to frequency noise, we write the laser frequency, f , as $f = f_0 + \delta f_N \cos(\omega t)$. Then the signal at the anti-symmetric port due to frequency noise is

$$S_{\text{AS},Q} = \Re g_{crt_{sb}} \frac{\delta f_N}{2f} [8\pi r_c \frac{f_c l_m}{c} \frac{f}{f_c} \frac{1 + if/f_c}{1 + if/f_{cc}} + \frac{\delta f_c}{f_c} (1 - r_c) \frac{f/f_c}{(1 + if/f_{cc})(1 + if/f_c)} + \delta r_c \frac{f/f_{cc}}{1 + if/f_{cc}}] \quad (4.13)$$

The first term in the above equation comes from the Schnupp asymmetry, $l_- \approx 175$ mm. The audio-frequency, frequency noise sidebands on the carrier light get different phase shifts in the two Michelson arms and so they do not perfectly cancel out at the AS port. This residual field beats with the static sideband fields to produce a signal.

The second term is proportional to $\delta f_c/f_c$, the fractional difference in the two arm cavity poles. For the 4 km arm cavities, $f_c \approx 85$ Hz and the fractional difference has been measured by cavity ringdown to be $\sim 2\%$ (see Appendix F). A mismatch in the arm cavity poles comes about through a difference in the round-trip loss (including mirror transmissions). The loss in the arms is dominated by the $\sim 3\%$ transmission of the input test masses. Note that since the end mirrors have a reflectivity of ~ 1 ,

an arm cavity with no internal scatter loss or absorption will still have an overall reflectivity of ~ 1 . So the carrier fields reflected from the two arms have the same amplitude, but different phase. At frequencies above the arm cavity pole the carrier audio sidebands do not resonate in the arms and so do not experience a differential phase shift from the cavity pole imbalance. Therefore the frequency noise coupling due to the arm cavity pole imbalance gets smaller above the arm cavity pole.

The third term in the equation is somewhat different and is, in practice, the dominant effect. At frequencies above the coupled cavity pole, the carrier's audio sidebands are filtered off but the audio sidebands of the RF sidebands couple directly to the AS port. In a perfect interferometer this would have no effect, but an imbalance in the reflectivity of the arm cavities will produce a static, TEM_{00} carrier field at the AS port. Since the differential arm servo loop only suppresses differential phase shifts, this static field is not nulled. The audio sidebands of the RF sidebands then beat against this static carrier to produce a signal in AS-Q.

As shown in Figure 4-8, the term from the reflectivity imbalance is dominant. For typical parameters at frequencies above the arm cavity pole the apparent displacement noise from frequency noise is:

$$\delta L_-(f) \simeq 3.5 \times 10^{-20} \left(\frac{\delta r_c}{5 \times 10^{-3}} \right) \left(\frac{\delta f_N}{1 \times 10^{-6} \text{ Hz}/\sqrt{\text{Hz}}} \right) \frac{\text{m}}{\sqrt{\text{Hz}}} \quad (4.14)$$

A reflectivity imbalance comes about through a difference in the losses of the two arms. A full description of the optics' characterization is in Appendix F, but stated simply, we know from the power buildup in the interferometer that the scatter loss (≈ 70 ppm/mirror) is more important than the ETM transmission (~ 10 ppm).

4.2.3 Oscillator Amplitude Noise

A commercial signal generator (IFR 2023A) is used to generate the modulation waveform for the resonant RF sidebands. The output of the oscillator is multiply split; several outputs are used to power the local oscillator input of the various mixers used to demodulate the RF signals from the detection ports.

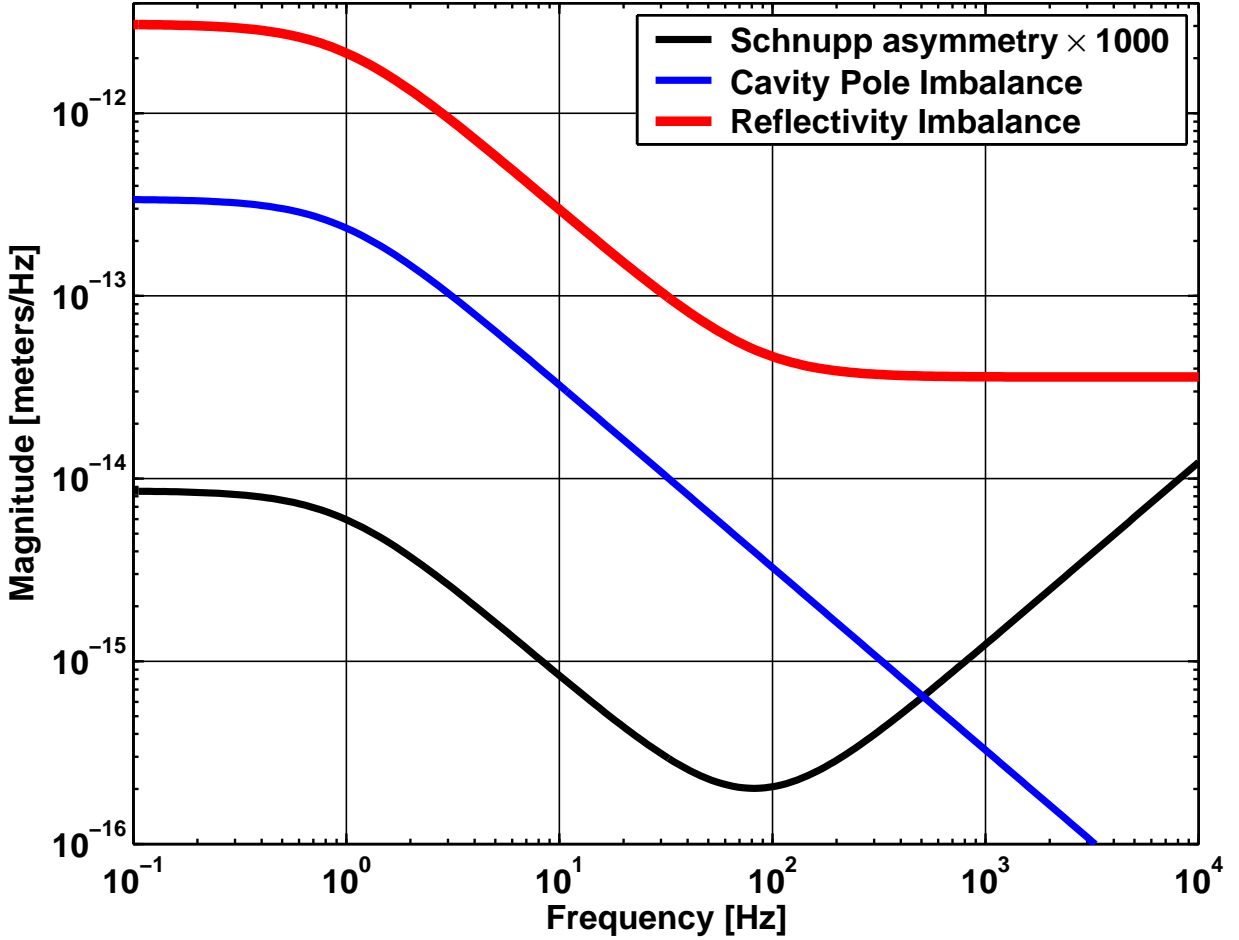


Figure 4-8: Shown are the three frequency noise coupling mechanisms. Asymmetries: $l_- = 175$ mm, $\delta f_c = 2$ Hz, $\delta r_c = 0.5\%$

One output of the splitter is actively amplitude stabilized and then used to drive a phase modulator (see Section G.5). Residual fluctuations in the modulation amplitude lead to sideband amplitude fluctuations. Noise on the amplitude of the sidebands modulates the optical gain at all of the readout ports. The RF mixers which demodulate the RF signal from the photodiodes are driven to saturation on the Local Oscillator (LO) port and so there is no sensitivity to amplitude fluctuations of the LO drives. Oscillator amplitude noise shows up as [67]

$$S_{AS_Q} = \aleph g_{crt_{sbr}} r'_c \frac{\Delta \Gamma}{\Gamma} k \Delta L_- \quad (4.15)$$

where Γ is the modulation depth in radians. At frequencies above the arm cavity

pole, for typical parameters we get:

$$\delta L_- \simeq 1 \times 10^{-19} \left(\frac{\Delta\Gamma(f)/\Gamma}{1 \times 10^{-7}/\sqrt{\text{Hz}}} \right) \left(\frac{f}{1 \text{ kHz}} \right) \left(\frac{\Delta L_-}{1 \times 10^{-13} m_{\text{RMS}}} \right) \frac{m}{\sqrt{\text{Hz}}} \quad (4.16)$$

The amplitude noise of the oscillator has been measured to be just below 10^{-7} from 100-1000 Hz and falling rapidly above 1 kHz.

4.2.4 Oscillator Phase Noise

Another noise source is phase jitter on the oscillator. So far the exact coupling mechanism of oscillator phase noise has not been determined but measurements have been made which show that it is currently a limiting noise source and so it pays to speculate about the coupling mechanism in order to have some theory to test.

In principle, there is no first order coupling of oscillator phase noise to the dark port since any noise is common to both the signal and the local oscillator and is therefore canceled in the demodulated signal. Relative phase lags in the two paths between the oscillator and the mixer break this symmetry and can produce a sensitivity to phase noise.

There are 3 main sources of phase lag:

- Relative path length differences lead to an overall time delay. The difference is ~ 30 m. Although this gives a substantial phase shift at the modulation frequency, once this is compensated for (by e.g. a length of cable) the remaining phase shift at audio frequencies around the carrier are negligible: $\sim 10^{-4}$ radians at 1 kHz.
- The power recycling cavity has a pole frequency of ≈ 170 kHz. This filters the phase noise on the optical RF sidebands, but does not affect the local oscillator and so makes a small differential phase shift proportional to $f/(170$ kHz) below the recycling cavity pole.

- The dominant phase shift for the optical RF sidebands comes from the mode cleaner which acts as a ≈ 4 kHz low pass filter on the phase noise.

Oscillator phase noise can be represented by modifying the expression for the input field:

$$E_{in} = E_0 e^{i\Gamma \cos(\omega_m t + \phi_N \cos \omega_a t)} \quad (4.17)$$

In principle, even with this asymmetry there would be no coupling. In both the symmetric and anti-symmetric ports, however, there is a large unsuppressed signal in the demodulation phase quadrature which is not used in the interferometer length control (REFL_Q & AS_I, respectively). These large low frequency signals get mixed into the signal phase by the fractional phase angle difference between the LO and RF paths.

The signal at the anti-symmetric port due to this signal can be written as:

$$S_{AS_Q} = S_{AS_I} \frac{if/f_{MC}}{1 + if/f_{MC}} \phi_N(f) \quad (4.18)$$

The particular model of signal generator (IFR 2023A w/ option 14) used to generate the modulation waveform was chosen because of its low phase noise spectrum (-130 dBc/ $\sqrt{\text{Hz}}$). Custom built quartz oscillators having phase noise as low as -160 dBc/ $\sqrt{\text{Hz}}$ can be purchased, although the commercial signal generator allowed the kind of frequency tuning flexibility which is outside the range of the quartz oscillators.

If it is true that the coupling mechanism depends on the amplitude of the AS_I signal, future reductions of the signal in this quadrature would also reduce the oscillator phase noise contribution to the strain sensitivity.

4.2.5 Beam Clipping on the Optical Tables

As the sensitivity in the interferometers improved, it became clear that there is a great deal of sensitivity to the acoustic noise on *every* optical table.

This acoustic sensitivity comes about through clipping of the beam on the optical

table through apertures and dusty optics. A hypothesis is that the large diameter junk fields, from the contrast defect for the carrier or the instability of the recycling cavity for the sidebands, produce a signal when clipped. The aperturing of the higher order fields produces some light which overlaps with the TEM₀₀ mode to produce a signal.

This is largely reduced by enforcing the standard practices of cleanliness, careful alignment, and dumping of secondary beams (into beam dumps which are dark at 1 micron). This type of noise is what was mainly responsible for the 100-1000 Hz structure in the H1 and H2 curves in Figure 4-14. It has been greatly reduced by the installation of an acoustic isolation enclosure around the AS port tables of each interferometer and by the use of larger optics on the table.

4.2.6 Auxilliary Length Controls

Fluctuations of lengths other than the differential arm cavity degree of freedom can produce signals at the Anti-Symmetric port. The average length of the arm cavities is not controlled at most frequencies but is tracked by the laser as described in Section 5.1.4.

The other two lengths, l_- , the differential mode of the recycling cavity and l_+ , the common mode of the recycling cavity, produce AS port signals in very different ways.

$$\begin{aligned}\delta L_-(f) &= \frac{r_c}{r'_c} \delta l_- \\ &\simeq \frac{1}{140} \delta l_-\end{aligned}\tag{4.19}$$

The l_- coupling is straightforward; it is described by Equation 3.4. The mechanism is similar to the way the differential arm signal is generated, the difference being that the l_- signal does not get amplified by the arm cavity finesse.

$$\begin{aligned}\delta L_-(f) &= 2\delta r_c \frac{1}{r'_c t_{RMT} t_M} g_{sb} r_M \delta l_+ (1 + if/f_c) \\ &\simeq \frac{1}{1400} \delta l_+ (1 + if/f_c)\end{aligned}\quad (4.20)$$

The l_+ coupling turned up unexpectedly in the course of commissioning. It is produced in a similar way to laser frequency noise coupling: audio sidebands on the RF sidebands beat with a static carrier at the AS port to produce an audio frequency signal. In this case, the audio sidebands are created by modulation of the l_+ length. The static carrier is produced by a reflectivity imbalance between the two arms, same as frequency noise coupling.

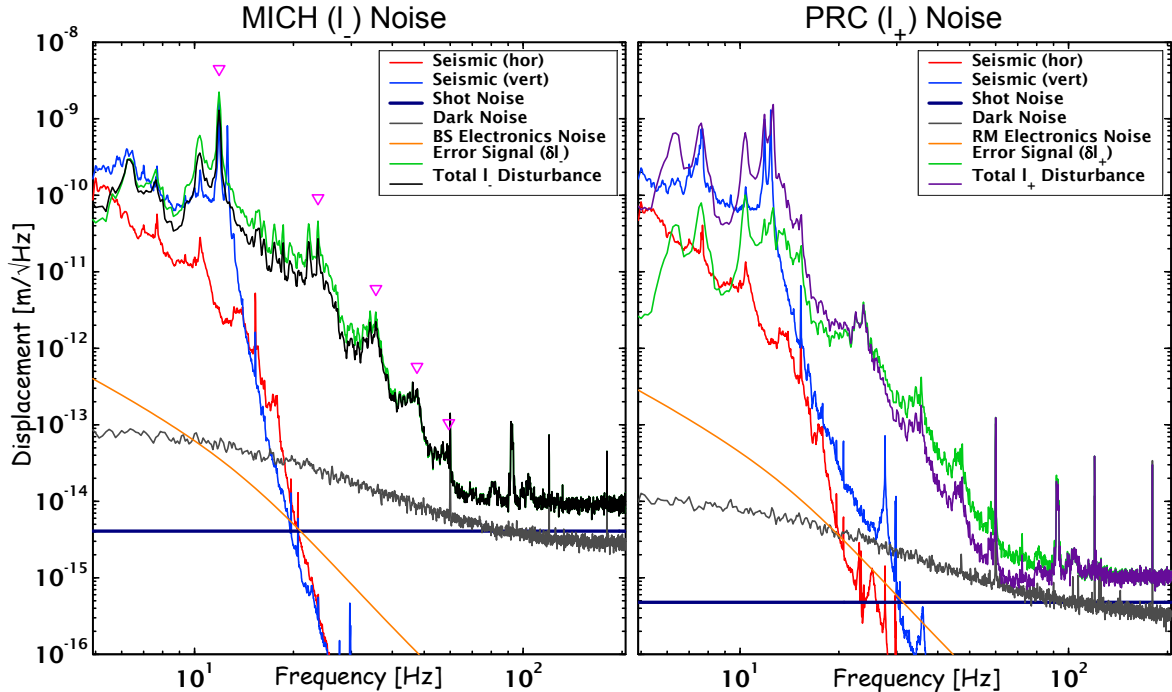


Figure 4-9: The two plots show the displacement spectra for both of the recycled Michelson DOFs; MICH (l_-) & PRC (l_+) and their known contributing noise sources. The triangles on the MICH plot indicate the harmonics of suspended optic's vertical bounce mode.

Both of these lengths must be controlled in order to keep the interferometer resonating. The length controls servos' gain must also be high enough that the residual fluctuations of these lengths do not compromise the strain sensitivity (more on this

in 5.1).

The largest disturbance to these lengths comes from seismic noise. As shown in the plots, the dominant contribution is from vertical noise. The 'vertical noise' traces actually refer to the apparent cavity length fluctuations which arise from vertical motion of the optic.

The coupling is much larger for the recycling cavity than for the arm cavities. In this case, the ~ 1 degree vertical wedge angles are the main coupling source. The exact positions and angles of each optic surface are documented [86]. The 'vertical noise' trace is estimated by first measuring the vertical motion with an accelerometer mounted external to the vacuum chamber. This trace is converted into displacement units, multiplied by the modeled vertical \Rightarrow vertical transfer function of the stack, and then multiplied by the vertical \Rightarrow vertical transfer function of the pendulum suspension which takes into account the compliance of the steel suspension wire.

This is done separately for each of the four recycling cavity masses and then summed with the appropriate geometrical factors to make the displacement noise.

In principle, the only other noise limit to these lengths should be in the sensing chain. The dark noise curve in Figure 4-9 is the result of ADC noise below 100 Hz and the noise of the photodetector above 100 Hz. The shot noise limited displacement sensitivity of these degrees of freedom is rather high compared to the Anti-Symmetric or Reflected ports; only a small fraction of the circulating field in the recycling cavity is picked-off for the signal detection.

It is clear from these plots, that the normal linear coupling mechanisms are not good enough to predict the noise that we actually see. The indicators in the MICH plot of Figure 4-9 show what appears to be significant upconversion of the large amplitude low frequency motions, implying that the bilinear noise mechanism has, as one of its terms, the vertical bounce mode.

4.2.7 Shot Noise

Vacuum field fluctuations entering the interferometer through the anti-symmetric port affect the interferometer's phase sensitivity by beating with the RF sidebands [83, 87].

This is often described as 'shot noise': Poisson arrival time statistics of the light on the photodetector.

In addition to this more fundamental noise source, there is also extra shot noise introduced by the presence of junk light on the photodiode. The differential arm signal is in principle only dependent on the amount of light in the TEM₀₀ mode but the shot noise level depends on the total light level since the light power level is not dominated by the beat between the carrier and sideband fields.

The expression for the shot noise signal at the AS port is[67]:

$$S_{\text{AS-Q}} = 2\sqrt{[J_0(\Gamma)^2 g_{cr}^2 c_d + \frac{3}{2} 2J_1(\Gamma)^2 t_{sb}^2] P_{in} h\nu} \quad (4.21)$$

where $c_d \equiv P_{AS}/P_{BS}$ is the carrier contrast defect. The two terms in the bracket are essentially just the carrier power ($\propto J_0(\Gamma)^2$) and the sidebands' power ($\propto J_1(\Gamma)^2$). The factor of 3/2 in the term for the sidebands' power derives from the non-stationary nature of the shot noise produced by the sidebands [88] and the fact that we are using effectively a sine wave demodulation [89]. Combining Equations 3.3 and 4.21 gives us an expression for the equivalent differential arm length noise:

$$\delta L_- \simeq 3.6 \times 10^{-17} \sqrt{\frac{1}{P_{in}} \frac{\sqrt{J_0(\Gamma)^2 g_{cr}^2 c_d + \frac{3}{2} 2J_1(\Gamma)^2 t_{sb}^2}}{J_0(\Gamma) J_1(\Gamma) g_{cr} t_{sb} r'_c}} \left(1 + i \frac{f}{f_c}\right) \frac{\text{m}}{\sqrt{\text{Hz}}} \quad (4.22)$$

We can then optimize the SNR, by adjusting the modulation depth, Γ , to minimize this function.

Mode Overlap and Optical Gain

The above formula and all of the formulae in Chapter 3 are valid in the limit that all of the light is in the same spatial mode. This is not exactly true at any port; the situation at the Anti-Symmetric port is of the most concern.

The differential arm strain signal is encoded on the carrier light returning to the beamsplitter as a differential phase shift. After interfering at the beamsplitter a small

field proportional to this phase difference comes out of the AS port. The spatial profile of this signal field is set by the *average* of the resonant modes in the two arm cavities. If the arms are well matched spatially, this is not a significant distinction to make.

What is significant is the spatial mode of the RF sidebands at the AS port. Due to the spatial mismatch between the recycling cavity 'mode' and that of the arm cavities (see Section 8.1.3 for details), some fraction of the sideband field at the AS port contributes to making shot noise but not to the signal gain.

Nominally, the length signal, AS_Q, is not sensitive to the higher order spatial modes except as it relates to the generation of shot noise. This is because a higher order TEM_{mn} mode is orthogonal to the nominally TEM_{00} local oscillator field of the RF sidebands. However, the presence of higher order modes in both the sidebands and carrier will contribute directly to the signal (some in AS_I and some in AS_Q). This signal is nulled in the I-phase quadrature with the AS_I servo (see Section H.1), but in the Q-phase this signal has to be nulled by introducing a differential arm length offset.

4.2.8 Readout Electronics

Another technical source of noise is the electronics chain which reads out the strain signal. The following block diagram shows the signal flow:

Since the goal is to achieve the minimum strain noise possible we design the electronics noise to be less than 1/10 of the noise coming from the more fundamental shot noise.

To accomplish this, the signal-to-noise ratio achieved at the front end electronics is not degraded throughout the chain into the ADC. The dark noise of the photodetector at the anti-symmetric port (described in more detail in Appendix H) is in principle, *dominated by the thermal noise of the LC resonant circuit formed by the photodiode and the inductor*. So the requirement on the whitening electronics is only to increase the signal from shot noise (or other 'fundamental' sources like thermal or seismic) to at least 10X the ADC noise level. This is balanced by the desire to maintain a factor of 30 or more in headroom between the RMS signal level and the ADC input range.

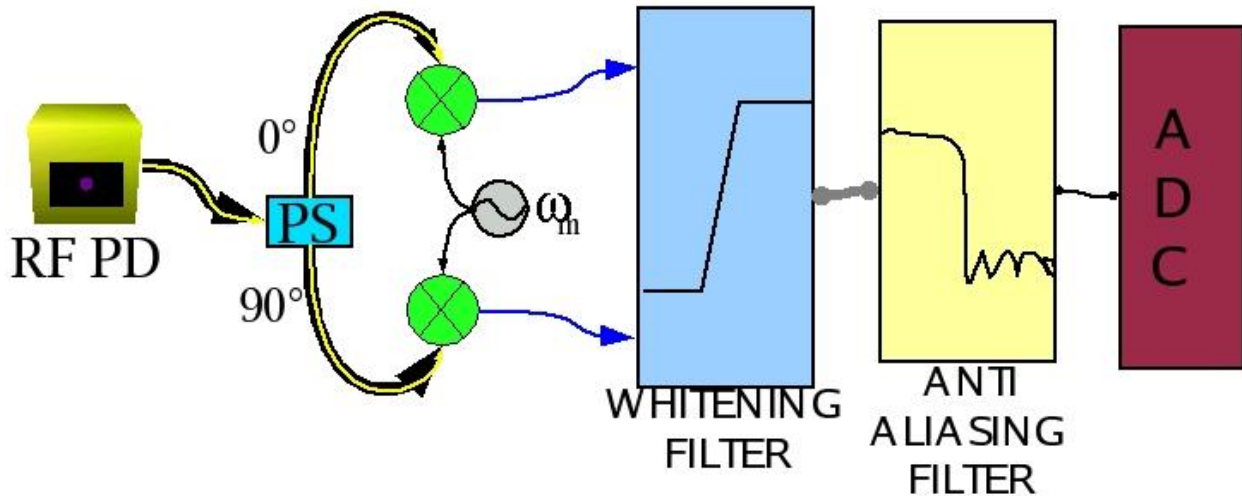


Figure 4-10: Shows the signal flow from the RF photodiode to the analog-to-digital (ADC) converter.

4.3 Some Notes about the Noise

The interferometer noise is usually unexplained in several frequency bands and it is always changing (sometimes for the better). Therefore, I have attempted here to give a good accounting of the noise as it was in 2002-2003, which were the years in which LIGO held its first three science runs (creatively named S1, S2 & S3).

4.3.1 The Status of the Noise

Figure 4-11 is a good summary of this entire chapter. The point of doing all of the noise analysis and budgeting is to always know what noise sources limit the interferometer sensitivity and how this noise can be reduced. The traces in the plot are not all made in the same way. Some of the traces (e.g. oscillator phase noise) are made by measuring the source of the noise (oscillator phase noise) and then the transfer function to AS_Q and then multiplying them. Other traces (e.g. internal thermal noise) are almost entirely based on a model for the noise with few measurements for support.

The noise will often fluctuate upwards by factors of a few due to short time transients or instabilities in the control servos. These plots of the amplitude spectral

density do not capture this character.

4.3.2 A Brief History of the Noise

These interferometers actually 'awoke' with noise levels at least 5 orders of magnitude higher. These next paragraphs attempt to give a short synopsis on the major developments between each noise epoch shown in Figure 4-12.

May 18th, 2001

Pre power-recycling. The RM is misaligned intentionally to allow locking of the Fabry-Perot Michelson in an optically recombined but not recycled mode. In this configuration there is very little light at the anti-symmetric port available for locking and so the noise above 1 kHz is dominated by the dark noise of the sensing electronics. The vast array of line spikes at multiples of 60 Hz are from the switching power supplies which were in use at this time. In addition, there is no feedback from the interferometer to suppress laser frequency noise which therefore dominates the noise from 80-500 Hz.

December 12th, 2001

The vacuum system was vented over the summer of 2001 to allow a number of repairs: several of the suspensions' local sensors had broken photodiodes, wires, etc. In addition this version of local sensor had a photodiode which was sensitive to the 1064 nm laser light. New sensor / actuator heads were installed on all optics which are more than 100X less sensitive at 1064 nm.

December 21th, 2001

Lower DAC Noise: First successful attempts to run the interferometer with the post-DAC dewhitening filters.

May 27th, 2002

Power recycling and frequency stabilization. The first part of this year was spent increasing the robustness of the power-recycled configuration. The common mode servo was installed in a preliminary configuration and gave some suppression of the frequency noise.

August 24th, 2002 (S1 Science Run)

Common mode servo was revamped: L_+ feedback to the arms was removed and the CM feedback to the mode cleaner length was changed to use a digital servo. At this point it was discovered that through some non-linear mechanism the noise at AS_Q around 100 Hz could be reduced by increasing the differential arm loop gain at 10-20 Hz. This later turned out to be large bilinear upconversion around the power line harmonics. The source was never identified, but the noise went away in the next major electronics upgrade.

March 6th, 2003 (S2 Science Run)

All the electronics for the suspension controls are replaced with a mostly digital system allowing for greater flexibility. The introduction of the AS_I servo made it possible to detect nearly all of the light at the anti-symmetric port. The large shelf of noise at 35 Hz from the optical lever servos is finally reduced by whitening the optical lever sensor signals before the ADC.

December 24th, 2003 (S3 Science Run)

Very little broadband improvement in sensitivity. An acoustic enclosure was installed over the anti-symmetric port optics table, greatly reducing the acoustic noise susceptibility. Efforts to commission the wavefront sensor based angular control system were only partially successful and most of the run had only 8 out of 16 degrees of freedom under control; 6 more than in S2, but not enough to greatly improve stability.

The noise improvements at low frequencies came from improved filtering of the

optical lever servos and the Michelson control loops. One notable improvement is the addition of an off diagonal drive in the length control which feeds a small fraction of the l_- control signal to the L_- length. This was implemented mid-run and greatly improved the character of the noise in the 30-70 Hz region.

4.3.3 Evolution of Phase Sensitivity

The original Michelson interferometers were able to resolve down to 1% of an optical fringe. The LIGO sensitivity goal requires a phase noise level of 3.5×10^{-11} radians/ $\sqrt{\text{Hz}}$. This very small phase shift can be sensed due mainly to the increased power levels in the Michelson part of the interferometer. Figure 4-16 shows the evolution of optical phase noise measurements in the last 40 years.

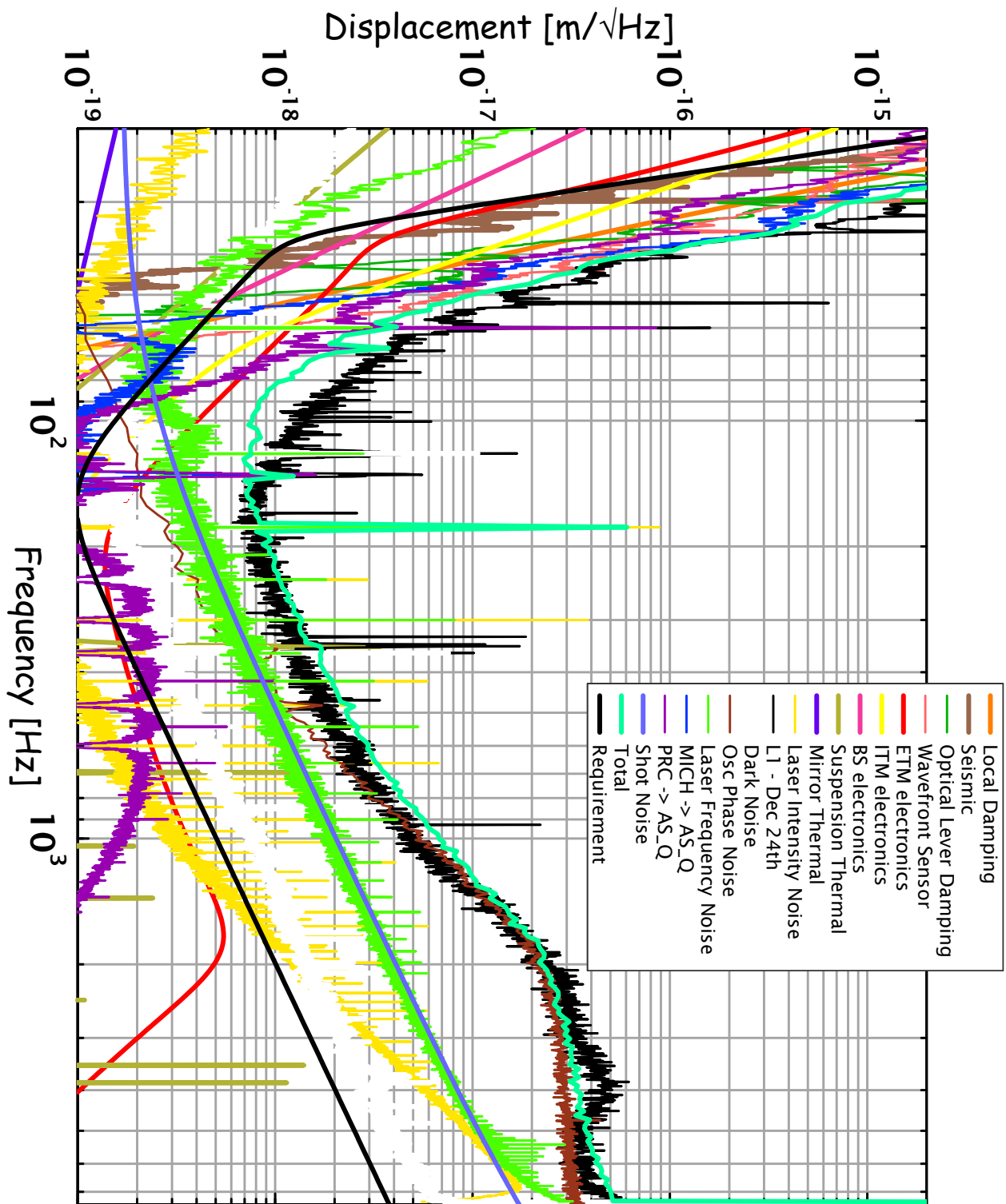


Figure 4-11: Full Noise Budget for L1 during S3 (data from Dec. 23, 2003)

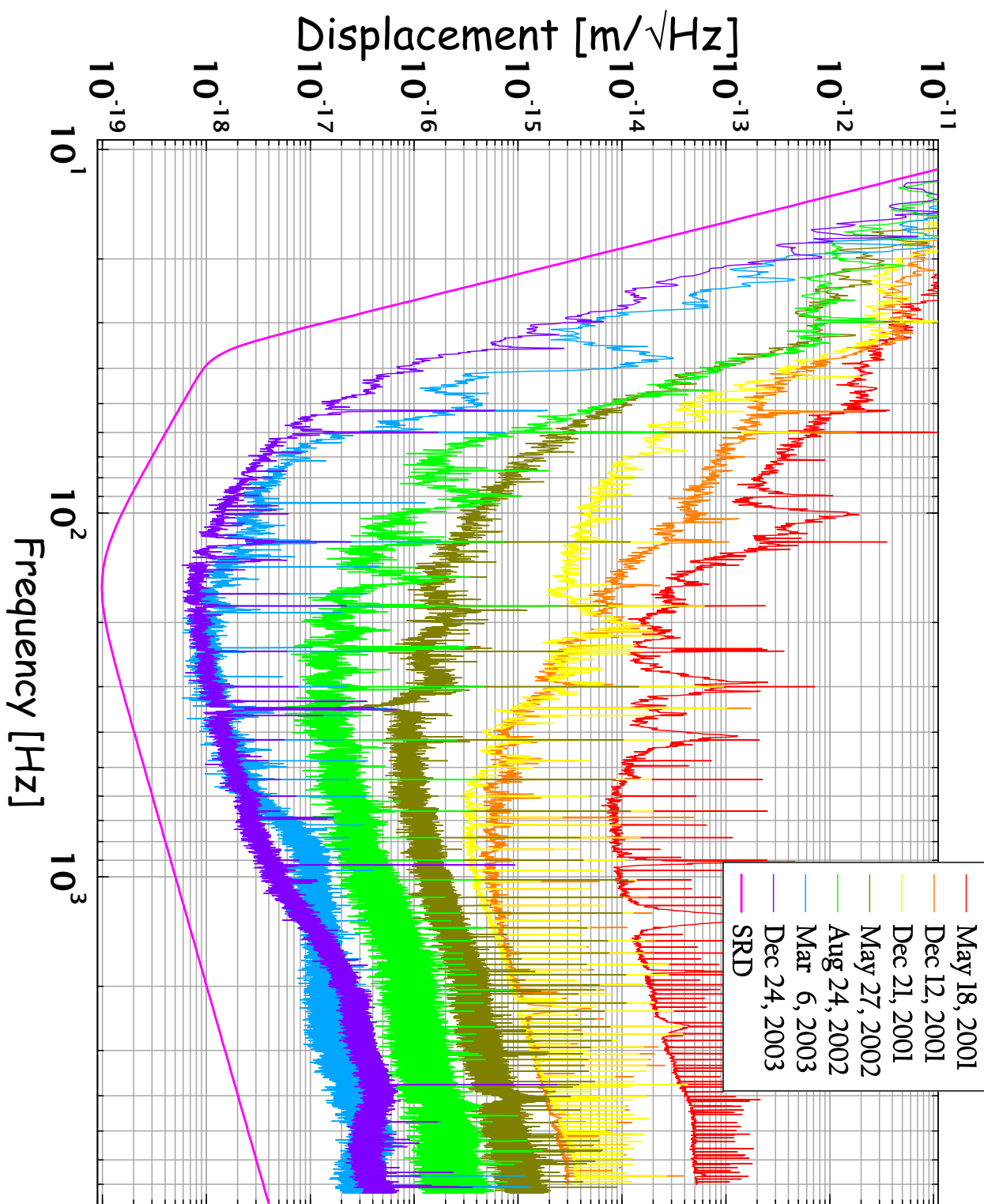


Figure 4-12: Noise history of the Livingston Interferometer from 2001-2003.

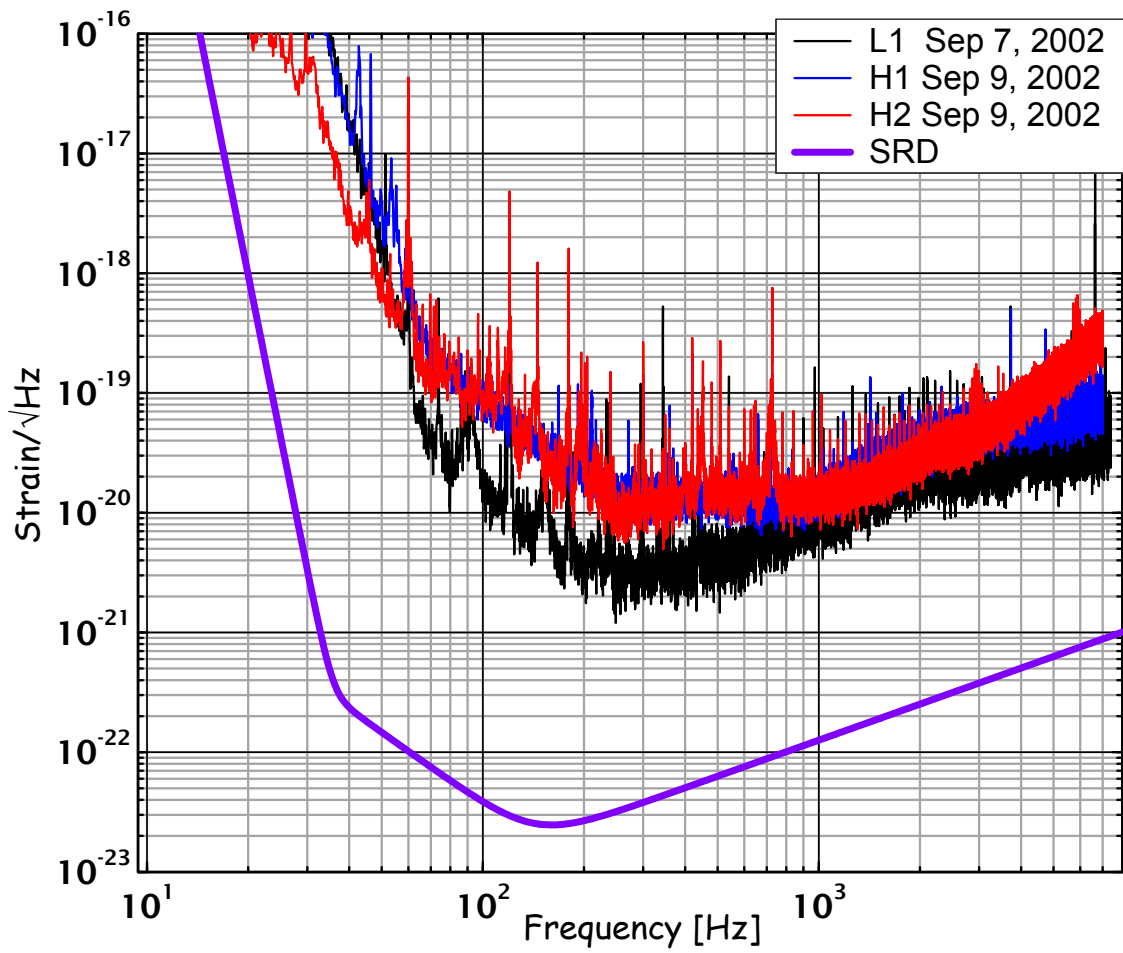


Figure 4-13: Comparison of the interferometer noises during the first Science Run (S1).

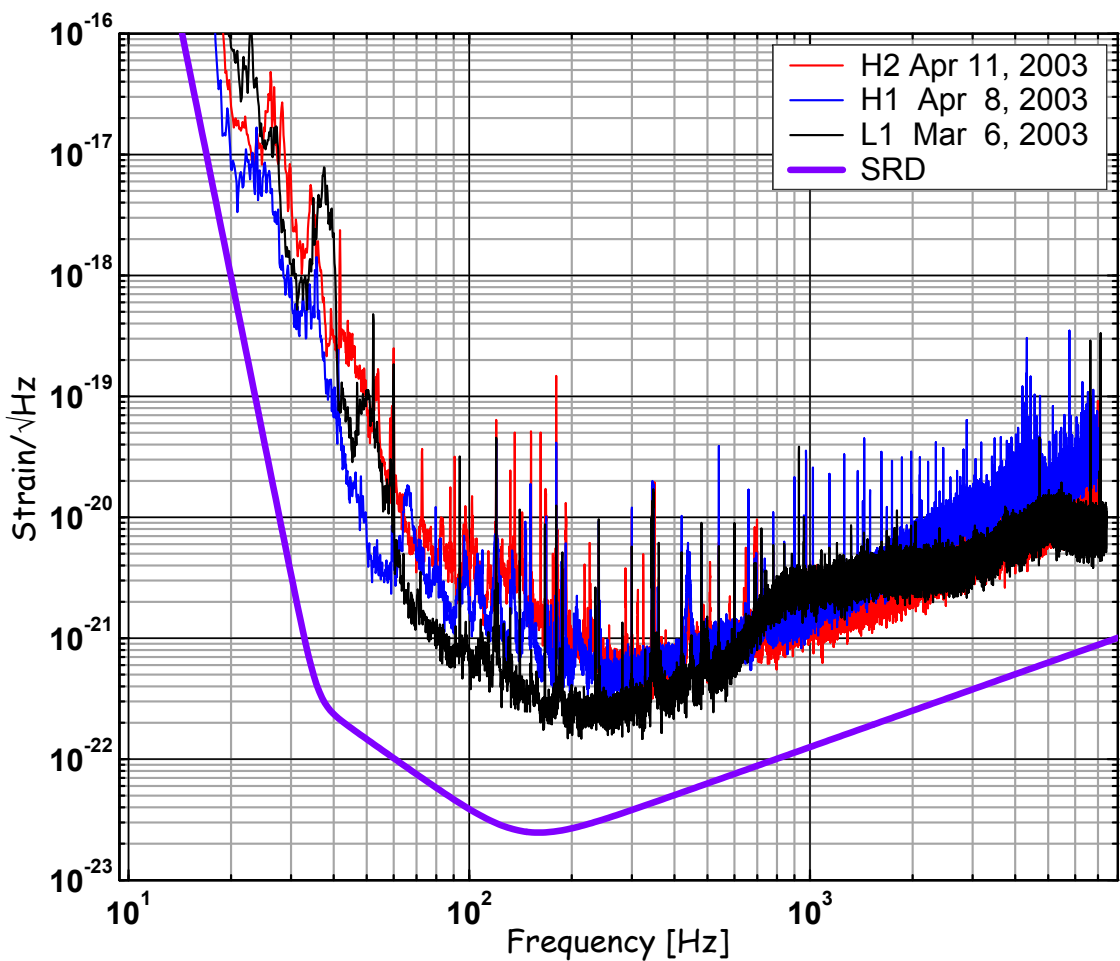


Figure 4-14: Comparison of the interferometer noises during the second Science Run (S2).

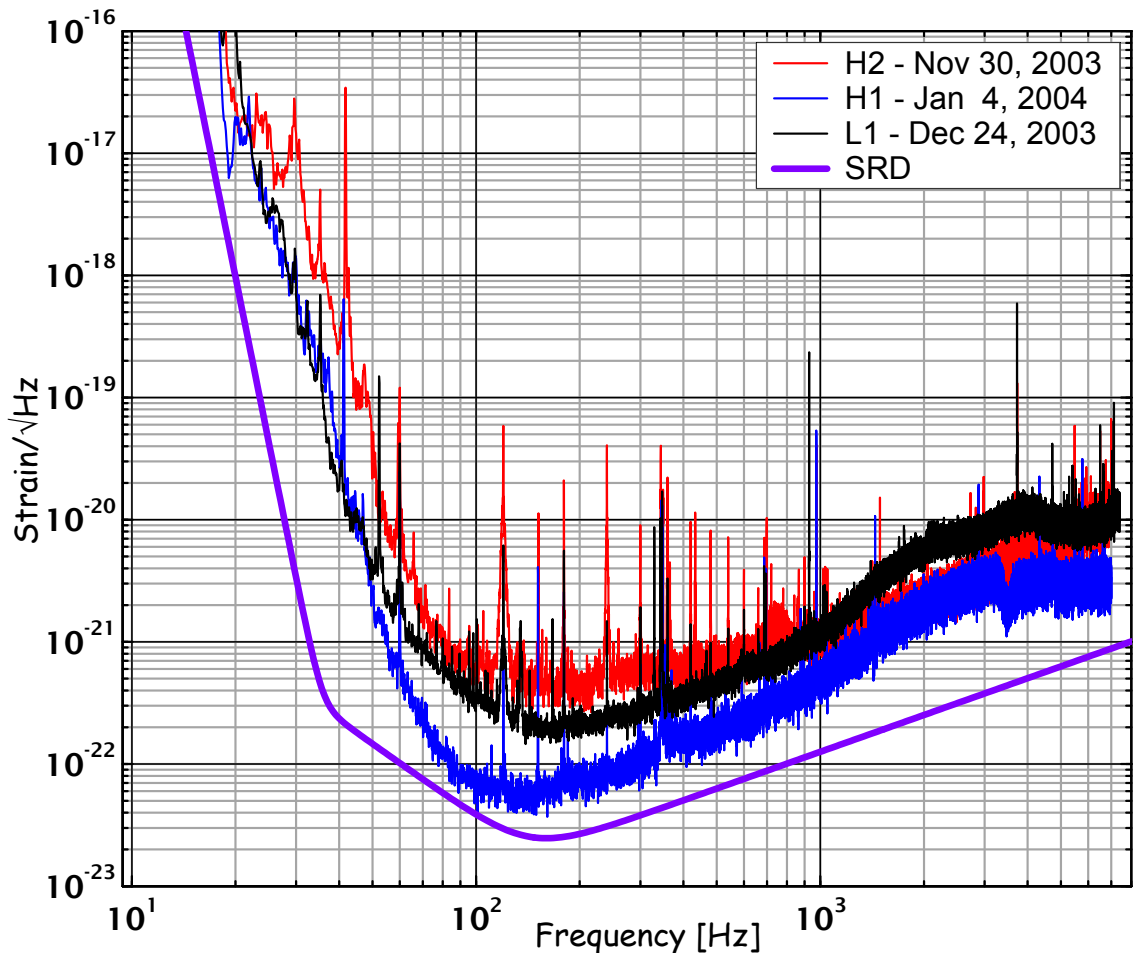


Figure 4-15: Comparison of the interferometer noises during the third Science Run (S3).

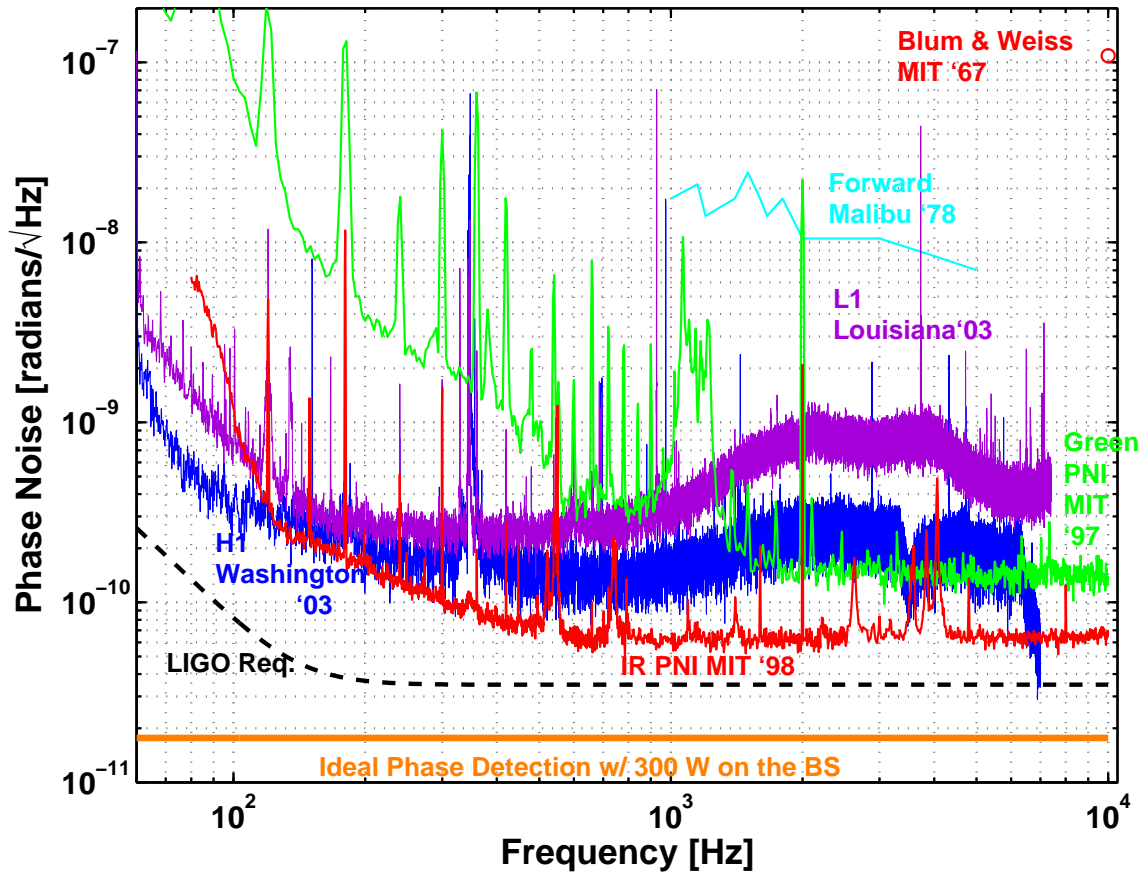
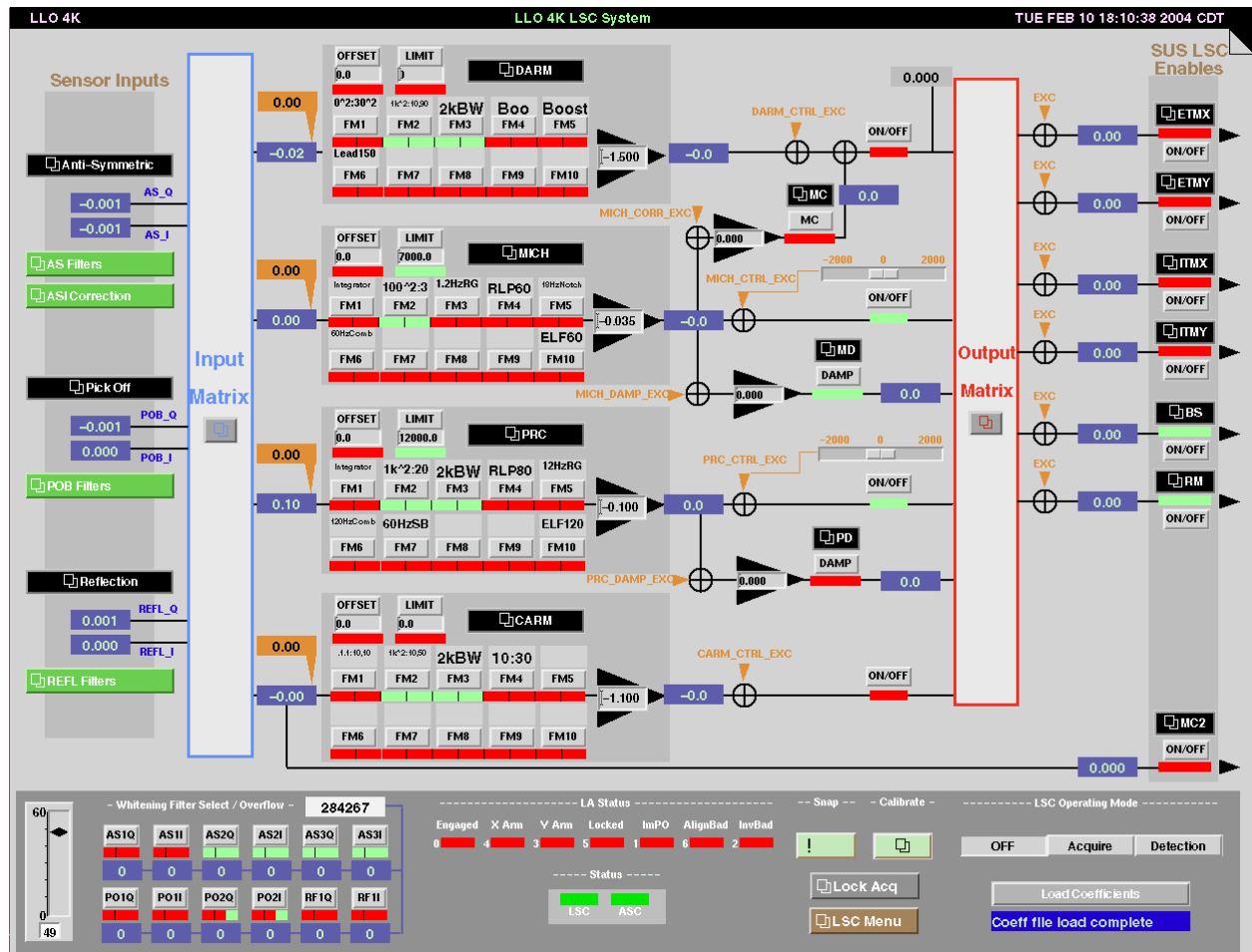


Figure 4-16: Evolution of Phase Noise Measurements. The phase shift here is defined as the single trip difference between the two arms. This convention makes all of the curves a factor of 2 lower than in other phase noise comparisons [90, 91]

Chapter 5

The Control Systems



This chapter describes the major feedback control systems used to keep the interferometer operating at a point of high sensitivity, and motivations for the requirements on the control loops and their performance as of 2003.

Most of the assertions made about the signal readout and the noise couplings in Chapters 3 and 4, respectively, are only valid at a very specific operating point: the point at which the light is resonant in all parts of the interferometer.

Firstly, resonance means that the round trip phase shift in a single cavity is an integer multiple of 2π . This is to ensure that there is constructive interference and therefore resonant buildup of the field in the cavity. In the one-dimensional picture where only the distance between the mirrors may be adjusted, this is a clear definition.

Secondly, the beam must spatially overlap the same region on each pass. If the cavity mirrors are overly misaligned the beam will simply miss the mirrors and fall out of the cavity. Between this gross level and perfect alignment, there will be some reduction in the power buildup. There will also be some increased noise couplings [92].

Finally, the beam's wavefront must remain unchanged on each round trip. This sets some constraint on the shape of the cavity mirrors. In fact, all of these criteria are just specific examples of a more general criterion which states that if the electric field is represented in a basis of orthogonal modes, the case of perfect resonance is one in which there is no mode mixing on any round trip of the cavity. This is further described in Appendix E.

The job of the control systems is to keep the light resonating in the interferometer. Secondarily, the control systems keep the interferometer's lengths and angles as close as possible to the perfect resonance condition in order to prevent degradation of the strain sensitivity.

At last count, there were 107 custom tailored, control loops running the interferometer; this does not include any of the systems associated with the building HVAC controls, the vacuum system, or the several PID type servos running inside of some of the commercial instruments. At the time of this writing there are no servos in operation to actively control the mirrors' curvature.

This chapter will focus on the active control of the length degrees of freedom of

the interferometer, with only a brief description of the angular controls.

5.1 The Length Control Loops

The most recent descriptions of the interferometer's length controls are given in [93] and [94]. The following paragraph gives a brief description of the generalities. The rest of the chapter goes into more detail by first motivating the need for control loops and setting requirements for them. Then constraints are placed on the loops in the gravitational wave band to reduce noise pollution from the auxiliary loops.

The average arm length is used in the overall frequency stabilization scheme and is discussed separately in Section 5.1.4.

There are several common elements among the 4 control loops:

- An RF photodetector is used to detect the AM modulated light exiting from one of the 3 detection ports. The RF signal is demodulated at the resonant sideband frequency (f_m). Both the in-phase and the quadrature-phase components of the demodulation are acquired by a 16 kHz ADC after a few stages of signal conditioning.
- The signals are all sent to a VME or rackmount CPU, running custom written digital signal processing (DSP) code. The code performs many functions including: digital filtering, signal summation, triggering, and also provides the signals to the data acquisition system.
- After some filtering, the digital signals are passed on to a separate set of processors which are set up to handle all functions of a specific suspended optic. There are typically 1 or 2 optics controlled per CPU.
- These suspension processors then send the final output signals for each optic to a digital-to-analog converter (DAC). The DAC signals then go through a set of signal conditioning circuits. Finally, there is a power amplifier stage for each coil of every suspended optic.

- The coil currents induce forces on the optic through the magnets glued onto them. The interferometer lengths and angles are adjusted by moving the suspended optics.

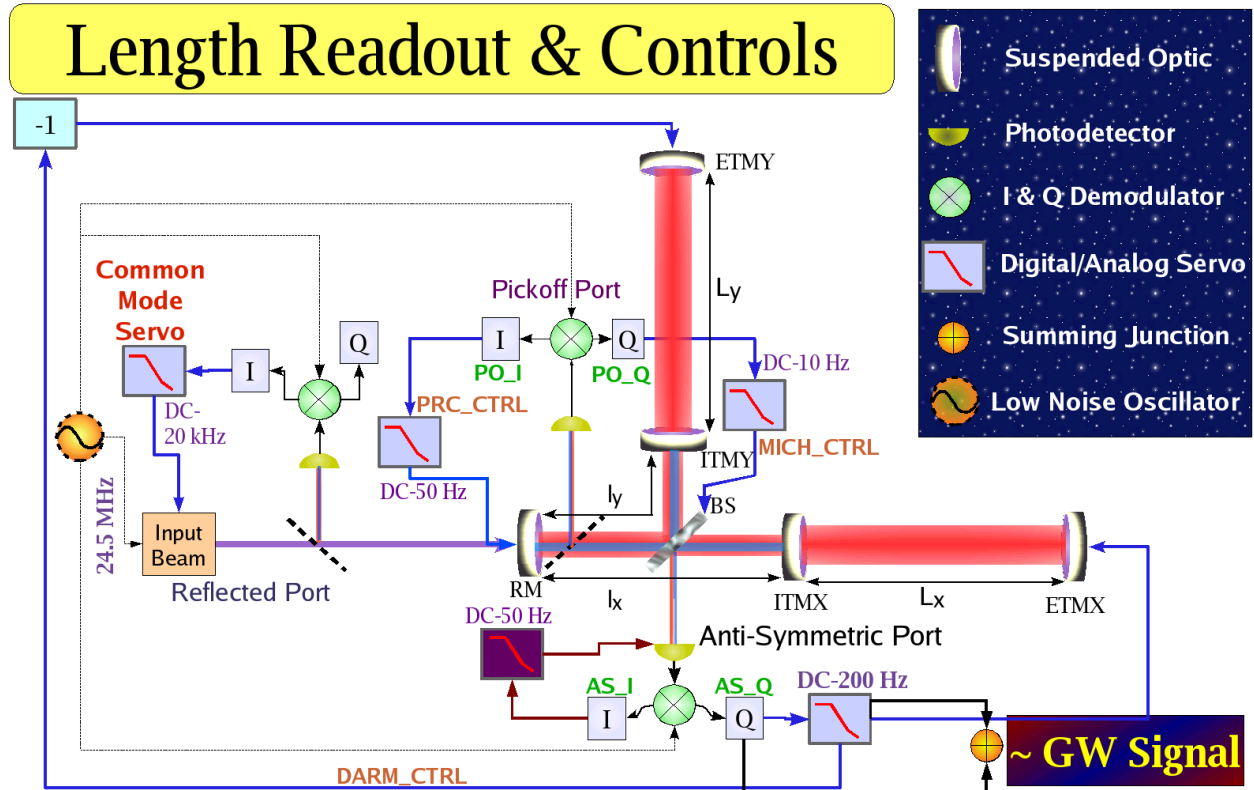


Figure 5-1: Block diagram of the Length Sensing and Control system.

5.1.1 Allowed Residual Deviations

The interferometer is said to be 'locked' when the light is resonating and the error signals of the control loops are still within their linear region. To determine how tightly the servos must hold the lock one must look at the stricter constraint of the apparent strain noise induced by the deviation from perfect resonance.

So for the length degrees of freedoms a requirement is set on either $\delta L(f)$, the residual error point spectrum or on δL_{RMS} , the total RMS deviation.

Differential Arm Length (δL_-)

As shown in Chapter 4, there are a few noise terms which scale linearly with δL_- . Both the laser amplitude noise and the oscillator amplitude noise are really the same physical noise mechanism; they modulate the gain of the gravity wave readout channel. Seen in that light, the requirement is really on the allowed dynamic range of the readout signal. Given that the displacement noise goal is $1 \times 10^{-19} \text{ m}/\sqrt{\text{Hz}}$ at 150 Hz, the requirement must be that the product of the low frequency error signal and the gain modulation not exceed this level.

Since the noise term is linearly dependent on two variables, the noise can be decreased by lowering either component. In practice, attempts were made to suppress both terms. Further iteration was determined by the success (or lack of it) in these attempts at suppression.

As a rough estimate, we set the requirement for the residual differential arm length fluctuations to be that $\delta L_- < 1 \times 10^{-13} \text{ m}_{\text{RMS}}$. This sets the requirement on the absolute gain modulation to be such that $\delta G < 10^{-7}$ for $f = 10 - 10000 \text{ Hz}$. This ensures that the bilinear noise introduced by laser amplitude noise does not exceed 1/10 the displacement sensitivity goal.

Differential Recycling Cavity Length (δl_-)

Excess noise in the sensing of this degree of freedom couples into the AS port through the l_- control loop. The coupling is determined by Equation 4.19 . Amplitude noise shows up in this loop the same as for the L_- loop. We would like the amplitude noise term to not exceed the shot limited sensitivity at this port.

From the shot noise formula for MICH in Appendix I, we have that the shot noise limited sensitivity is $1 \times 10^{-16} \text{ m}/\sqrt{\text{Hz}}$. Using the requirement for the gain modulation, we have a requirement on the residual differential recycling cavity length that $\delta l_- < 1 \times 10^{-9} \text{ m}_{\text{RMS}}$.

Common Arm Length (δL_+)

In order to retain the high power buildup in the interferometer, the coupled cavity formed by the recycling mirror and the arms must stay quite close to resonance. The field in the recycling cavity, just past the recycling mirror is

$$E_{RC} = \frac{t_{RM}}{1 + r_{RM}r_c} E_{in} \quad (5.1)$$

A small change in the average arm length changes r_c , the arm reflectivity, mostly in phase. This moves the carrier off resonance in the recycling cavity, reducing the overall buildup.

In the limit of perfect contrast, the shot noise at the AS port is entirely dominated by the sideband power. Then the reduction in signal-to-noise is proportional to $\sqrt{P_{BS}}$, the power on the Beamsplitter, and for a 1% reduction in signal-to-noise we can allow a 2% power reduction.

This sets a limit of $\delta L_+ < 2 \times 10^{-12}$ m_{RMS}.

Common Recycling Cavity Length (δl_+)

Using the same reasoning as above, the answer for the recycling cavity common mode length is that $\delta l_+ < 2.5 \times 10^{-10}$ m_{RMS}. Here the main difference is that a change in the recycling cavity length affects the phase of the carrier field in the recycling cavity directly and does not get the phase gain associated with the arm. In fact, the ratio between the requirements for the 2 lengths is just the phase gain factor for the arm, r'_c (≈ 140).

The recycling cavity Finesse for the sidebands is much less than that for the carrier and as such, the reduction in recycled sideband power does not drive this requirement.

External Disturbances

Ideally one would like to have an accurate model of the interferometer which could take as inputs all of the available environmental inputs and deliver all of the interferometer output signals by including all of the mechanical, electronic, and optical

dynamics from one end of the interferometer to the other. There is currently a time domain model under development [95] with exactly this goal.

Even better, however, is to measure the true length fluctuations interferometrically. So the design of the length control loops is bootstrapped. The interferometer was first locked with the simplest loops that would keep it operating in the linear regime. Then the loop shapes were iterated until the residual fluctuation requirement was met.

The disturbance, $\Delta(f)$, to a loop can be expressed in terms of a few standard servo parameters:

$$\delta(f) = \frac{\Delta(f)}{1 + G(f)} \quad (5.2)$$

$$C(f) = \frac{\Delta(f)G(f)}{1 + G(f)} \quad (5.3)$$

From the above equations, one can see that at frequencies where the open loop gain, $G(f)$, is high, the control signal, $C(f)$, is nearly equal to the disturbance. At frequencies where the gain is low, the error signal, $\delta(f)$, is a more accurate estimator. In practice, to get the most accurate estimate of the disturbance, either the control signal or the error signal can be used, but both must be corrected for the transfer function of the servo loop.

Figure 5-2 shows the disturbance signal for the L_- , l_- , and l_+ loops.

Gain Requirements

Having the external disturbance spectra and a goal for the residual fluctuations allows us to make a first iteration on the control loops. The fact that the loops are digitally implemented allows one to quickly iterate on the loop transfer functions and achieve the desired performance.

The Bode plots in Figure 5-3 show the open loop gain of three of the four main length control loops.

With these loops the measured loop residuals meet the requirement. Figure 5-4

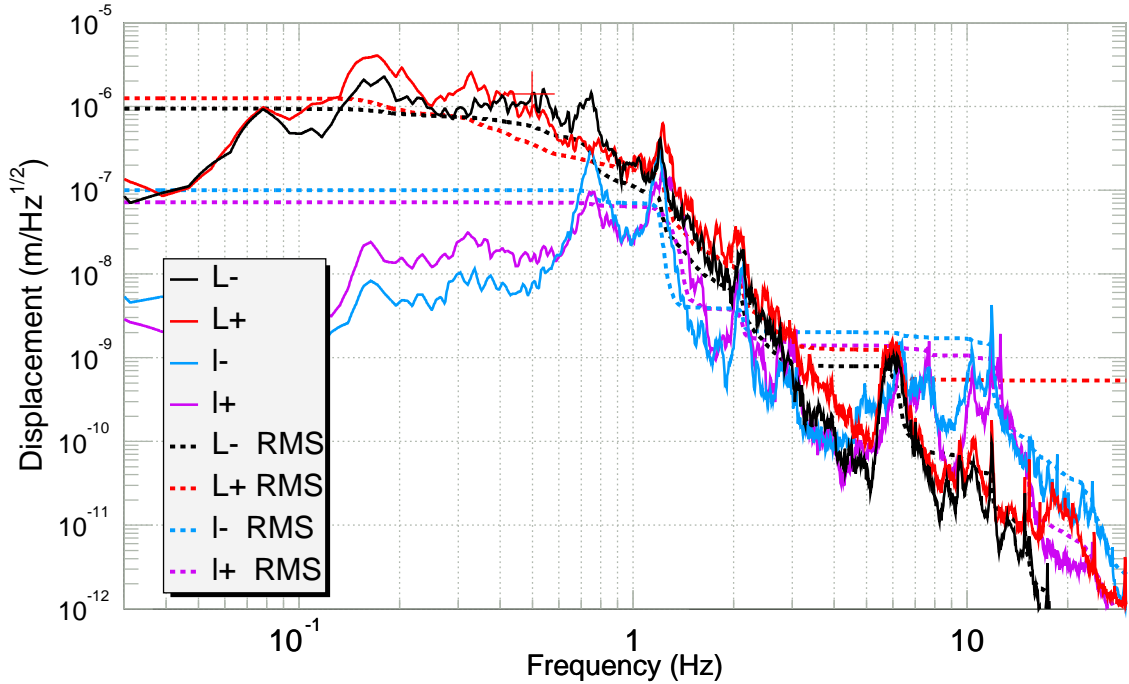


Figure 5-2: Apparent input length disturbance as inferred from the servo control signals. The traces labeled 'RMS' show the total RMS displacement in the signal in the band, $f - 50$ Hz.

shows the in loop error signals.

5.1.2 Noise Pollution

In the gravitational wave band the motion in the auxiliary loops must be controlled to a level such that induced strain noise spectral density is at the SRD/10 level. The introduced noise is a function of three parameters of the auxiliary loop: the sensing noise, the loop gain, and the coupling to AS_Q. So attempts were made to reduce all three terms.

Auxiliary Sensing Noises

In Figure 4-9, the noise in the l_- and l_+ loops is shown. All of the noise above 20 Hz can be seen as some sort of sensing noise in that it is not a direct representation of length fluctuations.

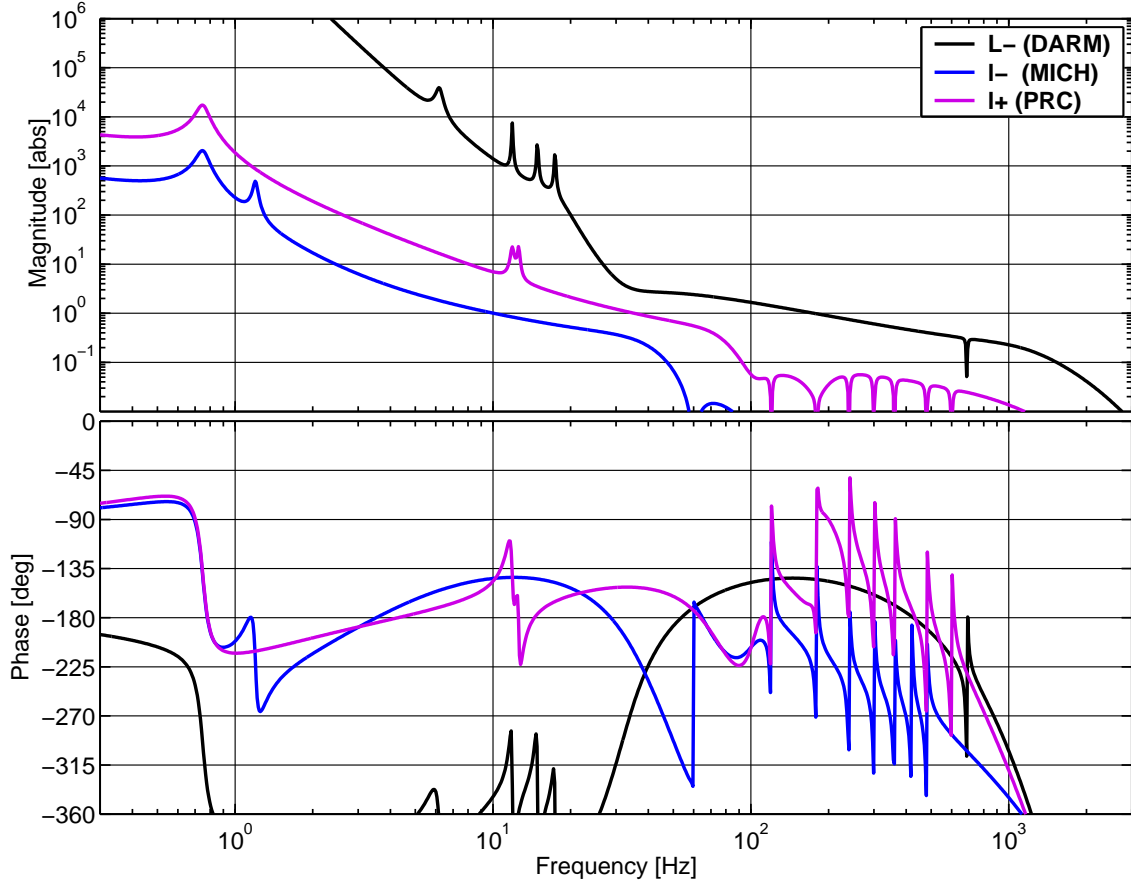


Figure 5-3: Open loop gain of three length control servos.

Gravitational wave band filtering

Since the l_- & l_+ signals are full of only sensing noise in the gravitational wave band one would like to reduce, as much as possible, the contribution of the control signals to AS_Q. To do this, aggressive digital stopband filters were designed to lower the loop gain in the sensitive 60-200 Hz band.

5.1.3 The real loops

Each of the three main length control loops were individually tailored and have intricate transfer functions (as shown in Figure 5-3). These following sections list a few of the driving considerations involved in designing the loops. In all cases, the gain at low frequencies must be high enough to suppress the noise shown in Figure 5-2 to the levels specified in Section 5.1.1. In addition, the servos must have sufficient gain

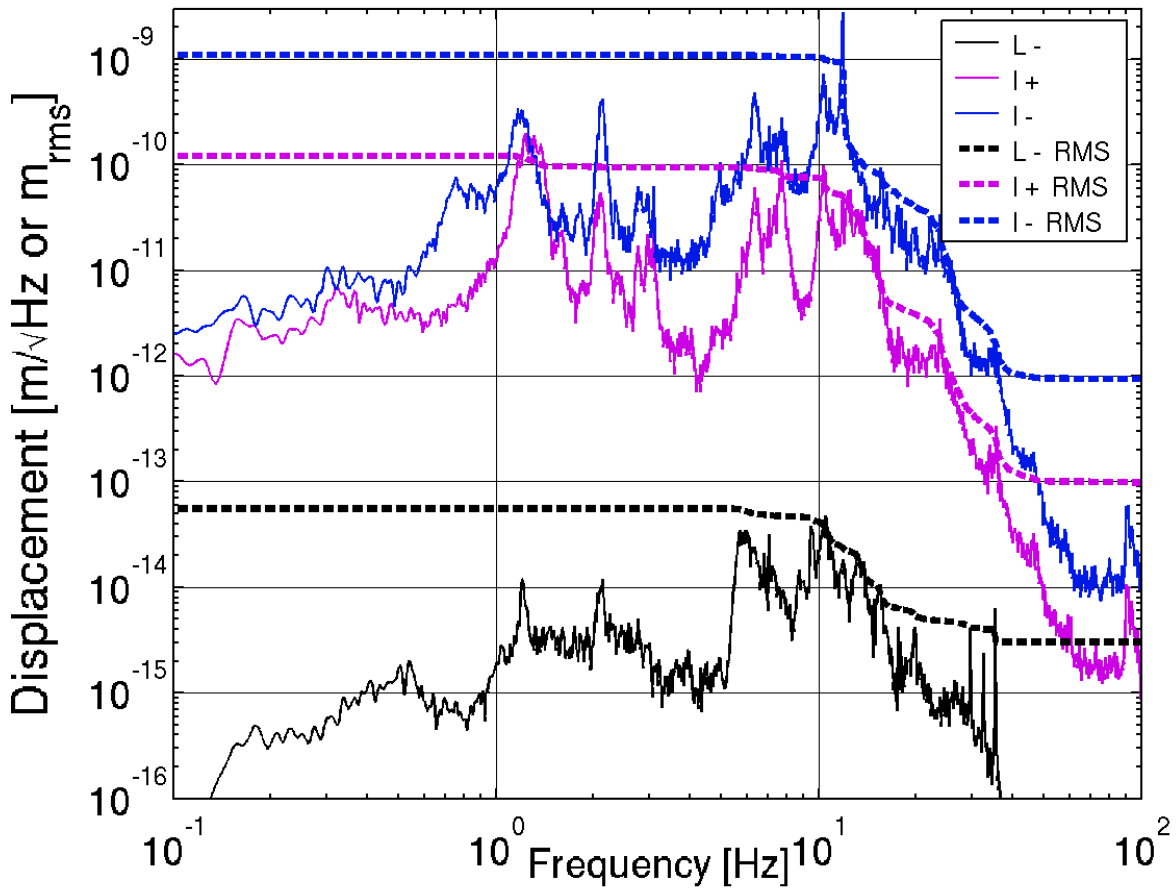


Figure 5-4: Spectra of the servo error points calibrated in meters. These are the true length offsets, assuming no significant offsets are added in at the error point.

and phase margin to remain stable in the face of fluctuating optical gain.

L₋ (a.k.a. DARM)

The DARM loop controls the differential arm length. The gravitational wave signal is reconstructed from the error point signal (AS_Q) of this loop.

This is the highest bandwidth digital servo loop in the interferometer. It is limited at high frequencies by the phase shifts associated with the anti-aliasing filters before the ADC and after the DAC (see Figure 6-1).

There is also the issue of the high Q ($\sim 10^5$) mechanical resonance of the suspension wire at the (≈ 345 Hz) 'violin' frequency; there is a poorly understood interaction

with this resonance which sometimes requires attenuation through the use of very narrow digital notch filters. The coupling seems to come and go; the interferometers often run for months without notches and without any instability.

At even higher frequencies (e.g. 6.6 kHz, 9.3 kHz, and 13 kHz), the servo must have a low enough gain to not excite the even higher Q ($10^5 - 10^7$) internal mode resonances of the mirrors themselves. These typically have stopbands of 80-100 dB, widths of a few Hz (to accommodate the temperature dependent frequency drift of the modes), and are very near the Nyquist frequency (8192 Hz) of the digital system. The modes with frequencies greater than 8192 Hz are excited through a double aliasing effect. They are finitely attenuated by the ADC's anti-aliasing filter, but then still show up in band at $f_{aliased} \simeq f_{Nyquist} - (f_{mode} - f_{Nyquist})$. If not filtered out, this then propagates out through the DAC and is again aliased up to high frequencies. This completes a loop involving the internal mode which can then get excited and cause saturation in the sensing electronics. Once a stopband filter has been tuned for every mode on every driven optic, the modes are no longer a problem.

l_- (a.k.a. MICH)

The MICH loop has a low (~ 10 Hz) unity gain frequency. There are two reasons for this:

The gain at high frequencies must be kept low to reduce the the coupling from l_- sensing noise to L_- strain noise. The unity gain frequency is constrained by the phase lag due to the ~ 50 Hz bandstop filter.

The other constraint is that this loop has a peculiar intermittent coupling to the *roll* mode of the recycling mirror. This mode is at ≈ 18 Hz and will occasionally get excited and grow exponentially if the MICH unity gain frequency is set to within a few Hz of 18 Hz. It is not understood why this coupling is unstable.

l_+ (a.k.a. PRC)

The PRC loop could be run with as high a bandwidth as the DARM loop and has the same considerations with respect to higher frequency mechanical resonances. The

main constraint on the bandwidth is the noise coupling. So the gain has been lowered to add aggressive filtering in the 60-200 Hz band. In the long term the sensing noise in both the l_+ and l_- loops will have to be reduced and the coupling to the anti-symmetric port reduced through the use of off diagonal length actuation: driving the L_- length by the just the amount necessary to cancel the measured coupling factor. This technique was implemented successfully on the Livingston interferometer for the l_- servo during the latest Science Run (S3).

5.1.4 The Common Mode Servo

Gravitational radiation can produce both differential and common mode strains of the arm cavities. We choose to only use the differential mode read out for gravitational waves because the common mode signal is polluted with a large level of laser frequency noise.

There is a choice to be made in what to pick as the reference in all of these length measurements. For the common arm length this amounts to whether the laser wavelength should be locked to the arms or the arms locked to the laser. Since we have made such effort to isolate the test masses from external disturbances the average arm length proves to be a much better reference at audio frequencies (above 20 Hz).

From Chapter 4, we have the coupling of frequency noise into the strain output. Figure 5-5 shows that the laser frequency noise must be suppressed by a factor of 10^8 to bring it to 1/10th of the strain sensitivity goal. There is more to the problem than just gain, however. As the laser is further quieted, each following reference to which the frequency is servoed must be more quiet than the last.

To achieve the required suppression, multiple, hierarchical servos are used. Before the light is injected into the vacuum, the large, raw laser fluctuations are actively and passively suppressed (see Section G.4). Laser noise above 1 MHz is filtered out by passing through a medium finesse ring cavity called the pre-mode cleaner. By locking the laser frequency to a short ($\approx 20\text{cm}$), rigid reference cavity with a ~ 100 kHz servo loop the laser frequency noise is stabilized by a factor of ~ 1000 .

This pre-stabilized light is then locked to a much quieter, suspended, 12 m cavity

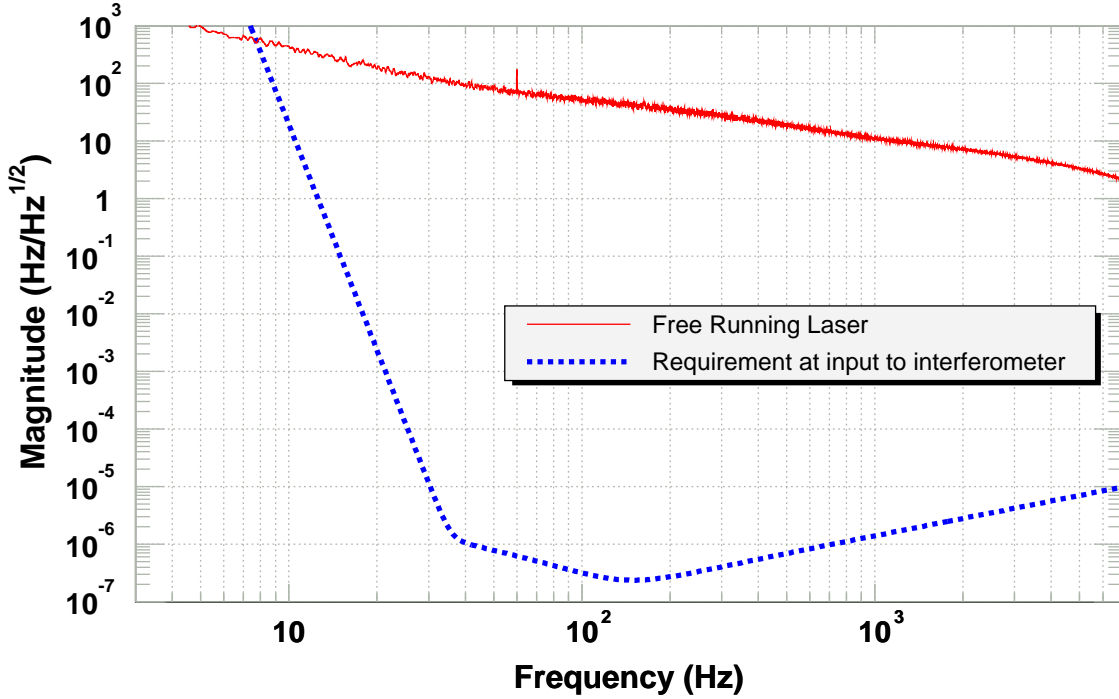


Figure 5-5: The spectral density of the free running frequency noise of the MOPA is compared to the SRD/10 requirement based upon an arm cavity reflectivity difference of 0.5%.

called the Mode Cleaner, described in Appendix C. Finally, the light transmitted through the Mode Cleaner is locked to the average length of the 4 km arm cavities.

Ignoring for the moment the internal workings of the mode cleaner and the laser we can focus on the mechanics of the common mode servo. The difficulty is that although the laser wavelength is already tightly locked to the mode cleaner length, it is necessary to adjust the wavelength to match the common mode arm length and yet keep the light resonating in all the cavities simultaneously.

To see how this is done, it is useful to look at what the MC servo really does. It derives an error signal which is nominally proportional to the difference between the round trip length of the cavity and the wavelength of the light incident on the cavity, modulo an integer number of wavelengths. The common mode servo works by adjusting the reference to which the laser wavelength is compared.

At low frequencies, the common mode servo drives the mode cleaner length. This adjusts the laser frequency since the laser frequency is already locked to the MC

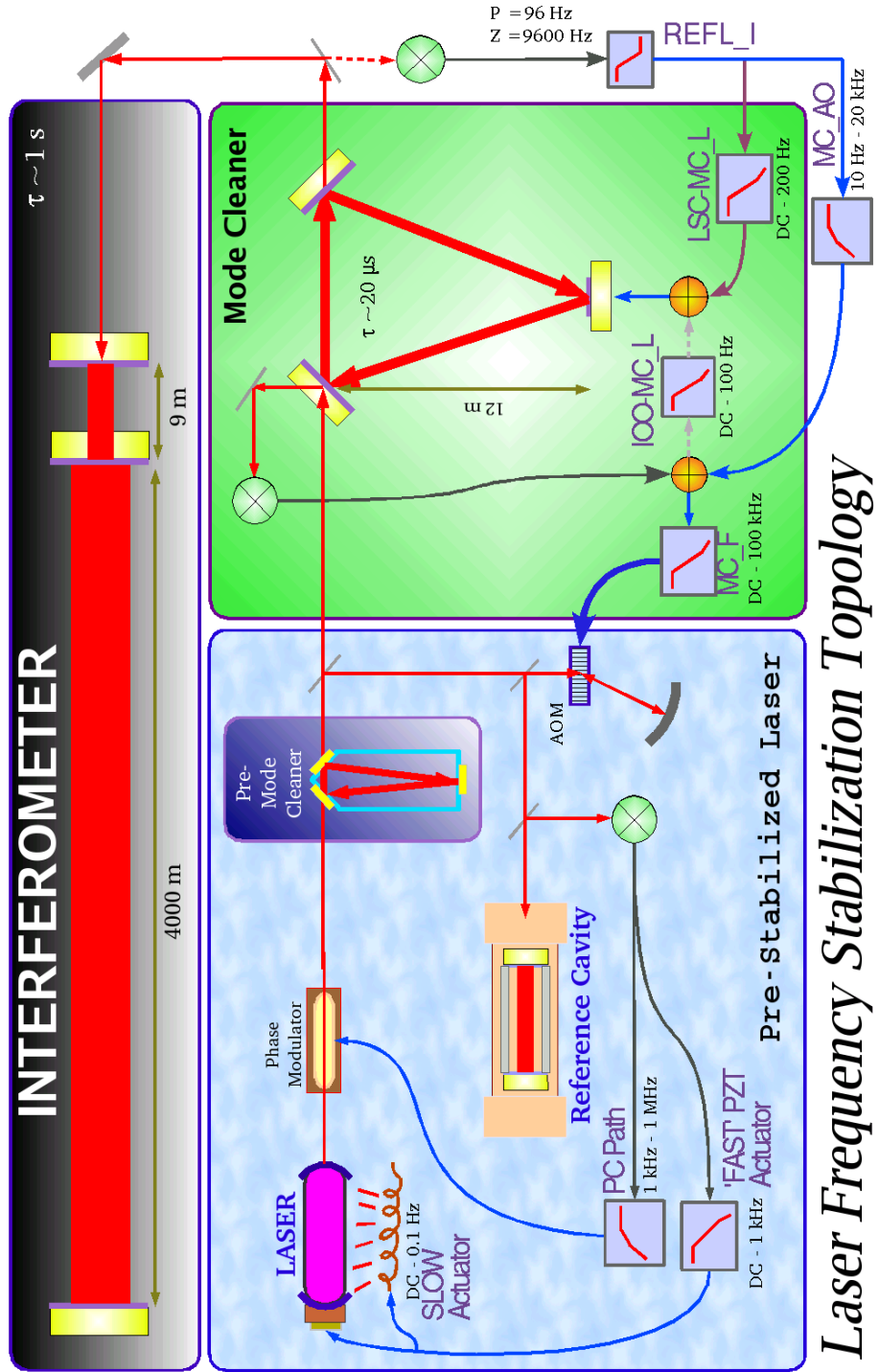


Figure 5-6: Block diagram of the Global Frequency Stabilization Topology.

length. Above a few hundred Hz, the length feedback is limited by the wire resonances of the MC suspension.

A fast, low dynamic-range path, called the additive offset (AO), is used up to 20

kHz. The AO path works by adding electronic offsets into the MC error point. The MC servo shifts the laser frequency in order to cancel this offset, but the resulting laser frequency offset serves the purpose of the AO. This might pose a problem, since by introducing an offset in the MC error point, the laser is being pulled off of resonance in the MC. However, the actual AO control signal is quite small; only a few Hz peak-peak, as compared to the \sim 8 kHz linewidth of the MC resonance.

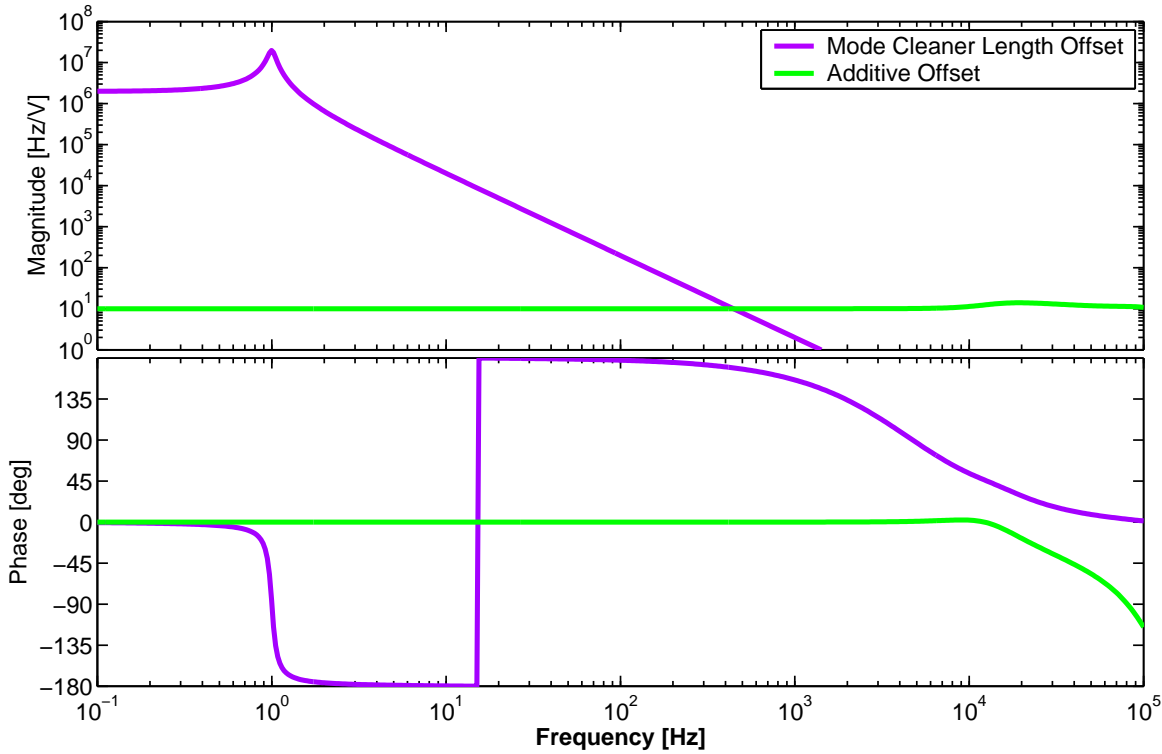


Figure 5-7: Shown are the frequency responses of the two actuators used in the common mode servo. The response is to voltage applied at the coil driver (MCL) and the MC servo mixer (AO).

Figure 5-7 shows the frequency response of the two CM servo paths. At high frequencies, very large voltages would be required to get sufficient actuation authority in the MC length path and so the two paths are crossed over as shown in Figure 5-8. The AO bandwidth is limited at high frequencies by the finite bandwidth of the MC servo.

Figure 5-9 shows the control signals of the CM servo. In the regime where the loop gain is high the control signal can be used to estimate the input disturbance -

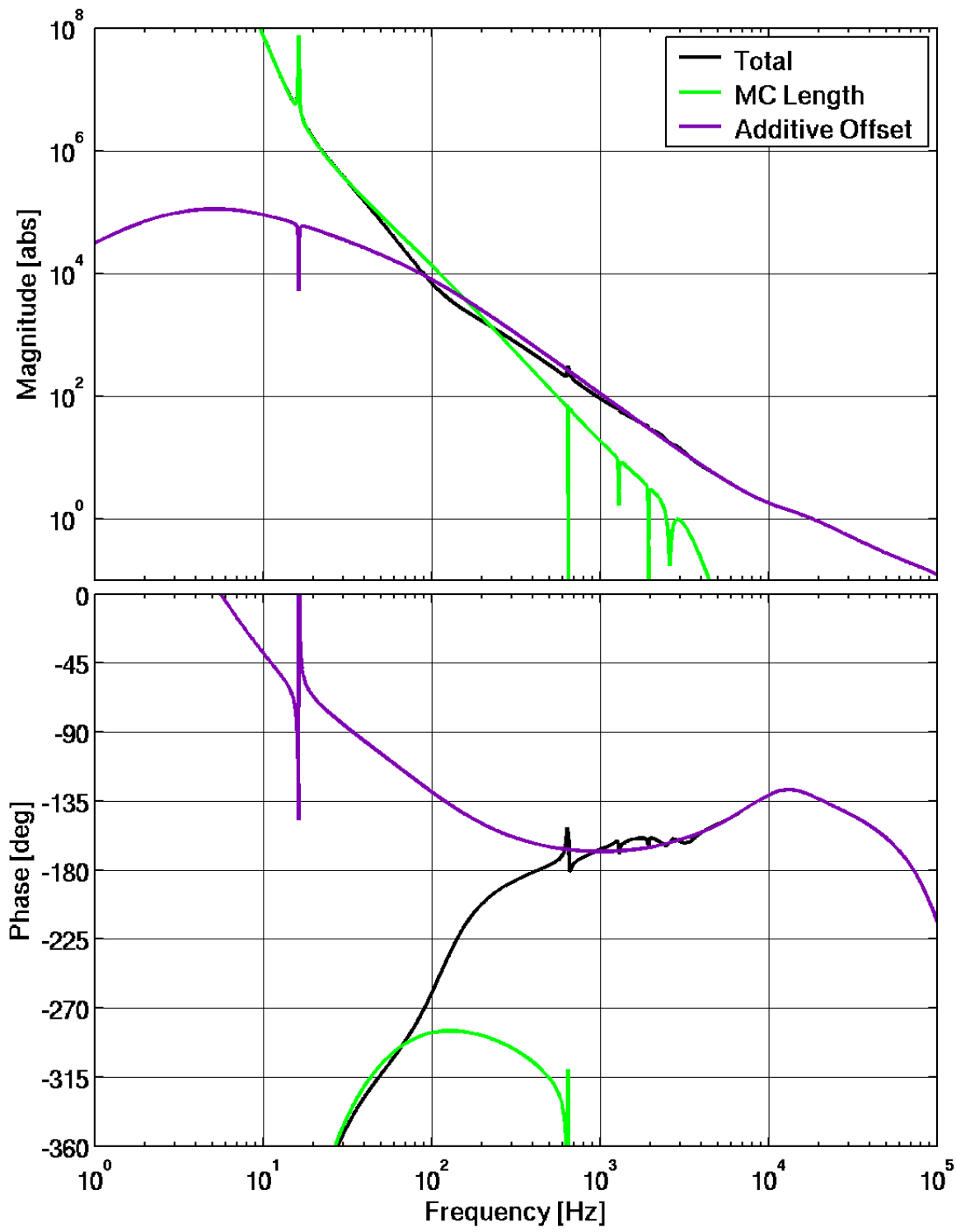


Figure 5-8: Open Loop Gain of the total Common Mode Servo and of the individual MCL and AO paths.

the frequency noise on the light transmitted by the MC.

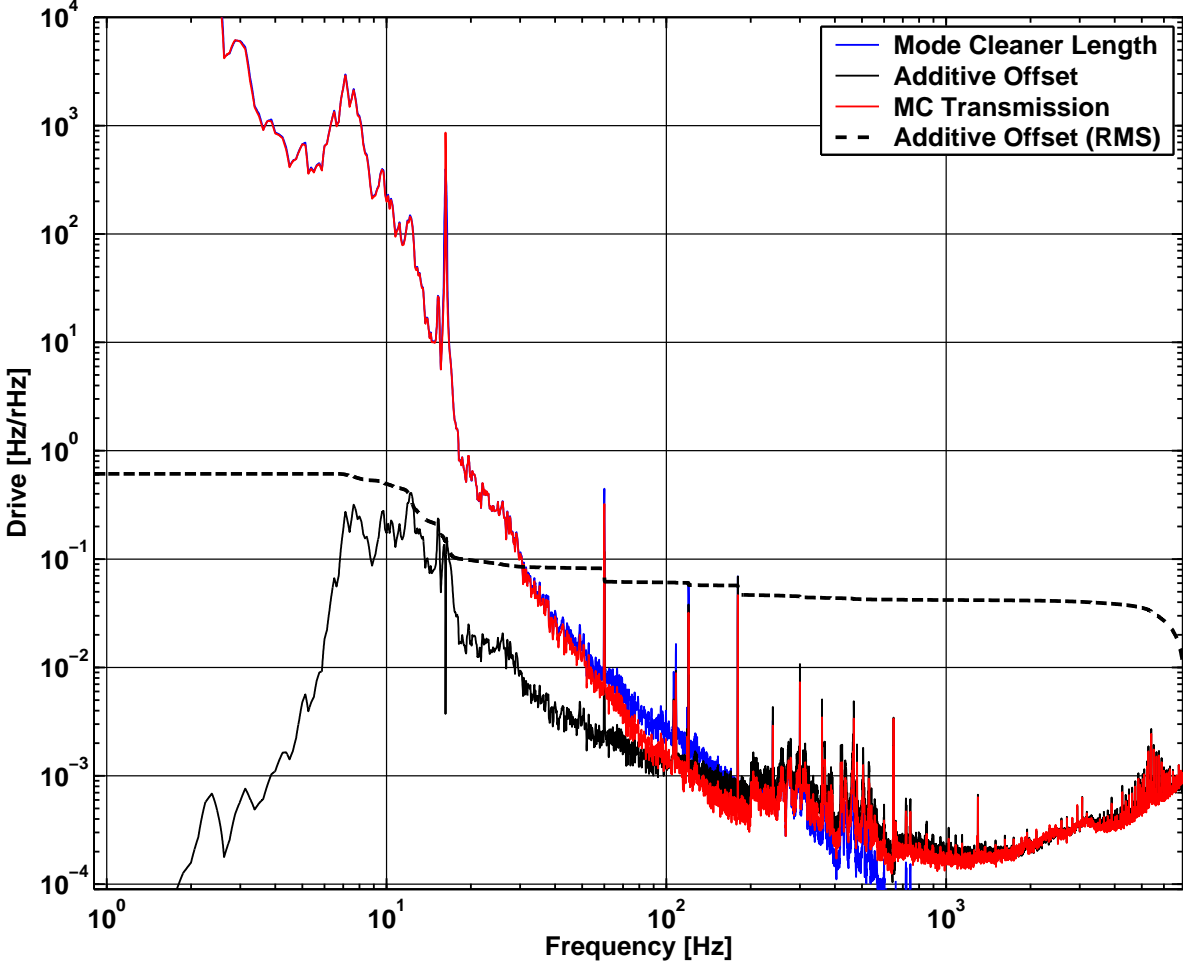


Figure 5-9: The MCL and AO control signals are shown. Also shown is the total frequency noise transmitted by the MC, calculated from the CM control signals. Also shows is the integrated RMS of the AO control.

Finally, the ultimate performance of the entire frequency stabilization scheme can be summed up by Figure 5-10. The plotted requirement is the level of frequency noise which will equal 1/10 of the strain sensitivity goal.

This curve is calculated using the frequency domain interferometer model which uses as inputs the measured frequency noise to differential strain coupling. This curve along with the measured CM servo loop gain establishes a requirement on the frequency fluctuations on the light leaving the mode cleaner. This requirement is compared to the measured performance of the mode cleaner in Appendix C.

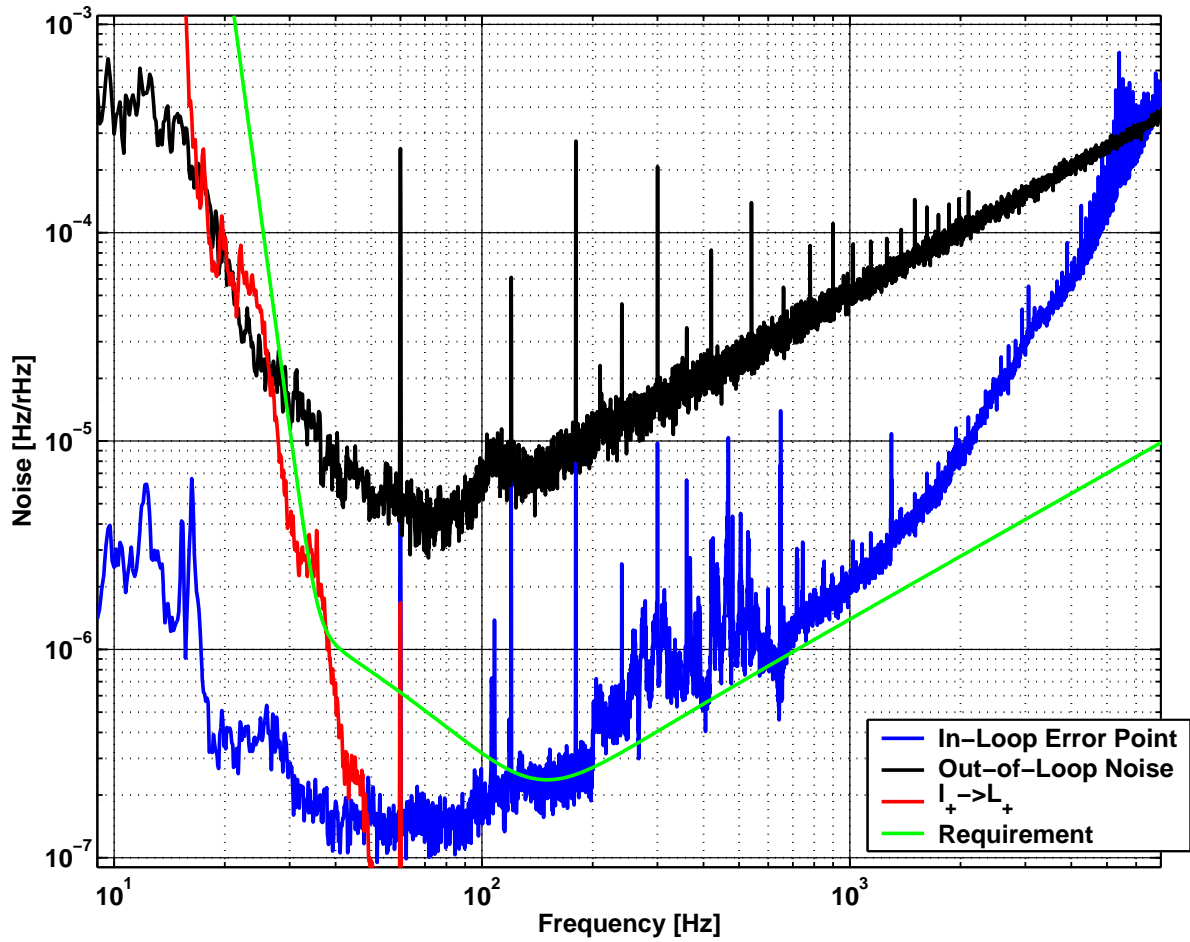


Figure 5-10: The in-loop error point is compared to the sensing noise floor to show that the in-loop error point underestimates the true noise. The plotted requirement is SRD/10.

Parasitic Interferometers

On the laser table, vibrations of the optical mounts put phase noise on the light which then is measured in the mode cleaner control signal. This frequency noise has been reduced somewhat through the use of stiffer mounts and acoustic isolation of the table. The mode cleaner servo gain is sufficient to make acoustics from the laser table an insignificant contributor to the interferometer noise.

Acoustic coupling on the mode cleaner's output optical table dominates the frequency noise on the light incident on the interferometer in the 100-1000 Hz band. This still needs to be reduced by ~ 10 .

The acoustic noise on the mode cleaner table is injected at the error point of the servo as sensing noise. It is only characterized because we then measure the mode cleaner noise performance with an even quieter reference in the common mode servo. For the common mode servo, there is no further check and so the acoustic noise coupling there is sent unsuppressed into the interferometer and is probably more severe.

The steep rise below 100 Hz in the 'out-of-loop' trace of Figure 5-10 is due to a parasitic scattering path somewhere in the path between the recycling mirror and the readout PD for the interferometer's reflected port.

5.2 Angular Controls

The Angular Sensing and Control system is still being commissioned and refined. This section briefly mentions the different angular sensing schemes which are used.

There are three chief feedback paths for the angular degrees of freedom of the interferometer:

- The first, primitive stabilization is done by damping the pitch and yaw eigenmodes of the suspended optics using the local sensors 5.3. These provide some stability at the pendulum frequencies, but is limited by the large motions of the isolation stack to which the suspension cage is mounted. The high frequency angular sensing noise of the local sensors is $\approx 10^{-10}$ radians/ $\sqrt{\text{Hz}}$. This requires a very low bandwidth servo (≈ 2 Hz) with aggressive low pass filtering.
- The second level of angular stabilization comes from optical levers. Each optical lever is a fiber coupled diode laser and a quadrant photodetector, each mounted to a steel pier outside of the vacuum. From $\approx 0.3\text{-}5$ Hz, these are better angular references than the local sensors. Their chief benefit is in simplicity: these servos work independent of the locked state of the interferometer. The noise in this sensor is somewhat better than the local sensors, $\approx 10^{-11}$ radians/ $\sqrt{\text{Hz}}$, in a broadband sense but is dominated by acoustic/mechanical resonances which

are 10-50X larger.

- The ultimate solution to angular sensing is the Wavefront Sensor (WFS) system [92, 96, 97]. These are RF quadrant detectors working on a heterodyne readout system similar to that used in the length sensing. The WFSs sense relative tilts and translations between the carrier and RF sideband fields by taking differences between the demodulated outputs of the quadrants. The shot noise limited sensing noise of these sensors is, in principle, far superior to the other sensors. The broadband noise floor varies from $10^{-13} - 10^{-14}$ radians/ $\sqrt{\text{Hz}}$, depending on which sensor.
- A non-RF part of the WFS scheme is the DC quadrant photodetectors monitoring the weak beams transmitted through the arm cavity end mirrors. These fix the beam position onto the center of the end mirrors. The angular sensitivity of these sensors is comparable to the WFS, but they have the disadvantage of being fixed to the local reference frame of the ground at the end stations.

Figure 5-11 shows a rough outline of the sensing and feedback topology. Each of the suspended large optics has an optical lever servo. The feedback diagram is a simplified version of the real feedback topology which uses multiple mirrors in the feedback for each WFS. The arrows in this diagram are only to indicate the principle degree of freedom of the feedback.

During the S2 run, the Livingston interferometer had only WFS1 running, with feedback set to drive the differential ETM angle. This is the most critical angle in the interferometer; without control of this degree of freedom, the power at the Anti-Symmetric port varies wildly, making many servos unstable. The Hanford 4 km interferometer had nearly all of the WFS loops closed with a low bandwidth and for the S3 run managed to close all WFS loops.

Angular Sensing & Controls

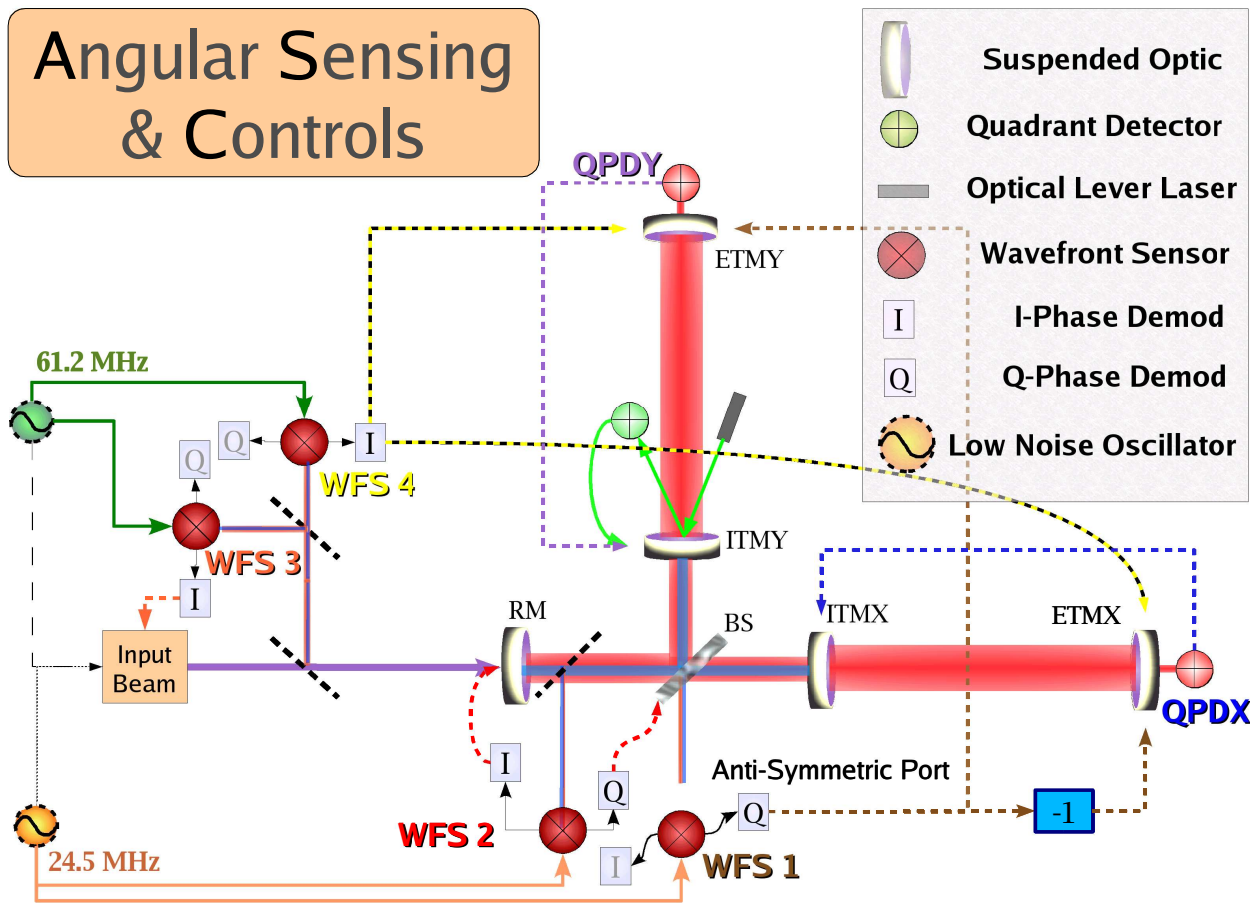


Figure 5-11: Block diagram of the Angular Sensing and Control system. Only one optical lever setup is shown for simplicity, although there is one per optic.

5.3 Local Damping

The wire suspension (see Section G.2) for the interferometer's central mirrors is soft in 4 of 6 DOFs: The two vertical modes have resonant frequencies from 10-20 Hz whereas, the horizontal eigenfrequencies are all from 0.5-1 Hz. To reduce the off-resonance thermal noise in the suspension wires, the mechanical losses have been kept as low as possible. The result is that the mechanical Q's are quite high; the intrinsic Q's of the suspended optic's free body modes are estimated to be $\sim 10^5$. Since the suspension structure is actually perched on a lightly damped isolation stack, the Q's of the full coupled resonant system are limited to $\sim 10^3$.

This is still very large and so to prevent uncontrolled swinging of the optic, it is locally damped by sensing its motion with respect to the suspension frame and

feeding back with a force proportional to the velocity.

The sensors and actuators used for local control of the suspended optic are described in Section G.2.1. The overview screen for the digital/analog controls of one of the suspended test masses is shown in Figure 5-13 (this is also a good block diagram for how the suspended optic is controlled).

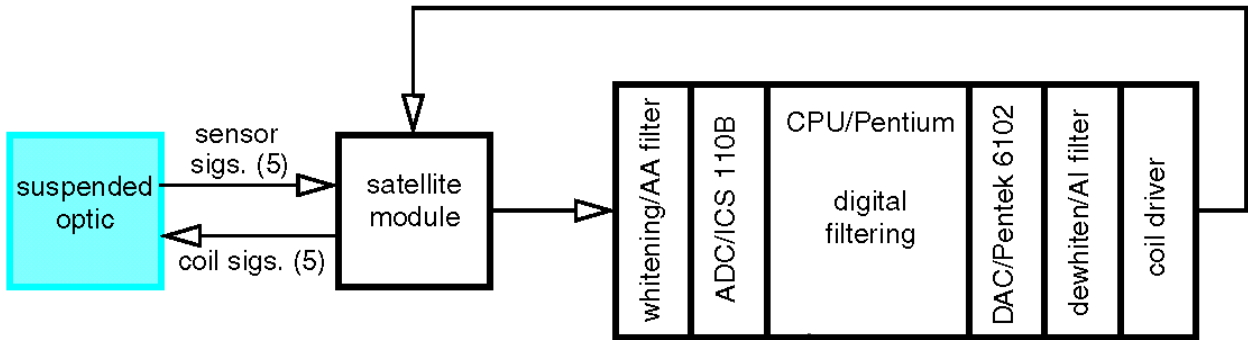


Figure 5-12: Block diagram for the local damping electronics.

The signals from the 4 shadow sensors on the mirror face are conditioned, acquired by an ADC, and then recombined in appropriate combinations to reproduce signals corresponding to 3 of the free body modes of the optic. Translation perpendicular to the optic face, pitch, and yaw are sensed and then controlled. Vertical motion and rotation around the axis perpendicular to the optic's face are not sensed or controlled. The sideways translation of the optic is damped through the use of only one sensor/actuator pair.

The sensing noise of the shadow sensor is $\approx 1 \times 10^{-10} \text{ m}/\sqrt{\text{Hz}}$ above 20 Hz, limited mostly by shot noise in the detected light power. Since this is 8 orders of magnitude above the displacement noise goal at 40 Hz, the filtering must be aggressive enough to allow a gain of more than 1 for stable damping around 1 Hz and also introduce less than $5 \times 10^{-19} \text{ m}/\sqrt{\text{Hz}}$ of displacement noise at 40 Hz. Figure 5-14 shows the open loop gain of the damping loop for the piston degree of freedom.

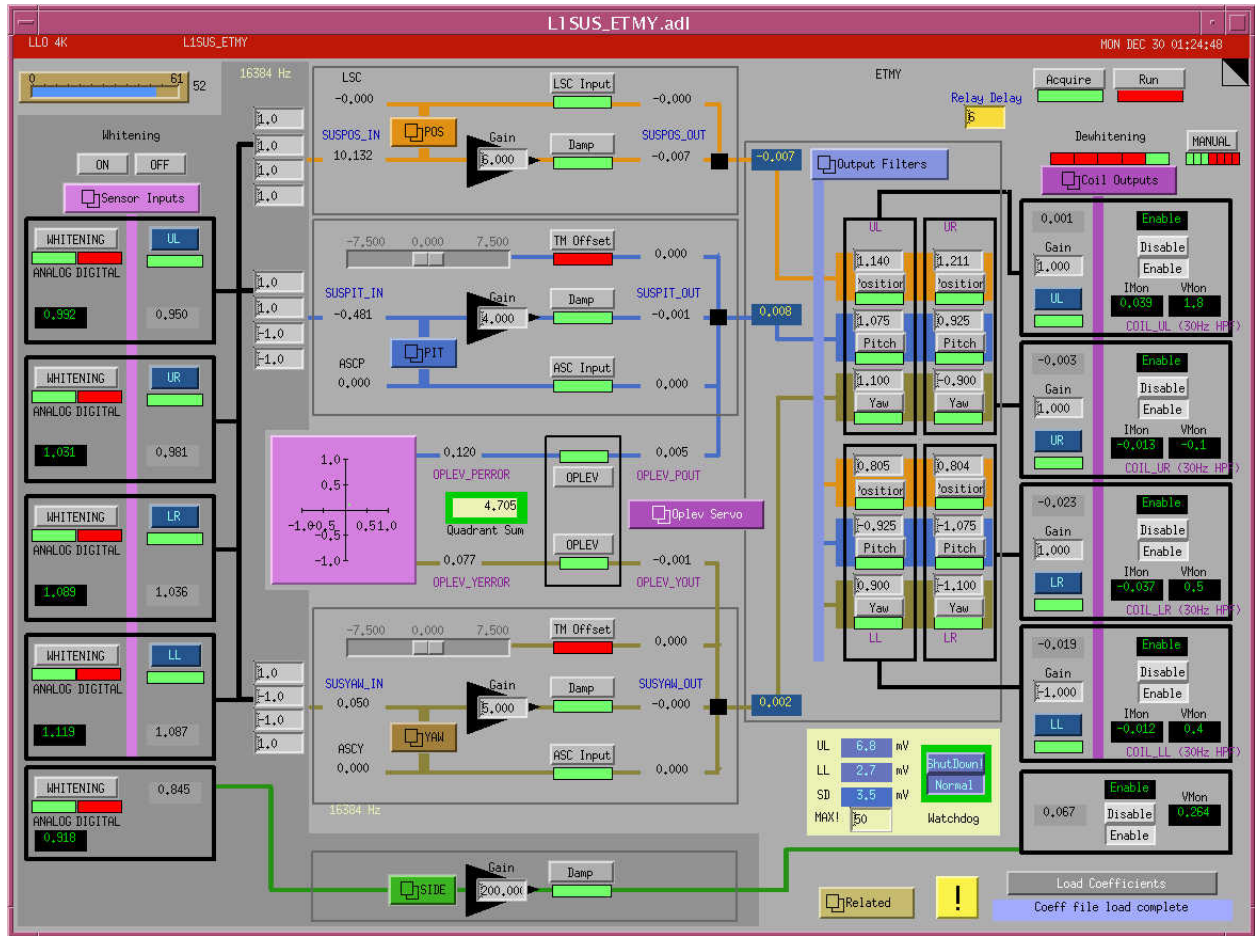


Figure 5-13: Overview screen for the ETMY digital suspension controls.

5.4 Seismic Servos

Seismic noise in the gravitational wave band affects the strain sensitivity directly by moving the test masses. The largely unattenuated seismic disturbance below 20 Hz, however, is several orders of magnitude larger than the in-band noise. These low frequency motions impact the strain sensitivity non-linearly:

- To keep the optical cavities resonant in the presence of large disturbances, the actuators must have a proportionally large dynamic range. Reducing the dynamic range with a fixed attenuator would proportionally reduce the noise contribution.
- Due to the finite gain in the control servos the cavity lengths are pulled off of

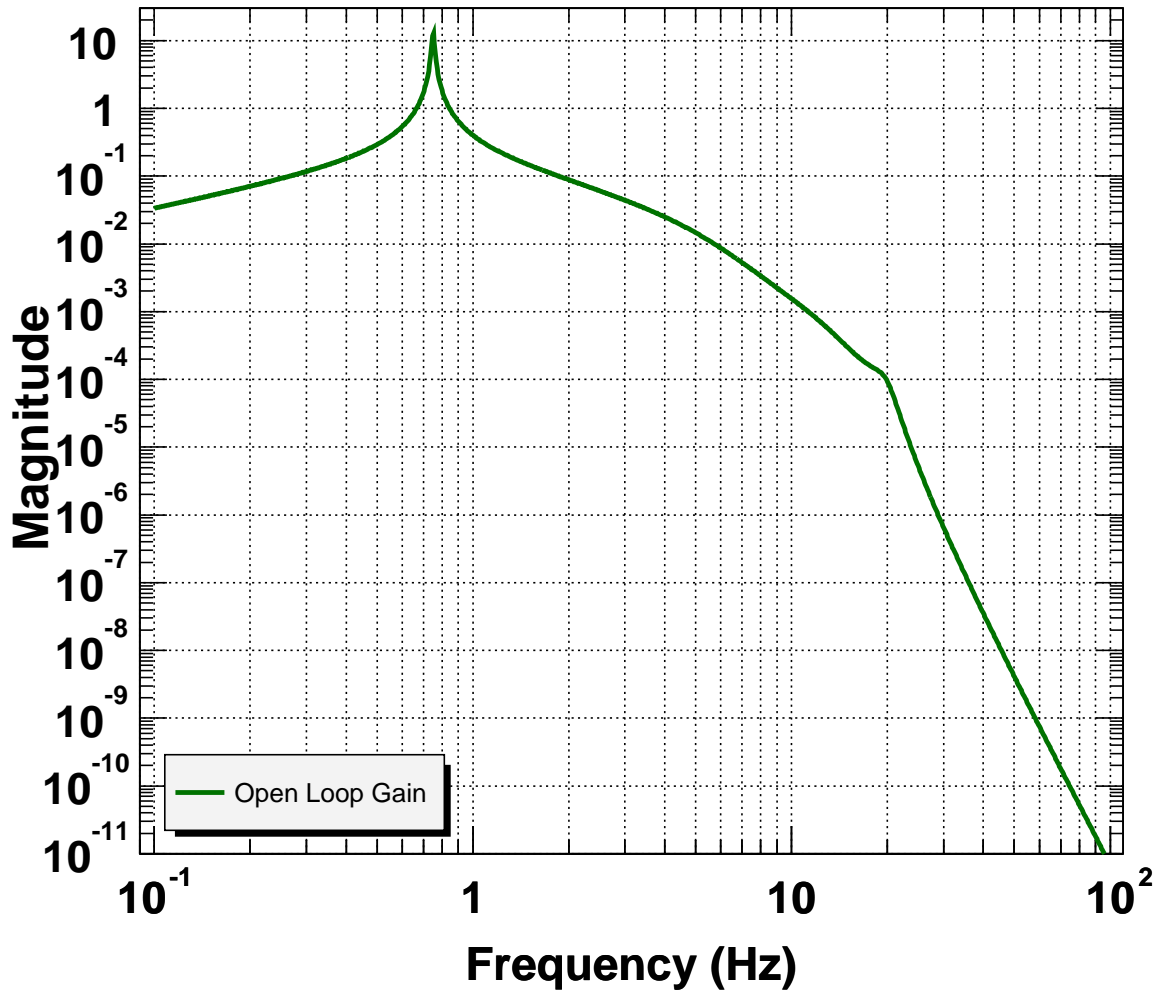


Figure 5-14: Magnitude of the open loop gain for the suspended optic's piston degree of freedom.

resonance, leading to bilinear up-conversion (see Section 5.1.1 and Figures 4-9 and 4-13 for examples).

- There is a finite amount of light scattered at each optical surface. Some of this light is re-introduced into the signal readout path, producing a parasitic optical resonator around the main interferometer. In the regime where multiple wavelengths are traveled the scattered light noise can show up in the signal band.
- Worst of all, often the ground noise is so large as to prevent any operation of the interferometer. At some point the velocities become so large that the lock

acquisition system can no longer bring the optical cavities into resonance.

Earth Tides

The tidal gravitational forces from the moon and the sun distort the earth with a ≈ 12 hour period. These strains are seasonally modulated, but on average create displacements of ≈ 400 microns peak-peak over a 4 km baseline. This displacement exceeds the dynamic range of the test mass coil drivers (≈ 10 microns).

To remove this large signal, the near DC component of the drive signals to the end test masses' coil drivers are fed to higher dynamic range (180 microns peak-peak) actuators made of piezo-electric stacks. This system was designed to finely actuate the seismic isolation stack at low frequencies. It is called the Fine Actuation System (FAS).

The strains from the earth tide can be divided into common and differential components. The common mode component can be accommodated by adjusting the laser wavelength as is done for the common mode servo. To accommodate a change, ΔL_+ , in the common mode arm length the laser frequency must shift by $\Delta\nu = \Delta L_+ \frac{c/\lambda}{L_{arm}}$. This is $\simeq 7$ MHz for a 100 micron length change. The slow, temperature actuator of the laser's master oscillator can easily give several hundred MHz of frequency shift.

Using an earth tide prediction program [98], a large portion of the tidal strain was offloaded from the FAS in this manner on the Hanford interferometers. Figure 5-15 shows a comparison of the measured tidal strains with the predictions for the Livingston interferometer during the S2 science run from February - April 2003. From the small size of the residuals it looks like implementing the feed forward to the laser wavelength would significantly reduce the size of the feedback signals sent to the external seismic actuators and should be done in the future.

5.4.1 Microseismic Feed-Forward

All over the earth, the largest ground motions (excepting earthquakes) are from the ~ 6 second period microseism discussed in Section 4.1.1.

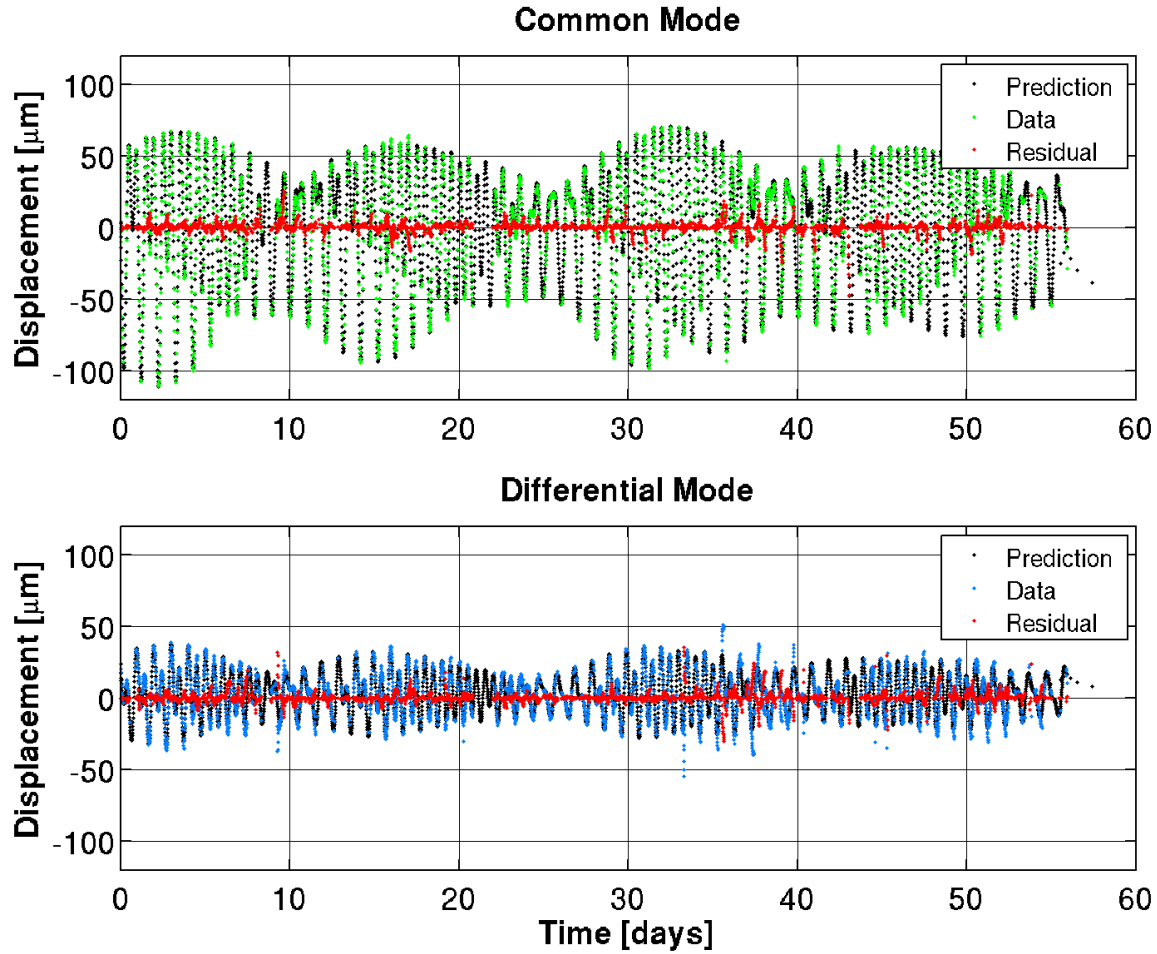


Figure 5-15: The common and differential mode earth tide displacements are shown. Also plotted are the calibrated piezo control signals (the real displacements) and residual (data-prediction).

To reduce the arm length fluctuations from 0.1-0.5 Hz, a feed forward scheme was implemented to measure the ground noise and apply this through suitable filtering to the FAS [99]. An excellent, low frequency seismometer (Streckheisen STS-2) was placed in each building to measure the local microseismic motion. By measuring the displacement in each building separately we were able to predict the microseismic arm length change and send this signal into the second input of the FAS on the end test mass chambers to reduce the relative motions between the mirrors at the two ends of the arms.

Figure 5-16 shows an example of the effect of the feed forward on the length fluctuations of a single arm cavity.

5.4.2 Piezo-electric Pre-Isolator

Out of necessity, the Livingston site was patched with 2 types of active isolation to lower the influence of the ground motion.

As seen in Figure 4-2 the low frequency, high Q resonances of the stack actually amplify the ground noise at some frequencies. This effect, coupled with the large levels of anthropogenic noise, produce the large velocities which impede interferometer operation. To reduce this effect, we installed a local, Piezo-Electric Pre-Isolation (PEPI) system [100].

PEPI works by sensing the horizontal velocities on the support structure of the isolation stack and then using a stand alone computer with DSP to feedback and reduce the seismic noise in the \sim 0.5-3 Hz band. The true power of PEPI comes from the digital nature of the feedback compensation. The servo loop shape was tailored to exactly suppress the noise at the frequencies where the isolation stack resonances would otherwise amplify. The PEPI feedback goes into the third input of the FAS.

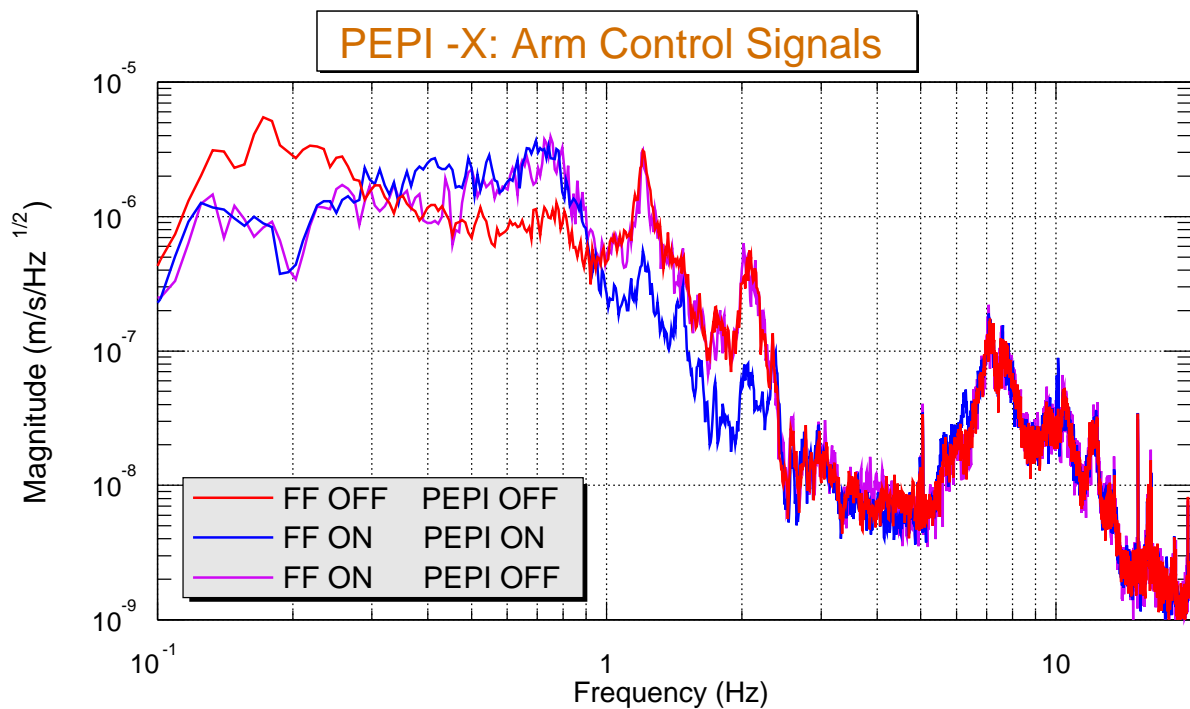
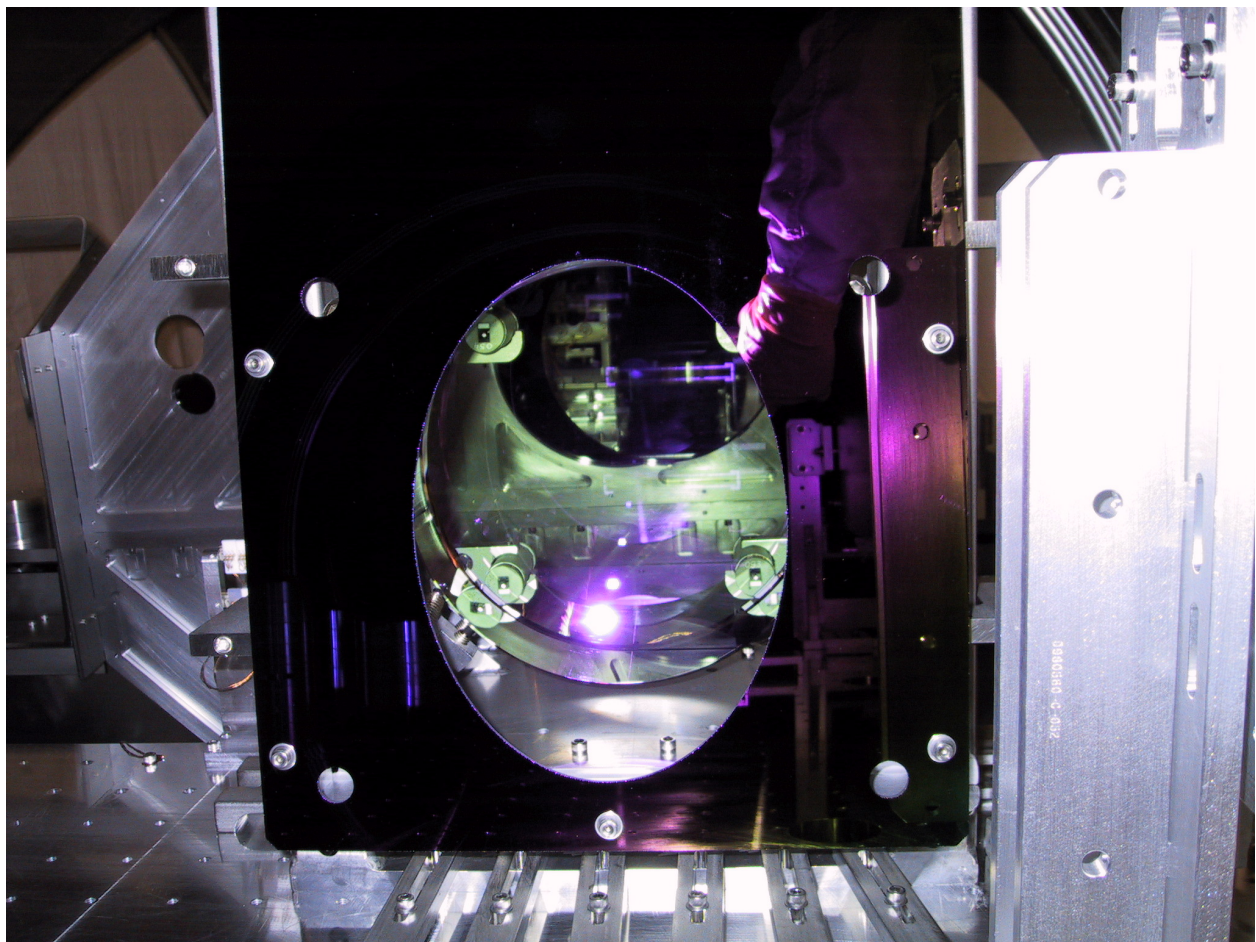


Figure 5-16: Shows the differential arm length control signal in units of velocity. The PEPI ON and PEPI OFF traces show the reduction in the arm length velocities with the PEPI servos on.

Chapter 6

Calibration



This chapter describes how the interferometer’s primary data channel is calibrated to produce a measure of the gravitational wave strain incident on the detector [101, 102].

The interferometer output is a photocurrent which is proportional to the light power modulation at the resonant sideband frequency (≈ 25 MHz). We then turn this into an integer time series after a series of analog signal conditioning electronics. These inputs from multiple photodetectors and their electronics are then further filtered digitally and then finally summed together to produce the floating point time series used in the analyses. The name of the channel (L1:LSC-AS_Q, H1:LSC-AS_Q, or H2:LSC-AS_Q) contains the following information: the interferometer designation (L1, H1, or H2), the sub-system designation (Length Sensing and Control), and the readout port and demodulation phase (AS port, Quadrature phase).

This channel has the differential arm strain encoded in it. To properly decode this signal, we need to accurately determine the interferometer’s *response function*, defined as the function relating the data to the strain.

There are 3 major steps in calibrating the data:

- Make a model of the interferometer response (counts/meter).
- Calibrate the mirror actuator drive (meters/count).
- Track the calibration with a calibration line(s).

6.1 Interferometer Response Model

The model of the interferometer’s L_- length control loop also serves to calculate the response of the DAQ channel (AS_Q) to strains. Figure 6-1 shows a block diagram of the model and where in the chain the data is extracted.

During standard interferometer operation, the ‘Interferometer Optical Dynamics’ block, which represents the transfer function between strain and the optical signal at the anti-symmetric port, is slowly varying (mainly due to interferometer alignment variations).

During the S2 run, this fluctuation in the gain was uncompensated in the interferometer control servos and led to instabilities and noise. In addition, these fluctuations cause changes in the overall response function. Section 6.3 describes how this is tracked.

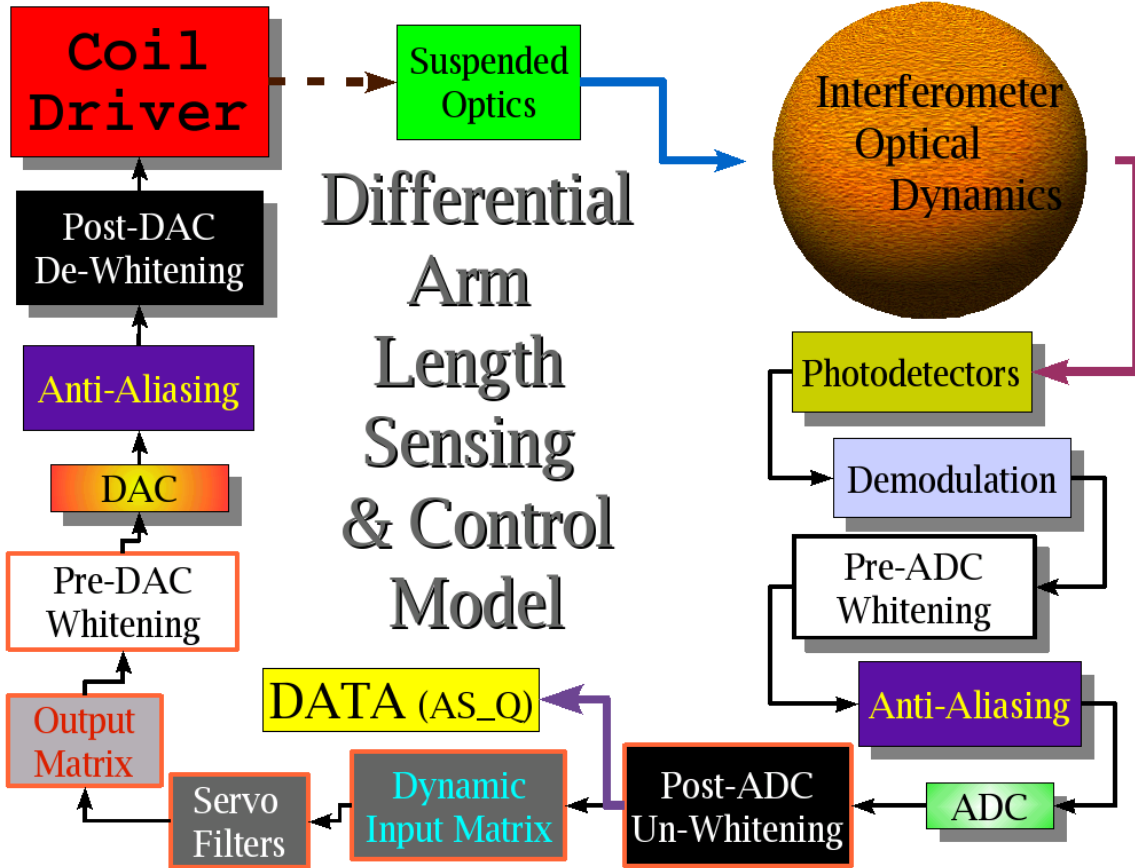


Figure 6-1: Block diagram of the model used to calculate the interferometer's response function. All analog circuit blocks have shadows. All digital blocks have orange borders.

The model outputs are all complex valued frequency domain transfer functions which are supplied to all of the data analysis groups. The most commonly used product is the response function, $R(f)$:

$$R(f) \equiv \frac{AS_Q(f)}{Strain(f)} \quad (6.1)$$

6.2 Actuator Calibration

To verify the response function given by the model, swept sine measurements are made between the actuator and the readout in AS_Q. To calibrate the actuator we use the laser wavelength as the ultimate reference.

6.2.1 Absolute Calibration

A Michelson interferometer is a good displacement sensor. By misaligning the end mirrors and the recycling mirror we get a Michelson interferometer made up of the two arm cavity input mirrors (ITMX & ITMY) and the beamsplitter (BS) as shown in Figure 2-1.

We lock the Michelson using the standard RF heterodyne readout of AS_Q, but limit the feedback bandwidth by putting an aggressive digital low-pass filter in the servo loop. Then the AS_Q signal is, in principle, directly proportional to the differential length, l_- .

Since the actuator response is that of a damped pendulum with a $\simeq 0.75$ Hz resonant frequency, it is well approximated as a free mass in the band of interest (40-7000 Hz).

To get the absolute calibration, we have to calibrate AS_Q in this configuration. To do this, we allow the mirrors to free swing over several fringes. The peak-peak signal in AS_Q corresponds to a differential phase shift, ϕ_- , of π , or correspondingly a change in the position of a single arm mirror of $\lambda/4$, where $\lambda = 1064$ nm, is the laser wavelength. So the AS_Q calibration in ADC counts / meter is given by:

$$\text{AS_Q cal} = \text{AS_Q}_{pp} \frac{4\pi}{\lambda} \frac{\text{ADC counts}}{\text{meter}} \quad (6.2)$$

where this is meters of motion of a single mirror.

Systematic errors are continuously being eliminated and statistical errors reduced through more patient measurement. The estimates on the S2 errors are +/- 10% in magnitude and phase [102].

6.2.2 Frequency Response

To get the displacement response of the mirror to an actuation signal we measure the transfer function of each piece of the mirror actuation chain shown in Figure 4-7. The digital compensation filters ("pre-DAC Whitening" and "post-ADC un-whitening" in Figure 6-1) are constructed to be exactly the inverse of their analog counterparts. This reduces the amount of frequency dependent calibration error. The overall check is to again measure the swept sine response of AS_Q to the drive of a single mirror and ensure that it faithfully follows the f^{-2} power law of a free mass.

6.3 Calibration tracking

The variations in the interferometer optical gain are tracked by injecting a sinusoidal drive into the digital control servo controlling the piston drive to one or both of the arm cavity end mirrors. For the S2 run, three such calibration lines were injected in each interferometer: one at a low frequency (≈ 50 Hz) where the servo loop gain is high, one at a frequency (≈ 150 Hz) where the loop gain is ≈ 1 , and one at a high frequency (≈ 900 Hz) where the loop gain is low.

We use the actuator calibration to determine the amount the mirror is being moved and monitor the amplitude and phase of the line in the data to get a measure of the interferometer response.

6.4 Directions for the future

There has been substantial progress in pinning down the absolute strain calibration of the instruments and of tracking the calibration drift. The following are some projects being pursued to further improve things:

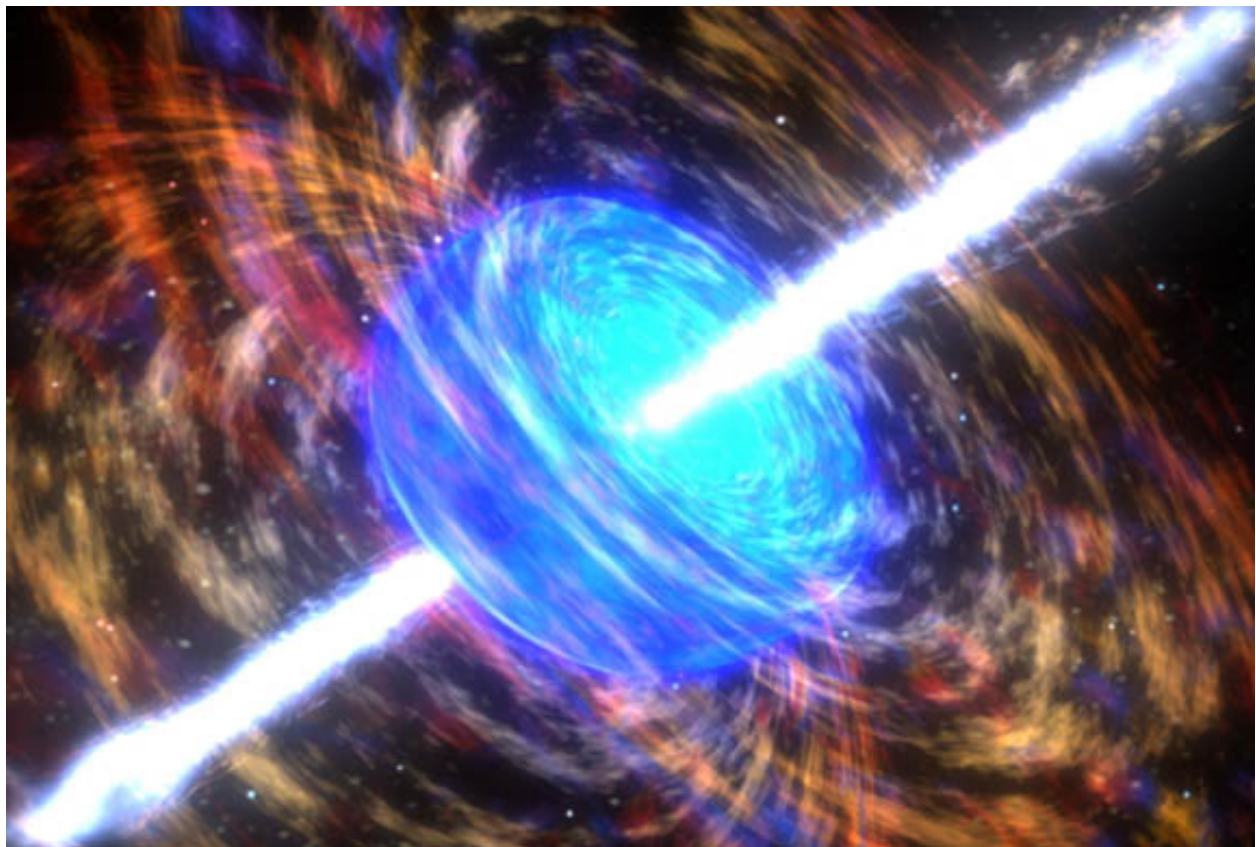
- Optical gain fluctuations are currently tracked by the use of calibration lines and post-processing the data to correct for this. The real-time length control servos cannot afford such luxury, however. Instead, after S2, a dynamic digital

gain correction was added. This system measures a few power levels in the interferometer and adjusts the digital gain in real time to correct the optical gain changes. In the future we should use the post-correction signal as our gravitational wave readout (this is the point just after the "Input Matrix" in Figures 6-1 and 5). This should not only correct slow drifts in the calibration, but actually increase the measured strain sensitivity by removing bilinear upconversion from optical gain modulation at \sim 1 second time scales.

- The absolute calibration of the arm cavity end mirrors are now made by referencing them to the calibrated input mirrors. One can skip the intermediate step by directly referencing the end test mass drive to a laser wavelength shift. The laser frequency stabilization servo has a test input port (the AOM in Figure 5-6) available for this purpose. The VCO can be directly calibrated against a spectrum analyzer or a high precision frequency counter.
- It is possible to directly actuate the arm cavity mirrors through the radiation pressure force of an external laser. At 100 Hz, the displacement from a fully modulated 1 W laser at normal incidence is $\approx 10^{-15}$ meters; quite a bit larger than what is currently used for a calibration line height. This radiation pressure calibration technique is a completely independent method to get the absolute calibration and avoids the complication of knowing the analog filtering chain of the test mass actuators.

Chapter 7

Data Analysis for Black Hole Ringdowns



This chapter describes an analysis done of the data from the second LIGO Science Run (called S2) to look for damped sinusoid signals such as are expected from the ringdown of black hole quasi-normal modes (see Section 1.2.5). The analysis was carried out over all times during which both of the 4 km interferometers were running in their nominal data taking state.

This was an exploratory analysis, whose purpose was to answer the following questions:

- What is the sensitivity of the interferometers to ringdowns?
- How much worse is the sensitivity than that of an interferometer with Gaussian noise of the same strain spectral density?
- What specific things cause the sensitivity to be degraded?
- What improvements can be made to the standard matched filter search as it applies to ringdowns?

7.1 Overview of the Method

This section describes the steps involved in producing ringdown triggers from the raw data. This part of the analysis is similar to the analysis done by the LIGO Inspiral [31] group.

The ringdown signals are searched for using a matched filtering code. The matched filter templates are damped cosine waveforms which span the frequency and quality factor (Q) space over the sensitive band of the detector and among the Q 's expected for Kerr black holes.

All of the code up to and including the trigger generation was taken from the LIGO Algorithm Library (LAL)¹. It is C code compiled as a stand-alone executable to run on UNIX from the command line. For this analysis, it was sufficient to individually launch the jobs on ~ 10 CPU's at a time. It took ~ 50 hours to run the full 300 hour S2 data set for 2 interferometers using ~ 350 templates per interferometer.

¹ <http://www.lsc-group.phys.uwm.edu/lal/>

The post-processing is all done using MATLAB ² scripts.

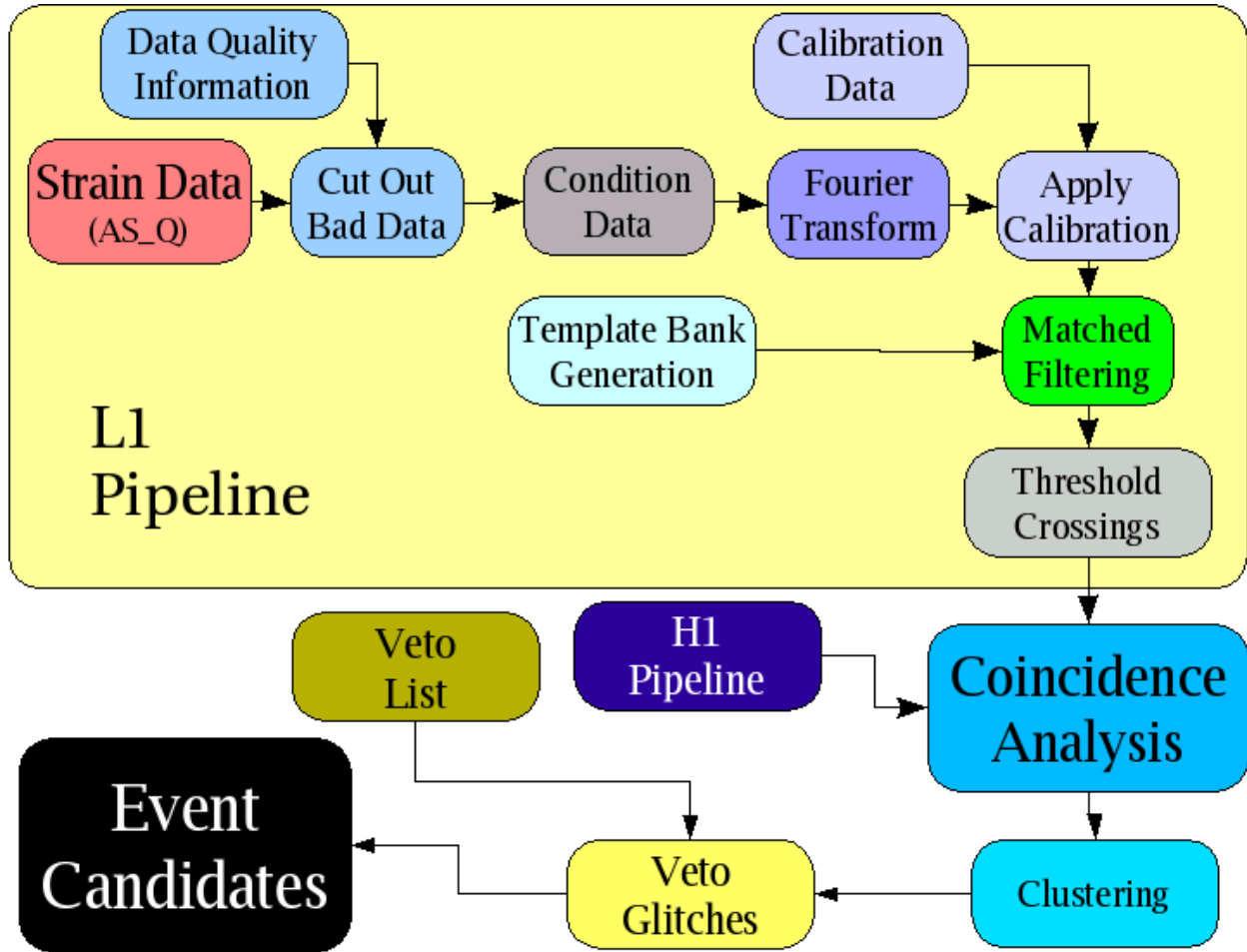


Figure 7-1: The analysis pipeline.

7.1.1 Matched Filtering

The front end of the analysis pipeline uses matched filtering to produce an initial set of ringdown triggers. Matched filtering is a commonly used technique to look for signals of a known waveform in a noisy data stream [?]. A matched filter is the optimum linear filter for the detection of a known waveform.

We can write the calibrated detector output as a time series, $h(t)$, which is the sum of the signal, $s(t)$ and some noise, $n(t)$:

² <http://www.mathworks.com>

$$h(t) = s(t) + n(t) \quad (7.1)$$

The Fourier transform of the template is

$$s(f) = \int_{-\infty}^{\infty} s(t) e^{-2\pi i f t} dt \quad (7.2)$$

The matched filter output is

$$x(t) = 4 \int_0^{\infty} \frac{s(f)h(f)}{S_n(f)} e^{2\pi i f t} df \quad (7.3)$$

The matched filter variance is given by

$$\sigma^2 = 4 \int_0^{\infty} \frac{s(f)^2}{S_n(f)} df \quad (7.4)$$

Thresholding on the signal-to-noise ratio (SNR),

$$\rho = x/\sigma \quad (7.5)$$

is the optimal detection statistic for stationary, Gaussian detector noise [43].

FFT the data

The data are Fourier transformed using the Fast Fourier Transform (FFT) algorithm, which allows the matched filter output to be calculated by using, of order $N \ln(N)$ operations.

Inverse power spectrum

The power spectrum which is in the denominator of Equation 7.3 is estimated in nearly the same way as Welch's method: By doing a 50% overlapping average of 8 data segments of length 4 seconds, but in this case a median average is done of the segments rather than a mean to reduce the bias from one statistical outlier.

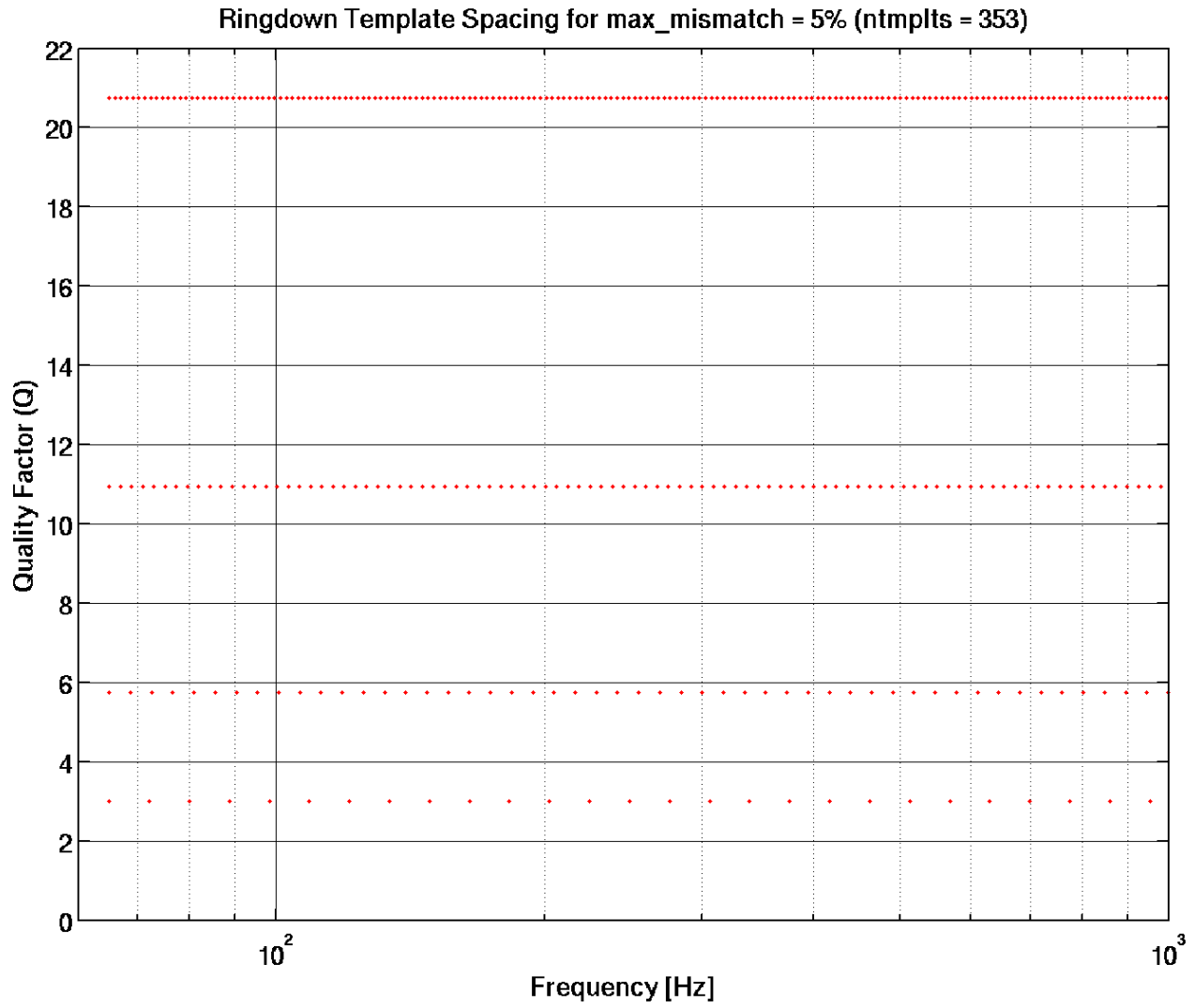


Figure 7-2: Template spacing for maximum mismatch $\rightarrow 5\%$ in SNR. Each dot represents one template.

Apply calibrations

The interferometer response function is applied to the FFT of the data and to the power spectrum estimate. The response function is generated as described in Chapter 6.

Choosing the event time

The matched filter output due to a true ringdown signal will actually cross the threshold several times in the few hundred milliseconds around the real start time of the

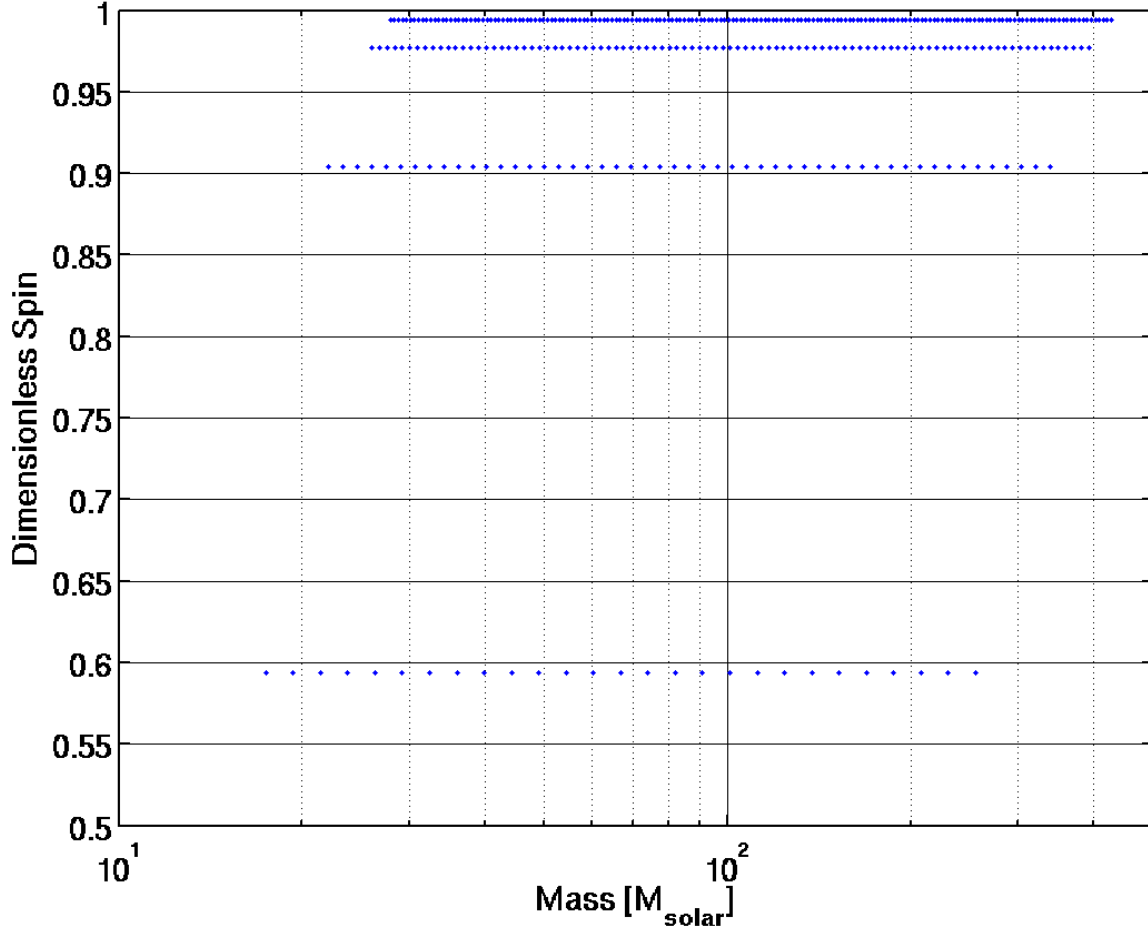


Figure 7-3: Template spacing in the (Mass, Spin) plane. These are the same templates plotted in Figure 7-2 but in terms of black hole Mass and Spin

signal.

The event is localized by clustering all threshold crossings within a time, $\tau_{dur} = \frac{10Q}{\pi f}$. The time with the maximum SNR is chosen to be the event time.

7.1.2 Data Conditioning

Before the data are examined for signals, the raw time series must undergo some conditioning. The data are whitened and decimated.

Whitening

The raw time series of the interferometer's output spans a very large dynamic range. The purpose of whitening the data is to prevent data corruption. Since the data

are analyzed in the frequency domain, there is the possibility of power bleeding into adjacent frequency bins. This effect is strongest in some of the LIGO data streams where the amplitude of the noise at low frequencies is several orders of magnitude larger than the noise in the gravitational wave signal band.

Without the suppression by the servo loop, the differential arm motion would span \sim 13 orders of magnitude on time-scales of 10's of seconds. With the servo on the in-loop error point at the demodulator output spans \sim 8 orders of magnitude. Although this is then further whitened by an analog filter to fit into the dynamic range of the ADC, this analog filter is canceled by a digital filter before the data channel, AS_Q, is written to disk.

Numerous schemes have been proposed to do very detailed whitening of the data including line removal [103] and linear predictive filtering [104]. For this analysis the data was merely high-passed to remove the large low frequency power.

The data are filtered with a fourth order infinite impulse response (IIR) Butterworth high pass filter. By filtering the data backwards and forwards, the dispersion in the filter is canceled. The high pass filter frequency in this analysis was set at 60 Hz, just 5 Hz below the frequency of the lowest frequency template.

Decimation

The data is decimated from 16384 Hz down to 2048 Hz. This is done by first filtering with a finite impulse response (FIR) low pass filter, then by subtracting a time shift to compensate for the linear $d\phi/df$ from the FIR filter, and then downsampling by the appropriate amount. The decimation essentially reduces the analysis time by the decimation factor since the other overhead (data retrieval, writing to disk, etc.) does not contribute significantly to the computation time.

Preliminary runs with a 4096 Hz sample rate revealed that the number of triggers generated by L1 above \sim 800 Hz is enormous; as mentioned in Chapter 4 we know that this band was dominated by oscillator-phase noise coupling in through the highly non-stationary RF sideband imbalance. So in that respect this low quality data is not surprising. The large number of triggers and the poor sensitivity above 1 kHz

motivated the choice of sample frequency.

With a 2048 Hz sample rate there is no information left above the new Nyquist frequency, 1024 Hz. By choosing this band, we are cutting out a range of low mass black holes. From Equation 1.12 we see that this choice loses all masses below $\sim 10 M_\odot$.

7.1.3 Template Bank Generation

Methods have been developed to find the minimal number of templates required to span the templates' parameter space and yet maintain a small loss in the SNR [43, 105, 106, 107]. The basic idea is to use the minimum number of filters possible without losing more SNR than some small number. By calculating the SNR loss due to a small mismatch of waveform parameters, one can define a metric in the coordinates relevant for the waveform; in our case frequency and Q. Using the same method as in [43]:

$$ds^2 \approx \frac{1}{8} \frac{dQ^2}{Q^2} + \frac{1}{4} \frac{dQ}{Q} \frac{df}{f} + Q^2 \frac{df^2}{f^2} \quad (7.6)$$

where ds^2 is the SNR mismatch between two templates one at (f, Q) and one at $(f + df, Q + dQ)$. For this analysis we placed the templates by imposing the requirement that the maximum SNR loss be $< 5\%$.

The number of templates is:

$$N_{filters} \approx \frac{1}{4\sqrt{2}} \frac{Q_{max}}{ds_{max}^2} \ln \frac{f_{max}}{f_{min}} \quad (7.7)$$

For this analysis, $N_{filters} \simeq 350$. With the present computing speeds available it takes only a few days to run the analysis for 350 hours of two interferometer data on a dozen nodes. The main bottleneck in the analysis pipeline is still the speed of the human data analyst and not the cleverness of the tiling algorithm.

Figures 7-2 and 7-3 show the templates spacing used in this analysis in the (f, Q) plane as well as the (M, a) plane. Almost all of the templates bunch into the region of spin from 0.9 to 1.0 since there is not much variation of Q at low to mid spin values.

7.2 Coincidence Analysis

The waveform from a true gravitational wave should be almost the same as seen by both interferometers. So to reject false events, we demand some consistency in the waveform parameters. Each trigger is labeled by five parameters: the start time (t_{start}), the SNR, the peak strain (h_{peak}), the frequency (f_{ring}), and the quality factor (Q_{ring}).

7.2.1 Time

The gravitational wave arrival time difference can be as much as 11 ms between sites. With a perfect detection algorithm and noiseless data, we could use this number as our time coincidence cut. In reality, there is some uncertainty in the arrival time due to having a low SNR and that there is a small mismatch between the signal and the template. It is true that we are ultimately limited by the sample time (0.5 ms) and the relative timing error on the two data streams (< 0.1 ms), but the residual timing errors on the simulations did not reach this level.

We empirically determine the timing uncertainty by injecting a large number of events in software and measuring the resulting timing error (see Figure 7-4).

7.2.2 Frequency

Similar to the arrival time cut, we can do a frequency consistency check. To cut down on the false alarm rate, it is desirable to have the smallest frequency cut possible, maintaining a small false dismissal probability.

7.2.3 Q

By the same reasoning, we would like to demand a tight Q cut.

Since the same template bank is used for both interferometers, we are able define a coincidence as occurring only when exactly the same template is triggered on both interferometers within the allowed time coincidence window.

For both the f & Q cuts, it is true that we lose some detection efficiency on the low SNR events for which the parameter estimation is not good. However, these events are discarded anyway *because* of their low SNR.

7.2.4 Amplitude

The amplitude cut is more complicated than the other three cuts. Demanding a strict amplitude cut requires that the relative calibration errors between the two interferometers be small. In addition, for a true signal, the relative antenna response functions of the interferometers must be taken into account (see Appendix I for plots of the antenna response).

For this preliminary analysis, no amplitude cut was used.

7.3 Simulations

To test the efficacy of the entire analysis pipeline, ideally we would inject events to mimic exactly the presence of a true gravity wave. We use the mirror actuator (the photon calibrator will be used in the future) to move the test masses as a gravitational wave would. This is described in Section 7.3.2.

Since injecting signals by hardware pollutes the data stream, we do not do this very often. Instead, we do many simulations by adding the ringdown waveforms directly to the data.

7.3.1 Software Injections

The software injections are added to the time series by taking fake, damped co-sine waveforms, calibrating them, and then adding to the raw uncalibrated data (just before the 'Condition Data' block in Figure 7-1). Then the rest of the analysis machinery progresses in the same way as if there had not been an injection. All of the simulations done here were done on a $\approx 10\%$ sample of the full data.

Parameter Estimation

We would like to know what the error is in determining the signal parameters. To do this we compare the recovered waveform parameters to the intended injection parameters.

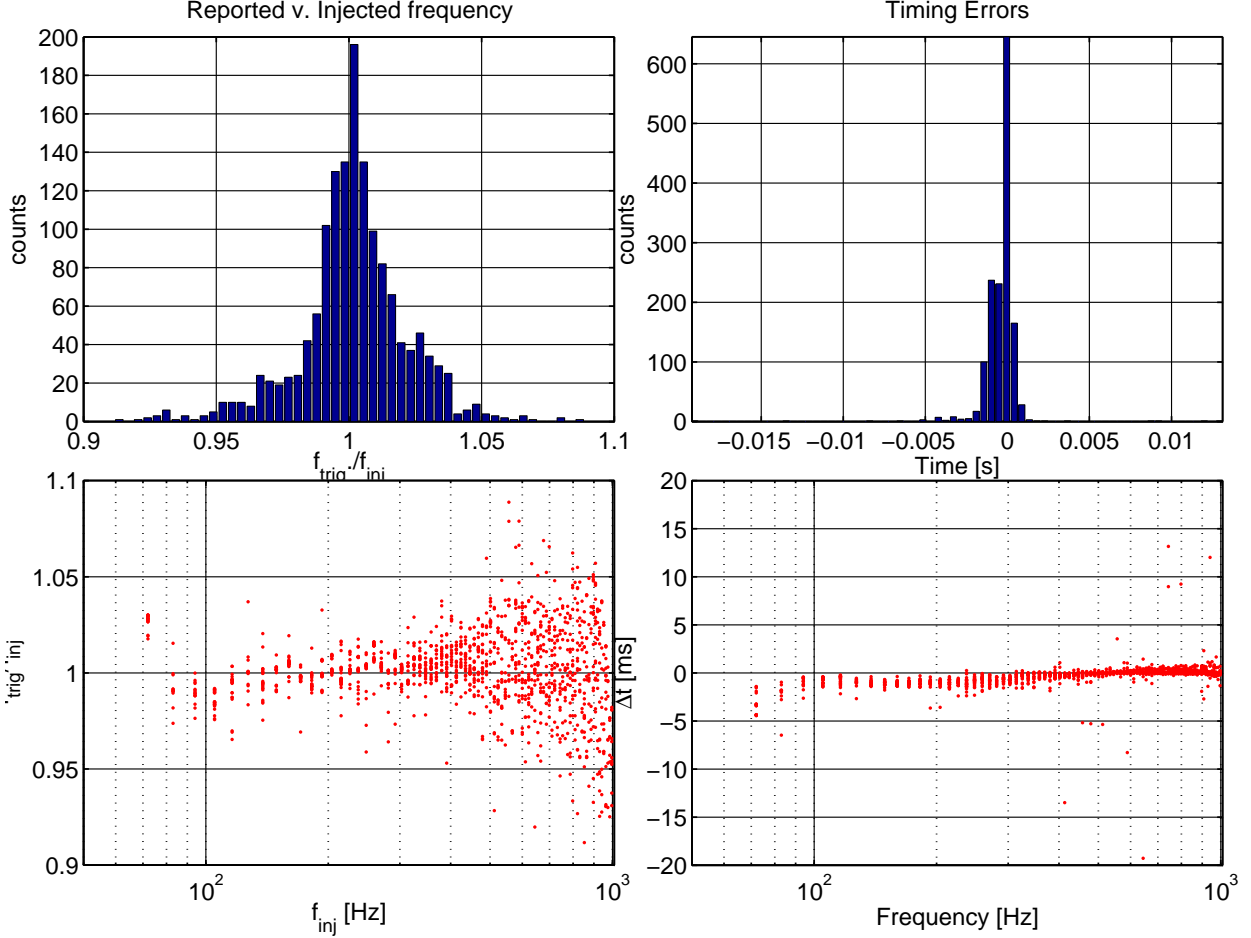


Figure 7-4: Parameters reported by the pipeline versus the injected parameters. In this plot the 'loudest' 10% of the triggers for each event are used to estimate the trigger parameters by doing an $(\text{SNR})^2$ weighted average.

Detection Efficiency

To interpret the results of the analysis, we measure the detection efficiency of the software injected signals. As shown in Figures 7-5 and 7-6, we detect almost all of the high SNR events and none of the low SNR events. There is a gradual increase in

the probability of detecting a signal as the SNR is increased, which we have fit to a sigmoid function [108]:

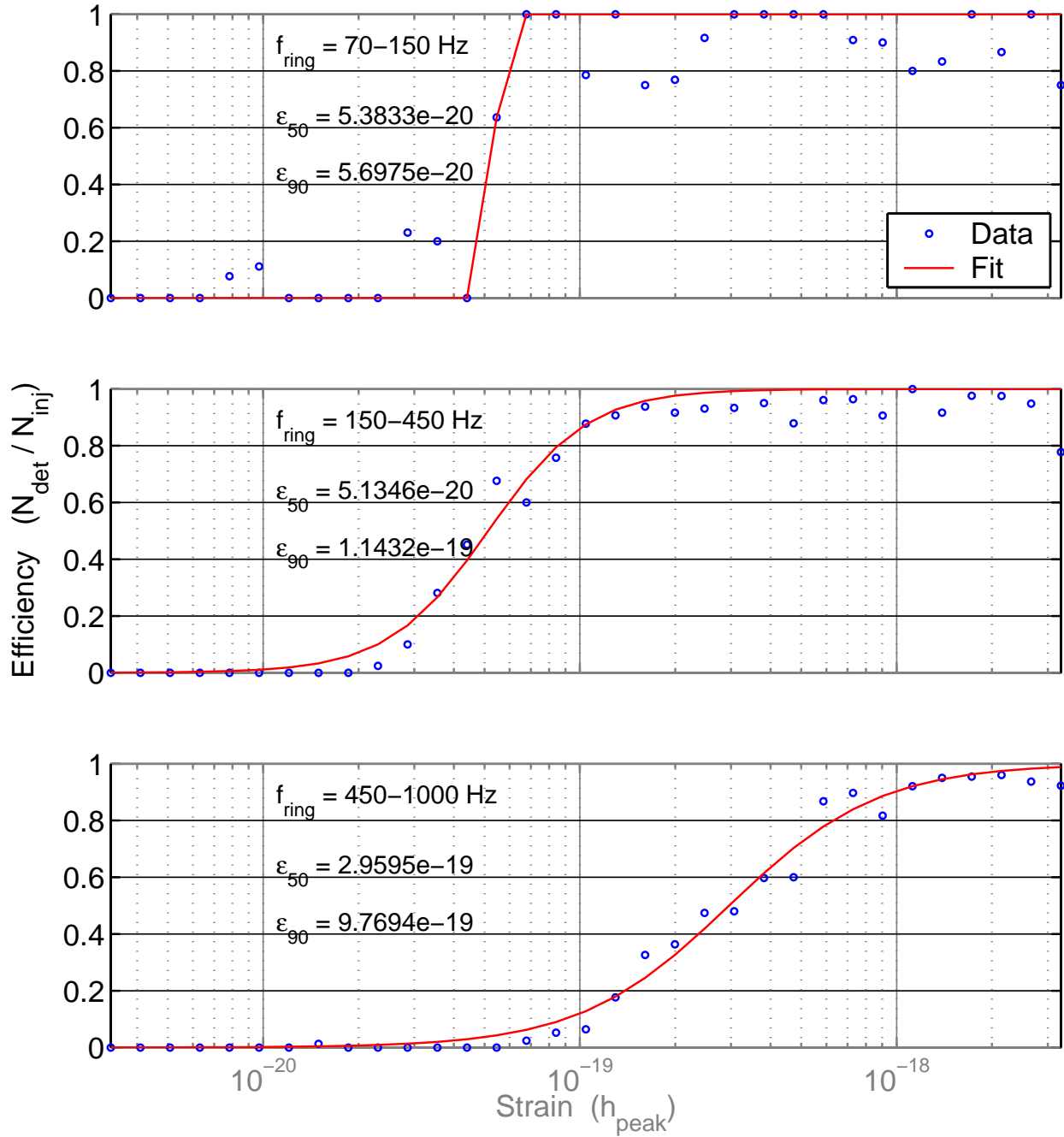


Figure 7-5: Detection efficiency of L1 as a function of peak strain. The three plots show the results in 3 frequency bands. Also indicated are the 50% and 90% efficiency levels corresponding to a 50% and 10% false dismissal probability, respectively.

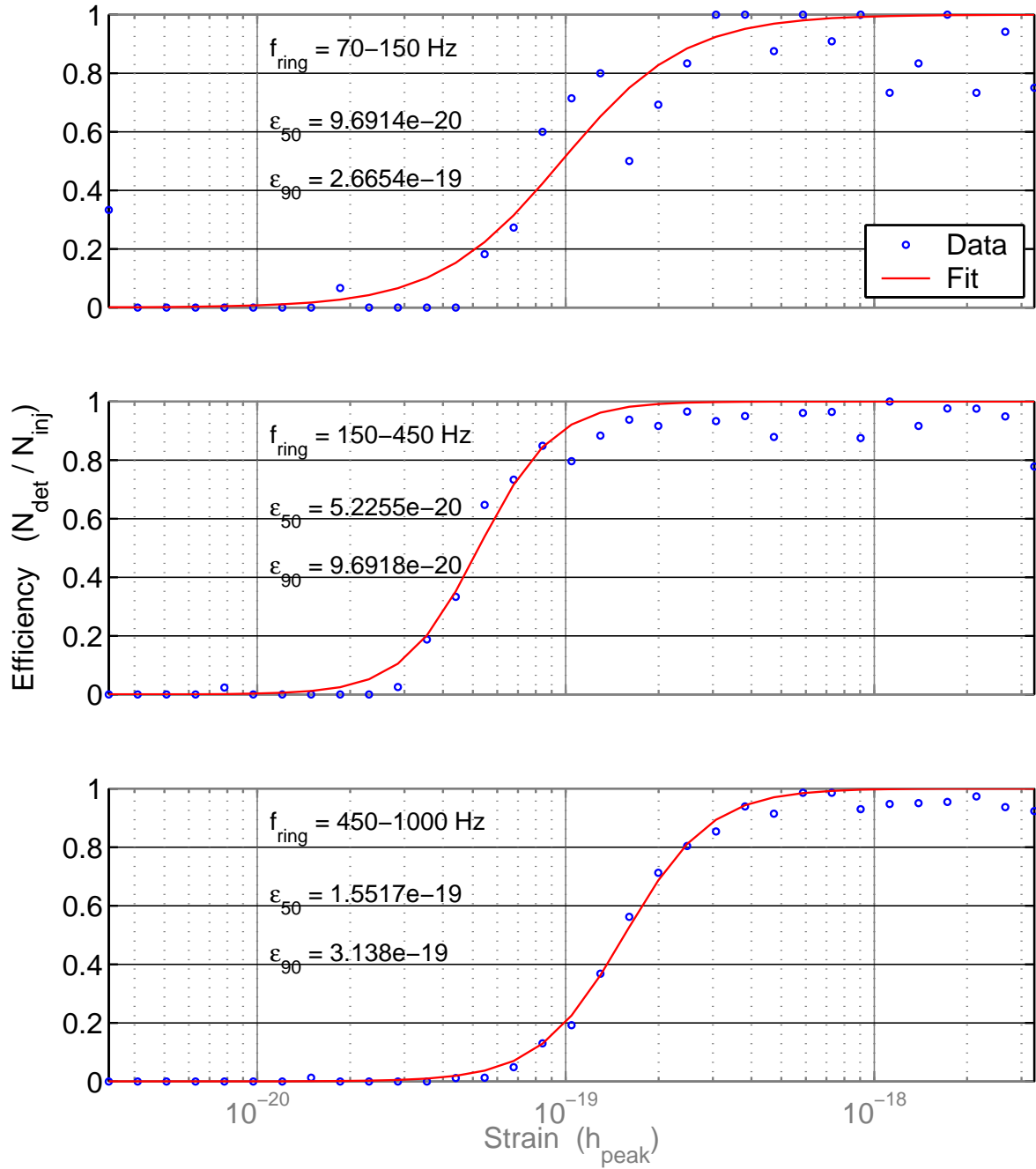


Figure 7-6: Detection efficiency of H1 as a function of peak strain. The three plots show the results in 3 frequency bands. Also indicated are the 50% and 90% efficiency levels corresponding to a 50% and 10% false dismissal probability, respectively.

$$E(h) = \left[1 + \exp\left(-\frac{\log_{10}(h) - \log_{10}(h_{50})}{a}\right) \right]^{-1} \quad (7.8)$$

We call the point at which there is a 50% probability of detection, ϵ_{50} . This ϵ_{50} , in terms of strain, is a function also of frequency and Q.

7.3.2 Hardware Injections

Signals are also injected in real time via hardware; more to test the realism of the software injections than anything else. The signals are calculated ahead of time and saved into a file. The file is then loaded and the waveform is injected into the number stream driving the longitudinal degree of freedom of the optic. The injection point is labeled as 'EXC' in the ETMX path on the right hand side of Figure 5.

Figure 7-7 shows the amplitude of the injected ringdowns compared with the noise in the detectors.

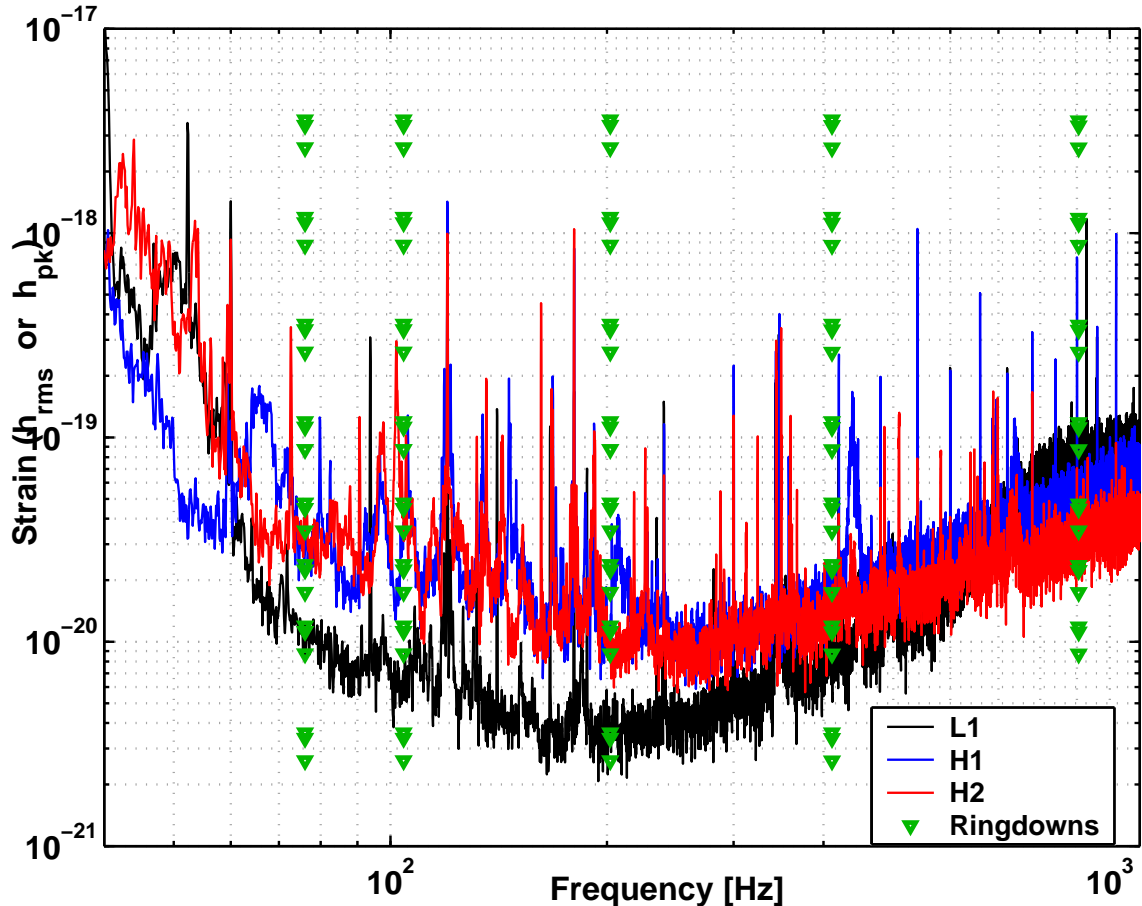


Figure 7-7: The peak amplitudes of the hardware injections are plotted versus the noise, $h_{rms} = \sqrt{f S_h(f)}$ for the three interferometers during the S2 Science Run.

Comparison between the hardware and software injections is ongoing.

7.4 Results

The entire pipeline was then run on all the H1-L1 double coincident segments. The run was done with a SNR threshold of 6 on L1 and a threshold of 5 on H1.

7.4.1 Distribution of triggers

Figures 7-8 and 7-9 show the distribution of the triggers from the individual interferometers.

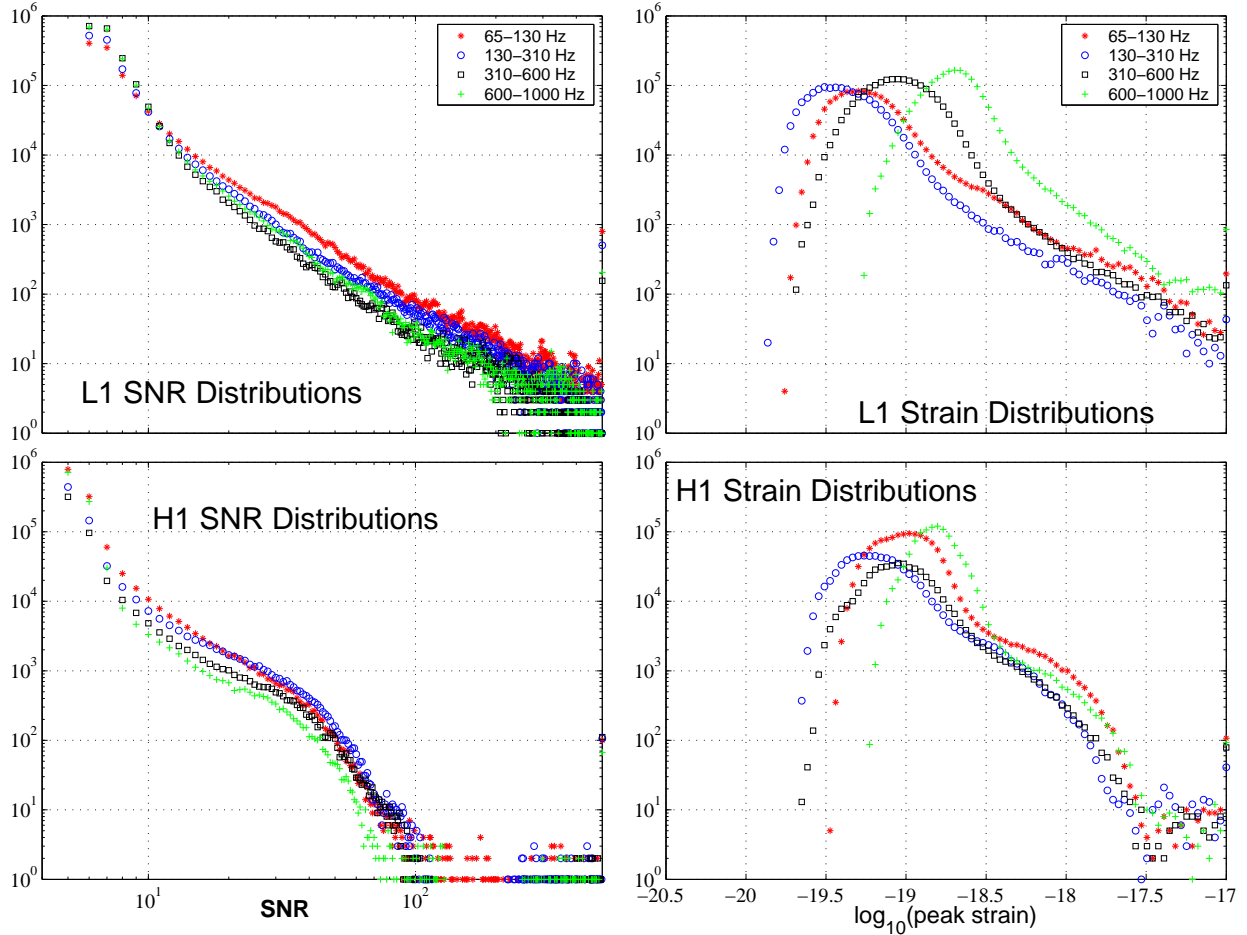


Figure 7-8: Amplitude distribution of the triggers in four separate bands. The choice of bands was made to highlight the different noise character in the different bands.

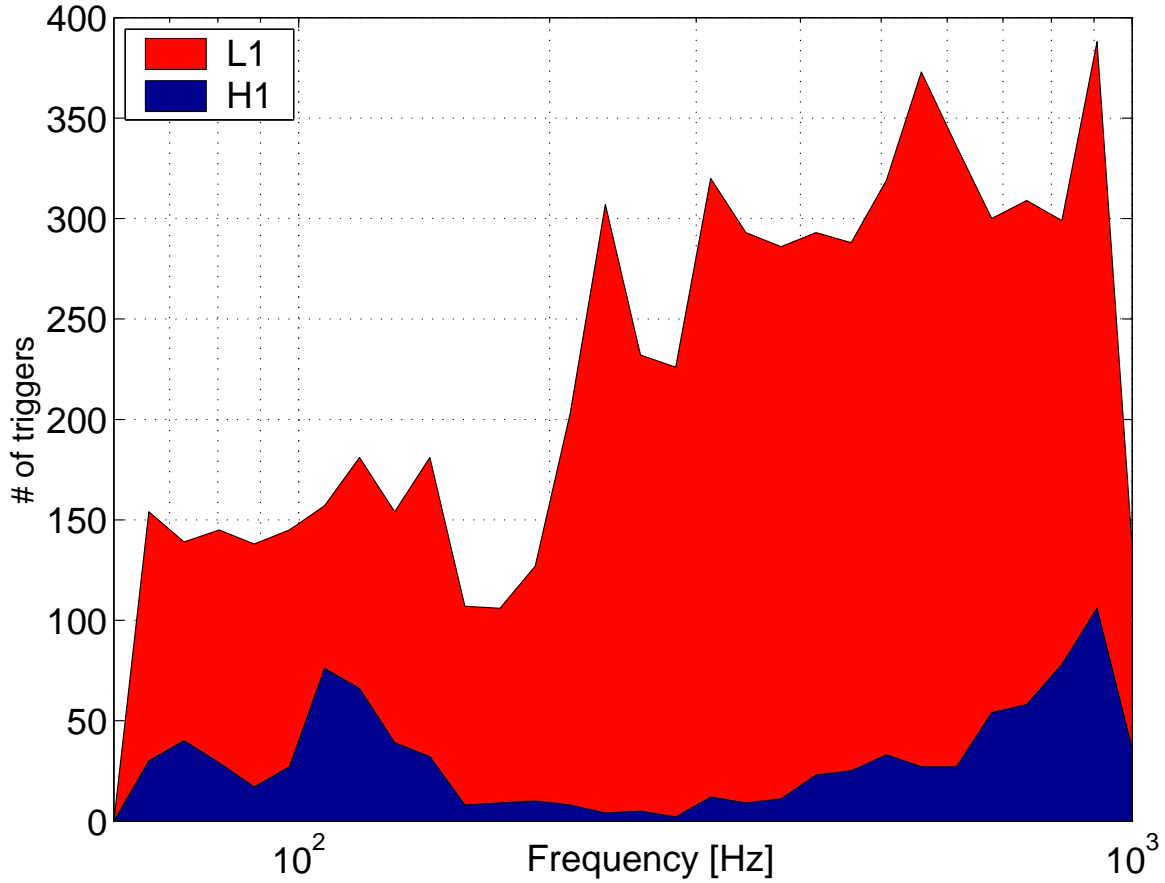


Figure 7-9: The total number of triggers per frequency binned logarithmically. The total number of triggers in any bin is dominated by the large population of low SNR events.

7.4.2 Coincident Events

After applying the coincidence criteria listed in Section 7.2 there will be some remaining events; how many depends on the threshold used. Figure 7-10 shows the distribution of the (L1) SNR of the coincident events after clustering in 100 ms chunks.

Since the character of the instrument noise is not Gaussian, it is difficult to tell if the non-Gaussian outliers are signal or noise.

To see if there are a statistically significant number of coincident events within the time window determined by the light travel time between the detectors, we re-ran the coincidence analysis many times, each time inserting a pseudo-random time shift in the triggers of one of the interferometers. Figure 7-11 shows an example of one of these time lag simulations.

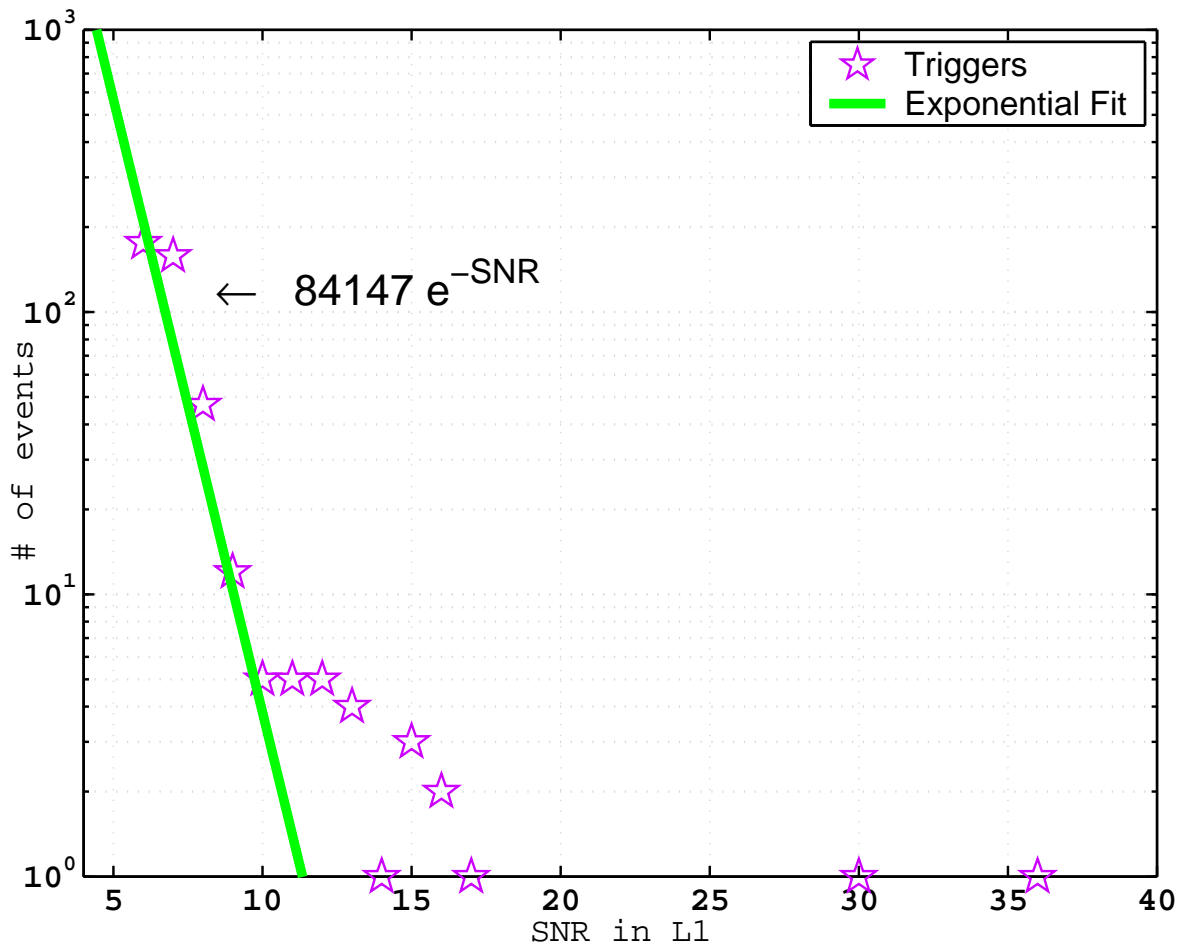


Figure 7-10: SNR Distribution of clustered coincident events with $\text{SNR} < 50$

If there had been a number of real events (noise or otherwise) which were coincident between detectors, then one would expect there to be an excess of triggers at a lag of zero seconds. At various thresholds and with many choices of frequency bands, there are no excess coincident events above the level of one standard deviation above the background.

The same plot as in Figure 7-11 was made for several other choices of threshold and frequency band, always with similar results: the number of events at zero lag are always within 1σ of the background.

From these time shift plots, we can see that there is nothing special about the events at zero lag. In the most sensitive band (150-500 Hz), there are no coincident events above an SNR of 9, except for two instrumental artifacts.

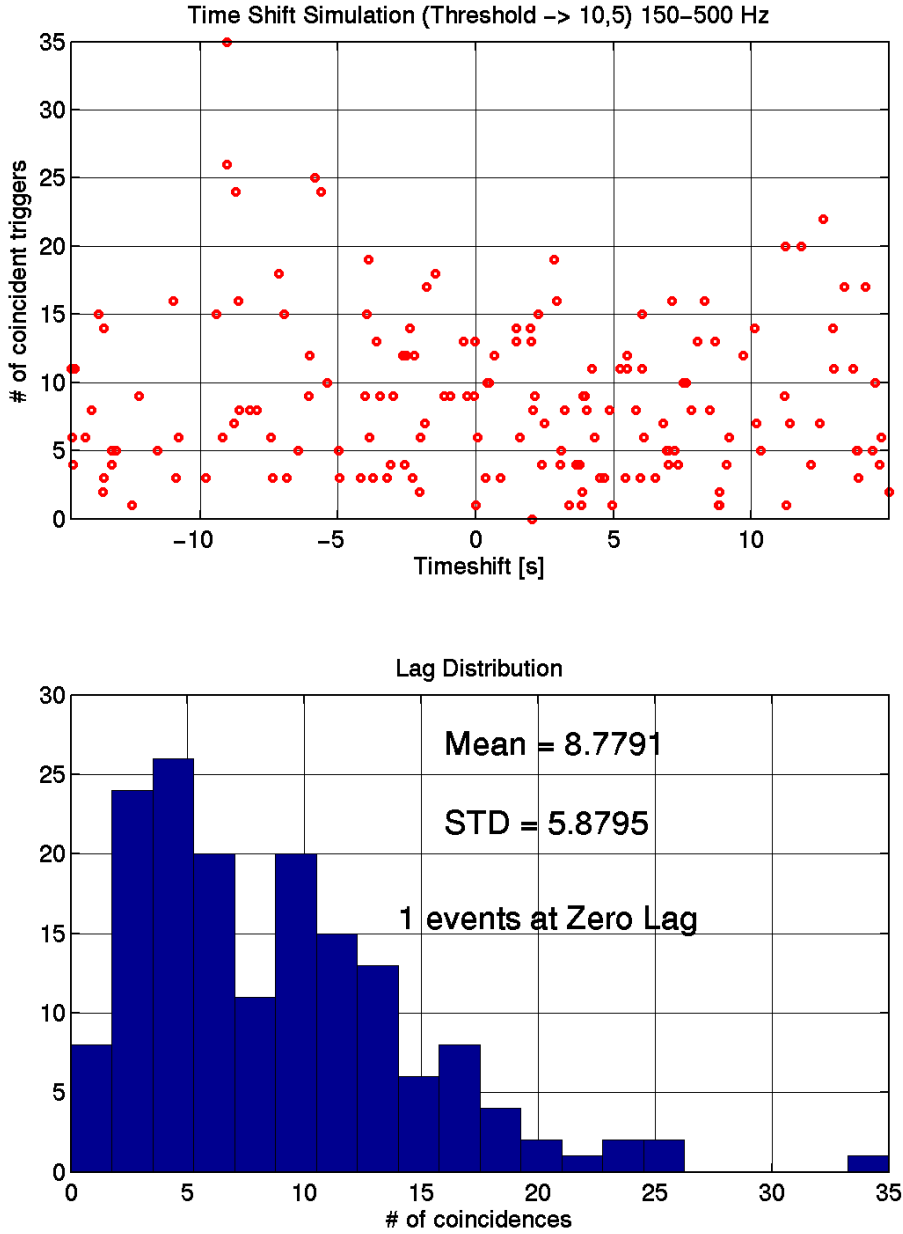


Figure 7-11: Upper plot shows the number of coincident events as a function of artificial time lag between the interferometers. The lower plot shows the distribution of the upper plot. Both plots include only the triggers from the sensitive 150–500 Hz region. The L1 threshold = 10 and the H1 threshold = 5.

7.5 Examination of the Remaining Coincidences

This section looks at the coincident events at zero lag. Each event is tagged with an event # in Table 7.1.

Event Triggers							
Event #	GPS Start Time	SNR	Strain (h_{peak})	f	Q	Note	
1	729434662.741	12	8.9e-20	84	2	—	
2	729531388.721	16	1.5e-19	78	17	60 Hz	
3	729541448.431	10	4.7e-19	803	6	—	
4	729920354.113	15	2.0e-19	65	21	60 Hz	
5	730094894.358	11	1.4e-19	566	21	—	
6	730133435.403	152	7.3e-18	994	21	ADC	
7	730137174.219	16	5.0e-19	690	21	Vio^2	
8	730284595.603	17	2.4e-19	65	3	60 Hz	
9	730285409.016	12	8.6e-20	94	18	—	
10	730443122.214	12	7.3e-20	91	21	—	
11	730443379.098	36	2.9e-19	80	11	60 Hz	
12	730462872.134	30	1.7e-19	83	21	SNR	
13	730528198.849	13	8.7e-20	97	11	—	
14	730528295.260	13	6.2e-20	118	21	—	
15	730570357.681	11	2.5e-19	637	14	—	
16	730581701.429	12	5.0e-20	135	21	—	
17	730592358.344	12	8.0e-20	87	11	—	
18	730605715.704	10	3.7e-20	136	21	—	
19	730669046.827	10	1.0e-19	80	21	—	
20	730881699.750	132	4.7e-19	180	21	ADC	
21	732581991.246	1580	5.4e-17	734	11	ADC	
22	732637065.650	11	7.7e-20	119	11	—	
23	732639925.100	14	5.0e-19	848	17	—	
24	733037033.244	71	6.1e-19	353	21	Violin	
25	733037804.016	15	6.4e-20	112	21	???	
26	733592255.881	11	2.4e-19	695	21	—	
27	733749193.282	13	2.1e-19	669	18	—	
28	733751635.889	15	7.8e-20	78	21	—	
29	734139127.398	13	8.5e-20	78	16	—	
30	734149435.240	12	5.8e-20	94	21	—	

Table 7.1: Parameters for the coincident events in S2 with SNR > 10

7.5.1 Study of the Remaining Events

The coincident events with a SNR in L1 above 10 were examined 'by hand' by looking at the time series plots after bandpassing the data in a few hundred Hz band around the trigger's central frequency.

Event #21 - SNR = 1580

Event #21 is an ADC saturation. The AS_Q time series that we record is a digitally processed version of the raw ADC inputs. To determine what the ADC recorded we apply the inverse of that digital processing. Applying this procedure to #21 we see that the ADC signal suddenly rails several times at +32767 and -32768. The signal then recovers and the interferometer resumes normal operation.

During the course of the run several of these events were observed and more often than not these saturations caused a loss of lock. This was tracked down to be a malfunctioning piece of electronics; voltage noise on the gain control of the AS port whitening board caused fast steps in the AS_Q ADC signal.

Following the S2 run, software monitors were put in place to record all ADC saturations and the flagged data have been vetoed. Even better, a new design for the whitening electronics uses a TTL logic control for the gain command, eliminating this type of malfunction.

Event #6 - SNR = 152

This one is another ADC saturation, although of a different nature. Just below the sensitive 70-1000 Hz band is a large 'wall' of noise which is of a seismic nature, although not the standard seismic coupling mechanism. It comes from a variety of noise sources including mechanical resonances of the optical lever piers, unfiltered electronics noise from the wavefront sensors, and in this case, nonlinear upconversion of the \sim bounce mode of a suspended large optic. During the run, we noticed that ground noise due to some malfunctioning HVAC equipment would excite the mechanical modes of several optics. Large amplitude signals (through some unknown mechanism) would also produce a large component at $3\times$ the fundamental frequency. This large signal at \sim 35 Hz is then amplified by the analog whitening filter.

The RMS from this signal is several times smaller than the ADC range, but statistically we expect to see a large excursion once in awhile. These excursions can either cause a loss of lock or, as in this case, produce a strong glitch.

Based on these experiences, a new whitening filter design was implemented before the next science run. The new whitening filter has $\sim 4\times$ less gain in this noisy band. In addition, there are some efforts to fix noisy HVAC equipment.

Event #20 SNR = 132

Another ADC saturation. Essentially the same behavior as Event #6.

Event #24 SNR = 71 f = 353 Hz

Nothing in H1. A sudden sharp transient in L1. The template frequency is the same as that of one of the test mass violin modes, but it is not clear if this is a coincidence or not.

Event #11 SNR = 36 f = 80 Hz

Looks like some transient upconversion around 60 Hz. It is only a small increase in the RMS of the 60 Hz shoulders; this is a common occurrence and this ~ 20 Hz band around 60 and 120 Hz often show this non-stationary behavior.

Event #12 SNR = 30 f = 83 Hz

Interesting looking glitch in L1, but at too low of a level to show up in the bandpassed H1 or H2 time series.

Event #8 SNR = 17 f = 65 Hz

Just like #11. 60 Hz junk.

Event #7 SNR = 16 f = 690 Hz

A random fluctuation in the 2nd harmonic of a violin mode in both interferometers. It seems like the data in a small band around the first and second violin mode harmonics is constantly getting rung up. If this cannot be suppressed by further notching in the control servos, it may be necessary to ignore all the triggers from these bands.

Event #2 SNR = 16 f = 78 Hz

L1 AS_Q goes to +/- 20000 ADC counts but does not saturate. Looks like a 35 Hz and 60 Hz problems evident in events #6 and #11.

Event #4 SNR = 15 f = 65 Hz

Event #25 SNR = 15 f = 112 Hz

There is nothing visible in the time series above the background.

7.6 Future Improvements

This analysis is a preliminary attempt to look for ringdown signals with the main emphasis being on uncovering gross problems or difficulties. As such, there a number of ideas / methods / techniques which were not implemented yet but are listed here for posterity.

- It seems clear that the burden is on the commissioning team to reduce the large variability in the noise floor and the high rate of transients. A noble goal would be to reduce the rate of transients until the random double coincident rate meets the expectations from Poisson statistics up to SNR= 15. Efforts are underway to develop a 'ringdown' monitor program to run in the control room at both sites to give a feel for the variability of the false rate as instrument parameters are adjusted during commissioning of the interferometer.
- A method needs to be developed to veto non-ringdown events which cause the templates to exceed threshold. One method may be examining the software injections to determine the amplitude and start times in neighboring templates[43]. A true ringdown signal should have a well defined distribution in template space. One has to be careful not to veto a potential merger-ringdown signal by placing too tight a criteria.

- Do a direct waveform consistency check by cross-correlating the interferometer outputs in the neighborhood of the events. This is a technique currently being developed for detecting unmodeled bursts [109].
- Do a real Monte-Carlo simulation over the matched filter and coincidence parameters to optimize the search sensitivity.

7.7 Conclusions

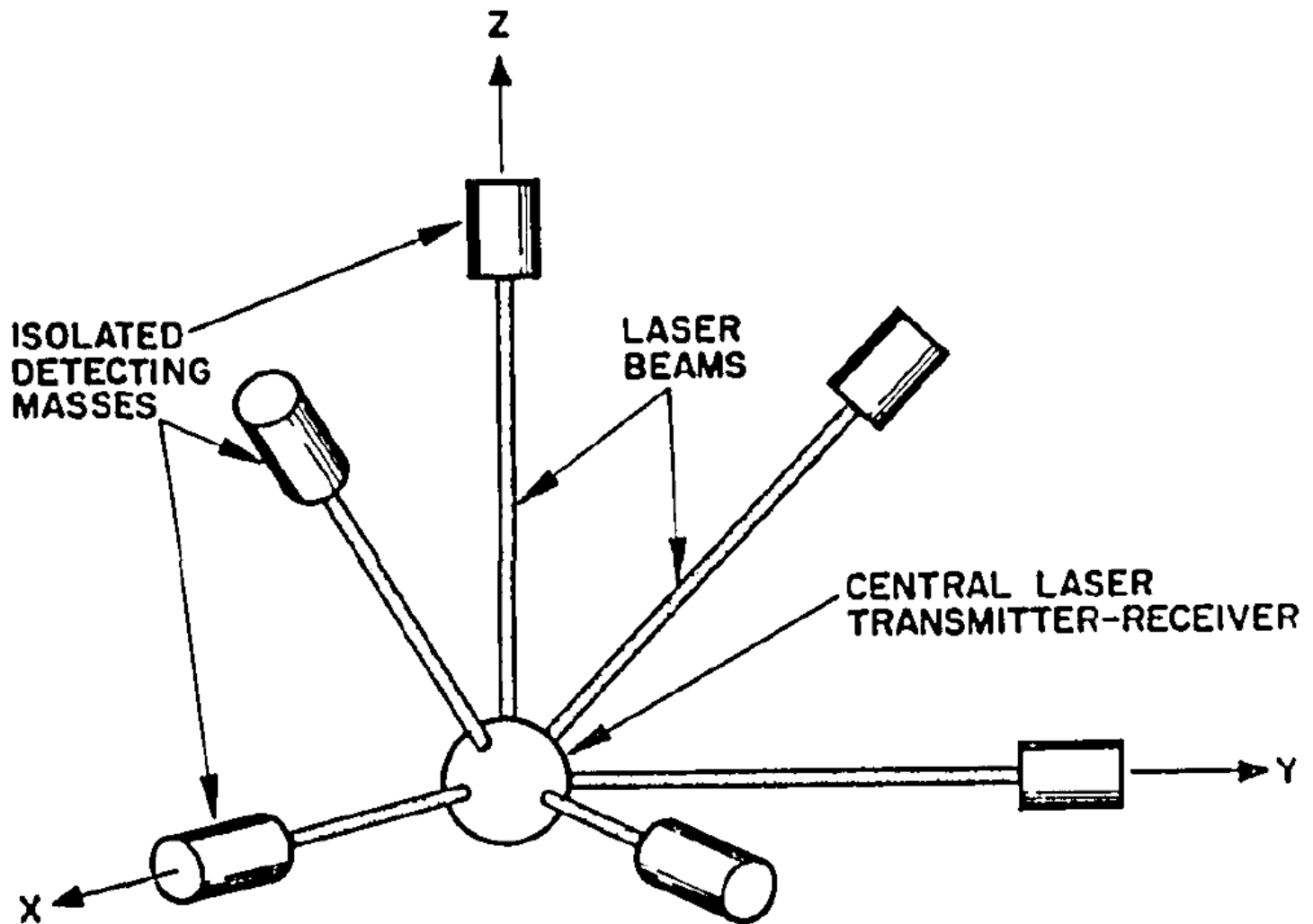
A preliminary search was done for damped sinusoids in the data. The search highlighted several problems in the interferometers and in the search method.

The equivalent strain amplitude of the coincident events at SNR of 10 agrees with the rough estimate made by comparison with noise spectral density.

It is clear that more simulations will have to be done to determine precisely the detection efficiency as a function of time for each interferometer. A method of vetoing the non-ringdown triggers needs to be developed to reduce the false rate.

Chapter 8

The Future



8.1 Possible Future Improvements

At present none of the three interferometers operates at the designed sensitivity level. In addition, the duty cycles (especially of the Livingston detector) are not at the 90% level which they were designed for. The following are some ideas for improving the state of affairs. Some are currently being explored and some only exist on paper.

8.1.1 Seismic Isolation

During the course of this writing, a scheme has been developed for mitigating the excess seismic noise which limits the duty cycle and data quality of the Livingston interferometer.

Quiet hydraulic actuators [110] with collocated sensors are being installed on the existing seismic isolation support structure. This system, the Hydraulic External Pre-Isolator (HEPI), is also intended for the Advanced LIGO upgrade.

Since the in-vacuum, passive isolation stack has various cross-couplings (e.g. from pitch to horizontal motion), the HEPI is designed to reduce the vibration in all 6 DOF on the outside of the vacuum chamber. Preliminary testing indicates that the HEPI performance will exceed the factor of 5-10 reduction in broadband displacement noise which was the goal.

The Hanford site seems to be sufficiently quiet (with the exception of occasional periods of high winds), such that at present, no such drastic retrofit is planned. However, the dramatic success of HEPI could make the Hanford sites ground noise seem egregiously large in comparison to the isolated Livingston platforms.

8.1.2 Output Mode Cleaner

The current interferometers have many problems associated with poor beam quality or imperfect interference at the interferometer's dark port:

- Excess carrier light at the dark port produces excess shot noise.

- The reflectivity difference of the two arms will produce a static, TEM_{00} , carrier field at the dark port. This static field beats with noise on the sideband light to produce noise in the signal channel.
- The portion of the sideband field which does not spatially overlap with the carrier does not contribute to increasing the optical gain. Instead, it produces many junk effects: shot noise, acoustic sensitivity, jitter sensitivity, etc.

One solution to these problems which is being currently pursued is the use of an output mode cleaner. This would be a short, rigid, triangular cavity placed on the anti-symmetric port output table. Such a short (~ 5 cm), low (~ 30) finesse cavity would have large enough linewidth to transmit the RF sidebands and the carrier in the same resonance. Higher order spatial modes, however, would be passively rejected just as in the input mode cleaners. The suppression of the higher order spatial modes is given by Equation C.2.

Once the contrast defect due to higher order modes has been effectively removed, one can re-optimize the SNR by adjusting the modulation depth for the resonant sidebands as described in Section 3.3.

8.1.3 Thermal Compensation

A serious problem with the interferometers is the unstable nature of the power recycling cavity.

The power absorbed by the optics forms a thermal lens in the bulk of the glass through the temperature dependence of the index of refraction. The original design planned on a precise amount of thermal lensing and pre-polished the power recycling mirror to account for this. Preliminary estimates indicate that the absorption levels vary substantially from optic to optic.

The carrier mode in the recycling cavity is determined by the average spatial mode of the arms and so the carrier field is largely immune to curvature errors in the recycling cavity. The sideband fields are not resonant in the arms and so the mode matching of the sideband to the recycling cavity depends critically on the amount of

thermal lensing. The experience with the interferometers so far has shown that it will be necessary to control the recycling cavity resonant mode to keep it well matched to the arms.

The three most deleterious consequences of the unstable recycling cavity are:

- The RF sideband is not spatially mode-matched to the recycling cavity. So most ($\approx 90\text{-}95\%$) of the sideband power is reflected from the recycling cavity. This results in low optical gain at both the recycling cavity pickoff and anti-symmetric ports.
- The RF sideband field which does make it to the AS port does not overlap well with the carrier field and therefore the gravitational wave signal sidebands. This means that much of the RF sideband field which is there contributes to increased shot noise and not to the signal strength.
- The unstable nature of the PRC results in large optical gain modulation for small angular fluctuations. This leads to instability in all of the conditionally stable servo loops.

To compensate for the lack of thermal lensing, a system, initially intended for Advanced LIGO [111], is being commissioned to stabilize the cavity. By applying the correct spatial distribution of heat to each ITM, one can induce a thermal lens in the test mass bulk. This will pull the recycling cavity from unstable to marginally stable.

The plan is to heat each ITM with a CO₂ laser with a fixed mask to shape the heat distribution. The Nd:YAG laser power will be turned up all the way and the CO₂ beam will be adjusted accordingly to maximize the SNR of the $\delta L_- \rightsquigarrow AS_Q$ readout.

8.1.4 Oscillator Phase Noise

During the course of commissioning, a strange and large sensitivity to phase noise on the RF oscillator was measured. This noise source dominates the interferometers' noise budgets above 1 kHz.

While the source of the coupling is not established as of yet, it is believed that reducing the phase noise of the oscillator itself will partially mitigate the problem. In the near future low noise, crystal oscillators will be installed. These oscillators have a narrow tuning range compared to the existing frequency synthesizers, but have a SSB phase noise of $-165 \text{ dBc}/\sqrt{\text{Hz}}$ at 1 kHz (as compared to the $-150 \text{ dBc}/\sqrt{\text{Hz}}$ of the currently installed units).

8.1.5 Laser Frequency Noise

A Better Frequency Reference

As shown in Figure 5-10, the overall frequency stabilization factor would be almost good enough except that the noise in our frequency noise readout channel is too high to produce a quiet laser beam. The main work that needs to be done is to reduce the shot noise limited sensitivity at that port.

Until now we have been using a signal readout scheme where each length signal is constructed by demodulating at the resonant sideband frequency. Unfortunately, this causes us to suffer problems similar to those experienced at the AS port with junk light. The uncontrolled Q phase signal in reflection dominates, by a few orders of magnitude, the I phase signal used to readout the $L_+(f)$ or $\nu(f)$ signal. This limits the total amount of light we can detect without saturating the RF photodetector. At such low levels ($\sim 1 \text{ mA}$, 30X smaller than designed) the shot noise limit is quite high.

An alternative scheme is to use the non-resonant sideband (which is already used for angular sensing). Whereas the resonant sideband level at the reflected port is slowly extinguished as the recycling cavity is thermally lensed, the non-resonant sideband is, in principle, unaffected by the state of the recycling cavity and can produce a strong signal, largely independent of the problematic recycling cavity. There is also no Q phase signal expected at the non-resonant sideband frequency, in principle.

More Loop Gain

Above a few kHz, the frequency noise exceeds its designed noise level. The result is that the interferometer sensitivity would be compromised at high frequencies once the other noise sources are reduced.

The reason for this high frequency excess is that early in the commissioning phase for the Mode Cleaner, the servo loop gain was reduced to make the servo more stable. In this low gain state the VCO phase noise dominates the MC noise (see Figure C-1) and this propagates into the interferometer.

Some combination of higher loop gain in the MC and a quieter VCO will have to be explored in the future to meet the noise requirements.

8.1.6 Wavefront Sensing

At the time of this writing, the full Wavefront Sensing (WFS) and angular control system has been demonstrated to work on all the interferometers, although it has only stably operated on the Hanford interferometers.

In order to have some day to day stability and consistent data quality, it is vital that this system work on all interferometers. In the near future it is envisioned that the WFS system will be commissioned in Livingston to bring it to the level of the Hanford instruments.

On all the interferometers, there remains substantial work to be done on the electronics for this system to reduce the noise contributed to the gravity wave channel. The reduced noise will allow operation with higher gain. There does not seem to be any fundamental roadblock here.

8.1.7 Increased Laser Power

In the past few years of detector commissioning, the laser power into the interferometer has been run, usually, at lower power than designed for. This is due to a number of reasons:

- Low transmission through the optics between the laser and the interferometer.

- Unintentional low power due to degraded Power Amplifier pump diodes, poor amplifier alignment, or low power from the master oscillator.
- Intentional low power from the laser by lowering the pump diode current to extend diode lifetime.
- Not being able to handle high power in the interferometer itself (scattering, radiation pressure, wimpy photodetectors, etc.)

Efforts are now underway to chip away at this power deficit by better alignment, mode-matching through the PMC, increased pump power, etc. It looks promising that there soon can be the full 6 Watts of power entering the interferometer.

A hypothetical question to pose is, what can be done to further increase the laser power by another factor of 2-5. Some concepts to quantitatively explore over the next two years are:

- Increase the power output of the master oscillator. Currently we are pumping the NPRO master oscillators at \sim 500 mW. At this power level the PA is only partially saturated and so while doubling the MO power will not double the MOPA power, we should explore how much this will give.
- Add another amplifier. By taking the MOPA output and putting it through a single pass, commercially available amplifier or another double-pass PA like we have now would make a much more powerful laser; a MOPAPA.
- Convert the PA into a ring cavity and injection-lock it to the NPRO.

8.1.8 Low Noise DAC

The noisy digital-to-analog converters currently used require us to use aggressive, complex analog filtering to both achieve low displacement noise and yet have enough range to accommodate the low frequency seismic noise.

The development and testing of DACs with $\sim 30X$ less noise is being pursued. These would lower the influence of DAC noise below the SRD/10 level in all interferometers and also allow one to rework the post-DAC filtering to give increased dynamic range.

8.1.9 Sweet Spot on the Suspension

The estimate made for suspension thermal noise in Section 4.1.2 assumed that the beam was centered on the test mass. This is not the position in which the suspension thermal noise is minimized.

It was recognized several years ago [79, 112] that there is a 'sweet spot' on the optic which minimizes the thermal noise. When the test mass pendulates, most of the loss is due to bending in the wire at the top suspension point and at the bottom of the wire, near where it contacts the optic (see Figure G-1). By symmetry, only the thermal forces generated at these two points affects the test mass motion.

For the thermal forces generated at the bottom of the wire, there is a node in the optics motion slightly below the center of mass. By adjusting the cavity axis so that the beam resonates at this point, one can make the measured interferometer strain noise insensitive to the this thermal noise and only sensitive to the loss in the top of the wire.

Following the method of [79] we can get a numerical result and find that the minimum is ~ 1 cm below the center of mass. In the case where suspension thermal noise is the only noise in that band we can get a $\sim 20\%$ reduction from ~ 50 -100 Hz.

8.1.10 Low internal mode noise

Between the time the interferometers were designed and the present, the state-of-the-art in thermal noise modeling has crept forward somewhat. In particular, it has been recognized that the substrate thermal noise should be less than what was assumed in the initial design and that coating thermal noise is approximately equal to the substrate thermal noise for the LIGO-I choice of beam parameters and coating

materials.

In particular, it appears that the overall test mass thermal noise will come out $\sim 2X$ smaller than was expected originally.

8.1.11 DC Readout

In the current signal readout scheme, the GW signal is encoded as an amplitude modulation on the RF carrier (which is itself generated as a beat between an optical frequency carrier and an RF sideband). This method has a historical origin; in the 20th century, the amplitude and phase noise on commercial lasers was so bad that there was no hope of reaching the shot noise limit at the audio frequencies where GW's are expected.

Recently [113] it has come to light that this is no longer the case. The combination of quiet, solid-state lasers with the high-gain, low noise, amplitude and frequency stabilization servos already significantly reduces these noises. The advantage to eliminating the RF sidebands, however, is revealed through the way the laser noise couples into the interferometer. As described in Sections 4.2.1 and 4.2.2, the RF sidebands do not experience the ~ 1 Hz low pass filter of the full coupled cavity resonance that the carrier does and so eliminating them would reduce the coupling from laser amplitude and frequency noise and of course, completely eliminate oscillator based noises.

Instead of reading out the signal by doing a phase modulation on the input beam, one can just shift the differential arm length slightly, yielding a first order change in the AS port power as a function of differential arm length.

There are a few other advantages to employing a DC readout:

- Exploring the possible space of modulation/demodulation waveforms [89], we know that the theoretical best SNR is achieved by using no modulation or demodulation.
- Even better than the fact that it is the theoretical best, is the fact that it guarantees perfect overlap between the local oscillator and signal fields: The

'LO' in this case is just the static carrier generated by the intentional arm length offset.

- Instead of all of the complicated electronics associated with an RF readout, one can just readout the DC power on the photodiode. With an Output Mode Cleaner this requires only a few mW total.

8.2 Estimating the future performance

In the past, predictions about the detectors' noise performance have had a mixed level of accuracy. It is certainly true, however, that the predictions have gotten more accurate as the noise is reduced and the instrumental characterization becomes more advanced.

Determining the ultimate sensitivity of the detectors is of great interest, since we would like to know sooner than later if some major upgrade or redesign will be required to reach the design sensitivity.

The initial LIGO design curve was made \sim 15 years ago, based upon the knowledge available at that time. Now that the interferometers are built we are able to make more accurate estimates of many of the parameters involved in generating these noise curves. There are three particularly important cases:

- The initial design noise curve was dominated at the \sim 150 Hz minimum by thermal noise in the mirrors. The loss in the mirrors appears to be 10X less than expected. This makes the thermal noise from the mirror substrate 3X less than the design.
- The interferometers' contrast defects are all 20-100X better than the conservative estimate made in the design. This gives a reduced level of shot noise which dominates above 200 Hz.
- After the initial design, it was recognized that the true mechanism for suspension thermal noise gave a steeper frequency dependence and so the suspension thermal noise contribution is much less above the pendulum resonance frequency.

As shown in Figure 8-1, I predict that the sensitivity of the initial interferometers will significantly surpass the design, as long as we are able to reduce the technical noise sources to their initial design levels and no unforeseen, insurmountable noise sources are discovered.

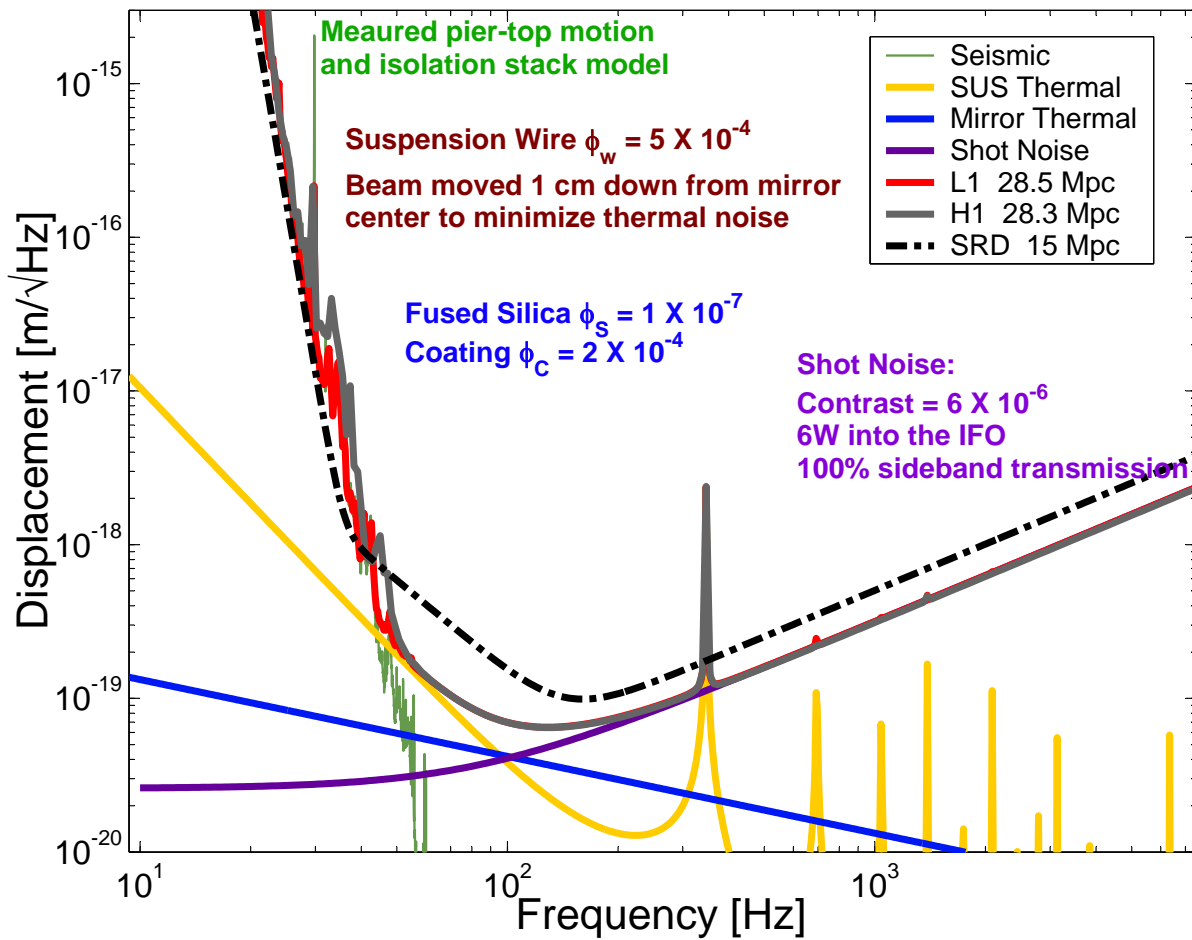


Figure 8-1: Best possible noise curve using the existing IFO components. The significant sensitivity improvements from using a DC readout and higher laser power are not shown.

Conclusion

The sensitivity of the LIGO interferometers continues to improve, almost monthly, due to a large concentrated effort by the detector commissioning team. The noise floor has been reduced by 6 orders of magnitude in the last few years and is now less than a factor of 10 away from the initial sensitivity goals.

Vital to the noise reduction effort has been the modeling of the interferometer's response to noise coming from all significant sources.

A simple analysis has been done of two months of data from one of the LIGO science runs for damped sinusoid signals. The sensitivity of the detectors to this type of signal was seen to be degraded by the non-Gaussian noise character of the interferometers and there are good ideas for future work.

A number of options have been outlined for near term upgrades to the interferometer. It is expected that implementing these fixes would let us exploit the true astrophysical reach of these instruments, surpassing the initial expectations of the sensitivity by a factor of 3.

Appendix A

Tables of Parameters

Physical Constants			
Parameter	Symbol	Value	Units
Speed of Light	c	299792458	m/s
Planck's Constant	h	6.6261×10^{-34}	J s
Boltzmann's Constant	k_B	1.380×10^{-23}	J/K
Electron Charge	e_c	1.602×10^{-19}	C
Gravitational Constant	G	6.674×10^{-11}	$\text{m}^3/\text{kg}\cdot\text{s}^2$
Fine Structure Constant	α	1/137.036	-
Stefan-Boltzmann Constant	σ_B	5.67×10^{-8}	$\text{W}/\text{m}^2/\text{K}^4$
Avogadro Constant	N_A	6.022×10^{23}	mol^{-1}

Table A.1: Values of constants from the NIST CODATA webpage [114]

Large Optic Parameters			
Parameter	Symbol	Value	Units
Specific Heat	c_H	740	J/kg
Refractive Index (@ 1064 nm)	n	1.45	-
Thermal Conductivity	k	1.38	$\text{W m}^{-1} \text{ K}^{-1}$
Young's Modulus (substrate)	Y_S	72.80	GPa
Young's Modulus (coating)	Y_C	100	GPa
Poisson Ratio	σ	0.170	-
Thickness (coating)	d_C	8×10^{-6}	m
Loss Angle (substrate)	ϕ_S	1×10^{-7}	-
Loss Angle (coating)	ϕ_C	2×10^{-4}	-
Density	ρ	2196	kg/m^3
Optic Radius	R_{LOS}	0.125	m
Optic Diameter	dia	0.250	m
Optic Thickness	h_{LOS}	0.100	m
Optic Thickness (BS)	h_{BS}	0.040	m
Optic Mass	m_{LOS}	10.5	kg
Optic Mass (BS)	m_{BS}	4.2	kg

Table A.2: Parameters for the optics are only approximate. There is an optic to optic variation in dimensions due to the varying wedge angles. Thickness is measured at the *thickest* point for all optics except the BS where it is measured at the *thinnest* point.

Description of Variables	
Variable Symbol	Description
P_{in}	Power into the interferometer
g_{cr}	Carrier amplitude recycling gain
g_{sb}	Sideband amplitude recycling gain
t_{sb}	Sideband transmission to the AS port from the IFO input
r_{cr}	Interferometer carrier reflectivity
r_c	Arm cavity carrier reflectivity
r'_c	Derivative of r_c w.r.t. cavity length
t_M	Michelson transmission for the sidebands
ω_m	Resonant sideband angular frequency
ω_{nr}	Non-resonant sideband angular frequency
\aleph	Optical gain pre-factor
Γ	Modulation depth in radians

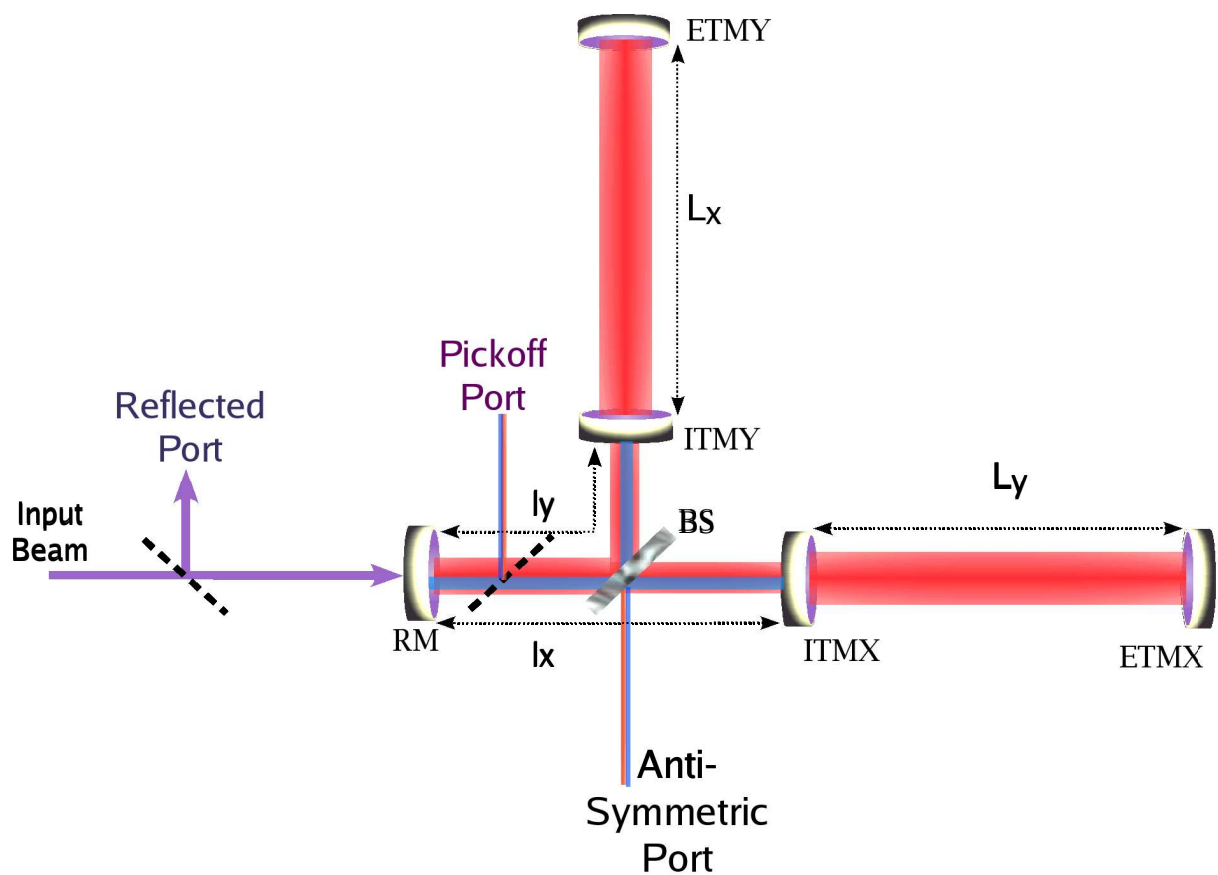
Table A.3:

DEFINITIONS of ACRONYMS	
ACRONYM	DEFINITION
RM	Recycling Mirror
BS	Beam Splitter
ITMX	Input Test Mass, X-Arm
ITMY	Input Test Mass, Y-Arm
ETMX	End Test Mass, X-Arm
ETMY	End Test Mass, Y-Arm
LSC	Length Sensing & Control
ISC	Interferometer Sensing & Control
PD	Photo-Detector
RFPD	Radio Frequency Photo-Detector
ASC	Alignment Sensing & Control
WFS	Wavefront Sensor
QPD	Quadrant Photo-Detector
SEI	Seismic Isolation
TCS	Thermal Compensation System
IOO	Input Output Optics
PSL	Pre-Stabilized Laser
FSS	Frequency Stabilization Servo
PMC	Pre-Mode Cleaner
ISS	Intensity Stabilization Servo
PC	Pockels Cell
MC	Mode Cleaner
OMC	Output Mode Cleaner
BSC	Barbecue Sauce Container
HAM	Horizontal Access Module
RGA	Residual Gas Analyzer
PZT	Lead Zirconate Tantinate
FAS	Fine Actuation System
PEPI	Piezo-Electric Pre-Isolator
HEPI	Hydraulic External Pre-Isolator
COC	Core Optics Components
MMT	Mode Matching Telescope
LVEA	Large Vacuum Equipment Area
SUS	Suspension
LOS	Large Optic Suspension
SOS	Small Optic Suspension
IIR	Infinite Impulse Response
FIR	Finite Impulse Response

Table A.4:

Appendix B

Definitions and Conventions



The interferometer output signals are naturally represented in basis which separates common and differential lengths:

$$\begin{aligned} L_+ &= \frac{L_y + L_x}{2} & L_- &= L_y - L_x \\ l_+ &= \frac{l_y + l_x}{2} & l_- &= l_y - l_x \end{aligned} \quad (\text{B.1})$$

It is a little awkward that there's a factor of 2 difference between how common and differential lengths are defined. It is this way because we generally are interested in the *average* of the two arms. On the other hand, in the literature, strain is usually defined as

$$h \equiv \frac{L_y - L_x}{L_+} \quad (\text{B.2})$$

Most of the conventions in this thesis for defining reflectivities, lengths, etc. follow [67]. They are restated here for convenience.

There is a convention followed for macroscopic lengths and microscopic lengths. The use of Δ or δ implies a microscopic deviation from resonance, whereas the lack of either implies a macroscopic length. The upper case, Δ , is used to imply a static or quasi-static shift from resonance. The lower case, δ , is used to denote a quantity fluctuating at AC, in the GW band.

The variable naming convention for reflection and transmission coefficients and cavity gain coefficients is that the lower case variables (r , t , and g) refer to amplitude coefficients and the upper case (R , T , and G) is for power. So, e.g. $R = r^2$.

On resonance, the amplitude reflectivity of an arm for the carrier is

$$r_c = \frac{r_{\text{ITM}} - r_{\text{ETM}}}{1 - r_{\text{ITM}} r_{\text{ETM}}} \quad (\text{B.3})$$

where r_{ITM} and r_{ETM} are the amplitude reflectivity of the Input Test Mass and the End Test Mass, respectively. For the LIGO interferometers, $r_{\text{ETM}} > r_{\text{ITM}}$, and so r_c is negative. So as the cavity shifts from off resonance to on resonance the reflected field gets a sign flip, but has nearly the same amplitude. This is because the leakage field from the cavity has \sim twice the amplitude but the opposite sign as the field promptly

reflected from the input mirror.

The RF sidebands are almost exactly anti-resonant in the arm cavities, so the reflectivity of the combined Fabry-Perot Michelson for the sidebands is determined entirely by the Schnupp asymmetry:

$$r_M = \cos \frac{2\omega_m l_-}{c} \quad (\text{B.4})$$

Also frequently used is, r'_c , the derivative of the arm cavity reflectivity with respect to the round trip phase, ϕ , evaluated at 2π :

$$r'_c = \frac{(1 - r_{\text{ITM}}^2)r_{\text{ETM}}}{(1 - r_{\text{ITM}}r_{\text{ETM}})^2} \quad (\text{B.5})$$

In Equations B.6, the amplitude transmission to the anti-symmetric port, the reflectivities for the entire interferometer, and the recycling cavity's recycling gains for the carrier and the sideband are defined.

$$\begin{aligned} t_{cr} &= 0 & t_{sb} &= \frac{t_{\text{RM}}t_{\text{M}}}{1 - r_{\text{RM}}r_{\text{M}}} \\ r_{cr} &= \frac{r_{\text{RM}} + r_c}{1 + r_{\text{RM}}r_c} & r_{sb} &= \frac{r_{\text{RM}} - r_{\text{M}}}{1 - r_{\text{RM}}r_{\text{M}}} \\ g_{cr} &= \frac{t_{\text{RM}}}{1 + r_{\text{RM}}r_c} & g_{sb} &= \frac{t_{\text{RM}}}{1 - r_{\text{RM}}r_{\text{M}}} \end{aligned} \quad (\text{B.6})$$

Also, since most of the measured signals are proportional to the product of the carrier and sideband field, a standard pre-factor is defined which is included in almost all of the sensing matrix elements:

$$\mathfrak{N} = 4J_0(\Gamma)J_1(\Gamma)P_{in} \quad (\text{B.7})$$

Appendix C

Mode Cleaner

The Mode Cleaner (MC) is a suspended, in-vacuum, triangular cavity. Its purpose is to condition the laser beam before it enters the main interferometer.

Specifically, it serves three purposes:

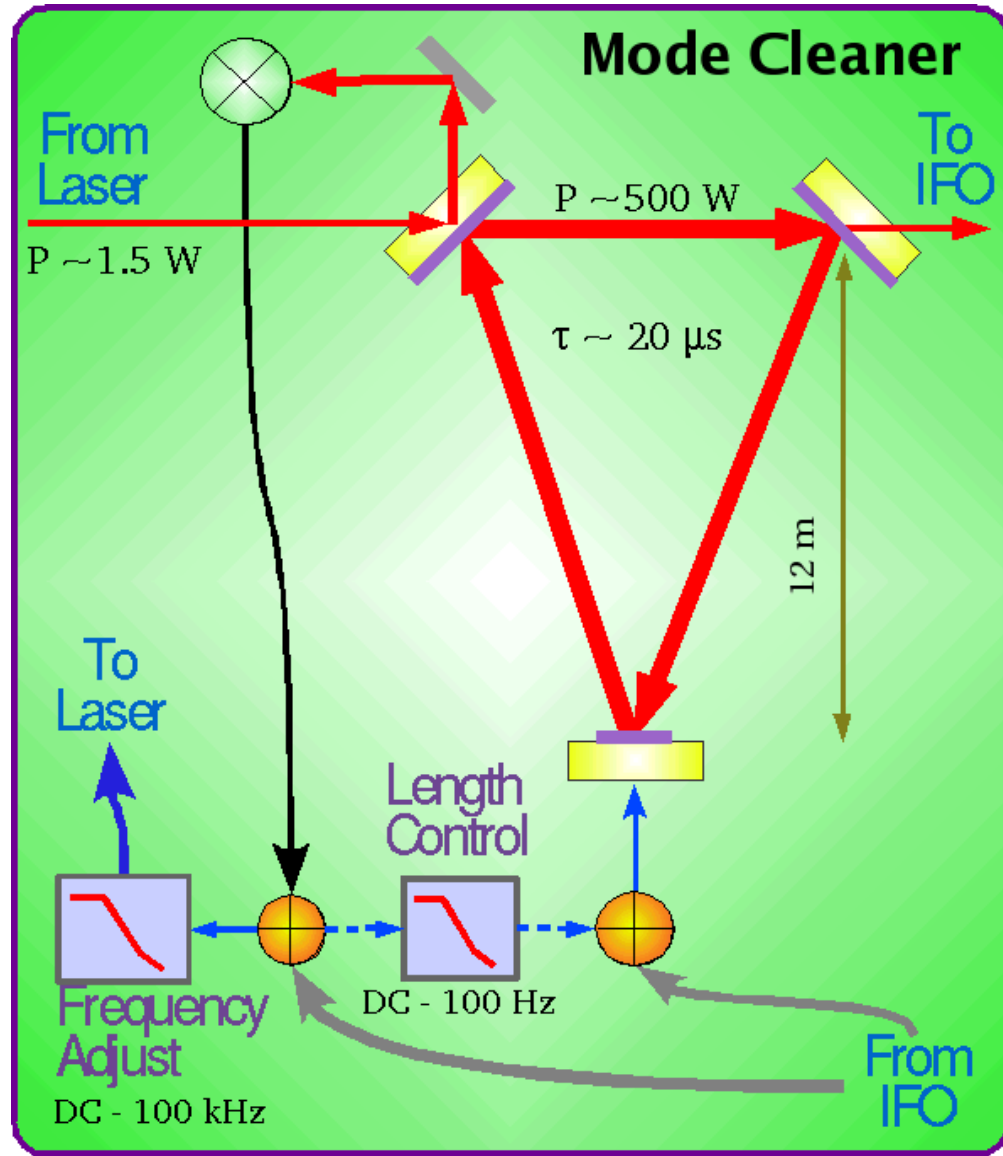
- It is called a mode cleaner because it is resonant only for a single transverse spatial mode. Higher order spatial modes experience a larger phase shift per each round trip and so fall out of the very narrow resonance. The effective frequency shift for the higher order modes is given by [115]:

$$\Delta f_{mn} = (m + n + 1) \arccos(g_{\text{MC}}) \frac{c}{2\pi L} \quad (\text{C.1})$$

Since we know the transmission as a function of frequency, we can easily write down the amplitude transmission as a function of mode index:

$$t_{mn} = \frac{1 - R}{1 + R^2 - 2R \cos(m + n) \arccos \sqrt{g_{\text{MC}}}} \quad (\text{C.2})$$

- The MC is also a very stable angular reference. Angular fluctuations of the input beam can be represented as higher order transverse modes of the MC cavity basis. So the input beam jitter is passively filtered out.
- The Mode Cleaner is used as a quiet length reference which the laser wavelength



is compared to in an intermediate stage of the interferometer's Common Mode Servo. (See Figure 5-6)

- The cavity passively filters laser frequency and amplitude fluctuations above the mode cleaner cavity pole, $f_{MC} \sim 4 \text{ kHz}$. The cavity's amplitude transmission response falls like $\sim 1/f$ for frequencies above the pole and below the next resonance frequency.
- Lastly, the mode cleaner is also a polarization filter. There is a 180 degree phase flip for horizontally polarized light relative to vertically polarized light.

This phase shift comes from the triangular geometry of the cavity. Tracing the propagation of the E-field vector in a single round trip makes this effect clear. In addition to this purely geometric effect, there can be a different phase shift upon reflection for light of the two polarizations. This phase shift has not been measured yet. The power transmission of the flat mirrors (MC_1 and MC_3) is 10X greater ($\approx 2\%$) for the horizontal polarization than for the vertical and so the Finesse of the cavity for horizontally polarized light is 10X less.

Small Optic Parameters			
Parameter	Symbol	Value	Units
Thickness (coating)	d_C	8×10^{-6}	m
Optic Diameter	dia	0.075	m
Optic Thickness	h	0.025	m
Optic Mass	m_{sos}	0.25	kg

Table C.1: Parameters for the optics are only approximate. Only parameters which are different from the large optics (see Table A.2) are listed. There is an optic to optic variation in dimensions due to the varying wedge angles. Thickness is measured at the *thickest* point for all small optics.

Mode Cleaner Parameters			
Parameter	Symbol	Value	Units
Plane mirror transmittance	T_{MC1}, T_{MC3}	2×10^{-3}	-
Curved mirror transmittance	T_{MC2}	1×10^{-5}	-
Cavity length	L_{MC}	12.243	m
Free Spectral Range	f_{fsr}	12.243	MHz
g - factor	g_{MC}	0.290	-
Finesse	\mathcal{F}_{MC}	1400	-
Cavity pole	f_{MC}	4000	Hz

Table C.2: Parameters for the suspended, in-vacuum Mode Cleaner cavity. The mirror transmittances, radii of curvature, and cavity g-factor are the designed parameters (not measured). All others are measured in-situ.

C.1 Noise

The mode cleaner length fluctuations must be kept low enough to not compromise the frequency noise stabilization. In addition, since the laser wavelength is stabilized to the mode cleaner in one stage of the frequency stabilization system, the mode cleaner length sensing noise must also be kept low.

As done for the main interferometer (in Chapter 4), the noise budget for the mode cleaner was made early on and used to motivate the design of the electronics associated with the mode cleaner.

The old requirement curve in Figure C-1 is based on the initial interferometer design which used a much more conservative frequency stabilization scheme. In the existing situation, there is more gain in the final servo stage which stabilizes the wavelength of the light transmitted by the mode cleaner to the average length of the arms. The new requirement curve, then, is relaxed by the amount shown in the plot.

C.1.1 Radiation Pressure

Fluctuations in the stored power of the mode cleaner cause length fluctuations through radiation pressure forces on the suspended mirrors. The effect is more significant in the mode cleaner than in the main interferometer due to the $40\times$ smaller mass of the mode cleaner mirrors.

To calculate the radiation pressure effect on the MC round trip cavity length we have to take into account the non-normal angle of incidence of the beam on the flat mirror surfaces (the angle of incidence on the curved mirror, MC2, is small enough to approximate as zero).

The change in the round trip length for small displacements of the MC mirrors (in the direction perpendicular to their respective surfaces) is

$$\delta L_{\text{RT}} \simeq \frac{2}{\sqrt{2}}\delta x_{mc1} + 2\delta x_{mc2} + \frac{2}{\sqrt{2}}\delta x_{mc3} \quad (\text{C.3})$$

The displacements of the MC mirrors resulting from a fluctuating circulating power are:

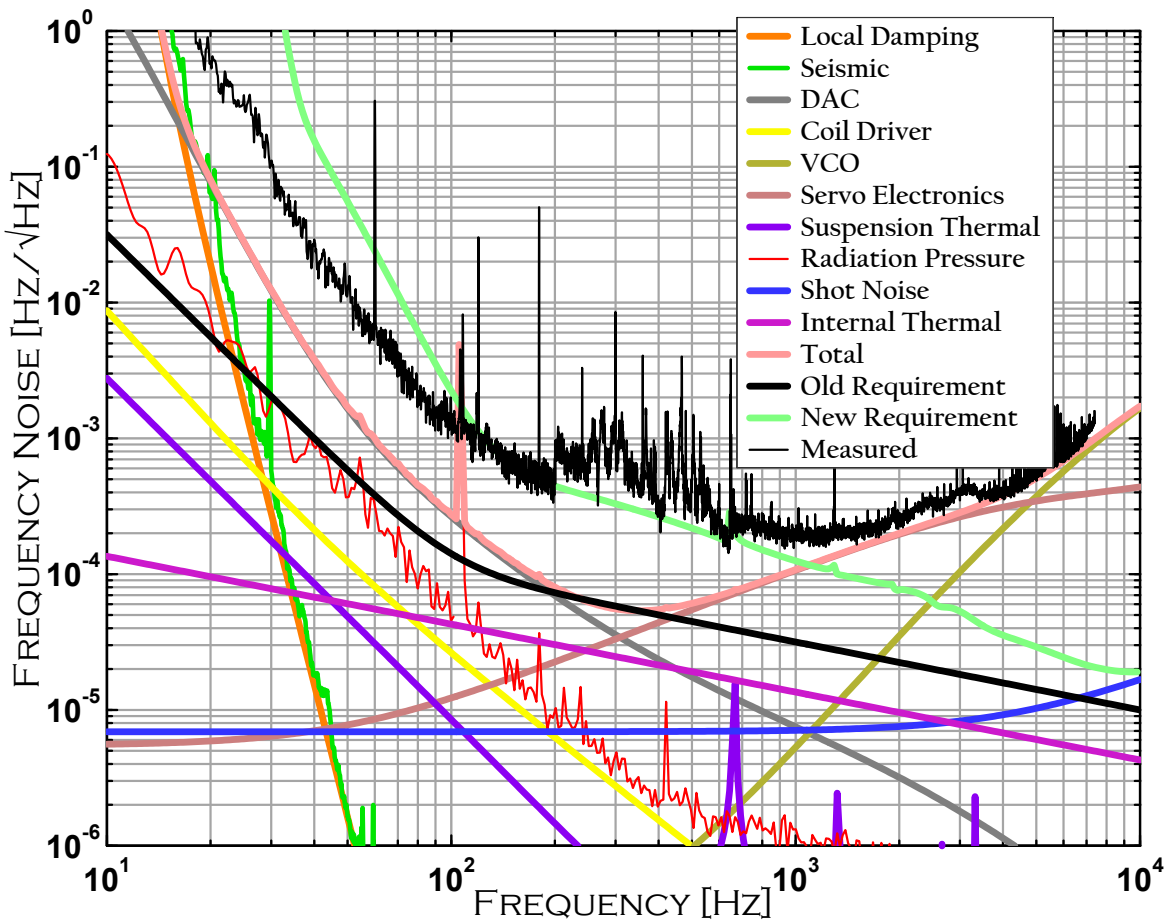


Figure C-1: Frequency noise spectrum of the light transmitted by the mode cleaner. The true output noise is measured by taking power spectra of the Common Mode Servo control signals and correcting appropriately for the CM loop gain.

$$x_{mc1} = \sqrt{2} \times \frac{\delta P_{circ}}{m c \omega^2} \quad (C.4)$$

$$\delta x_{mc2} = 2 \times \frac{\delta P_{circ}}{m c \omega^2} \quad (C.5)$$

$$\delta x_{mc3} = \sqrt{2} \times \frac{\delta P_{circ}}{m c \omega^2} \quad (C.6)$$

So then the corresponding change in the cavity length, ($L_{MC} \equiv L_{RT}/2$) is:

$$\begin{aligned}\delta L_{\text{MC}} &= 4 \frac{\delta P_{\text{circ}}}{mc f^2} \\ &\simeq 6 \times 10^{-19} \left(\frac{\text{RIN}(f)}{10^{-8}/\sqrt{\text{Hz}}} \right) \left(\frac{P_{in}}{1W} \right) \left(\frac{\mathcal{F}}{1400} \right) \left(\frac{100}{f} \right)^2 \frac{\text{m}}{\sqrt{\text{Hz}}}\end{aligned}\quad (\text{C.7})$$

C.1.2 VCO Phase Noise

The voltage controlled oscillator (VCO) which drives the acousto-optic modulator (AOM) used as a frequency shifter in the first stage of the frequency stabilization servo (FSS) has a phase jitter associated with the 80 MHz carrier with which the AOM is driven.

The phase noise is multiplied by 2 for the double pass of the beam through the AOM. The resultant noise is incident on the mode cleaner and is suppressed by the mode cleaner servo, giving it the shape seen in Figure C-1.

The double-pass frequency noise induced on the light by the VCO has been measured to be a flat level of $\sim 20 \times 10^{-3} \text{Hz}/\sqrt{\text{Hz}}$.

From Figure 5-10, we see that this noise source is far above the requirement for the MC's transmitted frequency noise. There are a few options on this front:

- Lower noise VCO (probably at the cost of dynamic range).
- Higher gain in the Mode Cleaner servo in the 3-10 kHz band.
- Higher gain in the Common Mode servo in the 3-10 kHz band.

C.1.3 Servo Electronics

Due to excess noise coming from the laser, the signal entering the MC servo board was too large and saturated the electronics (the op amps used had a low slew rate limit). Attenuating this signal heavily resulted in a high effective sensing noise level in this servo. The induced noise is suppressed somewhat by the servo loop gain.

This noise will be reduced by using faster, low-noise components and switching the filtering configuration to one that preserves the input referred SNR up to 10 kHz.

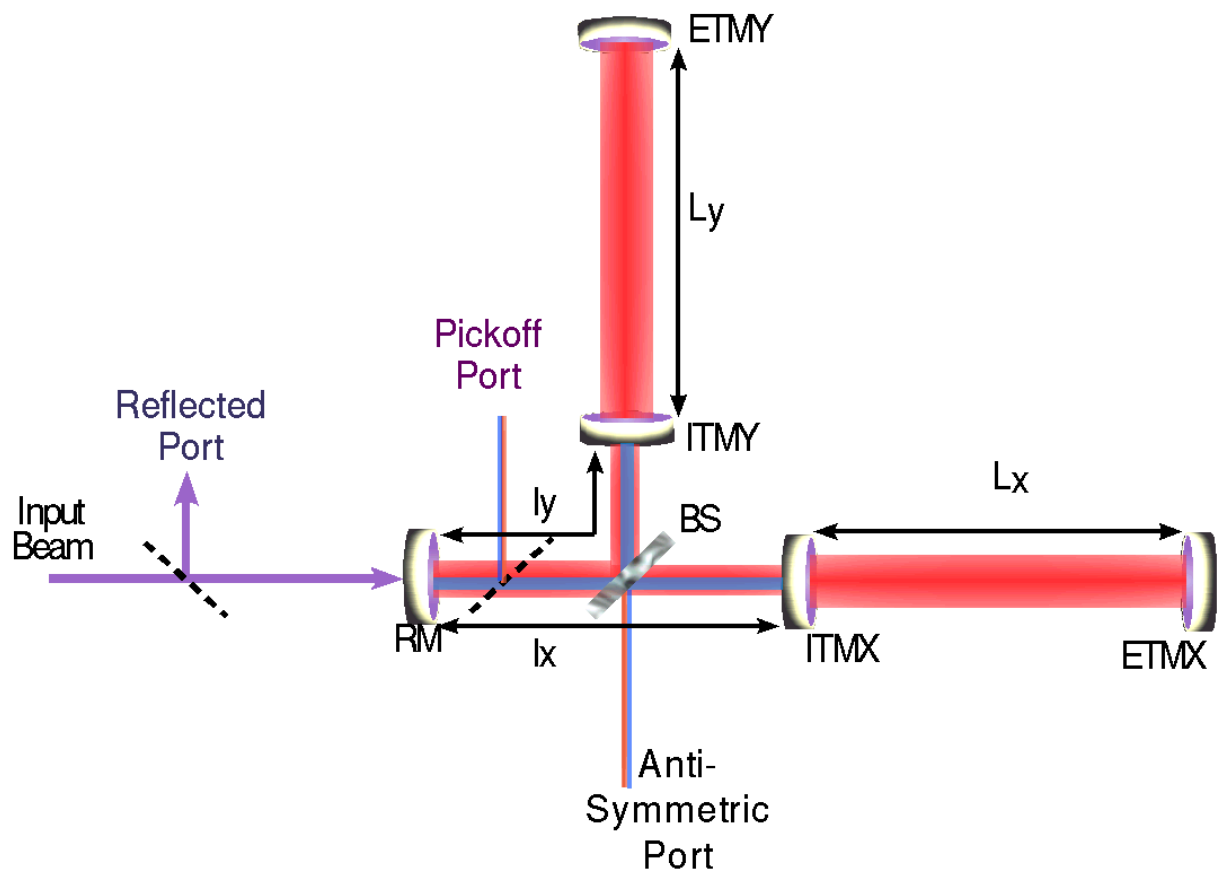
C.1.4 Acoustics/Clipping/Scattering

Just like in the main IFO, there is noise introduced into the MC sensing somewhere on the out-of-vacuum optics table on which the MC sensing optics and electronics are housed. There is evidence that this accounts for the rich, unmodeled structure in the noise in the 100-1000 Hz band.

As shown in Figure 5-10, the frequency noise on the light leaving the MC is too high above 100 Hz. In the 100-1000 Hz band, it will be necessary to pursue some mitigation of the acoustic sensitivity of the MC sensing chain; namely, some sound dampening foam and better alignment of the beam and expansion of some of the limiting optical apertures.

Appendix D

Lock Acquisition



This appendix briefly describes lock acquisition. To acquire lock means to take the interferometer from an uncontrolled state where the mirrors swing around and the interferometer 'flashes' through resonances to the 'locked state' where the light

is resonant in the interferometer and the length control loops have been switched on. The lock acquisition scheme is described in detail in Matt Evans' thesis [116] and in a related paper [117].

In this scheme, various power levels and servo error signals are used to estimate the field amplitudes for the carrier and sidebands at the 3 signal ports. These estimates are then used in the real time digital length control system to dynamically calculate coefficients of an input matrix. This input matrix is what takes the 6 demodulated outputs from the 3 signal ports and produces 4 servo error signals. The inputs to the matrix calculation (power levels, etc.) are acquired at 16 kHz and so the matrix is calculated at 16 kHz.

One of the chief difficulties in acquiring lock is the notion of a threshold velocity. The threshold velocity, v_t , is the velocity beyond which the chances of acquiring lock become small or when the Mean Time To Lock, MTTL, exceeds ~ 10 minutes.

It is easy to estimate this velocity for a single arm cavity given some of the optics' and electronics' parameters. In the limit of small velocities, as the cavity length sweeps through a resonance, there is enough time for the field to build up to a steady-state inside. In this limit, the cavity's error signal will be mostly linear in the region around the resonance and we can define a fringe width, x_{fringe} , as

$$x_{\text{fringe}} = \frac{\lambda}{2\mathcal{F}} \quad (\text{D.1})$$

which is $\approx 3 \times 10^{-9}$ meters for the LIGO arm cavities. Since the distance is so small we can also approximate the mirror velocity as being constant throughout the fringe crossing and then say that the crossing time is just, $t_c = x_{\text{fringe}}/v_t$, at the threshold velocity.

The other factors which determine the threshold velocity have to do with the control system:

- What is the maximum force that the control system can apply to the mirror?
- How fast is the control system triggered when the cavity approaches resonance?

To lock, the linear momentum of the mirror must be reduced far enough that the

cavity stays resonant long enough for the field to build up. In the case of a single arm, this condition is trivially met since the cavity time constant is of order 1 ms. In the case of the full interferometer, the relevant time constant is that of the coupled cavity resonance which is more like 1 second. To a good approximation this means that the mirror momentum must be reduced to zero. The momentum change effected by a constant force is $\Delta p = F t_c$. Combining this with the expression for the threshold velocity, we an expression for, F_{req} , the required force:

$$F_{req} = \frac{mv}{t_c} = \frac{mv^2}{x_{\text{fringe}}} \quad (\text{D.2})$$

Equation D.2 highlights very simply why the interferometers' duty cycles are so sensitive to seismic noise. Since the threshold velocity goes like the velocity squared, a slight noise increase can make the average required force exceed the limits of the electronics and push the interferometer into the realm where the MTTL = hours. This exceeds the patience of even the most devoted interferometrist.

As shown in Section 4.1.4, the coil driver for the optic could output a maximum current of $150V/160\Omega \simeq 1$ Ampere. To protect the actuator coil from overheating, the amplifier has been limited to a maximum impulsive current of 400 mA (and a slow blow fuse to prevent extended operation above 150 mA). With four coils, each having a force coefficient of 0.016 N/A, we get that the maximum applicable force is ~ 25 mN. This gives a threshold velocity of ~ 4 microns/second.

The other factor is the delay between the time the cavity approaches resonance and when the servo turns on and pushes the mirror in the direction which slows it down. The light level from a single arm cavity resonance is $\approx 1000X$ smaller than the level of the light during the full interferometer lock. This makes the SNR small enough that the trigger threshold for acquisition has been set to 10-15% of the single arm level and a digital filter is employed to reduce the sensitivity to the high frequency electronics noise. The result is a delay in the lock acquisition turn on process and an overall increase of the MTTL.

Appendix E

Cavity Formulas

A useful set of basis functions for representing laser beams in cavities is in terms of the Hermite-Gaussian modes [57]:

$$\Psi_{mn}(x, y, z) = \frac{1}{z + iz_R} \sqrt{\frac{2z_R}{2^{m+n} m! n! \lambda}} H_m\left(\frac{\sqrt{2}x}{w(z)}\right) H_n\left(\frac{\sqrt{2}y}{w(z)}\right) \times \exp\left[-i\frac{x^2 + y^2}{z + iz_R} \frac{k}{2} + i(m + n + 1) \arctan\left(\frac{z}{z_R}\right)\right] \quad (\text{E.1})$$

Here the $H_l(\eta)$ are the Hermite polynomials of order l . A characteristic scale at which the beam size has increased by $\sqrt{2}$ is z_R , the Rayleigh range and it is defined as $z_R = \pi w_0^2 / \lambda$. The equation describing the expansion of the beam is

$$w(z) = w_0 \sqrt{1 + (z/z_R)^2} \quad (\text{E.2})$$

where w_0 is the minimum in the beam size, similar to the focus in geometric optics. $w(z)$ is defined as the 1/e point in field for a pure Gaussian beam, i.e. the lowest order, TEM₀₀, Hermite Gaussian mode.

Appendix F

Characterization of the Optical Parameters

This Appendix describes characterization of many of the optical parameters of the interferometer, including lengths, losses, reflectivities and the cavity time constants and build-up factors.

F.1 Cavity Length Measurements

There are 4 primary lengths which are controlled. In addition to the microscopic lengths, the macroscopic absolute lengths of these degrees of freedom must also be set. Typically, this is done to the accuracy of the initial surveying techniques.

After the interferometer was running we measured these lengths interferometrically and then adjusted the lengths accordingly.

F.1.1 Arm Cavity Lengths

The nominal arm lengths are 3995.15 meters. This was initially set by reference to the GPS satellites [118]. We then determined the arm lengths interferometrically by measuring the frequency between successive resonances. We did this by applying a frequency modulation to the laser, generating a set of frequency sidebands on the

carrier field. We then did a swept sine measurement between the laser excitation and the response in the reflection locking signal for each arm individually. Measurements made in November of 2003 for L1 gave:

$$L_x = 3995.032 \text{ m} \quad L_y = 3995.001 \text{ m}$$

This took place after the translation of ITMY to correct the lengths of the power-recycled Michelson. The ITMY was moved 4 cm closer to beamsplitter and so lengthened the y-arm. This appears to imply that the arm lengths were ≈ 7 cm different before the summer of 2003 (which includes S1 & S2).

Even more accurate measurements of arm length were made on the Hanford 4 km interferometer [119] using a more sophisticated optical model of the interferometer and a rubidium frequency standard. This resulted in arm length measurements with a precision of $80 \mu\text{m}$, which is less than the daily stretching of the arm by the tidal gravitational force from the moon.

F.1.2 Schnupp Asymmetry

The macroscopic difference in the two Michelson lengths l_y and l_x determines the transmission of the resonant sidebands to the dark port: $t_M = \sin(\frac{2\pi f_m l_-}{c})$.

This length difference is measured by finding the dark port demodulation phase appropriate for each arm cavity separately. The difference in RF phase for the two arms comes only from the different path length traveled by the sideband to the AS port.

Typically, these measurements achieve an absolute accuracy of $+/- 1$ mm in this length. There have not been significant efforts to improve on this accuracy and there does not seem to be any reason to do so.

There was an error in the initial calculation to set this length for both 4 km interferometers, with the result that the asymmetry was too small by ~ 4 cm. This was corrected by venting the corner station vacuum and moving the optics' suspension towers in the summer of 2003 between the S2 & S3 runs.

F.1.3 Recycling Cavity Length

The average length between the power recycling mirror (RM) and the two input test masses (ITMs) is defined as the macroscopic length, l_+ . It is chosen to make the recycling cavity resonant for the resonant sidebands (hence the name).

Hypothetically, a gross error in the placement of one of the mirrors (e.g. the RM) would shift the resonant frequency of the cavity. This would result in a reduced build up for both the carrier and the sidebands. Two methods have been used to measure this length:

The first method was to misalign the RM, ETMX, and ETMY, forming a simple Michelson interferometer. The differential Michelson length signal at the AS port then appears in only one demodulation quadrature. This phase is recorded and then measured again when the full interferometer is locked by driving the differential arm length.

The difference in the RF phase between the two states gives a measure of how much the RF sidebands have been phase shifted upon transmission through the resonant power-recycling cavity. If the power recycling cavity length (l_+) is not an integer multiple of $c/(2f_m)$, there will be a differential phase shift applied to the upper and lower RF sidebands as they transmit to the AS port.

F.1.4 Mode Cleaner Length

The mode cleaner length is set to be resonant for the interferometer's resonant sideband. The non-resonant sideband frequency, f_{NR} , is then set to be a multiple of the mode cleaner free spectral range (see Table C.2), but not resonant in the power recycling cavity.

F.2 Transmissivity, Reflectivity, and Loss

None of the optics have exactly the same transmissivity as was asked for or measured in the metrology lab, but they're pretty close mostly. The AR coating reflectivities

seem to be as much as 10X different than their lab measured values.

While disturbing, we can use this to our advantage by using the most powerful pickoff in the control loops for the l_- and l_+ lengths.

F.2.1 Common arm loss via recycling gain

The carrier power recycling gain is given by the following formula:

$$G_{cr} = |g_{cr}|^2 = \left[\frac{t_{RM}}{1 + r_{RM}r_c} \right]^2 \quad (F.1)$$

where r_c is the average amplitude reflectivity of the arms for the carrier. By modifying Equation B.3 to include a finite loss upon reflection from the arm cavity mirrors we get:

$$r_c = \frac{r_{ITM} - \sqrt{1 - T_{ETM} - L}}{1 - r_{ITM}\sqrt{1 - T_{ETM} - L}} \quad (F.2)$$

which gives the handy approximate relation $(1 - r_c) \approx 1\%(L/140\text{ppm})$ for small losses. Here L is defined as the round trip *power* loss in the arm cavity, including the ETM transmission, but not the ITM transmission.

The measured power recycling gain factor of ≈ 50 gives us an average arm loss of 140 ppm, or 70 ppm per mirror.

F.2.2 Differential arm loss via PRC to AS_Q & CMRR

Several pernicious noise sources highlighted in Chapter 4 are proportional to the amplitude of the TEM_{00} carrier field at the AS port which is in the orthogonal phase from the carrier field produced by a differential arm length offset.

Another way to describe this is that a differential arm length shift causes the carrier fields interfering at the beamsplitter to have a relative phase shift. The AS_Q signal is *not* first order sensitive to an amplitude difference in the two fields, and so the L_- servo does not null this component of the carrier field. This amplitude unbalance can only come about through a difference in the resonant reflectivity of

the arms.

As described above, the measurement of the cavity reflectivity gives a measure of the loss in the arm. By calibrating the frequency noise coupling and the $l_+ \sim AS \cdot Q$ coupling (see Sections 4.2.2 and 4.2.6, respectively) we know that the difference in the resonant reflectivity of the two arms, δr_c is 0.5%. This corresponds to a differential loss of 70 ppm between the two arms for the Livingston interferometer. Similar measurements done on the Hanford 4 km interferometer give roughly the same average loss but a factor of ~ 2 less differential loss.

F.2.3 T_{ITM}

The transmission of the ITM (≈ 0.028) is the dominant loss in the arm cavities. To determine the exact number, we measure the decay time of the arm cavities by quickly switching off the light incident on the interferometer.

The best way to quickly shut off the light is to very quickly shift the laser frequency with the FSS by electronically changing the sign of the servo [120]. The switch off time is then dominated by the time constant of the in-vacuum Mode Cleaner ($\approx 20 \mu s$ decay time).

F.2.4 T_{ETM}

T_{ETM} is measured by directly measuring the power transmitted through the end of the arms with the interferometer locked. The circulating power in the arm is measured through two methods: by using the known arm cavity build up factor and the carrier recycling gain or by looking at the radiation pressure offset induced on the ITMs (which are free to move at DC).

F.2.5 $R_{BS} - T_{BS}$

Almost all of the calculations so far in this thesis have assumed that the Beamplitter is truly a 50/50 beamsplitter; that $R_{BS} = T_{BS}$. One known consequence of this, an increased radiation pressure coupling, was discussed in Section 4.1.3.

There are no first order offsets introduced at the AS port from this effect, however. Neglecting radiation pressure, all of the fields at the AS port depend on the product ($r_{BS} t_{BS}$) and not on the difference.

F.3 Contrast

To have good sensitivity at high frequencies, the interferometer must be shot noise limited. The shot noise limit must also be low to have a good sensitivity, as described in Section 4.2.7.

The contrast measurements to date have been made by measuring the recycling gain for the carrier, the sideband power at the AS port, and then the total power at the AS port. The contrast defect, c_d , is then defined as:

$$c_d = \frac{P_{AS}}{P_{BS}} = \frac{P_{AS}}{G_{cr} P_{in}} \quad (\text{F.3})$$

where P_{BS} is the total carrier power on the beamplitter and P_{AS} is the total carrier power at the anti-symmetric port.

The contrast defect in the Livingston interferometer has been measured to be $c_d < 4 \times 10^{-5}$. This is an upper limit; the angular fluctuations of the interferometer kept the dark port power fluctuating by an order of magnitude over minute time scales.

F.4 Metrology

All of the optics metrology data is available at Core Optics website [82] and interesting related comments in an internal LIGO technical report [121].

Appendix G

Interferometer Sub-Systems

This appendix has some very brief descriptions of the various subsystems of the interferometer.

G.1 Core Optics

The main interferometer mirrors are monolithic fused silica (SiO_2) masses. They are 25 cm in diameter and 10 cm thick. Their mass is ≈ 10.5 kg.

The fused silica substrates were supplied by Corning. The polishing was done by General Optics and CSIRO. The mirrors were then coated by Research Electro-Optics with alternating Ta_2O_5 and SiO_2 layers. Each layer is one quarter wavelength thick.

Extensive metrology was done to establish that the various physical properties of the mirror are within the design specification: reflectivities, absorption, surface figure, and surface roughness.

G.2 Suspensions

All of the critical in-vacuum optics in LIGO are each suspended by a single wire loop [122] of steel music wire. The large optics are suspended by wire of ≈ 300 micron diameter and the small optics by ≈ 40 micron wire. Figure G-1 shows a schematic diagram (from [79]) of the suspended optic.

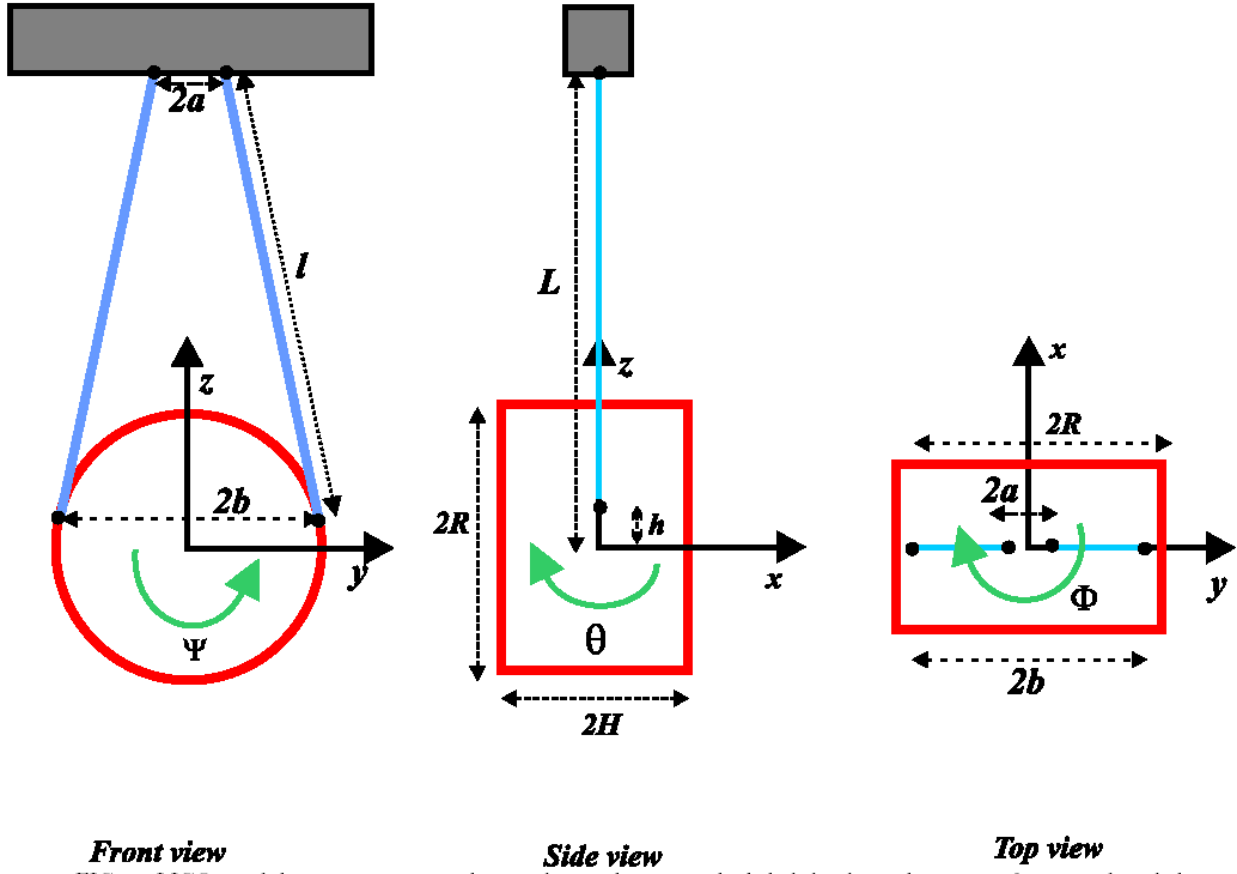


Figure G-1: A Schematic Diagram of the LIGO Suspensions.

G.2.1 Local Sensing and Actuation

Five coil/magnet pairs are used to actuate the optic in four degrees of freedom. There are six magnets attached to the optic; one each on the sides (the x-y origin in Figure G-1) and four on the Anti-Reflection (AR) coated side arranged in a square pattern. Each of the magnets is glued first to a small aluminum "dumbbell". The other end of the "dumbbell" is glued to the optic. Each magnet/dumbbell pair is equidistant from the center of the AR face so that the magnet pattern forms a square circumscribed by the circular edge of the optic face.

A 2.5 cm dia. ceramic head attached to the suspension cage is used to sense the magnet's axial position as well as generate magnetic field for the actuation. An LED operating at 880 nm illuminates a small photodiode. The LED/PD pairs are positioned so that in the optic's free hanging position, all magnets occlude half of

the LED light incident on the PD. The sensors have a linear range of ≈ 1 mm and a shot noise limited sensitivity of $\approx 1 \times 10^{-10} \text{ m}/\sqrt{\text{Hz}}$ each, above 40 Hz. Summing the four face sensors to make a positional super-sensor gives a slightly better noise floor of $\approx 0.5 \times 10^{-10} \text{ m}/\sqrt{\text{Hz}}$.

The two side magnets' dipole moments are anti-parallel to reduce the coupling between external magnetic fields and optic motion. The four face magnets are arranged so that each diagonal pair has parallel magnetic moments.

Each ceramic head has also a coil wound onto it through which current can be sent to apply forces to control the optic motion.

G.3 Seismic Isolation

There are also two type of seismic stack. All of the main interferometer optics excluding the recycling mirror are on a 4-layer mass-spring stack. The recycling mirror and all of the input and output optics are on a 3-layer stack. Figure G-2 shows a cutaway diagram of the 4-layer variety and its placement relative to the vacuum chamber.

G.4 Pre-Stabilized Laser

Before the laser beam enters the interferometer it is conditioned in several ways by both in-vacuum and out of vacuum optics.

The Pre-Stabilized Laser (PSL) sub-system consists of: the 10 W CW Nd:YAG laser, a fixed reference cavity for frequency stabilization, a triangular, 'pre-mode cleaner' cavity which passively filters laser noise above 1 MHz, and an intensity stabilization servo which actively quiets laser power fluctuations below 100 kHz.

G.4.1 Laser

The interferometer is illuminated by a Master-Oscillator, Power Amplifier (MOPA) style Nd:YAG laser which has a nominal output power of 10 W [123]. The laser was

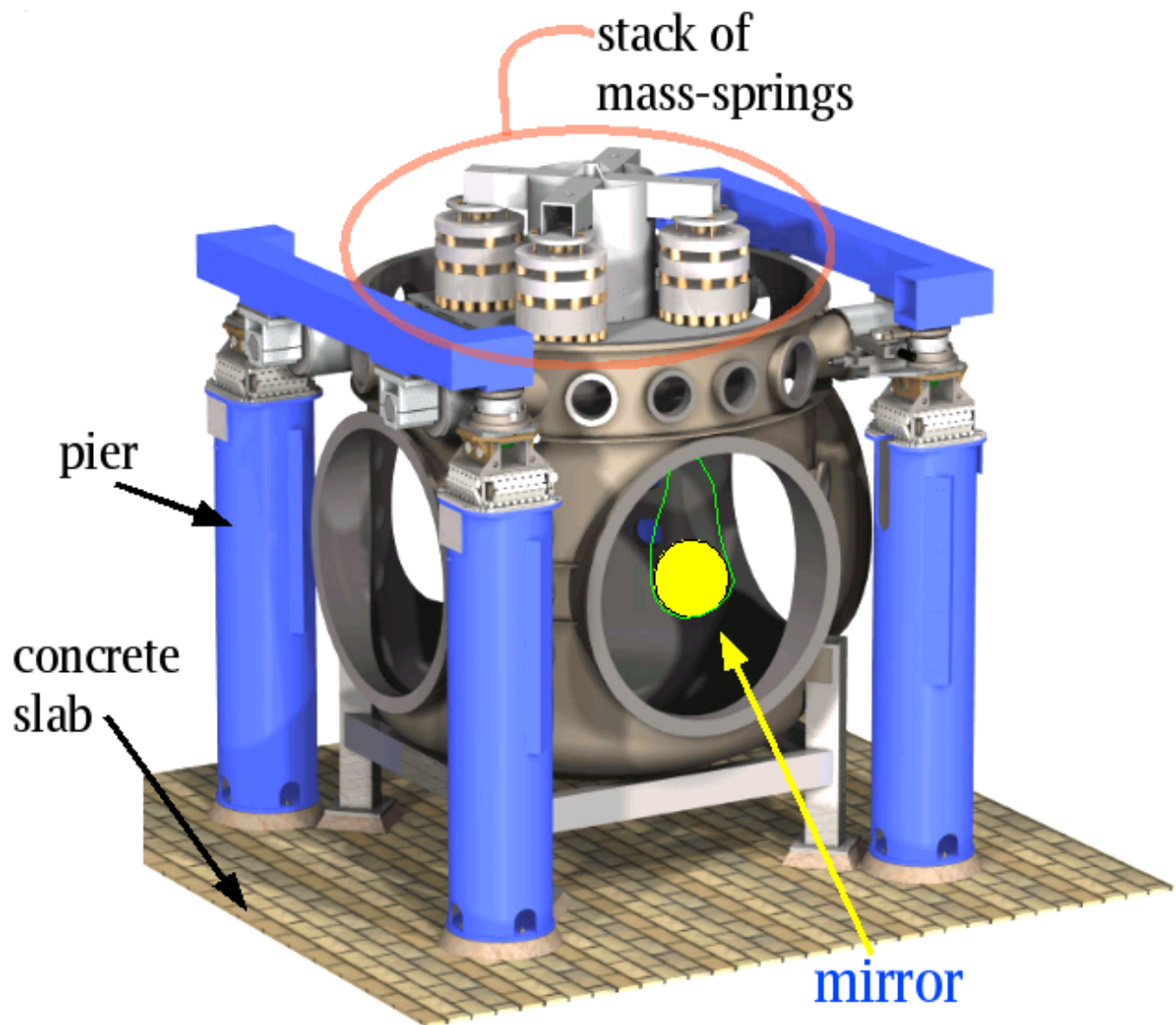


Figure G-2: A Schematic Diagram of an isolation stack.

purchased from Lightwave Electronics ¹. It uses a Model 126-1064-700 NPRO (Non-Planar Ring Oscillator) as the master oscillator and a double pass through a set of Nd:YAG rods for the amplifier.

G.4.2 Frequency Stabilization Servo (FSS)

The purpose of the Frequency Stabilization Servo (FSS) is to suppress the frequency (phase) fluctuations of the laser from 0-100 kHz and to provide a wide bandwidth

¹ <http://www.lwecorp.com>

frequency actuator for inputs from the main interferometer. The place of the FSS within the interferometer's overall frequency stabilization scheme is shown in Figure 5-6.

AOM

A small fraction (~ 10 mW) of the laser light is picked off and locked to a fixed reference cavity after double passing through an Acousto-Optic Modulator (AOM) as shown in Figure 5-6. The AOM is just a crystal with a PZT bonded to it. The PZT is driven at 80 MHz by a high power RF source to set up a standing acoustic wave in the crystal. The varying density fluctuations in the crystal act like a transmissive diffraction grating. The resulting first order diffracted beams have a frequency shift relative to the incident carrier which is equal to the RF drive frequency. The spherical mirror catches only the first-order beam (the +1 beam in the diagram) and redirects it to the crystal where it gets diffracted again, but this time along back along the path of the incident carrier. The light which finally gets to the reference cavity has experienced a frequency shift equal to twice the AOM drive frequency.

Reference Cavity

The reference cavity is a 200 mm long, monolithic, fused silica cylinder, with mirrors of equal reflectivity optically contacted onto each end. The entire cylinder is suspended by springs from a set of posts mounted to a stack of stainless steel plates. The three plates are separated by RTV (Room Temperature Vulcanizing) silicone spacers which act as springs to provide further seismic isolation. The pendulum mode resonance of the cavity/spring system is damped by eddy current damping between the cavity and the first stack layer. This entire assembly is mounted in a small (~ 1 m) vacuum chamber which is pumped down to an ultra-high vacuum by an ion pump.

The cavity must be isolated from the environment well enough to serve as a quiet wavelength reference. The total frequency noise coming out of the FSS is dominated by sources other than the cavity displacement noise: acoustic band vibrations of the steering optics on the optical table (80 mHz/ $\sqrt{\text{Hz}}$ at 50-1000 Hz) and electronics noise

in the VCO driving the AOM ($20 \text{ mHz}/\sqrt{\text{Hz}}$, broadband). From these measurements of the output noise of the FSS system, we can place an upper limit on the reference cavity displacement noise

$$\delta x < \left(\frac{20 \text{ mHz}/\sqrt{\text{Hz}}}{3 \times 10^{14} \text{ Hz}} \right) \times (L_{RefCav} \approx 20\text{cm}) \quad (\text{G.1})$$

which is $\sim 5 \times 10^{-17} \text{ m}/\sqrt{\text{Hz}}$.

As shown in Appendix C, the frequency noise coming out of the FSS is not a significant component of what actually gets to the interferometer since the Mode Cleaner is able to suppress the FSS noise enough below a few kHz. Further work needs to be done in the $\sim 3\text{-}7$ kHz band on either the VCO noise or the MC servo gain in order to meet the requirement for the frequency noise incident on the interferometer.

G.4.3 Pre-Mode Cleaner (PMC)

The PMC is a triangular ring cavity made by optically contacting three mirrors to a rigid, fused silica spacer. The main purpose of this cavity is to passively filter amplitude and phase fluctuations of the laser at the resonant sideband frequency (~ 25 MHz) which is used for the gravitational wave readout. The in-vacuum Mode Cleaner must transmit these sidebands and so it provides no filtering of noise at this frequency. Since there are no active stabilization servos with enough bandwidth to act at 25 MHz, the PMC must do all of the filtering.

The PMC has a cavity pole at ~ 1 MHz, reducing the laser noise by a factor of 25 at the sideband frequency.

G.4.4 Intensity Stabilization Servo (ISS)

The ISS senses a fraction of the laser power and feeds back the AC component of this signal to the laser, in order to suppress power fluctuations from 1-100,000 Hz. The feedback actuator is a current shunt [124] which modulates the current going into the laser diodes which pump the MOPA's power amplifier. This actuator has a ~ 2 kHz bandwidth.

Based upon the requirements for the laser intensity noise described in Section 4.2.1 and the intensity noise trace in Figure 4-11, we know that the existing servo is not sufficient to allow interferometer operation at the designed noise level.

A new servo with more gain and dynamic range is currently being designed. It is expected that the new servo will suppress the laser intensity noise contribution to below 1/10 of the Science Requirement.

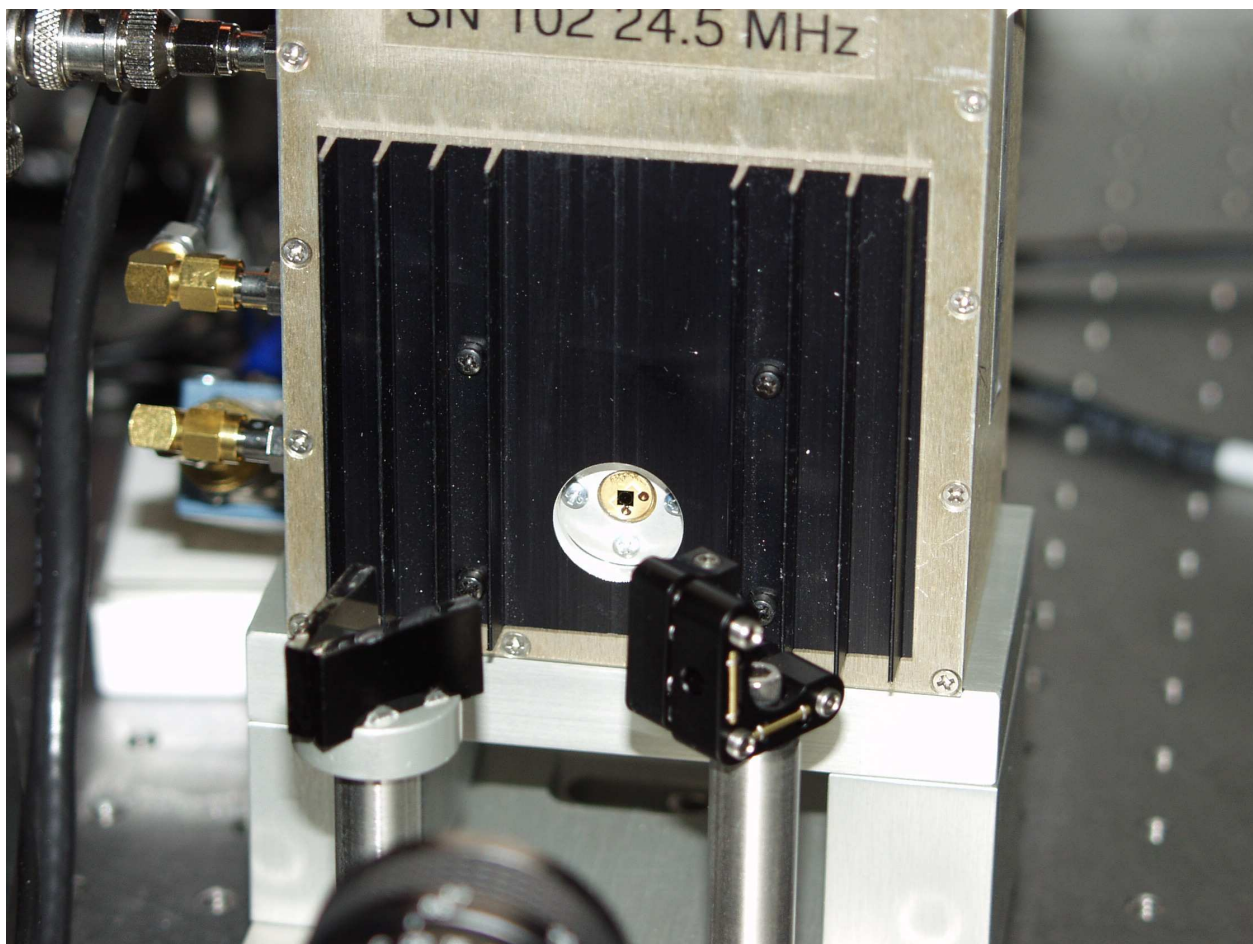
G.5 Input Optics

The Input Optics sub-system consists of three major components:

- Modulators. The phase modulation sidebands used to sense the interferometer lengths and angles are applied by passing the beam through commercial (New Focus Model 4003) Pockels cells made of MgO:LiNbO₃ crystals. A tunable inductor is attached to the crystal to form a resonant LC circuit with the crystal capacitance at the modulation frequency.
- A Mode Cleaner (detailed in Appendix C)
- Faraday Isolator. An in-vacuum Faraday rotator is mounted rigidly to the top of a HAM isolation stack between the suspended Mode Cleaner and the suspended Mode Matching Telescope.
- Mode Matching Telescope. This suspended, three mirror telescope expands the beam exiting the Mode Cleaner and matches it to the resonant mode of the interferometer arms.

Appendix H

The Photodetectors



The photodiode in the photodetector is a an EG&G Canada Ltd., C30642G In-GaAs PIN photodiode. It has a circular active area with a 2 mm diameter and is

mounted in a TO-5 package with a built in glass window. The window has been removed with a can opener to reduce scatter losses from the glass surface.

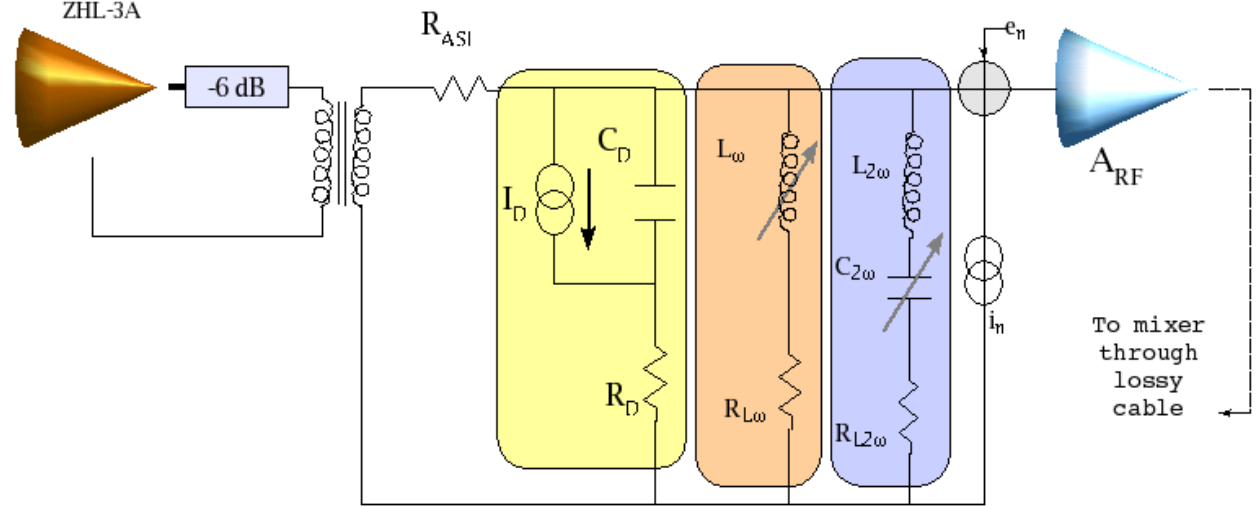


Figure H-1: The yellow region is the equivalent photodiode. The $L_\omega C_D$ resonance made with the inductor in the orange region is tuned to the resonant sideband frequency ($f_m \approx 24.5$ MHz). The $L_{2\omega}$ - $C_{2\omega}$ notch is tuned to dump the $2 f_m$ photocurrent. e_n and i_n are the equivalent noise generators associated with the input of A_{RF} (the MAX4107 RF Amplifier)

The photodetector circuit is shown in Figure H-1. The photodiode is modeled as a current source in parallel with a capacitance. Not shown in the diagram are circuits to read out the DC diode current and to dynamically adjust

The transimpedance, $Z(\omega)$, of the circuit is given by

$$\frac{1}{Z(\omega)} = \frac{1}{R_D + \frac{1}{i\omega C_D}} + \frac{1}{i\omega L_\omega + R_{L\omega}} + \frac{1}{R_{L2\omega} + \frac{1}{i\omega C_{2\omega}} + i\omega L_{2\omega}} \quad (\text{H.1})$$

The total voltage noise, e_T , referred to the non-inverting input of the amplifier is

$$e_T^2 = e_n^2 + i_n^2 Z_R^2 + 4k_B T Z_R \quad (\text{H.2})$$

where $Z_R \equiv Z(\omega_m)$.

H.1 AS_I Servo

The path to lower noise above a few hundred Hz has always involved putting more light on the photodetectors. Before the first science runs, it was noticed that the dynamic range of the photodetector circuit was being exceeded with light levels $\sim 100X$ smaller than the detectors were designed for.

This was due to a large signal at the anti-symmetric port in the orthogonal RF phase (AS_I) to the one which contains the gravity wave signal (AS_Q). This AS_I signal produced a large RF current at f_m , saturating the MAX4107 pre-amplifier shown in Figure H-1. The mechanisms to generate the AS_I signal are discussed in Section 3.3.

There was no practical way to null this signal optically and so a circuit was designed to null the signal electronically by adding in an RF current through a test input. The AS_I is digitally filtered and used to drive the IF port of a double-balanced mixer (Mini-Circuits ZP-3MH). The LO port of the mixer was driven into saturation by the same LO signal used to demodulate AS port RF signal. The RF port of the mixer is then an RF signal, amplitude modulated by the IF signal. The signal was sent through a high power RF amplifier (Mini-Circuits ZHL-3A), a bandpass filter to reject harmonics of the RF carrier and injected into the photodetector circuit through a step-up transformer as shown on the left hand side of Figure H-1.

At the time of this writing, the amount of detectable power at the AS port and the high frequency, shot noise limited sensitivity of the interferometers is limited by the size of the AS_I signal.

Photodiode Parameters			
Parameter	Symbol	Value	Units
Responsivity (@ 1064 nm)	R	0.80	A/W
Quantum Efficiency	η	0.95	-
Active Area	A	π	mm ²
Diode Capacitance (10 V Bias)	C _D	75	pF
Diode Resistance	R _D	11	Ω
Tuned Inductance	L _{ω}	0.4	μH
Tuned Inductor Resistance	R _{Lω}	1	Ω
Trap Inductance	L _{2ω}	0.5	μH
Trap Capacitance	C _{2ω}	20	pF
Trap Inductor Resistance	R _{L2ω}	5	Ω
RF Pre Amplifier	A _{RF}	MAX4107	-
MAX4107 Voltage Noise @ 100 Hz	e _n	1.3	nV/ $\sqrt{\text{Hz}}$
MAX4107 Current Noise @ 100 Hz	i _n	4	pA/ $\sqrt{\text{Hz}}$
AS.I Servo Resistor	R _{ASI}	500	Ω

Table H.1: These are the nominal parameters for the photodetector.

Appendix I

Antenna Response

An important consideration to make in evaluating the sensitivity of any detector is its directional response. The directional antenna response of an interferometer is derived in [125] and [18].

From Equation 1.2 we have the form for the strain perturbation tensor in the detector's coordinate system for a wave incident on the detector from the positive z-direction. The strain along the interferometer arms for a source from an arbitrary direction is

$$h_{xx} = -\cos(\theta) \sin(2\phi) h_{\times} + (\cos^2(\theta) \cos \phi^2 - \sin \phi^2) h_{+} \quad (\text{I.1})$$

$$h_{yy} = \cos \theta \sin 2\phi h_{\times} + (\cos \theta^2 \sin \phi^2 - \cos \phi^2) h_{+} \quad (\text{I.2})$$

The antenna response at DC is proportional to $|h_{yy} - h_{xx}|$. The next three plots show this DC response for + waves, for \times waves, and for unpolarized waves (quadrature sum of the two cases). In the coordinate system used in these plots, the interferometer is located at the origin with the arms parallel to the x and y axes.

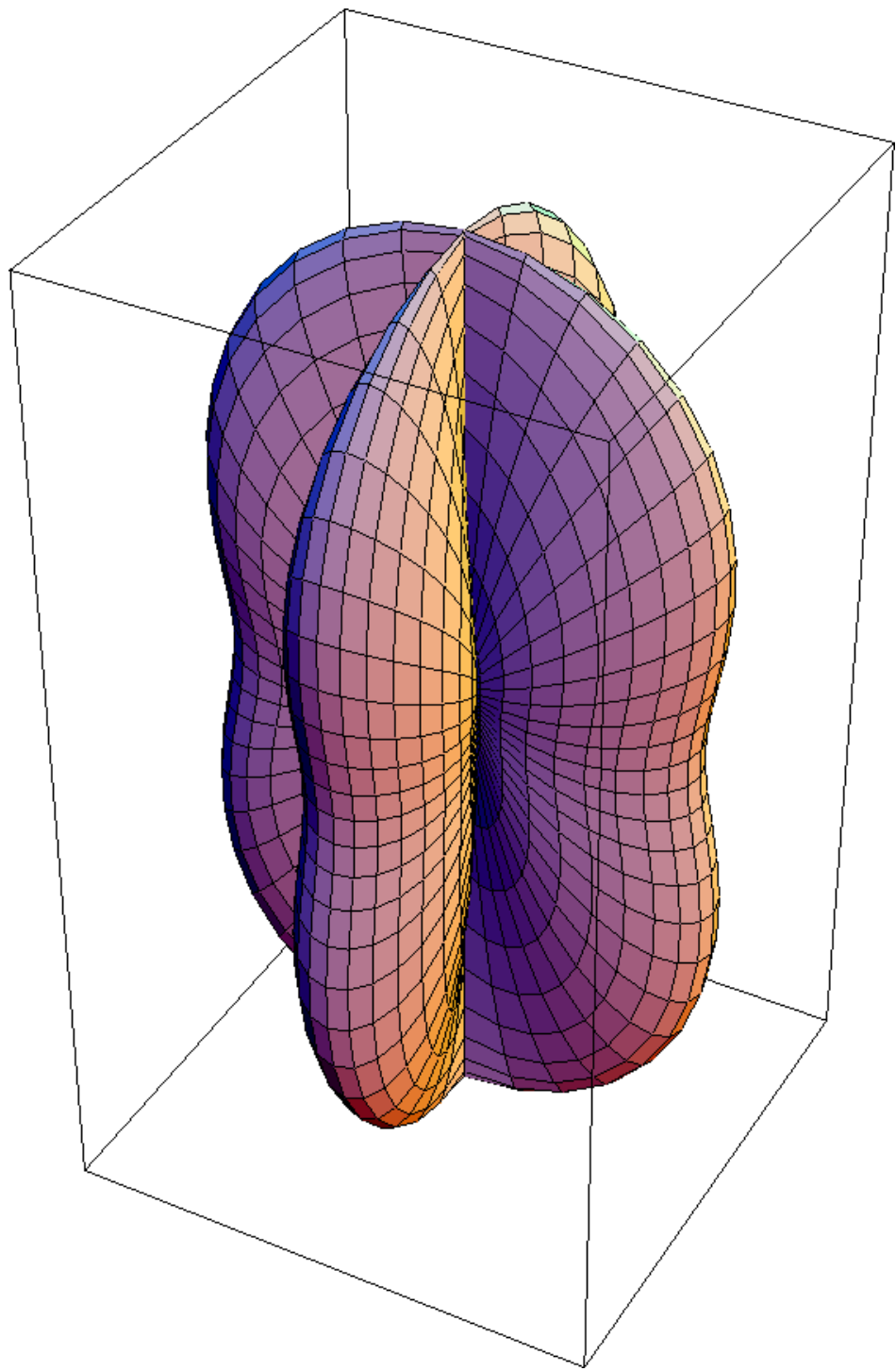


Figure I-1: Antenna response for the + polarization.

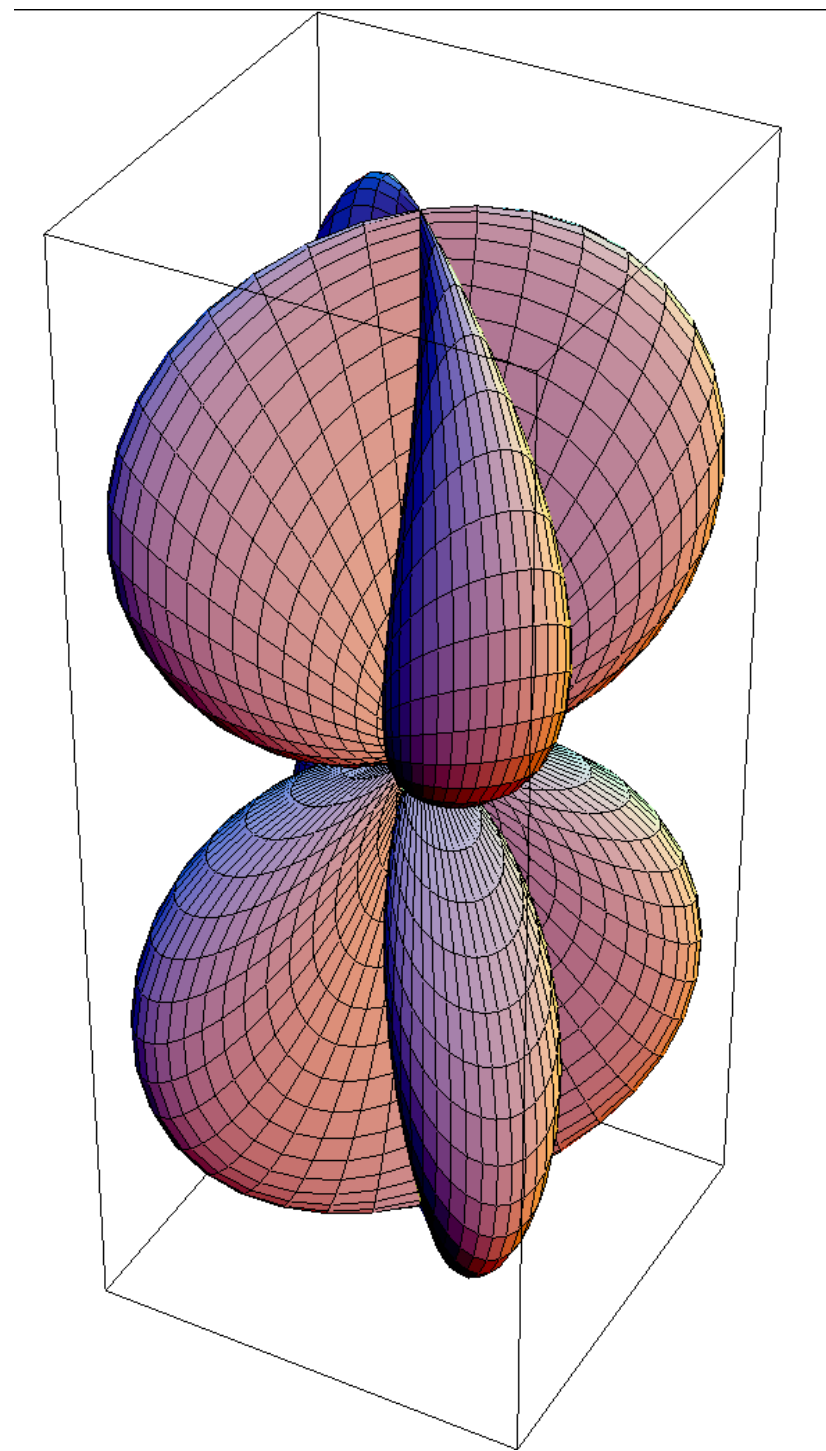


Figure I-2: Antenna response for the \times polarization.

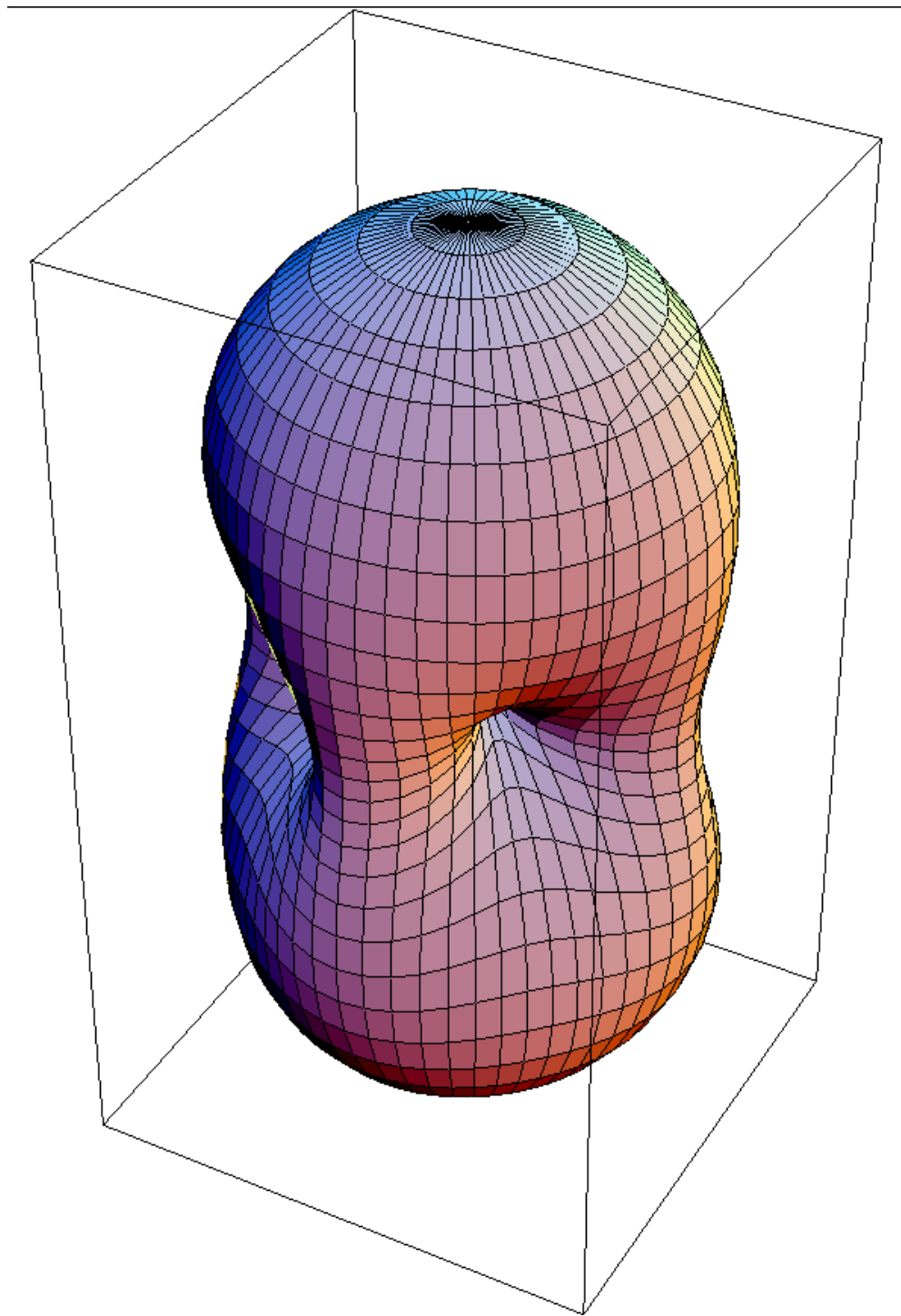


Figure I-3: Antenna response for the unpolarized waves. This is plotted as just the quadrature sum of the + and \times waves.

Bibliography

- [1] B. Willke and the GEO 600 Collaboration. Status of GEO 600. *Class. Quant. Grav.*, 21:S417–S423, 2004.
- [2] R. Takahashi and the TAMA Collaboration. Status of TAMA 300. *Class. Quant. Grav.*, 21:S403–S408, 2004.
- [3] Daniel Sigg. Commissioning of LIGO detectors. *Class. Quant. Grav.*, 21:S409–S415, 2004.
- [4] R. Weiss and B. Barish. LIGO and the detection of gravitational waves. *Physics Today*, 52:44–50, 1999. LIGO-P990039-00-R.
- [5] F. Frasconi for the VIRGO Collaboration. Status of VIRGO. *Class. Quant. Grav.*, 21:S385–S394, 2004.
- [6] Albert Einstein. *The Meaning of Relativity*. Princeton University Press, 5th edition, 1922.
- [7] C. W. Misner, K. S. Thorne, and J. A. Wheeler. *Gravitation*. W. H. Freeman and Co., 1970.
- [8] Kip Thorne. *300 Years of Gravitation*, chapter 9, page 390. Camb. Univ. Press, 1987.
- [9] L. D. Landau and E. M. Lifshitz. *The Classical Theory of Fields*. Pergamon Press, Ltd., 1951.

- [10] Kip S. Thorne. Probing black holes and relativistic stars with gravitational waves. arXiv, June 1997. <http://xxx.lanl.gov/abs/gr-qc/9706079>.
- [11] L. Bildsten. Gravitational radiation and rotation of accreting neutron stars. *Astro. Journal*, 501:L89–L93, 1998.
- [12] D. Chakrabarty, E. H. Morgan, M. P. Muno, D. K. Galloway, R. Wijnands, M. van der Klis, and C. B. Markward. Nuclear-powered millisecond pulsars and the maximum spin frequency of neutron stars. *Nature*, 424:42–44, July 2003.
- [13] Mark Hereld. *A Search for Gravitational Radiation from PSR 1937+214*. PhD thesis, California Institute of Technology, 1983.
- [14] Mike Zucker. *Experiments with a Laser Interferometric Gravitational Wave Antenna*. PhD thesis, California Institute of Technology, July 1988.
- [15] LIGO Scientific Collaboration. Setting upper limits on the strength of periodic gravitational waves from PSR j1939 + 2134 using the first science data from the GEO600 and LIGO detectors. *Phys. Rev. D*, 2004.
- [16] LIGO Scientific Collaboration. Analysis of first LIGO science data for stochastic gravitational waves. *arXiv*, 2003. <http://xxx.lanl.gov/abs/gr-qc/0312088>.
- [17] B. Allen. The stochastic gravity-wave background:sources and detection. In J.A. Marck and J. P. Lasota, editors, *Proceedings of the Les Houches School on Astrophysical Sources of Gravitational Waves*, page 373, Les Houches, 1995. Revised version: <http://xxx.lanl.gov/abs/gr-qc/9604033>.
- [18] Nelson Christensen. *On Measuring the Stochastic Gravitational Radiation Background with Laser Interferometric Antennas*. PhD thesis, Massachusetts Institute of Technology, August 1990.
- [19] Nelson Christensen. Measuring the stochastic gravitational-radiation background with laser-interferometric antennas. *Phys. Rev. D*, 46(12):5250–5266, 1992.

- [20] B. Allen and J. Romano. Detecting a stochastic background of gravitational radiation: Signal processing strategies and sensitivities. *Phys. Rev. D*, 59:102001, 1999.
- [21] Viviana Fafone. Resonant-mass detectors: status and perspectives. *Class. Quantum Grav.*, 21:S377–S383, 2004.
- [22] B. L. Brown, A. P. Mills, and J. A. Tyson. Results of a 440-day search for gravitational radiation. *Phys. Rev. D*, 26(6):1209–1218, September 1982.
- [23] B. Allen. A χ^2 time-frequency discriminator for gravitational wave detection. *arXiv*, pages gr-qc/0405045, 2004. <http://xxx.lanl.gov/abs/gr-qc/0405045>.
- [24] A. Buonanno, Y. Chen, and M. Vallisneri. Detection template families for gravitational waves from the final stages of binary black-hole inspirals: Nonspinning case. *Phys. Rev. D*, 67:024016, 2003.
- [25] G. Calabrese, J. Pullin, O. Sarbach, and M. Tiglio. Convergence and stability in numerical relativity. *Phys. Rev. D*, 66(4):041501, 2002.
- [26] M. Burgay, N. D’Amico, A. Possenti, R. N. Manchester, A. G. Lyne, B. C. Joshi, M. A. McLaughlin, M. Kramer, J. M. Sarkissian, F. Camilo, V. Kalogera, C. Kim, and D. R. Lorimer. An increased estimate of the merger rate of double neutron stars from observations of a highly relativistic system. *Nature*, 426:531–533, 2003.
- [27] C. Kim, V. Kalogera, D. R. Lorimer, M. Ihm, and K. Belczynski. The galactic double-neutron-star merger rate: Most current estimates. In F. Rasio, editor, *Binary Radio Pulsars*, 2004. <http://xxx.lanl.gov/abs/astro-ph/0405564>.
- [28] R. A. Hulse and J. H. Taylor. Discovery of a pulsar in a binary system. *Astrophys. Journ.*, 195:L51–L53, 1975.
- [29] J. M. Weisberg and J. H. Taylor. General relativistic geodetic spin precession in binary pulsar B1913+16: mapping the emission beam in two dimensions. *Astrophys. Journ.*, 576(2):942–949, 2002.

- [30] D. J. Champion, D. R. Lorimer, M. A. McLaughlin, J. M. Cordes, Z. Arzoumanian, J. M. Weisberg, and J. H. Taylor. PSR J1829+2456: a relativistic binary pulsar. *Mon. Not. R. Astron. Soc.*, 000:1–5, March 2004.
- [31] LIGO Scientific Collaboration. Analysis of LIGO data for gravitational waves from binary neutron stars. *Phys. Rev. D*, 69:122001, 2004.
- [32] B. Allen, J. K. Blackburn, P. R. Brady, J. D. E. Creighton, T. Creighton, S. Droz, A. D. Gillespie, S. A. Hughes, S. Kawamura, T. T. Lyons, J. E. Mason, B. J. Owen, F. J. Raab, M. W. Regehr, B. S. Sathyaprakash, Jr. R. L. Savage, S. Whitcomb, and A. G. Wiseman. Observational limit on gravitational waves from binary neutron stars in the galaxy. *Phys. Rev. Lett.*, 83:1498–1501, 1999.
- [33] H. Tagoshi et al. First search for gravitational waves from inspiraling compact binaries using TAMA300 data. *Phys. Rev. D*, 63, 2001.
- [34] S. F. Portegies-Zwart and S. L. W. McMillan. Black hole mergers in the universe. *Astrophys. J. Lett.*, 528:L17–L20, 2000.
- [35] R. P. Kerr. Gravitational field of a spinning mass as an example of algebraically special metrics. *Phys. Rev. Lett.*, 11:237–238, 1963.
- [36] E. E. Flanagan and S. A. Hughes. Measuring gravitational waves from binary black hole coalescences. i. signal to noise for inspiral, merger, and ringdown. *Phys. Rev. D*, 57(8):4535–4565, 1998.
- [37] S. L. Shapiro and S. A. Teukolsky. *Black Holes, White Dwarfs, and Neutron Stars*. John Wiley & Sons, 1983.
- [38] K. D. Kokkotas and B. G. Schmidt. Quasi-normal modes of stars and black holes. <http://relativity.livingreviews.org/Articles/lrr-1999-2/>, 1999.
- [39] T. Regge and J. A. Wheeler. Stability of a Schwarzschild singularity. *Phys. Rev.*, 108(4):1063–1069, 1957.

- [40] S. Chandrasekhar and S. Detweiler. The quasi-normal modes of the Schwarzschild black hole. *Proc. R. Soc. Lond. A*, 344(1639):441–452, Aug 1975.
- [41] F. Echeverria. Gravitational-wave measurements of the mass and angular momentum of a black hole. *Phys. Rev. D*, 40(10):3194–3203, 1989.
- [42] E. W. Leaver. An analytic representation for the quasi-normal modes of Kerr black holes. *Proc. R. Soc. Lond.*, A(402):285–298, 1985.
- [43] Jolien D. E. Creighton. Search techniques for gravitational waves from black-hole ringdowns. *Phys. Rev. D*, 60:022001–022009, June 1999.
- [44] S. L. Detweiler. Black holes and gravitational waves: Perturbation analysis. In L. L. Smarr, editor, *Sources of Gravitational Radiation*, pages 211–243, Seattle, WA, July 1979. Battelle, Camb. Univ. Press.
- [45] Y. Tsunesada and the TAMA Collaboration. Search for gravitational waves from black-hole ringdowns using TAMA300 data. *Class. Quantum Grav.*, 21:S703–S708, 2004.
- [46] J. Weber. Detection and generation of gravitational waves. *Phys. Rev.*, 117:306–313, 1960.
- [47] J. L. Levine and R. L. Garwin. New negative result for gravitational wave detection and comparison with reported detection. *Phys. Rev. Lett.*, 33(13):794–797, September 1974.
- [48] J. A. Tyson. Null search for bursts of gravitational radiation. *Phys. Rev. Lett.*, 31(5):326–329, July 1973.
- [49] J. Weber. Evidence for discovery of gravitational radiation. *Phys. Rev. Lett.*, 22:1320–1324, 1969.
- [50] C. W. Misner, R. A. Breuer, D. R. Brill, P. L. Chrzanowski, H. G. Hughes, and C. M. Pereira. Gravitational synchrotron radiation in the Schwarzschild geometry. *Phys. Rev. Lett.*, 28:998–1001, 1972.

- [51] S.W. Hawking. Theory of the detection of short bursts of gravitational radiation. *Phys. Rev. D*, 4:2191–2197, 1971.
- [52] A. Morse, W. O. Hamilton, W. W. Johnson, E. Mauceli, and M. P. McHugh. Calibration and sensitivity of resonant-mass gravitational wave detectors. *Phys. Rev. D*, 59, 1999.
- [53] M. Cerdonio, L. Conti, J. A. Lobo, A. Ortolan, L. Taffarello, and J. P. Zendri. Wideband dual sphere detector of gravitational waves. *Phys. Rev. Lett.*, 87, 2001.
- [54] F. A. E. Pirani. *Acta. Phys. Polon.*, 15:389, 1956.
- [55] G.F. Moss, L.R. Miller, and R.L. Forward. Photon-noise-limited laser transducer for gravitational antenna. *Applied Optics*, 10:2495–2498, 1971.
- [56] Rainer Weiss. Electromagnetically coupled broadband gravitational antenna. Quarterly Progress Report 105, Research Laboratory of Electronics, MIT, April 1972.
- [57] Jun Mizuno. *Comparison of optical configurations for laser-interferometric gravitational-wave detectors*. PhD thesis, Max-Planck-Institut Fur Quantenoptik, July 1995.
- [58] Rai Weiss. Caltech/MIT project for a laser interferometer gravitational wave observatory. Proposal to the National Science Foundation, 1987.
- [59] K. X. Sun, M. M. Fejer, E. G. Gustafson, and R. L. Byer. Sagnac interferometer for gravitational wave detection. *Phys. Rev. Lett.*, 76(16), April 1996.
- [60] Ronald W. P. Drever. Interferometric detectors of gravitational radiation. In N. Deruelle and T. Piran, editors, *Gravitational Radiation*, pages 321–338, Centre de Physique des Houches, 1982.
- [61] D. R. Herriot and H. J. Schulte. Folded optical delay lines. *Appl. Opt.*, 4(883–889), 1965.

- [62] D. Shoemaker, R. Schilling, L. Schnupp, W. Winkler, K. Maischberger, and A. Rdiger. Noise behavior of the garching 30-meter prototype gravitational-wave detector. *Phys. Rev. D*, 38(2):423–432, July 1988.
- [63] Ch. Fabry and A. Perot. On a new form of interferometer. *Astrophys. J.*, 13:265–272, 1901.
- [64] Peter K. Fritschel. *Techniques for Laser Interferometer Gravitational Wave Detectors*. PhD thesis, Massachusetts Institute of Technology, February 1992.
- [65] D. Schnier, J. Mizuno, G. Heinzel, H. Lück, A. Rüdiger, R. Schilling, M. Schrempel, W. Winkler, and K. Danzmann. Power recycling in the garching 30 m prototype interferometer for gravitational-wave detection. *Phys. Lett. A*, 225:210–216, 1997.
- [66] Martin W. Regehr. *Signal Extraction and Control for an Interferometric Gravitational Wave Detector*. PhD thesis, Caltech, 1995.
- [67] Daniel Sigg. Frequency response of the LIGO interferometer. Technical report, MIT, 1997. LIGO-T970084-00-D.
- [68] R. V. Pound. Electronic frequency stabilization of microwave oscillators. *Rev. Sci. Inst.*, 17:490–505, 1946.
- [69] R. W. P. Drever, J. L. Hall, F. V. Kowalski, J. Hough, G. M. Ford, A. J. Munley, and H. Ward. Laser phase and frequency stabilization using an optical resonator. *Appl. Phys. B*, 31:97–105, June 1983.
- [70] A. BenMenahem and Sarva Jit Singh. *Seismic Waves and Sources*. Springer-Verlag, 1981. 776-796.
- [71] J. Giaime, P. Saha, D. Shoemaker, and L. Sievers. A passive vibration isolation stack for LIGO: Design, modeling, and testing. *Rev. Sci. Inst.*, 67:208–214, 1996.

- [72] H. B. Callen and T. A. Welton. Irreversibility and generalized noise. *Phys. Rev.*, 83:34–40, 1951.
- [73] Peter R. Saulson. *Fundamentals of Interferometric Gravitational Wave Detectors*. World Scientific, 1994.
- [74] A. Gillespie and F. Raab. Thermally excited vibrations of the mirrors of laser interferometer gravitational-wave detectors. *Phys. Rev. D*, 52:577–585, 1995.
- [75] G. I. González and P. R. Saulson. Brownian motion of a mass suspended by an anelastic wire. *Journal of the Acoustical Society of America*, 96:207–212, 1994.
- [76] Yu. Levin. Internal thermal noise in the LIGO test masses: a direct approach. *Physical Review D*, 57:659–663, 1998.
- [77] G. M. Harry, A. M. Gretarsson, P.R. Saulson, S. E. Kittelberger, S.D. Penn, W.J. Startin, S. Rowan, M.M. Fejer, D.R.M. Crooks, G. Cagnoli, J. Hough, and N. Nakagawa. Thermal noise in interferometric gravitational wave detectors due to dielectric optical coatings. *Class. Quantum Grav.*, 19:897–917, 2002.
- [78] Gregg Harry. personal communication.
- [79] Gabriela González. Suspension thermal noise in the LIGO gravitational wave detector. *Class. Quantum Grav.*, 17:4409–4435, 2000. <http://arxiv.org/abs/gr-qc/0006053>.
- [80] G. Cagnoli, L. Gammaitoni, J. Kovalik, F. Marchesoni, and M. Punturo. Suspension losses in low-frequency mechanical pendulums. *Phys. Lett. A*, 213:245–252, 1996.
- [81] Joe Kovalik. private communication.
- [82] GariLynn Billingsley. LIGO core optics components website. <http://www.ligo.caltech.edu/~gari/index.htm>, 2002. A compilation of specifications and metrology data for the LIGO core optics.

- [83] C. M. Caves. Quantum-mechanical radiation-pressure fluctuations in an interferometer. *Phys. Rev. Lett.*, 45(2):75–79, July 1980.
- [84] Amnon Yariv. *Quantum Electronics*. John Wiley and Sons, Inc., Caltech, 1989.
- [85] P. Fritschel, A. Jeffries, and T. Kane. Frequency fluctuations of a diode-pumped Nd:YAG ring laser. *Optics Lett.*, 14(18):993–995, Sep 1989.
- [86] Dennis Coyne. Determination of the wedge angles for the core optics components. Technical report, LIGO/Caltech, 1997. <http://www.ligo.caltech.edu/docs/T/T970091-00.pdf>.
- [87] C. M. Caves. Quantum-mechanical noise in an interferometer. *Phys. Rev. D*, 23(8):1693–1708, April 1981.
- [88] T. M. Niebauer, R. Schilling, K. Danzmann, A. Rüdiger, and W. Winkler. Nonstationary shot noise and its effect on the sensitivity of interferometers. *Phys. Rev. A*, 43(9):5022–5029, 1991.
- [89] B. J. Meers and K. A. Strain. Modulation, signal, and quantum noise in interferometers. *Phys. Rev. A*, 44(7):4693–4703, October 1991.
- [90] Brian T. Lantz. *Quantum Limited Optical Phase Detection in a High Power Suspended Interferometer*. PhD thesis, Massachusetts Institute of Technology, February 1999.
- [91] P. Fritschel, G. Gonzalez, B. Lantz, P. Saha, and M. Zucker. High power interferometric phase measurement limited by quantum noise and the application to the detection of gravitational waves. *Phys. Rev. Lett.*, 80:3181–3184, 1998. LIGO-P970009-00-R.
- [92] Y. Hefetz, N. Mavalvala, and D. Sigg. Principles of calculating alignment signals in complex resonant optical interferometers. *J. Opt. Soc. Am. B*, 14(7):1597+, 1997. LIGO-P960024-A-D.

- [93] P. Fritschel, R. Bork, G. González, N. Mavalvala, D. Ouimette, H. Rong, D. Sigg, and M. Zucker. Readout and control of a power-recycled interferometric gravitational-wave antenna. *Applied Optics*, 40(28):4988–4998, October 2001.
- [94] The LIGO Scientific Collaboration. Detector description and performance for the first coincidence observations between LIGO and GEO. *Nucl.Instrum.Meth.*, 517:154–179, 2004.
- [95] B. Bhawal, M. Evans, H. Yamamoto, M. Rakhmanov, and V. Sannibale. The LIGO end-to-end simulation program. In J. Dumarchez and J. Tran Thanh Van, editors, *Proceedings of the XXXVIIIth Rencontres de Moriond workshop on “Gravitational Waves and Experimental Gravity”*, pages 131–138, 2004.
- [96] P. Fritschel, G. González, N. Mavalvala, D. Shoemaker, D. Sigg, and M. Zucker. Alignment of a interferometric gravitational wave detector. *Applied Optics*, 37:6734–6747, 1998.
- [97] Nergis Mavalvala. *Alignment Issues in Laser Interferometric Gravitational-Wave Detectors*. PhD thesis, Massachusetts Institute of Technology, 1997. January.
- [98] F. Raab and M. Fine. The effect of earth tides on LIGO interferometers. Technical report, LIGO project, 1997. <http://www.ligo.caltech.edu/docs/T/T970059-01.pdf>.
- [99] J. A. Giaime, E. J. Daw, M. Weitz, R. Adhikari, P. Fritschel, R. Abbott, R. Bork, and J. Heefner. Feedforward reduction of the microseism disturbance in a long-base-line interferometric gravitational-wave detector. *Rev. Sci. Inst.*, 74:218–224, 2003.
- [100] J. A. Giaime, E. J. Daw, R. Adhikari, H. Overmier, G. Taylor, and J. Hanson. 2 DOF active isolation of a gravitational wave interferometer. *Rev. Sci. Inst.*, 94:218–224, 2003.

- [101] R. Adhikari, G. González, M. Landry, and B. O'Reilly (for the LIGO Scientific Collaboration). Calibration of the LIGO detectors for the first LIGO science run. *Class. Quantum Grav.*, 20(17):S903–S914, 2003.
- [102] G. González, M. Landry, and B. O'Reilly. Calibration of the LIGO detectors for S2. Technical report, LIGO, 2004. <http://www.ligo.caltech.edu/docs/T/T040060-00.pdf>.
- [103] B. Allen, W. Hua, and A. Ottewill. Automatic cross-talk removal from multi-channel data. *arXiv*, pages gr-qc/9909083, 1999. <http://xxx.lanl.gov/abs/gr-qc/9909083>.
- [104] S. Chatterji, L. Blackburn, and E. Katsavounidis. Multiresolution techniques for the detection of gravitational-wave bursts. submitted to *Class. Quantum Grav.*, 2004.
- [105] B. J. Owen. Search templates for gravitational waves from inspiraling binaries: Choice of template spacing. *Phys. Rev. D*, 53(12):6749–6761, June 1996.
- [106] N. Arnaud, M. Barsuglia, M. Bizouard, V. Brisson, F. Cavalier, M. Davier, P. Hello, S. Kreckelbergh, and E. K. Porter. Elliptic tiling method to generate a 2-dimensional set of templates for gravitational wave research. *Phys. Rev. D*, 67:102003, 2003.
- [107] H. Nakano, H. Takahashi, H. Tagoshi, and M. Sasaki. An effective search method for gravitational ringing of black holes. *Phys. Rev. D*, 68:102003, 2003.
- [108] LIGO Scientific Collaboration. First upper limits from LIGO on gravitational wave bursts. *Phys. Rev. D*, 69:102001, 2004.
- [109] Laura Cadonati. Coherent waveform consistency test for LIGO burst candidates. to be published in the GWDW-8 proceedings.
- [110] R. Abbott, R. Adhikari, G. Allen, S. Cowley, E. Daw, D. DeBra, J. Giaime, G. Hammond, M. Hammond, C. Hardham, J. How, W. Hua, W. Johnson,

- B. Lantz, K. Mason, R. Mittleman, J. Nichol, S. Richman, J. Rollins, D. Shoemaker, G. Stapfer, and R. Stebbins. Seismic isolation for advanced LIGO. *Class. Quantum Grav.*, pages 1591–1597, 2002.
- [111] Ryan Lawrence. *Active wavefront Correction in Laser Interferometric Gravitational Wave Detectors*. PhD thesis, Massachusetts Institute of Technology, February 2003.
- [112] V. B. Braginsky, Yu. Levin, and S. Vyatchanin. How to reduce the suspension thermal noise in LIGO without improving the Q's of the pendulum and violin modes. *Measur. Sci. Tech.*, 10:598–606, 1999. <http://arxiv.org/abs/gr-qc/9805031>.
- [113] P. Fritschel and K. Strain. DC readout for advanced LIGO. in preperation, 2003.
- [114] NIST. 2002 codata values. <http://physics.nist.gov/constants/>, 2003. Latest constants as of December 2002.
- [115] Anthony E. Siegman. *Lasers*. University Science Books, Sausalito, California, 1986.
- [116] Matt Evans. *Lock Acquisition in Resonant Optical Interferometers*. PhD thesis, Caltech, 2002.
- [117] M. Evans, N. Mavalvala, P. Fritschel, R. Bork, B. Bhawal, H. Yamamoto, and S. Whitcomb. Lock acquisition of a gravitational wave interferometer. *Optics Lett.*, 27(8):598–600, 2002. LIGO-P010015-A-D.
- [118] W.E. Althouse, S.D. Hand, L.K. Jones, A. Lazzarini, and R. Weiss. Precision alignment of the LIGO 4 km arms using the dual-frequency differential global positioning system. *Rev. Sci. Inst.*, 72(7):3086–3094, July 2001.
- [119] M. Rakhmanov, F. Bondu, O. Debieu, and R. L. Savage Jr. Characterization of the LIGO 4 km fabry-perot cavities via their high-frequency dynamic responses

to length and laser frequency variations. *Class. Quantum Grav.*, 21:S487–S492, 2004.

- [120] Andri Gretarsson. personal communication.
- [121] Rai Weiss. Compilation of metrology data for the LIGO large optics. Technical report, MIT, 1998. <http://www.ligo.caltech.edu/docs/T/T980065-00.pdf>.
- [122] A. Gillespie and F. Raab. Suspension losses in the pendula of laser interferometer gravitational-wave detectors. *Phys. Lett. A*, 190:213–220, July 1994.
- [123] R. Savage, P. King, and S. Seel. A highly stabilized 10-watt Nd:YAG laser for LIGO. *Laser Phys.*, 8:679, 1998.
- [124] R. S. Abbott and P. K. King. Diode-pumped Nd:YAG laser intensity noise suppression using a current shunt. *Rev. Sci. Inst.*, 72:1346–1349, 2001.
- [125] Daniel Sigg. Gravitational waves. In *Proceedings of TASI 98*, Boulder, CO, 1998. LIGO-P980007-00-D.